

REPORT DOCUMENTATION PAGE				Form Approved OMB No. 0704-0188	
Public reporting burden for this collection of information is estimated to average 1 hour per response, including the time for reviewing instructions, searching existing data sources, gathering and maintaining the data needed, and completing and reviewing the collection of information. Send comments regarding this burden estimate or any other aspect of this collection of information, including suggestions for reducing the burden, to Department of Defense, Washington Headquarters Services, Directorate for Information Operations and Reports (0704-0188), 1215 Jefferson Davis Highway, Suite 1204, Arlington, VA 22202-4302. Respondents should be aware that notwithstanding any other provision of law, no person shall be subject to any penalty for failing to comply with a collection of information if it does not display a currently valid OMB control number. PLEASE DO NOT RETURN YOUR FORM TO THE ABOVE ADDRESS.					
1. REPORT DATE (DD-MM-YYYY) 31-03-2006		2. REPORT TYPE Final Report		3. DATES COVERED (From – To) 13-Aug-01 - 31-Mar-06	
4. TITLE AND SUBTITLE Active Laser And Raman Materials For 1.3-5 Um Spectral Range			5a. CONTRACT NUMBER ISTC Registration No: 2022p		
			5b. GRANT NUMBER		
			5c. PROGRAM ELEMENT NUMBER		
6. AUTHOR(S) Professor Tasoltan Basiev			5d. PROJECT NUMBER		
			5d. TASK NUMBER		
			5e. WORK UNIT NUMBER		
7. PERFORMING ORGANIZATION NAME(S) AND ADDRESS(ES) General Physics Institute of the Russian Academy of Sciences 38 Vavilov St Moscow 117942 Russia				8. PERFORMING ORGANIZATION REPORT NUMBER N/A	
9. SPONSORING/MONITORING AGENCY NAME(S) AND ADDRESS(ES) EOARD PSC 821 BOX 14 FPO 09421-0014				10. SPONSOR/MONITOR'S ACRONYM(S)	
				11. SPONSOR/MONITOR'S REPORT NUMBER(S) ISTC 00-7042	
12. DISTRIBUTION/AVAILABILITY STATEMENT Approved for public release; distribution is unlimited.					
13. SUPPLEMENTARY NOTES					
14. ABSTRACT This report results from a contract tasking General Physics Institute of the Russian Academy of Sciences as follows: The spectral range of 4 - 5 um is one of the most interesting atmospheric optical transmission windows. High peak power laser sources operating in this region are of special importance for various lidar applications. Solid state lasers with their compactness, high efficiency, and reliability in rugged conditions are quite promising for these purposes. Active laser materials for the mid IR spectral range (1.3-5 um), based on rare-earth doped heavy metal fluoride, chloride, and sulfide crystals and glasses will be developed, synthesized, studied, and tested. Selective laser pumping, laser oscillation, fluorescence decay and spectral measurements as well as radiative and nonradiative transitions calculations and optimization will be done. Stimulated Raman Scattering (SRS) nonlinear process was discovered in 1962 at the beginning of the laser era. Now application of solid-state Raman materials for stimulated Raman scattering (SRS) is one of the most perspective ways to develop high-gain, reliable, and small-size devices for shifting laser radiation frequency in new spectral regions. SRS devices are very promising for covering near and mid-infrared spectral range from 1.3 to 5 microns, which fits a lot of molecular resonances and is one of the best atmospheric windows for laser lidars. Prospective Raman materials for coherent radiation frequency shifting in mid IR will be studied and developed. Integral and peak Raman scattering cross-section, line broadening, gain, lasing and laser damage threshold measurements will be performed and analyzed. A number of Raman laser optical schemes and oscillation regimes with various pulse durations, wavelengths, spectral widths, and peak and average powers will be tested and characterized. Such solid-state and Raman lasers will be useful for communications in the atmosphere, lidar, medical practices, atmospheric probing, and environmental sensing.					
15. SUBJECT TERMS EOARD, Physics, Optics					
16. SECURITY CLASSIFICATION OF:			17. LIMITATION OF ABSTRACT UL	18. NUMBER OF PAGES 182	19a. NAME OF RESPONSIBLE PERSON DONALD J SMITH
a. REPORT UNCLAS	b. ABSTRACT UNCLAS	c. THIS PAGE UNCLAS			19b. TELEPHONE NUMBER (Include area code) +44 (0)20 7514 4953

**RUSSIAN ACADEMY OF SCIENCES
LASER MATERIALS AND TECHNOLOGIES RESEARCH CENTER OF
GENERAL PHYSICS INSTITUTE**

**ACTIVE LASER AND RAMAN MATERIALS FOR 1.3 - 5 MICRON
SPECTRAL RANGE**

Final report

Contract ISTC 2022p/ EOARD 207042

March, 2006

Moscow, Russia

Content

1 Theoretical and experimental study of rare – earth ions doped crystals for mid – IR 3 – 5 μm lasing	
1.1 Development of the nonlinear theory of multiphonon relaxation.....	3
1.2 Mid- IR and one micron transitions of trivalent neodymium in low phonon laser crystals	10
2 Research and development of laser ceramics	
2.1 Oxide ceramics.....	51
2.2 Fluoride ceramics.....	98
3 New high-efficient laser crystals operating under diode pumping (970 – 980 nm)	
3.1 Comparative study Yb-lasers and $\text{LiF:F}_2^{\cdot-}$ color center laser under LD pumping.....	113
3.2 Tungstate and molybdate crystals doped with Nd^{3+} ions for high efficient 1 μm lasers.....	145
4 New cavity schemes of high-power solid state lasers	
4.1 Efficient powerful single-mode Nd:YAG lasers with diffractively coupled self-phase-conjugate and self-phase-locked resonators.....	164
4.2 New cavity schemes for high-power lasers based on dielectric diffractive optics.....	172

I. Theoretical and experimental study of rare – earth ions doped crystals for mid – IR 3 – 5 μm lasing

1.1 Development of the nonlinear theory of multiphonon relaxation

Multiphonon relaxation (MR) rate of the energy of electronic excitation is the key parameter which determines the rate of population of initial laser level and the rate of depletion of the low laser level in four-level laser scheme for one micron lasing. Here, the faster the rate of multiphonon relaxation the easier to prepare population inversion at the initial laser level. On the other hand, the multiphonon transitions bypass the mid IR radiative transitions. And, here multiphonon relaxation should be minimized. The theory of multiphonon relaxation can be helpful for search of solid state laser matrixes with increased rates of MR for one- micron lasing and reduced rates of MR for mid IR lasing. In this connection during the reporting period we developed the nonlinear theory of multiphonon relaxation, which was used for the subsequent experimental results analysis.

In the frame of nonlinear theory of multiphonon relaxation [1-7] the total p - phonon transition probability $W_{J' \rightarrow J}(p)$ between the two J manifolds can be written in a form similar to Judd-Ofelt expression for an electro- dipole radiative transition probability between the same manifolds (see below first term of Eq. (1.2.5):

$$W_{J' \rightarrow J}(p) = \sum_{k=2,4,6} \omega_1^2(k, p) (LSJ \| U^{(k)} \| L'S'J')^2 J^{(p)}(\Omega_{JJ}) / (2J' + 1). \quad (1.1.1)$$

Here $\omega_1^2(k, p)$ depends on parameters of static crystal field; $(LSJ \| U^{(k)} \| L'S'J')$ is the reduced matrix element of the unit tensor operator $U^{(k)}$ of rank k that specifies the $J' \rightarrow J$ transition (the values of $(LSJ \| U^{(k)} \| L'S'J')^2$ are tabulated [8]); the frequency $\Omega_{JJ} = \Delta E_{JJ} / \hbar$, and ΔE_{JJ} is the energy gap between lowest Stark level of the manifold J' and highest Stark level of manifold J . The spectral $J^{(p)}(\Omega)$ is equal to:

$$J^{(p)}(\Omega) = \int_{-\infty}^{\infty} e^{i\Omega t} [K(t)]^n dt, \quad (1.1.2)$$

where the correlation function of the displacements

$$K(t) = \langle \mathbf{u}(t)\mathbf{u} \rangle / 3R_0^2 . \quad (1.1.3)$$

In Eq. (1.1.3) the symbol $\langle \dots \rangle$ denotes the average over the thermal lattice vibrations, R_0 is equilibrium distance between nearest ligand and RE ion; $\mathbf{u} = \mathbf{u}_L - \mathbf{u}_{RE}$; \mathbf{u}_L and \mathbf{u}_{RE} are the ligand and RE ion displacements from their equilibrium positions, respectively. It should be mentioned that $J^{(p)}(\Omega)$ depends on R_0 and the characteristics of the phonon subsystem, only.

The combined electronic factor $\omega_1^2(k, p)$ accounts for both the point-charge and the exchange-charge interaction between rare-earth ion and the nearest ligands can be presented as:

$$\omega_1^2(k, p) = \omega_{PC}^2(k, p) + \omega_{EX}^2(k, p) \quad (1.1.4)$$

with

$$\omega_{PC}^2(k, p) = Z \left(\frac{a_k^0}{4\pi\hbar} \right)^2 \begin{pmatrix} l & l & k \\ 0 & 0 & 0 \end{pmatrix}^2 (2l+1)^2 (2k+1) \frac{(2p+2k)!}{(2k)!p!2^p} \quad (1.1.5)$$

$$\omega_{EX}^2(k, p) = Z \left(\frac{b_k^0}{4\pi\hbar} \right)^2 \begin{pmatrix} l & l & k \\ 0 & 0 & 0 \end{pmatrix}^2 (2l+1)^2 (2k+1) \Phi_{kp} . \quad (1.1.6)$$

In Eqs. (1.1.5) – (1.1.6) Z is the number of the anions nearest to the RE ion; l is the orbital angular momentum of optical electrons ($l = 3$ for 4f electrons); $\begin{pmatrix} l & l & k \\ 0 & 0 & 0 \end{pmatrix}$ is 3j- symbol. In Eq.

(1.1.5) a_k^0 is parameter of point-charge crystal field

$$a_k^0 = \frac{4\pi e q}{(2k+1)} \cdot \frac{\overline{\xi^k}}{R_0^{k+1}} \quad (1.1.7)$$

where e is the electron charge; q is the effective charge of a ligand, and $\overline{\xi^k}$ is the mean value of the k -th power of the radius ξ of optical 4f-electron.

In Eq. (1.1.6) b_k^0 is parameter of exchange-charge crystal field

$$b_k^0 = 8\pi e^2 \left(G_s |S_s(R_0)|^2 + G_\sigma |S_\sigma(R_0)|^2 + \gamma_k G_\pi |S_\pi(R_0)|^2 \right) / (2l+1) R_0 \quad (1.1.8)$$

Here $G_s, G_\sigma, G_\pi = 5 - 10$ are the crystal field fitting parameters in the frame of exchange-charge model [9] which can be determined from fitting of the calculated and measured Stark structure of rare-earth manifolds; $\gamma_k = 2 - k(k+1)/12$; $S_\nu(R_0) = S_\nu^0 \exp(-\alpha_\nu R_0)$ are the overlap integrals of the

4f-electron wave functions with the wave functions of the external electronic shells of the ligands. The parameters α_v and S_v^0 are determined from the R -dependence of the overlap integrals $S_v(R)$. The function $S_v(R)$ is calculated on base of the known Hartree-Fock radial wave functions for RE ions and wave functions of the ligands. For important practical cases (chlorine, sulfur, fluorine and oxygen surrounding the trivalent rare-earth ions) this is the p_σ , p_π , and s orbitals of the ligands; Φ_{kp} can be easily calculated from expression given in Ref. [4].

The greatest difficulties appear in course of calculation of the spectral density $J^{(p)}(\Omega)$. The simplest model of lattice vibration is the single-phonon frequency model (model of “effective phonon”).

For the single-phonon frequency model the spectral density is determined as [1]

$$J^{(p)}(\Omega_{JJ'}) = 2\pi[K(0)]^p [\bar{n}(\omega_{eff}, T) + 1]^p / \omega_{\max} = 2\pi[2\eta]^p [\bar{n}(\omega_{eff}, T) + 1]^p / \omega_{\max}. \quad (1.1.9)$$

Here $p = \Omega_{JJ'} / \omega_{eff}$,

$$\eta = K(0) / 2 = \langle \mathbf{u}^2 \rangle / 6R_0^2 = \langle (\mathbf{u}_L - \mathbf{u}_{RE})^2 \rangle / 6R_0^2 \quad (1.1.10)$$

is parameter of the single-phonon frequency model, and

$$n(\omega, T) = 1 / [\exp(\hbar\omega / kT) - 1] \quad (1.1.11)$$

is the population of a phonon mode of frequency ω at temperature T described by the Bose-Einstein distribution. Thus, for the single-phonon frequency model we have

$$W_{J' \rightarrow J}(p, T) = W_{J' \rightarrow J}^0(p) \eta^p [n(\omega_{eff}, T) + 1]^p \quad (1.1.12)$$

with

$$W_{J' \rightarrow J}^0(p) = [2\pi / \omega_{\max} (2J' + 1)] \sum_{k=2,4,6} \omega_1^2(k, p) (LSJ \parallel U^{(k)} \parallel L'S'J')^2 2^p. \quad (1.1.13)$$

The phonon factor η can be roughly estimated using the following equation [5]:

$$\eta_{est} = [\langle \mathbf{u}_{cat}^2 \rangle + \langle \mathbf{u}_{anion}^2 \rangle] / 6R_0^2 \approx \hbar / 4M \omega_{\max} R_0^2 = \hbar / 8\pi c M \bar{\nu}_{\max} R_0^2, \quad (1.1.14)$$

where c is the velocity of light, $\bar{\nu}_{\max}$ is the maximum phonon frequency of the crystal lattice (in cm^{-1}), and M is the reduced mass of the atoms involved in the vibrations and can be calculated as [5]

$$\frac{1}{M} = \frac{1}{M_{cat}} + \frac{1}{M_{anion}}, \quad (1.1.15)$$

where $M_{\text{cat}} = (\text{Ca, Sr, La, Pb, ...})$; $M_{\text{anion}} = (\text{O, F, S, Cl, ...})$. Hence, values of η_{est} in the range of 10^{-3} - 10^{-4} are expected for the considered crystals.

Below we consider the more realistic (multi-frequency) model of lattice vibration than the single-frequency model of “effective phonon”. At present there are few data about the inelastic neutron scattering by crystals. The neutron scattering data analysis allows to extract the density of phonon states (DPS) $\rho(\omega)$. We shall employ the DPS data for calculation of spectral density $J(\Omega)$.

In approximation

$$K(t) = K(0) \cdot \int_0^{\omega_{\max}} \exp(-i\omega t) \rho(\omega) n(\omega, T) d\omega, \quad (1.1.16)$$

we can derive from Eq. (1.1.10) that

$$J^{(n)}(\Omega) = \int_{-\infty}^{\infty} \exp(i\Omega t) \cdot [K(t)]^n dt = 2\pi [K(0)]^n \rho_n(\Omega), \quad (1.1.17)$$

where the “multiphonon density”

$$\rho_p(\Omega) = \int_0^{\omega_{\max}} d\omega_1 \int_0^{\omega_{\max}} d\omega_2 \dots \int_0^{\omega_{\max}} \rho_T(\omega_1) \rho_T(\omega_2) \dots \rho_T(\omega_p) \delta(\Omega - \omega_1 - \omega_2 - \dots - \omega_p) d\omega_p \quad (1.1.18)$$

is the convolution of the p functions of

$$\rho_T(\omega) = \rho(\omega) [n(\omega, T) + 1]. \quad (1.1.19)$$

We emphasize that in Eqs. (1.1.16) - (1.1.19) the normalized DPS is employed, so

$$\text{that } \int_0^{\omega_{\max}} \rho(\omega) d\omega = 1.$$

Using Eq. (1.1.18) we can write Eq. (1.1.1) in form

$$W_{J' \rightarrow J}(p) = [2\pi / (2J' + 1)] \sum_{k=2,4,6} \omega_1^2(k, p) (LSJ \parallel U^{(k)} \parallel L'S'J')^2 2^p \rho_p(\Omega_{JJ'}) \eta^p \quad (1.1.20a)$$

or, in view of expression (1.1.13), as:

$$W_{J' \rightarrow J}(p) = W_{J' \rightarrow J}^0(p) \omega_{\max} \rho_p(\Omega_{JJ'}) \eta^p = W_{J' \rightarrow J}^0(p) \bar{v}_{\max} \rho_p(\Delta E_{JJ'}) \eta^p. \quad (1.1.20b)$$

(Here \bar{v}_{\max} and $\Delta E_{JJ'}$ are in cm^{-1}).

Thus, total MR rate is given by expression:

$$W_{MR}(J' \rightarrow J) = \sum_p W_{J' \rightarrow J}^0(p) \omega_{\max} \rho_p(\Omega_{JJ'}) \eta^p = \sum_p W_{J' \rightarrow J}^0(p) \bar{\omega}_{\max} \rho_p(\Delta E_{JJ'}) \eta^p \quad (1.1.21)$$

where all combinations of phonon frequencies make contributions to the p -phonon process and summation is made for all p . This multi-frequency model was used for the theoretical analysis of experimental data on multiphonon relaxation rates at $T = 0\text{K}$ in RE doped CaF_2 , SrF_2 , PbF_2 , and BaF_2 crystals [7]. (Here and above it is supposed that the crystal-field splitting ($\Delta\epsilon_{\text{CF}}$) of the low-lying J – manifold is small ($\Delta\epsilon_{\text{CF}} \leq \hbar\omega_{\max}$)). It resolves the contradiction between the “energy gap” law and the dependence of the MR rate W_{MR} on the number of phonon p ($W_{J' \rightarrow J}(p)$). Now, the energy gap always can be bridged by an integer number of phonons p by taking an appropriate combinations of phonon energies within a phonon spectrum of a crystal, which are compatible with the law of conservation of energy

$$\hbar(\omega_1 + \omega_2 + \dots + \omega_p) = \Delta E_{JJ'} \quad (1.1.22).$$

But p with maximum contribution can be determined as well. The outlined theory implies the validity of the continuous approximation for dependencies $\omega(\mathbf{k})$ of phonon frequencies ω on phonon wave vector \mathbf{k} . In general, one must take into account the confinement effects that can lead to impracticability of Eq. (1.1.22) in view of discrete character of frequencies for a grain of small size. Let us discuss the validity of continuous approximation for our samples. As indicated above, the considered ceramics is formed from grains of 30-50 μm size. The density of the Gd_2O_3 and La_2O_3 single crystals are equal to $\rho_{\text{singl.}} = 7.337 \text{ g/cm}^3$ and 6.281 g/cm^3 , respectively. The measured density of respective ceramics is equal to that of a crystal with a precision of a measurement. The porosity $(\rho_{\text{singl.}} - \rho_{\text{ceramics}})/\rho_{\text{singl.}}$ of the considered samples is much less than the unity. (Here ρ_{ceramics} is ceramics density). Taking the grain density equal to single crystal density $\rho_{\text{singl.}}$ we obtain that the 30 μm size grains contains about $N = 10^{14}$ atoms both for the Gd_2O_3 and La_2O_3 ceramics. As discussed above, the value of maximum phonon frequencies ω_{\max} for Gd_2O_3 and La_2O_3 is about 440 cm^{-1} and 400 cm^{-1} , respectively. The average frequency difference $\Delta\omega$ can be roughly estimated as $\Delta\omega = \omega_{\max}/3N$. Using the foregoing data we obtain that $\Delta\omega$ are of the order of 10^{-12} cm^{-1} both for Gd_2O_3 and La_2O_3 grains. This means that the continuous approximation is indubitably applicable to the considered cases and the outlined nonlinear theory of multiphonon relaxation can be used for an analysis of the multiphonon relaxation processes in considered ceramics without any modification.

There is no difficulty for straightforward calculation of “multiphonon density” $\rho_p(\Omega)$ by use of the modern computation technique. Nevertheless, it should be mentioned that a good approximation exists for convolution $\rho_p(\Omega)$ even for $p \geq 3$. Namely, due to the central limit

theorem (see Ref. [10]) the convolution $\rho_p(\Omega)$ can be approximated in range $0 \leq \Omega \leq p\omega_{\max}$ by a Gaussian:

$$\rho_p(\Omega) = \frac{(\bar{\rho}_T)^p}{\sigma\sqrt{2\pi p}} \exp\left[-(\Omega - p\bar{\omega})^2 / 2p\sigma^2\right] \quad (1.1.23)$$

with

$$\bar{\rho}_T = \int_0^{\omega_{\max}} \rho_T(\omega) d\omega, \quad (1.1.24)$$

$$\bar{\omega} = \int_0^{\omega_{\max}} \omega \rho_T(\omega) d\omega / \bar{\rho}_T, \quad (1.1.25)$$

$$\sigma^2 = \int_0^{\omega_{\max}} (\omega - \bar{\omega})^2 \rho_T(\omega) d\omega / \bar{\rho}_T. \quad (1.1.26)$$

At $T = 0$ the values of $\bar{\omega}$ and σ are the mean frequency and dispersion of phonon spectrum, respectively.

References

1. K.K. Pukhov, V.P. Sakun, Phys. Stat. Sol. (b) 95 (1979) 391.
2. K.K.Pukhov, Fiz. Tverd. Tela 31 (1989) 144; [Sov. Phys. Solid State, 31 (1989) 1557].
3. Yu.V.Orlovskii, R.J.Reeves, R.C. Powell, T.T.Basiev, K.K.Pukhov, Phys. Rev. B 49 (1994) 3821.
4. Yu.V.Orlovskii, K.K.Pukhov, T.T.Basiev, T.Tsuboi, Optical Materials 4 (1995) 583.
5. T.T.Basiev, Yu.V.Orlovskii, K.K.Pukhov, V.B.Sigachev, M.E.Doroshenko, I.N.Vorob'ev, Journal of Lumin. 68 (1996) 241.
6. T.T.Basiev, Yu.V.Orlovskii, K.K.Pukhov, F.Auzel, Laser Physics, 7 (1997) 1139.
7. Yu. V. Orlovskii, T. T. Basiev, K. K. Pukhov, N. A. Glushkov, O. K. Alimov, S. B. Mirov, "Multiphonon relaxation of mid IR transitions of rare- earth ions in fluorite type crystals", in *the Proceedings volume of the Advanced Solid-State Photonics 2004*, author: Gregory Quarles, (Optical Society of America, Washington, D.C., TOPS Volume 94, 2004), pp. 440-445.

8. W.T. Carnall, Hannah Crosswhite, and H.M. Crosswhite, “Energy level structure and transition probabilities in the spectra of the trivalent lanthanides in LaF_3 ”, Aragon National Laboratory, Internal Report (1977).
9. B.Z. Malkin, in *Spectroscopy of Solids Containing Rare Earth Ions*, A.A. Kaplyanskii and R.M. Macfarlane, eds. (North-Holland, Amsterdam 1987), Chap. 2.
10. M.D. Sturge, Phys. Rev. B, **8** (1973) 6.

1.2 Mid- IR and one micron transitions of trivalent neodymium in low phonon laser crystals

1.2.1 Mid - IR transitions of Nd³⁺ in low phonon laser crystals

One of the main problems of the 4 - 6 μm mid IR rare- earth (RE) doped laser crystal development is a bypass of radiative transitions by nonradiative ones caused by multiphonon relaxation (MR). This leads to fast excitation decay of the initial laser level and to low fluorescence quantum yield. Hitherto, it was only one theoretically well-proven method to minimize nonradiative losses, namely, to utilize the crystal matrixes with very low phonon spectra. For example, room temperature mid- IR lasing was obtained on Pr³⁺ [1] and Er³⁺ [2] doped chloride laser crystals with very low phonon spectra ($\hbar\omega_{\text{max}} \approx 200 \text{ cm}^{-1}$) due to the heavy anion. The main reason for the vanishingly small values of multiphonon relaxation rates of mid IR transitions in these crystals comparing to oxide and fluoride ones is the much larger number of phonons p bridging the energy gap ΔE to the next manifold below. And, it is a well- known fact that an increase of the number of phonons p by one decreases the MR rate by one – two orders of magnitude [3]. Recently mid IR lasing at 4.3 - 4.4 μm ($\Delta E = 2300 \text{ cm}^{-1}$) of the ${}^6\text{H}_{11/2} \rightarrow {}^6\text{H}_{13/2}$ transition in Dy³⁺ was obtained in calcium (CaGa₂S₄) [4] and lead (PbGa₂S₄) [5] thiogallate laser crystals with the extent of phonon spectra comparable with those for low phonon fluoride crystals like LaF₃ and fluorite- type crystals like SrF₂, CdF₂, BaF₂, and PbF₂. Interestingly, the measured room temperature lifetime of the ${}^6\text{H}_{11/2}$ initial laser level of Dy³⁺ doped PbGa₂S₄ is 2 ms [5] and is only 0.3 ms in BaF₂ [6]. However, the maximum phonon frequencies for these crystals are very close. It is 324 cm^{-1} in BaF₂ [7] and even higher in PbGa₂S₄. Usually in sulfide crystals the maximum phonon frequency is about 350 cm^{-1} . The scope of this paper is to enlarge the existent data on the measured MR rates of mid IR transitions in low phonon fluoride, sulfide and chloride RE doped laser crystals to extend our knowledge on multiphonon relaxation and to explain existing experimental results employing advanced nonlinear theory of multiphonon relaxation [8]. Thereto, measurement of multiphonon relaxation rates of Nd³⁺ low - lying ${}^4\text{I}_{15/2}$ and ${}^4\text{I}_{13/2}$ levels in calcium and lead thiogallate laser crystals are provided using direct laser excitation into the ${}^4\text{I}_{15/2}$ level. The results are compared with the measured MR rates for high-lying ${}^4\text{G}_{7/2}$ and ${}^4\text{G}_{5/2}$; ${}^2\text{G}_{7/2}$ levels of Nd³⁺ in sulfide, chloride, and fluoride crystals.

In Ref. [9-11] it was theoretically predicted and Refs. [8, 12] it was experimentally observed that the MR rates depend strongly on reduced matrix elements of electronic transitions $U^{(k)}$. In this paper it is shown that the MR rates of mid IR transitions in RE doped crystals with

similar phonon spectra (sulfide and fluoride crystals) depend strongly on a rare - earth – ligand distance R_0 . So, an increase of R_0 strongly decreases the MR rates for the same transition of specific rare - earth ion in different crystals with close values of maximum phonon frequencies, while increase of $U^{(k)}$ for different transitions of specific rare - earth ion in one crystal increases the MR rate [13]. This conclusion follows from our studies and is in a good agreement with nonlinear theory of multiphonon relaxation.

Crystals preparation

The PbCl_2 : Nd^{3+} (0.2, 0.5, and 0.8 m. %) crystals were synthesized by Laser Materials and Technology Research Center of General Physics Institute RAS. The PbCl_2 has an orthorhombic crystal structure with the space-group symmetry Pnma . Lattice parameters of the unit cell are $a = 4.526 \text{ \AA}$, $b = 7.605 \text{ \AA}$ and $c = 9.027 \text{ \AA}$. The number of molecules in a unit cell is $z = 4$. The density is 5.94 g/cm^3 .

The PbGa_2S_4 : Nd^{3+} (0.2 and 0.5 m.%) and CaGa_2S_4 : Nd^{3+} (0.16 m.%) crystals were synthesized by High Technologies Laboratory of Kuban State University by modified Bridgman technique in quartz ampoules. The PbGa_2S_4 and CaGa_2S_4 are biaxial crystals having an orthorhombic crystal structure with a space-group symmetry Fddd . The lattice parameters are $a = 20.706 \text{ \AA}$, $b = 20.380 \text{ \AA}$ and $c = 12.156 \text{ \AA}$ for PbGa_2S_4 and $a = 20.122 \text{ \AA}$, $b = 20.090 \text{ \AA}$ and $c = 12.133 \text{ \AA}$ for CaGa_2S_4 . The number of molecules per unit cell is $z = 32$ for both the crystals. The density is 4.92 g/cm^3 for PbGa_2S_4 and 3.34 g/cm^3 for CaGa_2S_4 . The Pb^{2+} or Ca^{2+} ions are partially substituted for Nd^{3+} ions and charge compensation is required during the process of crystal growth. In studied samples the charge compensation of two Nd^{3+} ions is provided by a vacancy and three Pb^{2+} ions and no foreign impurities present in the samples.

Oxygen - free CaF_2 : $\text{LaF}_3(0.25\%)$: $\text{NdF}_3(0.25\%)$ and SrF_2 : $\text{LaF}_3(1\%)$: $\text{NdF}_3(0.2\%)$ crystals with fluorite structure were grown in Laser Materials and Technologies Research Center of General Physics Institute RAS by the Bridgman - Stockbarger technique in a fluorinating atmosphere.

Experimental technique

Absorption spectra of the studied crystals were measured using Shimadzu UV- 3101 PC UV-VIS-NIR spectrophotometer and FTIR absorption spectrometer.

The fluorescence of the $^4\text{I}_{15/2}$ level in PbGa_2S_4 : Nd^{3+} (0.2 m. %) and CaGa_2S_4 : Nd^{3+} (0.16 m. %) at room temperature was excited by 1.61 \mu m wavelength obtained after YAP: Nd pump pulsed laser operating at 1.38 \mu m ($t_p = 40 \text{ ns}$) and solid- state Raman laser based on barium nitrate crystal with Raman shift of 1047 cm^{-1} ($t_p = 30 \text{ ns}$) directly into the maximum of

absorption spectral line. Fluorescence selection was provided by MDR- 23 monochromator (LOMO) with 150 grooves/mm grating. The fluorescence kinetics was detected by a Ge(Au) liquid nitrogen cooled photoresistor with two preamplifiers and digital Tektronix TDS 3032B oscilloscope. A temporal resolution of the whole system was about 10 μ s. The fluorescence spectrum for the direct excitation into the $^4I_{15/2}$ manifold was detected using the Tektronix oscilloscope as Boxcar averager under PC program control.

A sum of fluorescence kinetics decay curves of the low - lying $^4I_{15/2}$, $^4I_{13/2}$, and $^4I_{11/2}$ manifolds of Nd^{3+} (see Fig. 1.2.1 for energy level diagram) and its temperature dependence in $CaGa_2S_4:Nd^{3+}$, $PbGa_2S_4:Nd^{3+}$, and $PbCl_2:Nd^{3+}$ crystals were measured using 1.56 μ m laser excitation into the $^4I_{15/2}$ manifold obtained from the first Stokes of the D_2 Raman shifted 1.06 μ m YAG: Nd laser radiation. To separate pump radiation from fluorescence a special filter, transparent for wavelengths longer than 3 μ m (I.S.P. Optics, CF-BX-50-76) was used. Fluorescence monitoring was provided by a CdHgTe J15D14 photodetector (EG&G Judson) with an input window made from germanium and transparent for wavelengths longer than 2 μ m. The fluorescence signal was amplified by a two stage preamplifier PA-300 with response time of about 2 μ s.

The fluorescence kinetics decay curves and the temperature dependencies of the $^4G_{7/2}$ and $^4G_{5/2}$; $^2G_{7/2}$ manifolds of Nd^{3+} in $PbCl_2:Nd^{3+}$, $PbGa_2S_4:Nd^{3+}$, $CaGa_2S_4:Nd^{3+}$ and the $^4G_{5/2}$; $^2G_{7/2}$ manifold in $CaF_2:LaF_3(0.25\%):NdF_3(0.25\%)$ and $SrF_2:LaF_3(1\%):NdF_3(0.2\%)$ crystals were measured by direct excitation using a picosecond laser (EKSPLA) with OPO PG- 401 module tunable over the 0.4 -2.2 μ m spectral range. Resonant fluorescence selection and detection were provided by an ARC-750 spectrometer and a R928 Hamamatsu PMT.

A closed-cycle Janis cryostat with temperature controller was used for cooling of samples below room temperature down to 13 K. Fluorescence kinetics acquisition and recording was provided by a 1 GHz Tektronix TDS 5104 digital oscilloscope.

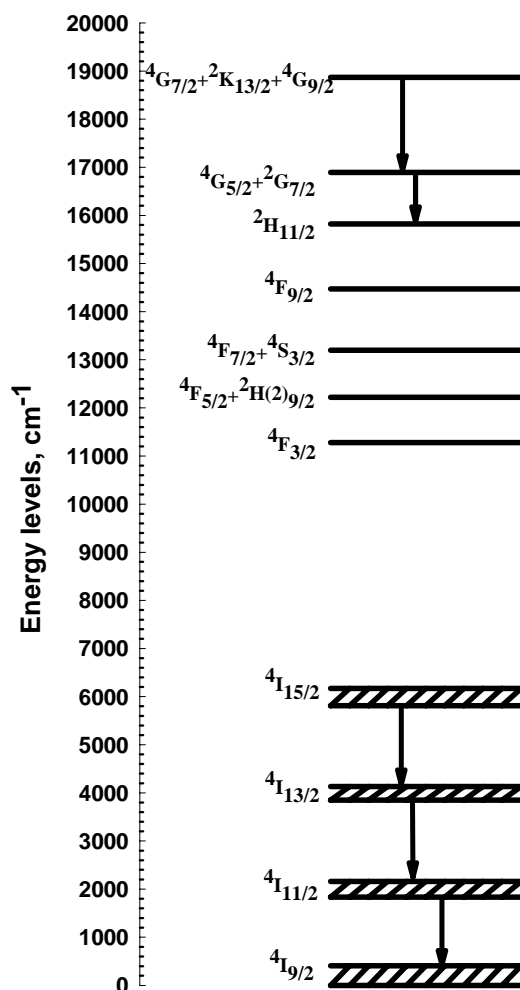


Fig. 1.2.1. Energy level diagram of Nd^{3+} ions in the $\text{PbGa}_2\text{S}_4: \text{Nd}^{3+}$ (0.2 m.%) crystal.

Also, mid- IR fluorescence spectra of the $\text{CaGa}_2\text{S}_4: \text{Nd}^{3+}$, $\text{PbGa}_2\text{S}_4: \text{Nd}^{3+}$, and $\text{PbCl}_2: \text{Nd}^{3+}$ crystals were measured using a CW high power (5W) laser diode array operating at 810 nm and a double grating high throughput SDL monochromator with 100 grooves/mm gratings and 9.6 nm/mm linear reciprocal dispersion. A special filter transparent in the 3.5 - 6 μm spectral range was used to separate the 4 - 6 μm fluorescence from an intensive 1.5 - 3 μm fluorescence observed in higher diffraction orders. The fluorescent signal was detected by a Ge(Au) liquid nitrogen cooled photoresistor. A lock-in amplifier was used to increase the signal to noise ratio. The detected signal was recorded using an ADC and a PC.

Results and discussions

Absorption spectra of the $\text{CaGa}_2\text{S}_4:\text{Nd}^{3+}$ (0.16 m. %) and $\text{PbGa}_2\text{S}_4:\text{Nd}^{3+}$ (0.2 m. %) crystals in the visible (Fig. 1.2.2a) and IR (Fig. 1.2.2b) spectral ranges were measured in the single orientation of the crystals.

Very strong absorption of the crystal matrix from 500 nm to UV in CaGa_2S_4 and from 580 nm to UV in PbGa_2S_4 was observed. In the mid IR spectral range both matrixes are transparent until 8 μm .

The absorption spectra are precisely measured in the PbGa_2S_4 crystal with concentration of Nd^{3+} ions 0.5 m. % or $N = 6.25 \times 10^{19} \text{ cm}^{-3}$. The measured absorption spectra are used for calculation of the line strength of the optical transitions employing Judd- Ofelt theory [17, 18].

The experimental integrated absorption cross-sections for the different $J - J'$ transitions are calculated as

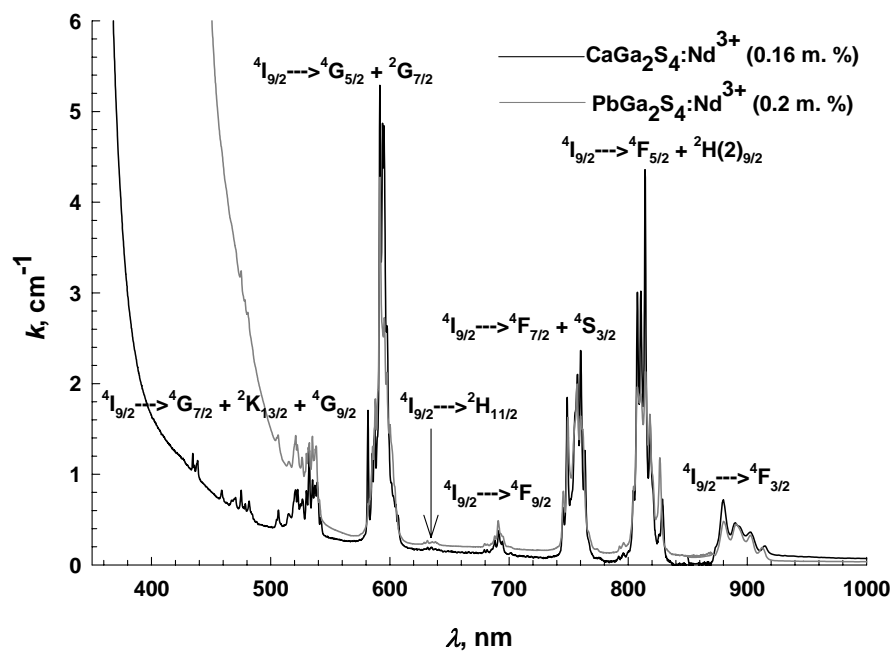
$$\sigma_{abs}(J - J') = \int k(\bar{\nu}) d\bar{\nu} / N, \quad (1.2.1)$$

where k is absorption coefficient in cm^{-1} , $\bar{\nu} = 1/\lambda$ in cm^{-1} .

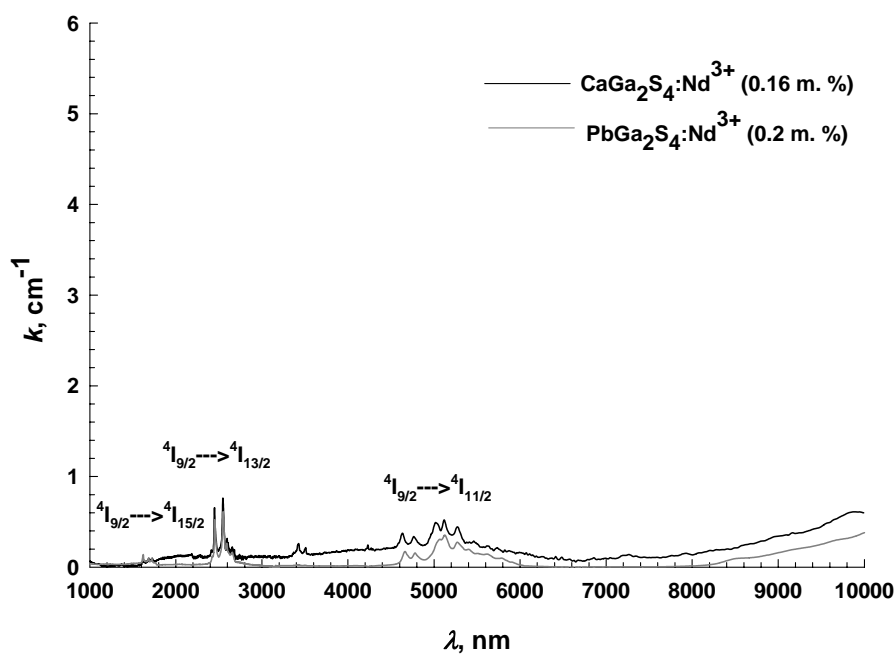
According to Ref. [19, 20] the integrated absorption cross-section of a $J - J'$ optical transition within the $4f$ shell of a rare- earth ion can be written as:

$$\sigma_{abs} = \sigma_{abs}^{ed} + \sigma_{abs}^{md} = \frac{4\pi^2 e^2}{3 \hbar c} \cdot \frac{\Delta E}{(2J+1)} \cdot \left(\frac{(n^2 + 2)^2}{9n} \cdot S_{ed} + n \cdot S_{md} \right), \quad (1.2.2)$$

where J is the angular momentum of the ground state, \hbar is Planck's constant, ΔE - transition energy in cm^{-1} , n is a refractive index, S_{ed} is the electric-dipole transition line –strength, and S_{md} is the magnetic-dipole transition line –strength.



(a)



(b)

Fig. 1.2.2. Absorption spectra in visible and infrared spectral ranges including mid IR of the $\text{CaGa}_2\text{S}_4:\text{Nd}^{3+}$ (0.16 m.%) (black curves) and $\text{PbGa}_2\text{S}_4:\text{Nd}^{3+}$ (0.2 m.%) (grey curves) crystals.

In Judd- Ofelt theory [17, 18] S_{ed} is expressed as

$$S_{ed} = \sum_{k=2,4,6} \Omega_k \cdot (LSJ \| U^{(k)} \| L'S'J')^2, \quad (1.2.3)$$

where Ω_k is the intensity parameter of the theory, S_{md} is expressed as

$$S_{md} = \frac{\beta^2}{e^2} \cdot (LSJ \| \mathbf{J} + \mathbf{S} \| L'S'J')^2, \quad (1.2.4)$$

where β is the Bohr magneton, $(LSJ \| \mathbf{J} + \mathbf{S} \| L'S'J')$ is the reduced matrix elements of operator $\mathbf{J} + \mathbf{S}$. The values are taken from Ref. [20].

It was found that the light beam of the Shimadzu spectrophotometer is polarized along a horizontal orientation of vector \mathbf{E} . The absorption spectra are measured for two orientations of the sample, one $\mathbf{E} \parallel c$ (black curve) and the other $\mathbf{E} \perp c$ (gray curve). The absorption lines shape was found to depend on polarization due to biaxial type of PbGa_2S_4 crystal matrix. During the measurements the light beam propagated along the b -axis of the crystal. For calculation of the integral absorption cross-sections σ_{abs} a spectral background related to the matrix absorption is subtracted (Fig. 1.2.3).

Then the measured polarized spectra are suitably averaged. Only strong optical transitions with large values of $(LSJ \| U^{(k)} \| L'S'J')^2$ having a decisive influence on the values of electric – dipole line strengths S_{ed} are used for the calculations (Table 1.2.1). For example, the $^4I_{9/2} \rightarrow ^4G_{5/2} + ^2G_{7/2}$ transition line- strength has a main contribution from terms with Ω_2 and Ω_4 , the $^4I_{9/2} \rightarrow ^4F_{5/2} + ^2H(2)_{9/2}$ transition line- strength from Ω_4 and Ω_6 , and the $^4I_{9/2} \rightarrow ^4F_{7/2} + ^4S_{3/2}$, $^4I_{9/2} \rightarrow ^4I_{15/2}$, and $^4I_{9/2} \rightarrow ^4I_{13/2}$ transitions line- strength from Ω_6 , only. The following parameters Ω_k were found for $\text{PbGa}_2\text{S}_4: \text{Nd}^{3+}$ by a least squares method, as applied to relevant σ_{abs}^{ed} obtained from experimentally measured absorption cross- sections σ_{abs} (Table 1.2.1): $\Omega_2 = 2.96 \cdot 10^{-20} \text{ cm}^2$, $\Omega_4 = 5.39 \cdot 10^{-20} \text{ cm}^2$, $\Omega_6 = 4.19 \cdot 10^{-20} \text{ cm}^2$.

The radiative relaxation rates for initial levels of mid IR transitions are calculated as

$$A^{JJ'} = A_{ed}^{JJ'} + A_{md}^{JJ'} = \frac{1}{(2J'+1)} \cdot \frac{32\pi^3 e^2}{3\hbar} \cdot \frac{n(n^2+2)^2}{9} \cdot \Delta E^3 \cdot \sum_{k=2,4,6} \Omega_k \cdot (LSJ \| U^{(k)} \| L'S'J')^2 + \frac{1}{(2J'+1)} \cdot \frac{32\pi^3 \cdot n^3}{3\hbar} \cdot \bar{v}^3 \cdot \beta^2 \cdot (LSJ \| \mathbf{J} + \mathbf{S} \| L'S'J')^2, \quad (1.2.5)$$

where J' is the angular momentum of the excited state.

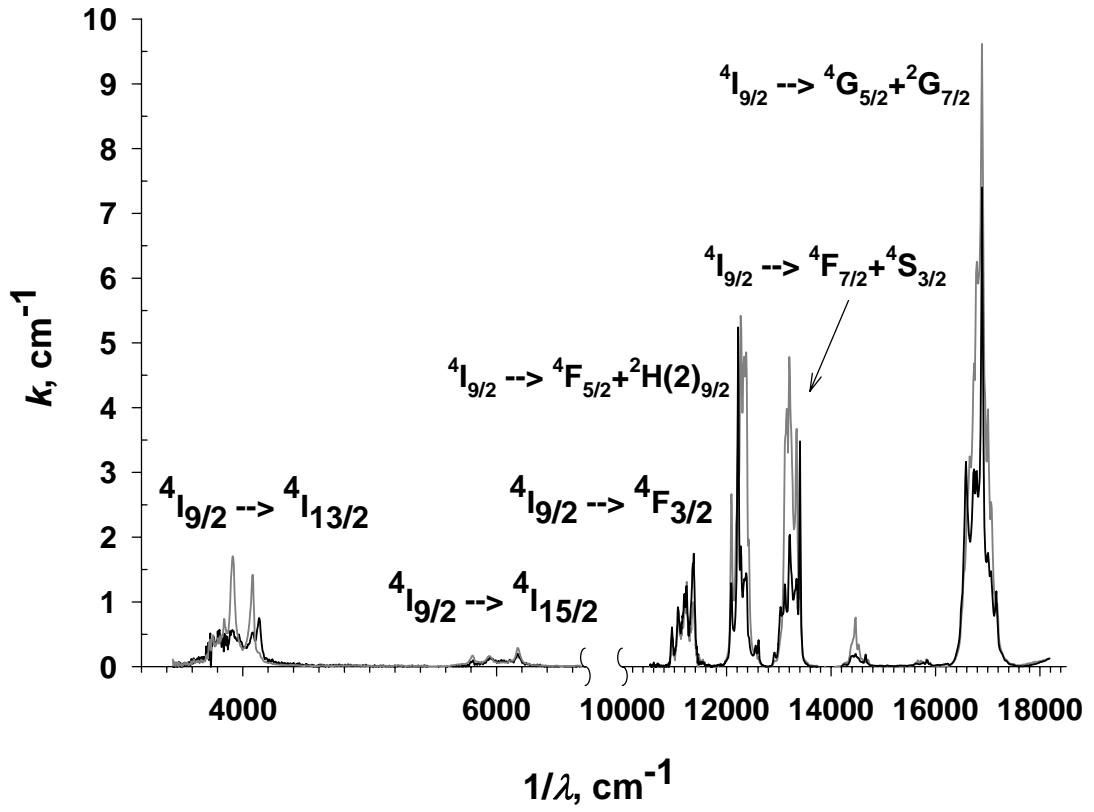


Fig. 1.2.3. Polarized absorption spectra of the $\text{PbGa}_2\text{S}_4:\text{Nd}^{3+}$ (0.5 m. %) crystal. Two orientations of the sample: $\mathbf{E}||\mathbf{c}$ (solid black curve) and $\mathbf{E}\perp\mathbf{c}$ (solid grey curve).

Table 1.2.1. Measured absorption cross - sections σ_{abs} in the $\text{PbGa}_2\text{S}_4:\text{Nd}^{3+}$ (0.5 m%) crystal	
Transition	$\sigma_{\text{abs}}, 10^{-17}, \text{cm}$
$^4\text{I}_{9/2} \rightarrow ^4\text{F}_{5/2} + ^2\text{H}(2)_{9/2}$	1.26
$^4\text{I}_{9/2} \rightarrow ^4\text{F}_{7/2} + ^4\text{S}_{3/2}$	1.18
$^4\text{I}_{9/2} \rightarrow ^4\text{G}_{5/2} + ^2\text{G}_{7/2}$	3.16
$^4\text{I}_{9/2} \rightarrow ^4\text{I}_{15/2}$	0.06
$^4\text{I}_{9/2} \rightarrow ^4\text{I}_{13/2}$	0.29

Very short radiative decay times for the $^4\text{G}_{7/2}$ ($\tau_{\text{R}} = 13.6 \mu\text{s}$); $^4\text{G}_{5/2} + ^2\text{G}_{7/2}$ ($\tau_{\text{R}} = 21.2 \mu\text{s}$) and $^4\text{F}_{3/2}$ manifolds ($\tau_{\text{R}} = 65.4 \mu\text{s}$) are calculated in $\text{PbGa}_2\text{S}_4:\text{Nd}^{3+}$ (Table 1.2.2).

Table 1.2.2. Calculated radiative rates ΣA_i and radiative lifetimes τ_R of the manifolds in study in the PbGa₂S₄: Nd³⁺ (0.5 m. %) crystal		
Manifold	A, s⁻¹	$\tau_R = 1/A$
⁴ I _{11/2}	47.5	21 ms
⁴ I _{13/2}	182	5.5 ms
⁴ I _{15/2}	205	4.9 ms
⁴ F _{3/2}	15200	65 μ s
⁴ G _{5/2} + ² G _{7/2}	47200	21.2 μ s
⁴ G _{7/2}	73500	13.6 μ s

The measured decay time ($\tau_R^{\text{meas}} = 60 \mu\text{s}$) of the ⁴F_{3/2} metastable level (Table 1.2.3) is found to be in a good agreement with the calculated one. The reason of the short radiative lifetimes found will be discussed in paragraph 1.2.2.

Let us turn to mid- IR transitions. The fluorescence kinetics of the ⁴I_{15/2} level in the PbGa₂S₄: Nd³⁺ (0.2 m. %) and CaGa₂S₄: Nd³⁺ (0.16 m. %) crystals at room temperature measured for selective fluorescence monitoring exhibits exponential decay. But rather weak signal, only one order of magnitude change of fluorescence intensity (curves 2 & 4 @ Fig. 1.2.4), forced to determine the temperature dependence of the decay time for both the crystals from a fluorescence kinetics of the sum of the cascade mid IR ⁴I_{15/2} → ⁴I_{13/2}; ⁴I_{13/2} → ⁴I_{11/2}; and ⁴I_{11/2} → ⁴I_{9/2} transitions at 1.56 μm laser excitation (curves 1 & 3 @ Fig. 1.2.4 and Figs. 1.2.5 and 1.2.8). This allows to acquire not less than two orders of magnitude change of fluorescence intensity with rather large signal-to – noise ratio and to determine the decay time at the long time scale of fluorescence kinetics decay with higher accuracy than in the case of selective fluorescence detection. The measured decay times at the long time scale of fluorescence kinetics decay for both detection methods are found nearly identical for both the crystals at room temperature (Fig. 1.2.4). A fast microsecond spike at the very beginning of the sum of fluorescence decay curves could be related to a small fraction of the powerful pump radiation passing through the filters.

Also, we calculated and analyzed solutions of the kinetic rate equations for a four level system with short pulse laser excitation into the highest lying ⁴I_{15/2} level taking into consideration radiative and multiphonon relaxation processes, only (see Appendix). As a result we found that the measured total fluorescence kinetics at the long time scale is defined by the slowest decay rate among the three cascade fluorescent ⁴I_i - ⁴I_j transitions. The initial and middle parts of the measured fluorescence decay curve is defined by a sum of decay curves related to all three cascade mid IR ⁴I_{15/2} → ⁴I_{13/2}; ⁴I_{13/2} → ⁴I_{11/2}, and ⁴I_{11/2} → ⁴I_{9/2} transitions. Two step excitation as a result of absorption transition from the ground ⁴I_{9/2} manifold to the excited ⁴I_{15/2} manifold with

the following (during the laser pulse) excited state absorption transition from the $^4I_{15/2}$ manifold to the $^4F_{5/2}$ manifold with subsequent relaxation to the lower-lying levels should be considered as well. With this consideration the measured fluorescence kinetics for a long time scale should be defined also by the slowest decay rate of participated energy levels including the $^4F_{3/2}$ and $^4F_{5/2}$ manifolds. At higher concentrations contribution of the cross-relaxation processes (up- and down conversion) should be taken into account. For example, at room temperature the measured decay time for the long time scale of the total fluorescence kinetics decay in $\text{PbGa}_2\text{S}_4:\text{Nd}^{3+}$ (0.5 m. %) crystal is shorter ($\tau = 215 \mu\text{s}$) than that in the $\text{PbGa}_2\text{S}_4:\text{Nd}^{3+}$ (0.2 m. %) crystal ($\tau = 315 \mu\text{s}$) (Fig. 1.2.5).

Table 1.2.3. Measured lifetimes of Nd^{3+} levels in studied crystals		
Manifold	$\tau_{\text{meas.}}, \mu\text{s}$ (T, K)	$\tau_{\text{meas.}}, \mu\text{s}$, T=295 K
PbGa_2S_4		
$^4G_{7/2}$	12.3 (77 K)	10.5
$^4F_{3/2}$		60
CaGa_2S_4		
$^4G_{7/2}$	14.5 (77 K)	13.6
$^4F_{3/2}$	77.5 (18 K)	76.1
PbCl_2		
$^4G_{5/2}; ^2G_{7/2}$	18.3 (14K)	5.5
$^4G_{7/2}$	32 (13 K)	23
$^4F_{3/2}$	115 (13 K)	119
$^4I_{11/2}$	11 ms (8 K)	9 ms

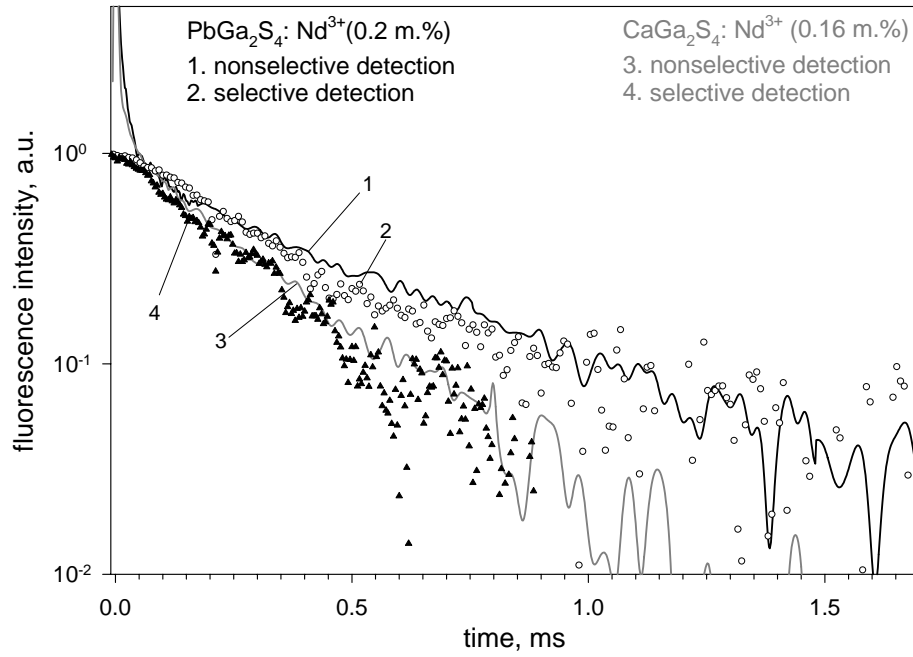


Fig. 1.2.4. Comparison of the fluorescence kinetics of the ${}^4I_{15/2}$ manifold excited at $1.61\ \mu\text{m}$ directly into the maximum of the ${}^4I_{9/2} \rightarrow {}^4I_{15/2}$ transition and selectively detected at $4.7\ \mu\text{m}$ in the $\text{PbGa}_2\text{S}_4:\text{Nd}^{3+}$ (0.2 m.%) and $\text{CaGa}_2\text{S}_4:\text{Nd}^{3+}$ (0.16 m.%) crystals at room temperature – curves 2 & 4, and of a sum of fluorescence kinetics of three low-lying 4I_J manifolds excited at $1.56\ \mu\text{m}$ and detected after optical filter transparent at wavelengths longer than $3\ \mu\text{m}$ – curves 1 & 3.

This corresponds to the energy transfer rate of $W = 1480\ \text{s}^{-1}$. However, a contribution of concentration quenching is negligible at 0.2 m. % of Nd^{3+} and the system response is linear, due to off-resonance $1.56\ \mu\text{m}$ excitation into a weak electron-phonon side-band of the ${}^4I_{15/2}$ level. For small concentration of Nd^{3+} a contribution of multiphonon relaxation can be calculated as the difference between the measured relaxation rate and calculated radiative relaxation rate. The calculated radiative rates of the ${}^4I_{15/2}$, ${}^4I_{13/2}$, and ${}^4I_{11/2}$ levels in the $\text{PbGa}_2\text{S}_4:\text{Nd}^{3+}$ crystal (see Table 1.2.2) are considerably lower than the measured rates (Table 1.2.4). As a result the measured fluorescence kinetics decay is mainly determined by multiphonon relaxation. To determine the 4I_J level with the slowest MR rate let us turn to the theory of multiphonon relaxation.

According to Eqs. (1.1.1, 1.1.5, 1.1.6, 1.1.13 and 1.1.21) the difference in MR rates for different transitions of a specific rare-earth ion in a specific crystal depends only on the energy gap $\Delta E = \Delta E_{\min}$ to the next manifold below (the factor $\rho_p(\Delta E) \times \eta^p$ of Eq. (1.1.21)), a degree of degeneracy of the initial level $(2J+1)$, and the values of the reduced matrix elements $U^{(k)}$ of the corresponding electronic transitions (Eq. (1.1.1)).

For three 4I_J - 4I_J mid- IR transitions of Nd^{3+} the $U^{(k)}$ parameters are very close [14]. The largest and close values of energy gaps ΔE and, therefore, minimal values $\rho_p(\Delta E_{JJ})\eta^p$, are found for the $^4I_{15/2}$ and $^4I_{13/2}$ transitions (Fig. 1.2.1). Thus, the MR rates of these two levels are slower than the MR rate of the $^4I_{11/2}$ level. But the degree of the degeneracy of the $^4I_{15/2}$ level is larger than that of the low-lying $^4I_{13/2}$ level.

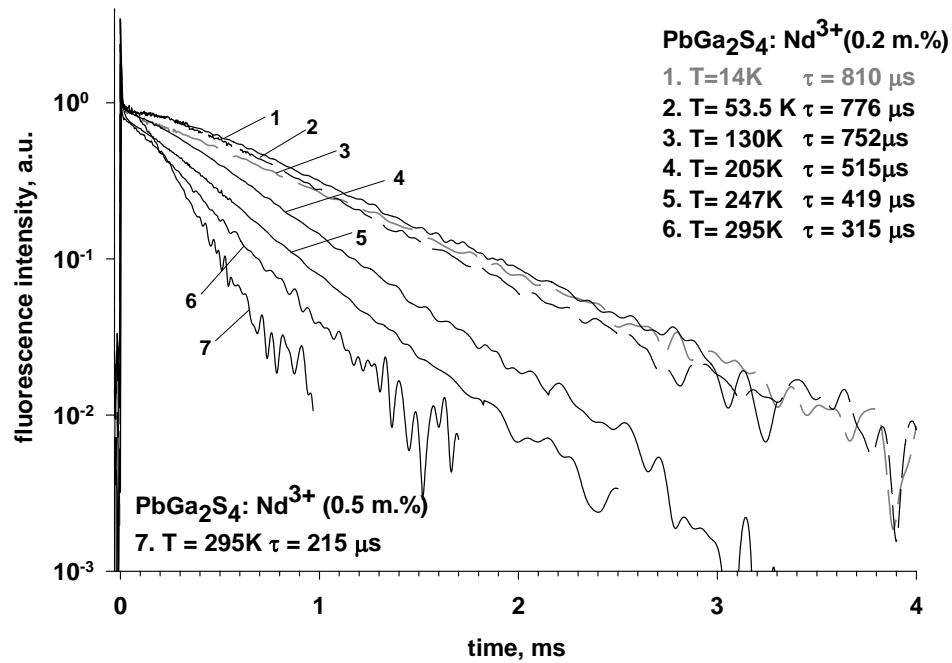


Fig. 1.2.5. Temperature and concentration dependencies of a sum of fluorescence kinetics of three low – lying 4I_J manifolds of the Nd^{3+} ion in PbGa_2S_4 under $1.56 \mu\text{m}$ laser excitation and fluorescence monitoring after optical filter transparent at wavelengths longer than $3 \mu\text{m}$.

Therefore, according to Eq. (1.1.1) the MR rate of the $^4I_{15/2}$ level should be slower and the final stage of the total 4I_J fluorescence kinetics in $\text{CaGa}_2\text{S}_4: \text{Nd}^{3+}$ and $\text{PbGa}_2\text{S}_4: \text{Nd}^{3+}$ should be defined by the $^4I_{15/2}$ multiphonon relaxation rate. This argumentation is confirmed experimentally (Fig. 1.2.4).

Now, one can calculate the multiphonon relaxation rates of the $^4I_{15/2}$ level in $PbGa_2S_4:Nd^{3+}$ and $CaGa_2S_4:Nd^{3+}$ at different temperatures assuming that the corresponding radiative rates are independent on the temperature for both the crystals. The value of radiative rate A calculated for the $^4I_{15/2}$ level for $PbGa_2S_4:Nd^{3+}$ is equal to $A = 205\text{ s}^{-1}$. For $CaGa_2S_4:Nd^{3+}$ $A = 170\text{ s}^{-1}$ was estimated. The estimation is based on the fact that the radiative rate of the $^4F_{3/2}$ metastable level in this crystal ~ 1.2 times lower compared to $PbGa_2S_4:Nd^{3+}$ and one may assume that the rates of the 4I_J levels in $CaGa_2S_4:Nd^{3+}$ are also ~ 1.2 times lower because the strongest radiative transitions from the $^4F_{3/2}$ metastable level to the $^4I_{11/2}$ and $^4I_{9/2}$ levels depend on the same matrix elements $U^{(4)}$ and $U^{(6)}$ as the transitions from the $^4I_{15/2}$ and $^4I_{13/2}$ levels.

The $W_{MR}(T)$ temperature dependence of the $^4I_{15/2}$ manifold obtained in $PbGa_2S_4:Nd^{3+}$ (Fig. 1.2.6) and $CaGa_2S_4:Nd^{3+}$ (Fig. 1.2.7) is analyzed in a single- frequency model of lattice vibrations [21] (see Eqs. (1.1.11, 1.1.12)). The theoretical curves of Eqs. (1.1.11, 1.1.12) which have been drawn for the process of temperature stimulated p - phonon emission in $PbGa_2S_4:Nd^{3+}$ ($p = \Delta E_{min}/\hbar\omega_2 = 1680\text{ cm}^{-1}/420\text{ cm}^{-1}$ - curve $p=4$ @ Fig. 1.2.6, $p = \Delta E_{min}/\hbar\omega_1 = 1680\text{ cm}^{-1}/336\text{ cm}^{-1}$ - curve $p=5$ @ Fig. 1.2.6, and $p = \Delta E_{min}/\hbar\omega_3 = 1680\text{ cm}^{-1}/280\text{ cm}^{-1}$ - curve $p=6$ @ Fig. 1.2.6) depict the boundaries of the area which covers all experimental points. It may be concluded that 5- phonon transitions have the dominant contribution to multiphonon relaxation of the $^4I_{15/2}$ manifold in $PbGa_2S_4:Nd^{3+}$ crystal.

For $CaGa_2S_4:Nd^{3+}$ a five and four phonon transitions give contributions to the $^4I_{15/2}$ relaxation rate (Fig. 1.2.7). It should be noted that dispersion of experimental points is larger for $CaGa_2S_4:Nd^{3+}$ than for $PbGa_2S_4:Nd^{3+}$ because of weaker fluorescence response concerned with lower concentration of Nd^{3+} in the former crystal. At low temperatures the MR rate is two times higher for the $CaGa_2S_4:Nd^{3+}$ crystal than that for the $PbGa_2S_4:Nd^{3+}$ one probably due to significant contribution of four phonon transitions to the MR rate. The fluorescence kinetics decay for both the crystals at liquid helium temperatures is presented in Fig. 1.2.8 for comparison. The measured decay times of the high-lying $^4G_{5/2}$; $^2G_{7/2}$ manifold of Nd^{3+} in the $CaGa_2S_4:Nd^{3+}$ (0.16 m. %) crystal in the temperature range from 13 to 300K (Fig. 1.2.9) are practically equal to multiphonon relaxation decay times for this manifold due to the negligible contribution of radiative decay because of the nanosecond scale of multiphonon and microsecond scale of radiative relaxation (see Tables 1.2.2 and 1.2.4).

Table 1.2.4. Measured and multiphonon relaxation decay times for Nd³⁺ nonradiatively quenched manifolds in laser crystals with low phonon spectra and parameters of nonlinear theory having influence on multiphonon transition rate

Transition	ΔE_{\min} , cm ⁻¹	$\hbar\omega_{\text{eff}}=\Delta E_{\min}$ /p, cm ⁻¹	Phonon number p	$(U^{(2)})^2$	$(U^{(4)})^2$	$(U^{(6)})^2$	$\tau_{\text{meas.}}/\tau_{\text{MR}}$, 14K	$\tau_{\text{meas.}}$ 295 K
CaF₂ (pair Nd –La center) ($R_0(\text{Nd-F})= 2.36 \text{ \AA}$)								
² G _{7/2} → ² H _{11/2}	1125	375	3	0.0066	0	0.0048		
⁴ G _{5/2} → ² H _{11/2}				0	0.0003	0.0146	22 ns	
SrF₂ (pair Nd –La center) ($R_0(\text{Nd-F})= 2.505 \text{ \AA}$)								
² G _{7/2} → ² H _{11/2}	1130		3	0.0066	0	0.0048		
⁴ G _{5/2} → ² H _{11/2}		380		0	0.0003	0.0146	25 ns	
LaF₃ ($R_0(\text{Nd-F})= 2.50 \text{ \AA}$)								
² G _{7/2} → ² H _{11/2}	1200		3	0.0066	0	0.0048		
⁴ G _{5/2} → ² H _{11/2}		400		0	0.0003	0.0146	29 ns	15 ns
⁴ G _{7/2} → ⁴ G _{5/2} ;	1546	390	4	0	0.2246	0.0503		
² G _{7/2}				0.0575	0.0005	0.0377	110 ns	56 ns
PbCl₂ ($R_0(\text{Nd-Cl}) \geq 2.85 \text{ \AA}$)								
² G _{7/2} → ² H _{11/2}			5	0.0066	0	0.0048	18 μs/	5.5 μs/
⁴ G _{5/2} → ² H _{11/2}	1000	200		0	0.0003	0.0146	54.5 μs	6.9 μs
CaGa₂S₄ ($R_0(\text{Nd-S}) \geq 2.97 \text{ \AA}$)								
² G _{7/2} → ² H _{11/2}	1110		3	0.0066	0	0.0048	115 ns	71 ns
⁴ G _{5/2} → ² H _{11/2}		370		0	0.0003	0.0146		
⁴ I _{15/2} – ⁴ I _{13/2}	1680	420 - 336	4 - 5	0.0256	0.1353	1.2379	519 μs/	278 μs/
							566 μs	291 μs
PbGa₂S₄ ($R_0(\text{Nd-S}) \geq 3.12 \text{ \AA}$)								
² G _{7/2} → ² H _{11/2}			3	0.0066	0	0.0048	156 ns	83 ns
⁴ G _{5/2} → ² H _{11/2}	1110	370		0	0.0003	0.0146		
⁴ I _{15/2} – ⁴ I _{13/2}	1680	336	5	0.0256	0.1353	1.2379	810 μs/	315 μs/
							970 μs	336 μs

The theoretical curves of Eqs. (1.1.11, 1.1.12) which have been drawn for the processes of temperature stimulated *p*- phonon emission ($p = \Delta E_{\min} / \hbar\omega_1 = 1110 \text{ cm}^{-1} / 370 \text{ cm}^{-1}$ – solid curve $p = 3$ @ Fig. 4.9, $p = \Delta E_{\min} / \hbar\omega_2 = 1110 \text{ cm}^{-1} / 280 \text{ cm}^{-1}$ – dashed curve $p = 4$ @ Fig. 4.9) depict the boundaries of the area which covers all experimental points.

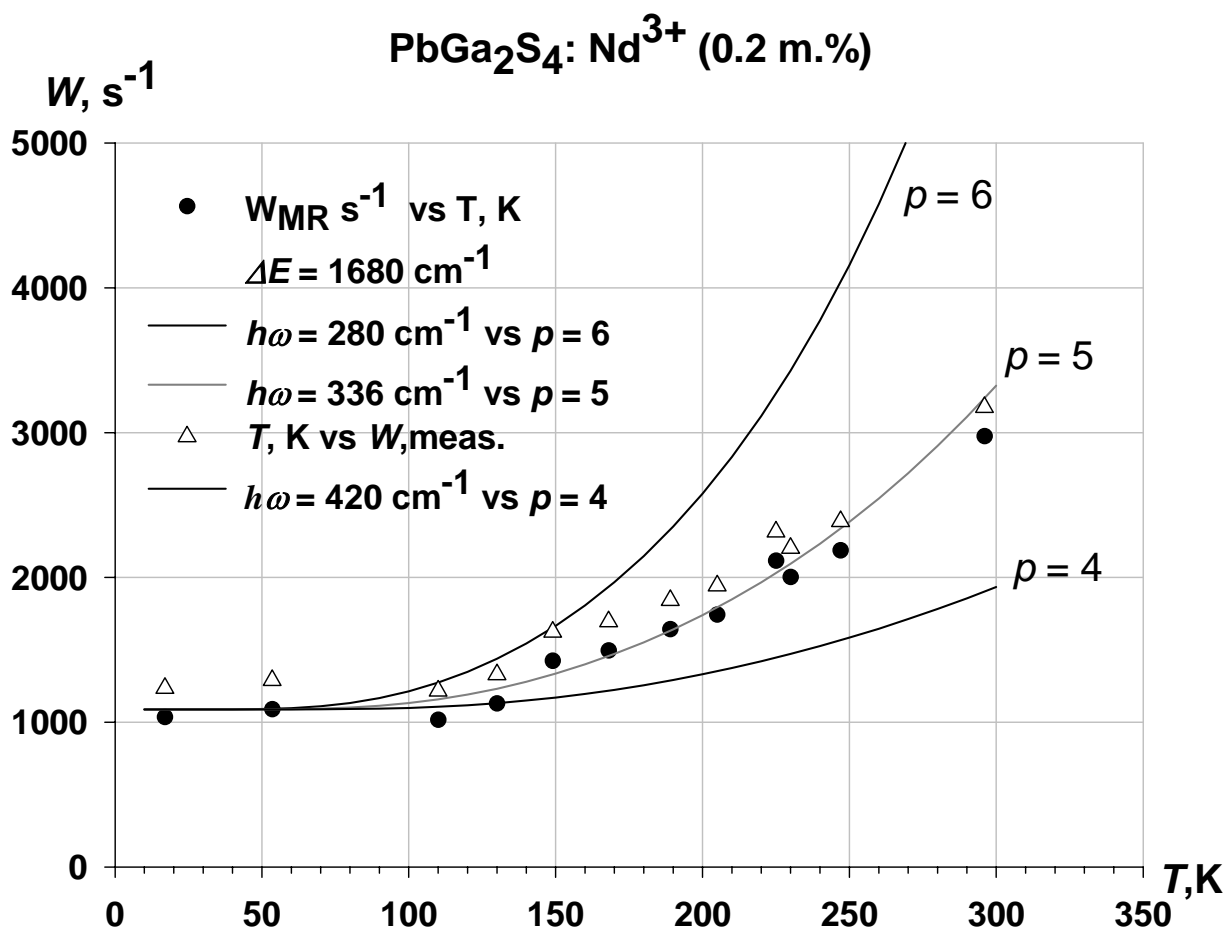


Fig. 1.2.6. Temperature dependence of the decay rate of the $^4\text{I}_{15/2}$ manifold measured at the long time scale of a sum of fluorescence kinetics of three low – lying $^4\text{I}_J$ manifolds of the Nd^{3+} ion and of calculated multiphonon relaxation rate ($W_{\text{MR}} = W_{\text{meas.}} - A$, $A = 200 \text{ s}^{-1}$) in the $\text{PbGa}_2\text{S}_4: \text{Nd}^{3+}$ (0.2 m.%) crystal and the fitting curves for the single frequency model of crystal lattice vibrations.

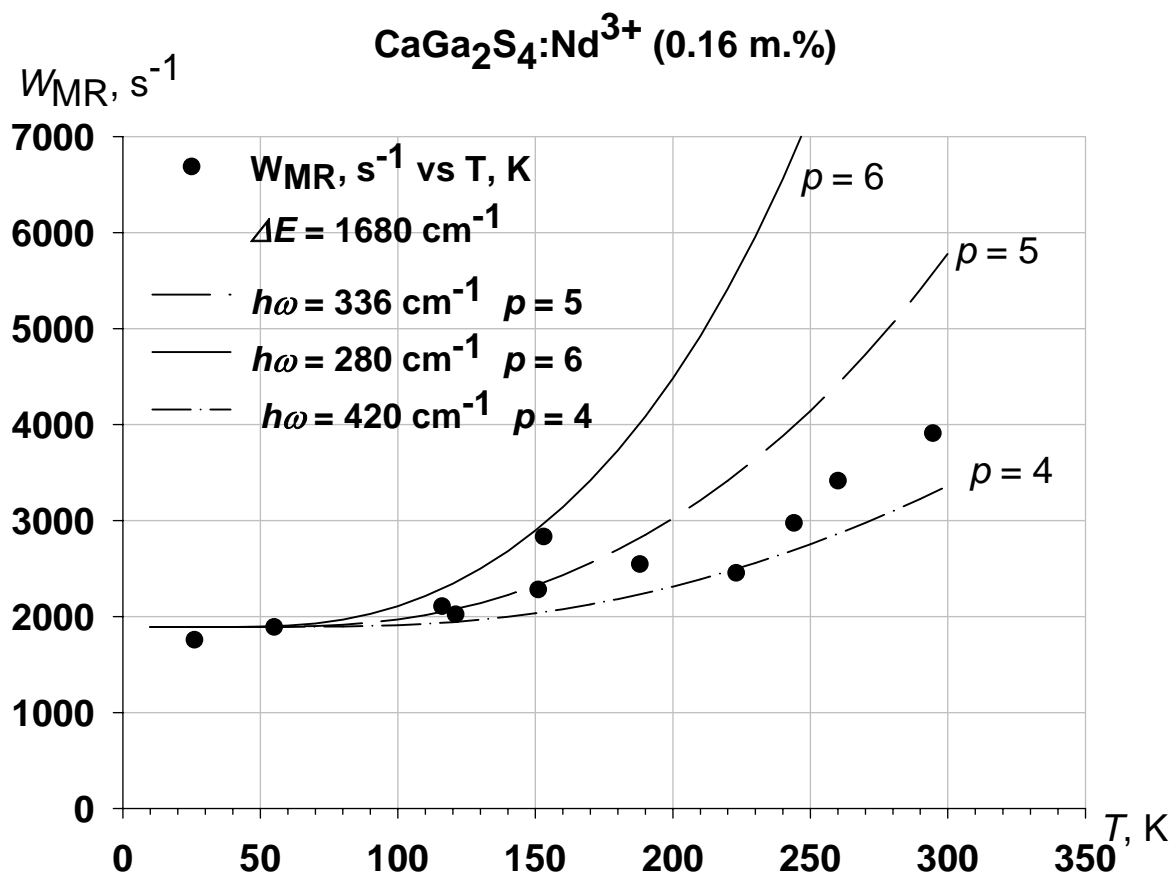


Fig. 1.2.7. Temperature dependence of the decay rate of the $^4I_{15/2}$ manifold measured at the long time scale of a sum of fluorescence kinetics of three low – lying 4I_J manifolds of the Nd^{3+} ion and of calculated multiphonon relaxation rate ($W_{MR} = W_{meas.} - A$, $A = 170 \text{ s}^{-1}$) in the $CaGa_2S_4:Nd^{3+}$ (0.16 m.%) crystal and the fitting curves for the single frequency model of crystal lattice vibrations.

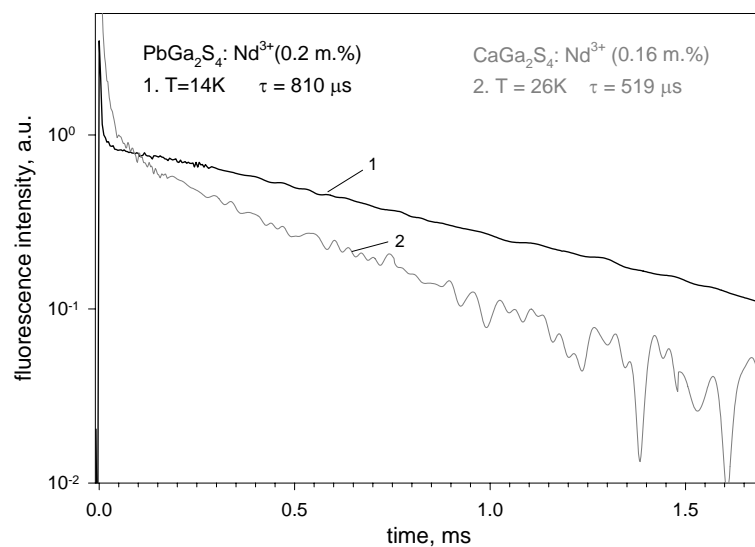


Fig. 1.2.8. A sum of fluorescence kinetics of three low – lying 4I_J manifolds of the Nd^{3+} ion measured after $1.56 \mu m$ of laser excitation in the $PbGa_2S_4: Nd^{3+}$ (0.2 m.%) (curve 1) and $CaGa_2S_4: Nd^{3+}$ (0.16 m.%) (curve 2) crystals at liquid helium temperatures.

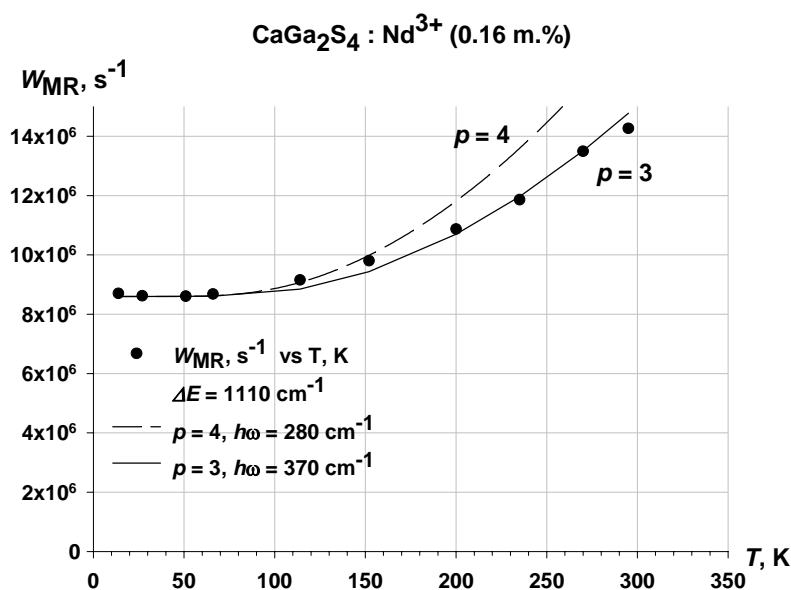


Fig. 1.2.9. Temperature dependence of the measured fluorescence kinetics decay rate of the $^4G_{5/2}; ^2G_{7/2}$ manifold in the $CaGa_2S_4: Nd^{3+}$ (0.16 m. %) crystal and the fitting curves for the single frequency model of crystal lattice vibrations.

It is also interesting to compare the measured MR rates in Nd^{3+} doped sulfide and fluoride crystal matrixes with close values of maximum phonon frequencies to verify regularities of multiphonon relaxation predicted by the nonlinear theory. As it was stated above the multiphonon relaxation rate depends on many parameters (see Eqs. (1.1.1, 1.1.5, 1.1.6, 1.1.12, and 1.1.21)). The dependence of the MR rate on ΔE and p was studied by many authors and it was established that an increase of the number of phonons p by one decreases the MR rate by one – two orders of magnitude (see Ref. [3] and the references therein). The number of phonons p is the strongest parameter and if it is fixed it is possible to find out the dependence of MR rate on other parameters, i.e. on the reduced matrix element of the unit tensor operator $U^{(k)}$ and on the rare- earth – nearest ligands distance R_0 . The $U^{(k)}$ parameter can be easily fixed by taking the same transition in different crystals. In doing so, the fluorescence decay curves of the $^4\text{G}_{5/2}$; $^2\text{G}_{7/2}$ manifolds of Nd^{3+} were measured in the CaF_2 : $\text{LaF}_3(0.25\%)$: $\text{NdF}_3(0.25\%)$ and SrF_2 : $\text{LaF}_3(1\%)$: $\text{NdF}_3(0.2\%)$ low phonon crystals at 14K by direct picosecond laser excitation and resonant fluorescence detection. These crystals have close values of maximum phonon frequencies with the thiogallate crystals. Selective excitation was provided at approximately 579.45 nm wavelength directly into the Nd - La pair center (M' center) to map out cross- relaxation quenching. Fluorescence monitoring was chosen at 657 nm in the case of SrF_2 [22] and at 653 nm in the case of CaF_2 [23, 24] when the maximum of fluorescence intensity comes from the M' - center. The measured lifetimes are presented in Table 1.2.4.

The dependence of the MR rate on the RE – nearest ligands distance R_0 was firstly observed in Ref. [25] in the row of fluorite- type crystals. For example, in CdF_2 : Er^{3+} ($\hbar\omega_{\text{max}} = 384 \text{ cm}^{-1}$) and SrF_2 : Er^{3+} ($\hbar\omega_{\text{max}} = 383 \text{ cm}^{-1}$), the crystals with close phonon spectra, a three times increase of a decay time of the $^4\text{I}_{9/2}$ manifold from $\tau(\text{CdF}_2)$ ($R_0 = 2.34 \text{ \AA}$) = 14 μs to $\tau(\text{SrF}_2)$ ($R_0 = 2.505 \text{ \AA}$) = 50 μs was found. The measured decay times are determined by the rate of six phonon $^4\text{I}_{9/2} \rightarrow ^4\text{I}_{11/2}$ transition ($\Delta E_{\text{min}} \approx 2180 \text{ cm}^{-1}$). The increase of a decay time of the $^4\text{G}_{5/2}$, $^2\text{G}_{7/2}$ level with an increase of Nd to the nearest ligands distance R_0 in the row of CaF_2 : Nd^{3+} , SrF_2 : Nd^{3+} , LaF_3 : Nd^{3+} , CaGa_2S_4 : Nd^{3+} and PbGa_2S_4 : Nd^{3+} crystals with close values of maximum phonon frequencies is observed now (Table 1.2.4). The measured decay times are determined by the rate of 3- phonon the $^4\text{G}_{5/2}$, $^2\text{G}_{7/2} \rightarrow ^2\text{H}_{11/2}$ transition of Nd^{3+} ($\Delta E_{\text{min}} \approx 1100 - 1200 \text{ cm}^{-1}$). The largest R_0 (Nd-S) $\geq 3.1 \text{ \AA}$ [26] in PbGa_2S_4 : Nd^{3+} correlates with the longest measured decay time $\tau = 156 \text{ ns}$ in this crystal, which is 5- 6 times longer than in LaF_3 ($\tau = 29 \text{ ns}$) and SrF_2 ($\tau = 25 \text{ ns}$), the crystals with much smaller the Nd –F distance $R_0 \approx 2.5 \text{ \AA}$ than the Nd –S distance $R_0 \geq 3.1 \text{ \AA}$. For CaGa_2S_4 : Nd^{3+} the distance $R_0(\text{Nd-S}) \geq 2.97 \text{ \AA}$ is in between for PbGa_2S_4 : Nd^{3+} and LaF_3 : Nd^{3+} . And the measured decay time $\tau = 115 \text{ ns}$ is shorter than that in

PbGa₂S₄: Nd³⁺ ($\tau = 156$ ns) but 3.8 times longer than in LaF₃: Nd³⁺ ($\tau = 29$ ns).

Let us address to the nonlinear theory of multiphonon relaxation to explain the measured relaxation rates $W_{MR} = 1/\tau_{meas}$ dependence on the Nd³⁺ to the nearest ligands distance R_0 . In the frame of point- charge model of RE ion - ligands interaction the following equation for the MR rate of a p - phonon transition can be written (see Eq. (1.1.1, 1.1.5, 1.1.7, 1.1.9))

$$W_{MR}(p) = \sum_{k=2,4, \text{ and } 6} A_{kp} R_0^{-(2k+2p)}, \quad (1.2.6)$$

where a factor of A_{kp} is independent on R_0 , and for single- frequency model of lattice vibrations it can be expressed as:

$$A_{kp} = \left(\frac{1}{137}\right)^2 \frac{cZ}{\bar{\nu}} \left(\frac{q}{e}\right)^2 \bar{\xi}^k \begin{pmatrix} l & l & k \\ 0 & 0 & 0 \end{pmatrix}^2 \frac{(2l+1)^2 (2p+2k)!}{(2k+1)!p!} \frac{(LSJ // U^{(k)} // L'S'J')^2}{2J'+1} \times \left(\frac{\hbar}{8\pi c M \bar{\nu}}\right)^p \quad (1.2.7)$$

It was shown in Ref. [11] that in the frame of the point charge model for the transitions with a small number of phonons ($p = 3$) the main contribution to the MR rate comes from the term with $k = 2$. Besides, if one neglects the exchange- charge interaction the only term left is A_{23} . In single frequency model of lattice vibrations this parameter can be easily calculated using Eq. (1.2.7). For Nd³⁺ the mean value of the square of the radius of optical electron is equal to $\langle \xi^2 \rangle = 1.01$ in units of Bohr radius [27]. The effective charge for the S²⁻ ligands is equal to $q = 2$ and that for the F⁻ ligands is equal to $q = 1$. For the studied crystals a number of the nearest ligands $Z=8$. The effective phonon frequencies of the crystal lattices are presented in Table 4.4. The mean value of the Nd –S distance for the CaGa₂S₄: Nd³⁺ crystal equal to $\langle R_0 \rangle = 3.02$ Å is calculated using crystallographic parameters of Ref. [26]. For PbGa₂S₄: Nd³⁺ the parameters for SrGa₂S₄: Nd³⁺ are taken and the mean value of $\langle R_0 \rangle = 3.12$ Å is used for calculations assuming that in PbGa₂S₄: Nd³⁺ the distance is slightly longer.

Our calculation in the studied solid state matrixes gives four times difference between the maximal (CaGa₂S₄: Nd³⁺) and minimal (PbGa₂S₄: Nd³⁺) values of A_{23} . For the PbGa₂S₄: Nd³⁺ and the LaF₃: Nd³⁺ crystals the A_{23} parameters were found almost to be equal. Within this accuracy the A_{23} parameter can be considered as a constant. In that case according to Eq. (1.2.6) the dependence W_{MR} on R_0 is proportional to R_0^{-12} . A theoretical dependence of Eq. (1.2.6) for $k = 2$ and $p = 3$ (solid curve) normalized to the measured multiphonon relaxation rate for the PbGa₂S₄: Nd³⁺ crystal fit rather well the measured MR rate for the CaGa₂S₄: Nd³⁺ crystal (Fig. 1.2.10) in spite of four times larger value of the calculated A_{23} parameter. For the LaF₃: Nd³⁺ crystal the measured MR rate is 2.6 times smaller than the predicted one in spite of equal A_{23}

with $\text{PbGa}_2\text{S}_4: \text{Nd}^{3+}$. Both results may be attributed to a change of A_{kp} due to change of the $\langle \mathbf{u}_{cat}^2 \rangle$ and $\langle \mathbf{u}_{anion}^2 \rangle$ values in $\text{CaGa}_2\text{S}_4: \text{Nd}^{3+}$ and $\text{LaF}_3: \text{Nd}^{3+}$ comparing to $\text{PbGa}_2\text{S}_4: \text{Nd}^{3+}$, which can not be predicted by rough estimation of phonon factor η using the right part of Eq. (1.1.14) and exact expression for the phonon factor η (Eq. (1.1.10)) should be employed. In this context the $\text{BaIn}_2\text{S}_4: \text{Nd}^{3+}$ crystal with the largest $\text{Nd}^{3+} - \text{S}$ distance ($R_0 \geq 3.194 \text{ \AA}$) and crystal structure similar to calcium and lead thiogallate crystals [26] can be proposed as a laser matrix with the reduced MR rates comparable or even slower than in $\text{PbGa}_2\text{S}_4: \text{Nd}^{3+}$.

The temperature dependence of the measured decay rates of the high-lying $^4\text{G}_{5/2}; ^2\text{G}_{7/2}$ manifold in the $\text{PbCl}_2: \text{Nd}^{3+}$ (0.2 m. %) crystal in the temperature range from 13 to 300K is presented in Fig. 1.2.11.

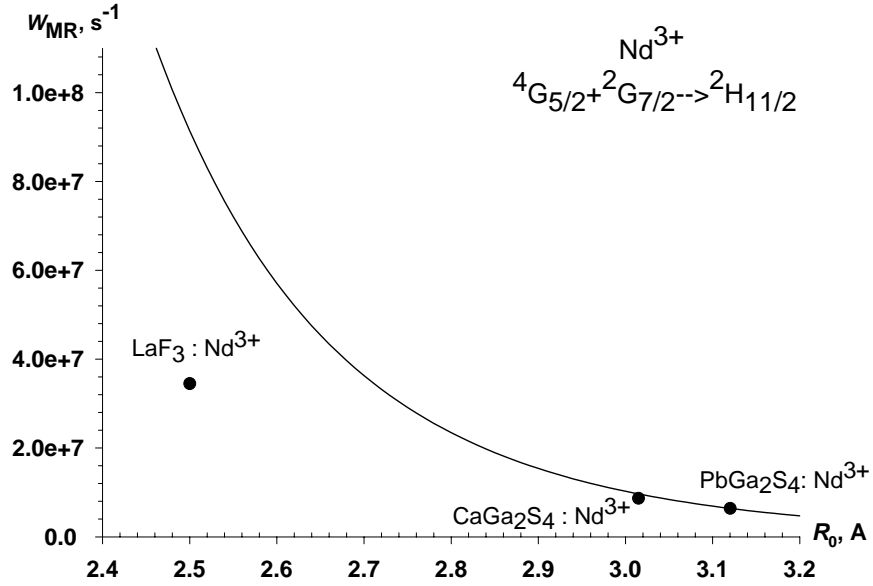


Fig. 1.2.10. The dependence of the measured multiphonon relaxation rates W_{MR} versus the distance R_0 between the Nd^{3+} ion and the nearest ligands in the $\text{PbGa}_2\text{S}_4: \text{Nd}^{3+}$ (0.2 m.%), $\text{CaGa}_2\text{S}_4: \text{Nd}^{3+}$ (0.16 m.%), and $\text{LaF}_3: \text{Nd}^{3+}$ (0.5 m.%) crystals at 13 K – solid circles. Theoretical dependence of Eq. (1.2.6) for $k = 2$ and $p = 3$ (solid line) normalized to measured multiphonon relaxation rate for the $\text{PbGa}_2\text{S}_4: \text{Nd}^{3+}$ crystal.

The radiative relaxation rate was calculated from the absorption spectra using Judd- Ofelt theory. The following parameters Ω_k were found in $\text{PbCl}_2: \text{Nd}^{3+}$ (0.5 m%) ($N = 1.6 \cdot 10^{19} \text{ cm}^{-3}$) by a least squares method, as applied to relevant σ_{abs}^{ed} obtained from the measured absorption cross-sections σ_{abs} . (Table 4.5): $\Omega_2 = 4.33 \cdot 10^{-20} \text{ cm}^2$, $\Omega_4 = 4.73 \cdot 10^{-20} \text{ cm}^2$, $\Omega_6 = 4.27 \cdot 10^{-20} \text{ cm}^2$.

The results of calculation of radiative rates of the manifolds in this study are presented in Table 4.6. Calculated radiative lifetime for the $^4\text{G}_{5/2}; ^2\text{G}_{7/2}$ manifold is $A = 37200 \text{ s}^{-1}$. The measured relaxation rate at $T = 14\text{K}$ is equal to $W_{\text{meas.}} = 1/\tau_{\text{meas.}} = 54650 \text{ s}^{-1}$ (Table 1.2.3).

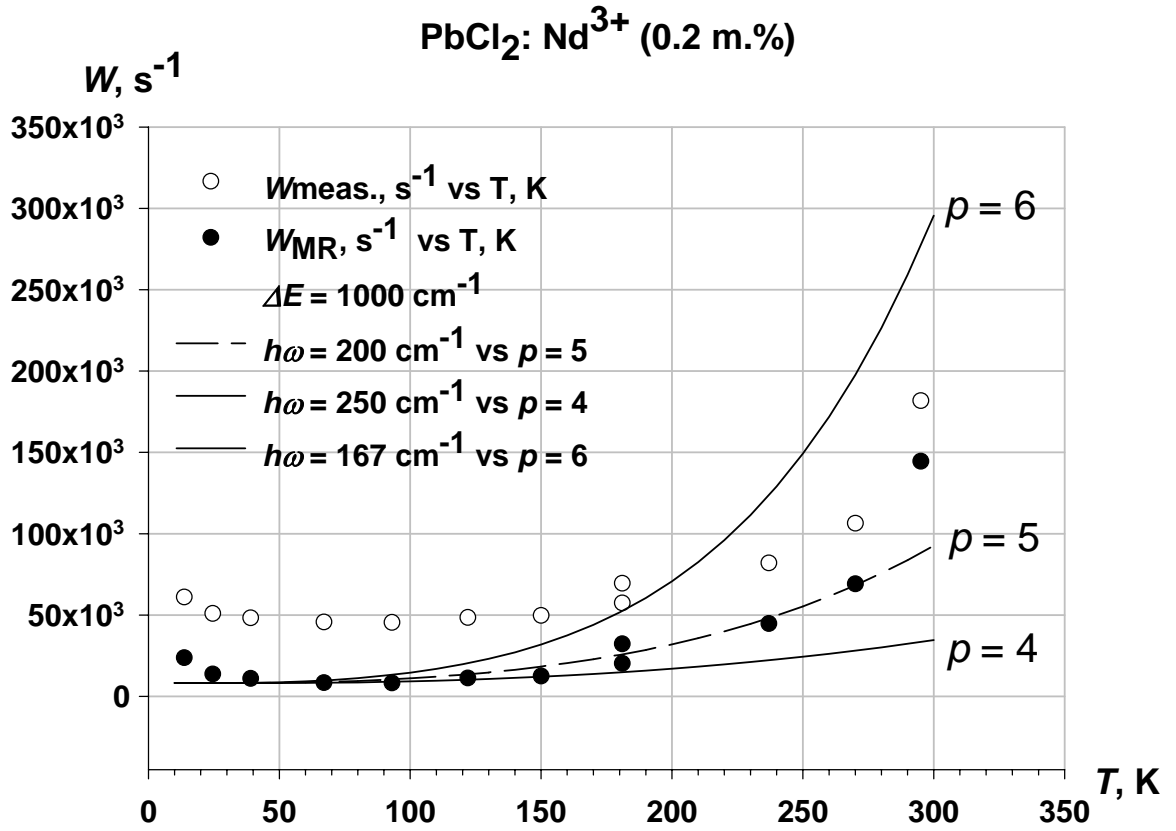


Fig. 1.2.11. Temperature dependence of the measured fluorescence kinetics decay rate and calculated multiphonon relaxation rate ($W_{\text{MR}} = W_{\text{meas.}} - A$, $A = 37236 \text{ s}^{-1}$) of the $^4\text{G}_{5/2} + ^2\text{G}_{7/2}$ manifold in the $\text{PbCl}_2: \text{Nd}^{3+}$ (0.2 m.%) crystal and the fitting curves for the single frequency model of crystal lattice vibrations.

Table 1.2.5. Measured absorption cross-sections σ_{abs} in the $\text{PbCl}_2\text{:Nd}^{3+}$ (0.5 m%) crystal	
Transition	$\sigma_{\text{abs}}, 10^{-17}, \text{cm}$
$^4\text{I}_{9/2} \rightarrow ^4\text{F}_{3/2}$	1.20
$^4\text{I}_{9/2} \rightarrow ^4\text{F}_{5/2} + ^2\text{H}(2)_{9/2}$	1.26
$^4\text{I}_{9/2} \rightarrow ^4\text{F}_{7/2} + ^4\text{S}_{3/2}$	0.54
$^4\text{I}_{9/2} \rightarrow ^4\text{G}_{5/2} + ^2\text{G}_{7/2}$	2.84

So, more than half of the contribution to $^4\text{G}_{5/2}; ^2\text{G}_{7/2}$ relaxation in the low phonon $\text{PbCl}_2\text{:Nd}^{3+}$ crystal accounts for the radiative decay in spite of the small energy gap $\Delta E = 1000 \text{ cm}^{-1}$. The difference between the measured and radiative rate gives the multiphonon relaxation rate. The theoretical curves of Eqs. (1.1.11, 1.1.12), which have been drawn for the processes of temperature stimulated p - phonon emission ($p = \Delta E_{\text{min}} / \hbar \omega_1 = 1000 \text{ cm}^{-1} / 250 \text{ cm}^{-1}$ – solid curve $p = 4$ @ Fig. 1.2.11, $p = \Delta E_{\text{min}} / \hbar \omega_2 = 1000 \text{ cm}^{-1} / 200 \text{ cm}^{-1}$ – dashed curve $p = 5$ @ Fig. 1.2.11, $p = \Delta E_{\text{min}} / \hbar \omega_3 = 1000 \text{ cm}^{-1} / 167 \text{ cm}^{-1}$ – solid curve $p = 6$ @ Fig. 1.2.11) depict the boundaries of the area which covers all experimental points. Most of the points except room temperature lie on the theoretical curve for $p = 5$. So, it may be concluded that mainly five phonon transitions make the contribution to multiphonon relaxation of the $^4\text{G}_{5/2}; ^2\text{G}_{7/2}$ manifold in the $\text{PbCl}_2\text{:Nd}^{3+}$ crystal at $T < 270 \text{ K}$.

Table 1.2.6. Calculated radiative rates ΣA_i and radiative lifetimes τ_R of the manifolds in study in the $\text{PbCl}_2\text{:Nd}^{3+}$ (0.5 m. %) crystal		
Manifold	A, s^{-1}	$\tau_R = 1/A$
$^4\text{I}_{11/2}$	34	29.2 ms
$^4\text{I}_{13/2}$	1090	9.2 ms
$^4\text{I}_{15/2}$	114	8.8 ms
$^4\text{F}_{3/2}$	8800	113 μs
$^4\text{G}_{5/2} + ^2\text{G}_{7/2}$	37200	26.9 μs
$^4\text{G}_{7/2}$	31900	31.4 μs

Twenty times higher the MR rate for five phonon the ${}^4G_{5/2}; {}^2G_{7/2} \rightarrow {}^2H_{11/2}$ transition in $\text{PbCl}_2 \text{Nd}^{3+}$ ($\tau = 54.5 \mu\text{s}$) in comparison with the MR rate of five phonon ${}^4I_{15/2} \rightarrow {}^4I_{13/2}$ transition in $\text{PbGa}_2\text{S}_4: \text{Nd}^{3+}$ ($\tau = 970 \mu\text{s}$) in spite of the lower values of $U^{(k)}$ for the former transition could be concerned with the smaller Nd–Cl distance ($R_0 \geq 2.85 \text{ \AA}$) in PbCl_2 [28] comparing to Nd – S distance ($R_0 \geq 3.1 \text{ \AA}$) in $\text{PbGa}_2\text{S}_4: \text{Nd}^{3+}$ or underestimated radiative rate A in $\text{PbCl}_2 \text{Nd}^{3+}$. A decrease of the MR rate from 14 to 77K (Fig. 1.2.11) may be concerned with the population of higher lying crystal field levels of the ${}^4G_{5/2}; {}^2G_{7/2}$ manifold. This increases the energy gap ΔE to the next manifold below and according to Eq. (1.1.21) decreases the MR rate. But above 80K the decrease of MR rate is compensated by temperature stimulation of multiphonon relaxation (right term of Eq. (1.1.12)).

The measured inverse lifetime temperature dependence of the ${}^4G_{7/2}$ manifold (Fig. 1.2.12) in $\text{PbCl}_2 \text{Nd}^{3+}$ is found to be completely different from the expected multiphonon relaxation $W_{\text{MR}}(T)$ temperature dependence predicted by Eqs. (1.1.11, 1.1.12) for $\Delta E_{\text{min}} \cong 1600 \text{ cm}^{-1}$, $\hbar\omega_{\text{max}} \approx 200 \text{ cm}^{-1}$ and $p = 8$. It shows that the measured fluorescence kinetics decay rate is practically constant above 80K. The dependence is similar to that measured for the ${}^2F(2)_{5/2}$ high-lying Nd^{3+} manifold in $\text{YAlO}_3: \text{Nd}^{3+}$ [29] and reflects the radiative nature of ${}^4G_{7/2}$ relaxation and its high fluorescence quantum yield in the $\text{PbCl}_2 \text{Nd}^{3+}$. The approximation used in Ref. [29] explained the measured $A(T)$ dependence by taking into consideration the difference in population n_i and radiative probabilities A_i of different crystal field levels of the studied manifold. The calculated radiative lifetime of the ${}^4G_{7/2}$ manifold $\tau_R = 32 \mu\text{s}$ (Table 1.2.5) coincides with the measured decay time at 13K (Table 1.2.3). Thus, the fluorescence related to ${}^4G_{7/2}$ manifold usually strongly quenched by multiphonon relaxation in Nd^{3+} doped oxide and fluoride laser crystals is easily observed in $\text{PbCl}_2: \text{Nd}^{3+}$. In the thiogallate crystals the MR rate of the ${}^4G_{7/2}$ manifold is also low compared to the radiative rate. For example, the measured decay time of the ${}^4G_{7/2}$ manifold in $\text{PbGa}_2\text{S}_4: \text{Nd}^{3+}$ (0.2 m.%) $\tau_{\text{meas.}} = 12.3 \mu\text{s}$ at 77 K and $10.5 \mu\text{s}$ at room temperature (Table 1.2.3), which is only slightly less than the calculated radiative decay time ($\tau_R = 13.6 \mu\text{s}$) (Table 1.2.2). So, the calculated fluorescence quantum yield of the ${}^4G_{7/2}$ manifold in $\text{PbGa}_2\text{S}_4: \text{Nd}^{3+}$ is equal to 77% at room temperature.

It is very likely that other manifolds having energies in between the energies of the ${}^4G_{5/2}; {}^2G_{7/2}$ and ${}^4F_{3/2}$ manifolds are also weakly quenched by multiphonon relaxation in $\text{PbCl}_2: \text{Nd}^{3+}$.

This is confirmed by the fluorescence spectra measured at room temperature in visible and near infra red spectral ranges in $\text{PbCl}_2\text{: Nd}^{3+}$ (0.5 m. %) under 532 nm pulsed laser excitation. The fluorescence is measured by standard gated Boxcar averaging technique with a one microsecond delay of the time gate 250 μs long. The fluorescence spectral lines related to the $^2\text{H}_{11/2}$, $^4\text{F}_{9/2}$, $^4\text{F}_{7/2}$, $^4\text{F}_{5/2}$ manifolds is observed (Fig. 1.2.13).

The sum of kinetics of fluorescence decay of the $^4\text{I}_J$ manifolds and its temperature dependence were measured in the $\text{PbCl}_2\text{: Nd}^{3+}$ (0.8 m. %) crystal under 1.56 μm laser excitation directly into the $^4\text{I}_{15/2}$ manifold (Fig. 1.2.14). The fluorescence intensity shows complicated temporal profile depending on temperature. At high temperatures it can be fit by double exponential decay and for temperatures lower than 190 K the temporal profile of the fluorescence kinetics decay is changed.

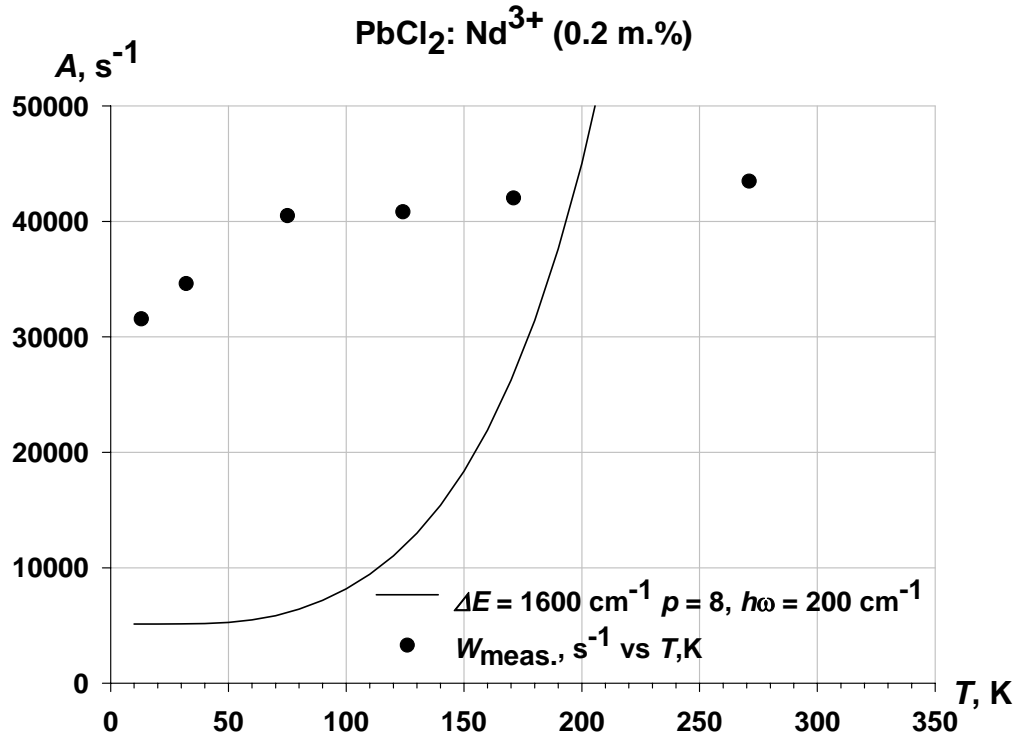


Fig. 1.2.12. Temperature dependence of the measured fluorescence kinetics decay rate of the $^4\text{G}_{7/2}$ manifold in the $\text{PbCl}_2\text{: Nd}^{3+}$ (0.2 m.%) crystal and the fitting curve for the single frequency model of crystal lattice vibrations.

For example, for $T = 8\text{K}$ it has twice the duration than at room temperature and exhibits long fluorescence build-up after switching off the excitation laser pulse. Full analysis of the measured fluorescence kinetics and its temperature dependence is beyond the subject of this paper related to multiphonon relaxation and requires consideration of cross-relaxation processes.

Here, we discuss only the influence of multiphonon relaxation on the fluorescence decay of the $^4\text{I}_J$ manifolds in $\text{PbCl}_2\text{:Nd}^{3+}$. Judd – Ofelt analysis gives the radiative decay times from approximately $\tau_R = 9\text{ ms}$ for the $^4\text{I}_{15/2}$ and $^4\text{I}_{13/2}$ levels to $\tau_R = 29\text{ ms}$ for the $^4\text{I}_{11/2}$ level (Table 1.2.6). The measured decay time at the long time scale of integrated fluorescence kinetics decay varies from $\tau_{\text{meas.}} = 9\text{ ms}$ at room temperature to 11 ms , or may be longer, at 8 K .

According to our analysis of kinetic rate equations (see Appendix) the integrated kinetics decay of the $^4\text{I}_J$ manifolds at the long time scale in any case is determined by the lowest relaxation rate of three $^4\text{I}_J$ levels. One may suppose that contribution of multiphonon relaxation is negligible for the $^4\text{I}_J$ manifolds in $\text{PbCl}_2\text{:Nd}^{3+}$.

If that's the case then the decay time of the measured curve at the long time scale would be 29 ms . But the measured decay time is about 11 ms at low temperature. The difference related to multiphonon relaxation gives the value of the MR decay time of the $^4\text{I}_{11/2}$ level about $\tau_{\text{MR}} = 18\text{ ms}$ at 8K and fluorescence quantum yield about 38% at room temperature. This is about six times higher than for the $^4\text{I}_{15/2}$ level in $\text{PbGa}_2\text{S}_4\text{:Nd}^{3+}$ ($\eta = 6.5\%$). Low submillisecond and millisecond decay rates of fluorescence kinetics of the $^4\text{I}_J$ levels of Nd^{3+} in CaGa_2S_4 , PbGa_2S_4 , and PbCl_2 allows to measure and compare $4 - 5.5\text{ }\mu\text{m}$ fluorescence spectra at 810 nm diode laser excitation into the $^4\text{F}_{5/2}$ level at room temperature (Fig. 1.2.15). The cut-off frequency of long wavelength spectral wings for all the crystals is partially defined by the cut-off frequency of SDL spectrometer.

The widest spectral range of mid IR fluorescence ($4.1 - 5.7\text{ }\mu\text{m}$) is measured for the $\text{PbGa}_2\text{S}_4\text{:Nd}^{3+}$ ($0.2\text{ m.}\%$) crystal and the narrowest one ($4.6 - 5.8\text{ }\mu\text{m}$) for the $\text{PbCl}_2\text{:Nd}^{3+}$ ($0.8\text{ m.}\%$) crystal. In case of selective fluorescence excitation into the $^4\text{I}_{15/2}$ level the maximum of fluorescence spectral peak in the PbGa_2S_4 crystal shifts from 4.9 to $4.7\text{ }\mu\text{m}$ and the spectral line becomes more narrow (Fig. 1.2.16). A $4.9\text{ }\mu\text{m}$ spectral peak most likely belongs to the $^4\text{I}_{11/2} \rightarrow ^4\text{I}_{9/2}$ transition because after laser excitation at 810 nm wavelength into the $^4\text{F}_{5/2}$ level it is rapidly relaxes to the $^4\text{F}_{3/2}$ metastable level. But the calculated branching ratio coefficient from the $^4\text{F}_{3/2}$ level to the $^4\text{I}_{11/2}$ level $\beta(^4\text{F}_{3/2} \rightarrow ^4\text{I}_{11/2}) = 0.443$ is much larger than those to the $^4\text{I}_{13/2}$ level ($\beta(^4\text{F}_{3/2} \rightarrow ^4\text{I}_{13/2})$).

$^4I_{13/2}) = 0.0765)$ and to the $^4I_{15/2}$ level ($\beta(^4F_{3/2} - ^4I_{15/2}) = 0.004$). The rest of excitation goes to the background $^4I_{9/2}$ level. As a result only one excited $^4I_{11/2}$ level among the 4I_J levels populates significantly. And in the case of direct excitation into the $^4I_{15/2}$ level the 4.7 μm fluorescence spectral peak most likely belongs to the $^4I_{15/2} \rightarrow ^4I_{13/2}$ transition.

Thus, we may conclude, that long submillisecond and millisecond decay times of fluorescence kinetics of the 4I_J levels of Nd^{3+} are observed and analyzed in the CaGa_2S_4 , PbGa_2S_4 , and PbCl_2 crystals. Mid IR 4- 5.5 μm fluorescence spectra of Nd^{3+} are measured in these crystals at 810 nm and 1.61 μm laser excitation wavelengths at room temperature. For 5 μm mid IR transitions of Nd^{3+} the radiative relaxation rates are found to be several times higher and multiphonon relaxation (MR) rates are several times lower in lead and calcium thiogallate crystals comparing to fluoride crystals with similar low phonon spectra. Large values of radiative rates in $\text{PbGa}_2\text{S}_4: \text{Nd}^{3+}$, $\text{CaGa}_2\text{S}_4: \text{Nd}^{3+}$ and $\text{PbCl}_2: \text{Nd}^{3+}$ crystals are explained by large refractive indices n of a crystal host. As for multiphonon relaxation rate it is observed that, for example, the MR rate in the row of the $\text{PbGa}_2\text{S}_4: \text{Nd}^{3+}$, $\text{CaGa}_2\text{S}_4: \text{Nd}^{3+}$ and $\text{LaF}_3: \text{Nd}^{3+}$ low phonon crystals of a three phonon $^4G_{5/2}; ^2G_{7/2} \rightarrow ^2H_{11/2}$ transition decreases with an increase of Nd^{3+} to the nearest ligands distance R_0 .

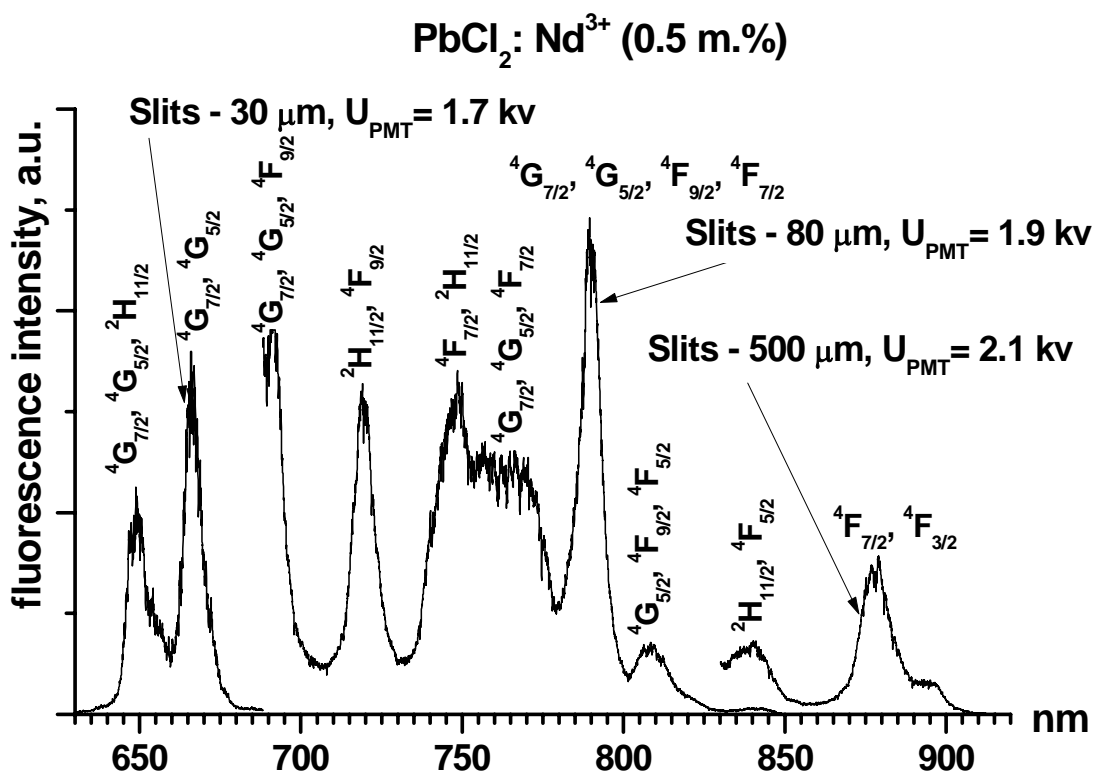


Fig. 1.2.13. The fluorescence spectra of the PbCl₂: Nd³⁺ (0.5 m. %) crystal in red and near IR spectral regions at room temperature measured under 532 nm second harmonics of pulsed Nd: YAG laser excitation and fluorescence monitoring using standard gated Boxcar averaging technique with one microsecond delay of time gate 250 μs long.

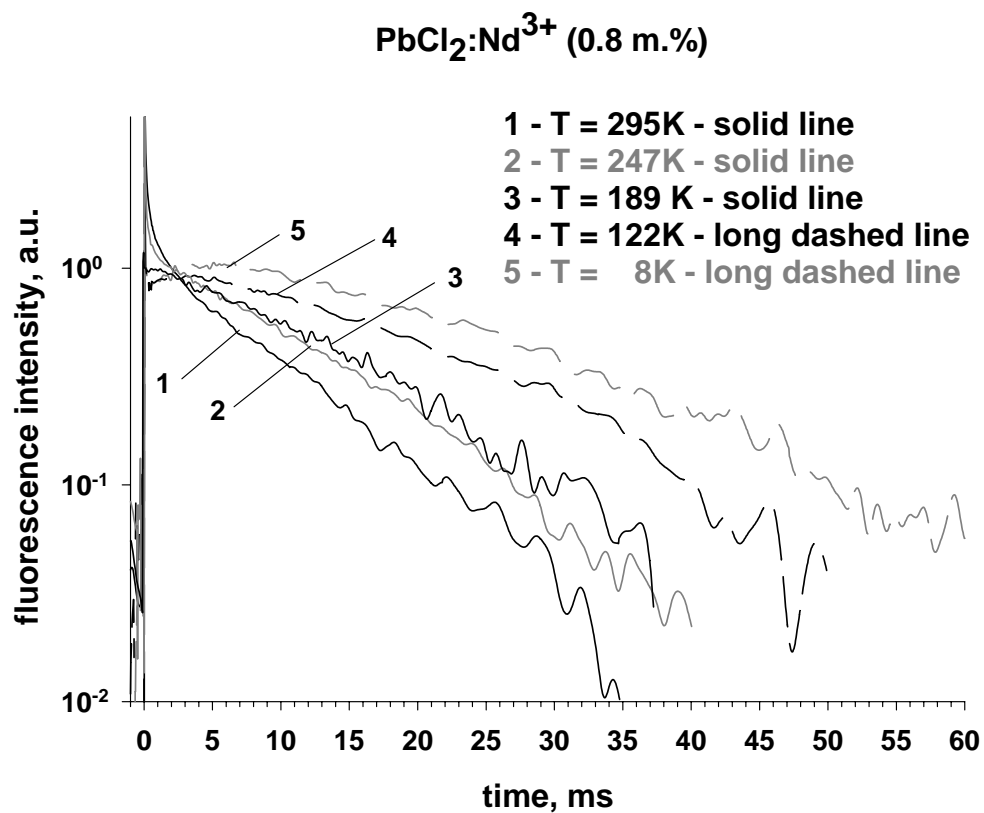


Fig. 1.2.14. Temperature dependence of integrated fluorescence kinetics of three low – lying 4I_J manifolds in PbCl₂: Nd³⁺ (0.8 m.%) under 1.56 μm laser excitation and fluorescence monitoring after optical filter transparent at wavelengths longer than 3 μm .

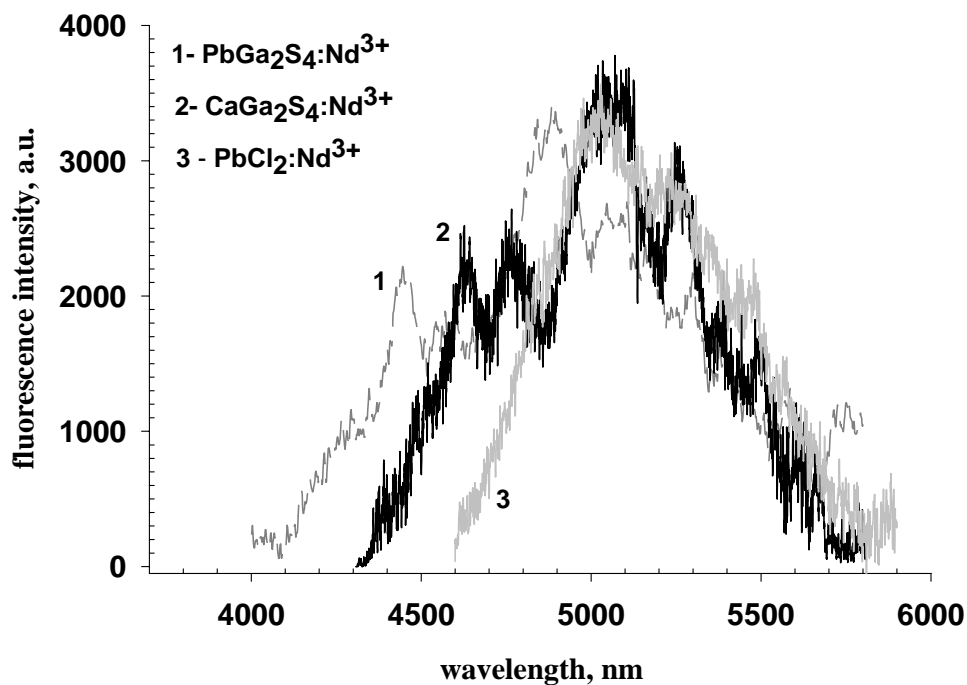


Fig. 1.2.15. Mid IR fluorescence spectra of the PbGa₂S₄: Nd³⁺, CaGa₂S₄: Nd³⁺, and PbCl₂: Nd³⁺ crystals under CW high power (5W) laser diode array excitation at 810 nm and fluorescence monitoring using lock-in amplifier and Ge(Au) photoresistor.

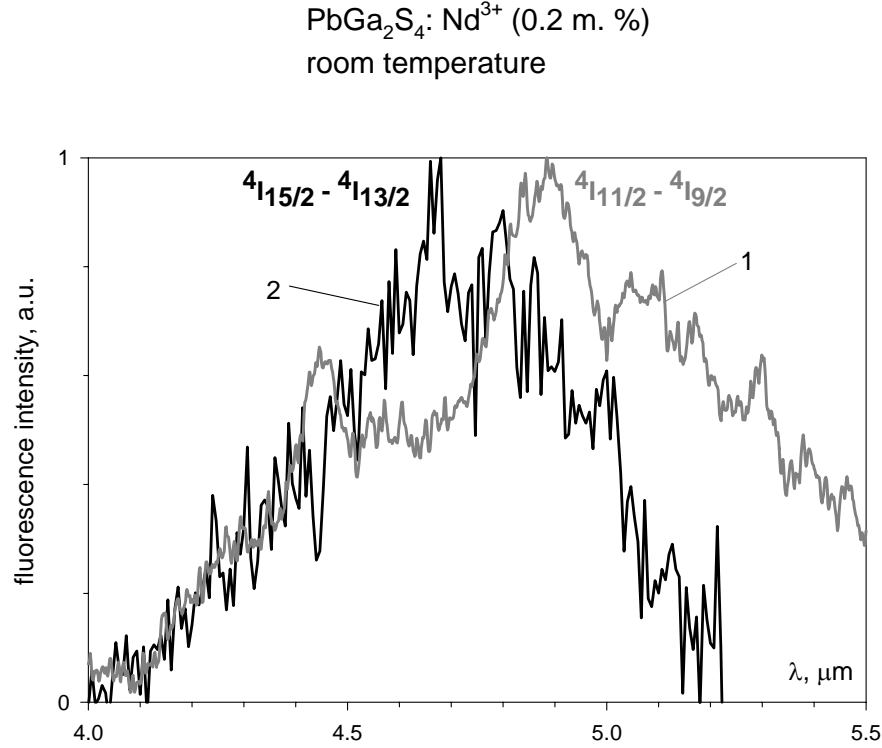


Fig. 1.2.16. A 4- 5.5 μm fluorescence spectra in the PbGa₂S₄: Nd³⁺ (0.2 m.%) crystal for different excitation wavelengths: 810 nm - 1, 1.61 μm – 2.

This result is in a good qualitative agreement with the nonlinear theory of multiphonon relaxation where, for example, the MR rate for p - phonon transition in the frame of point- charge model of RE to the nearest ligands interaction is equal to $W_{\text{MR}}(p) = \sum_{k=2, 4, \text{ and } 6} A_{kp} R_0^{-(2k+2+2p)}$,

where A_{kp} is the parameter independent on R_0 . The slowest MR rates of mid IR transitions of Nd³⁺ among the studied fluoride and sulfide crystals are found for PbGa₂S₄: Nd³⁺ with the largest $R_0 \geq 3.1 \text{ \AA}$. This result explains the much lower MR rates in the studied sulfide crystals comaring to low phonon fluoride crystals with much smaller RE – ligands distance.

The PbCl₂: Nd³⁺ crystal exhibits more than two orders of magnitude lower MR rates of mid IR transitions comparing to PbGa₂S₄: Nd³⁺ due to lower phonon spectrum concerned with heavier anion.

1.1.2 One micron transitions of Nd³⁺ in low phonon laser crystals

The PbGa₂S₄ and PbCl₂ crystals doped by Nd³⁺ can also be perspective for 1 μm laser generation. The new PbGa₂S₄: Nd³⁺ crystal is characterized by high values of Ω_4 and Ω_6 parameters and comparatively small value of Ω_2 parameter (Table 1.2.7). If one compares the obtained values with those for the PbCl₂: Nd³⁺ crystal interesting results can be found. First of all the Ω_4 parameter is 1.14 times higher for the PbGa₂S₄ Nd³⁺ crystal while Ω_6 parameters are practically equal for both the crystals. For the $^4F_{3/2} \rightarrow ^4I_{11/2}$ one-micron laser transition the

Table 1.2.7. The parameters calculated with Judd – Ofelt theory in low phonon Nd³⁺ doped laser crystals.

Crystal	Judd-Ofelt intensity parameters x10 ⁻²⁰ , cm ²			$^4F_{3/2} \rightarrow ^4I_{11/2}$ radiative transition probability A, s ⁻¹	$^4F_{3/2} \rightarrow ^4I_{9/2}$ radiative transition probability A, s ⁻¹	Calculated (measured) $^4F_{3/2}$ level lifetime, τ , μs
	Ω_2	Ω_4	Ω_6			
PbGa ₂ S ₄ :Nd ³⁺	2.96	5.39	4.19	6955	7475	64 (60)
PbCl ₂ :Nd ³⁺	4.33	4.73	4.27	4051	4003	115 (119)

increase in the Ω_6 parameter should result in noticeable rise of the radiative transition probability A (and emission cross- section σ_{em}) in PbGa₂S₄: Nd³⁺ in comparison with PbCl₂: Nd³⁺, because electronic matrix element $U^{(6)}=0.41$ is three times higher as compared to $U^{(4)}=0.14$. As was found in paragraph 4.1 the calculated value of radiative lifetime τ_R of the $^4F_{3/2}$ upper laser level is unusually short in PbGa₂S₄: Nd³⁺ ($\tau_R = 64\mu s$). It is twice shorter than that for the PbCl₂: Nd³⁺ crystal ($\tau_R = 115 \mu s$) and much shorter than, for example, for oxide and fluoride, laser crystals. Both the values are very close to experimentally measured the $^4F_{3/2}$ level lifetimes (see Table 1.2.7).

Due to zero $U^{(2)}$ matrix element for all the $^4F_{3/2} - ^4I_J$ transitions the Ω_2 value has no influence neither on $^4F_{3/2}$ level lifetime nor on the $^4F_{3/2} \rightarrow ^4I_{11/2}$ and $^4F_{3/2} \rightarrow ^4I_{9/2}$ transitions radiative rates. The value of Ω_2 is of importance for transitions where $U^{(2)}$ is rather high. Due to

the large Ω_2 value the intensity of absorption transition in the range of diode pumping near 0.8 μm is rather intensive ($k_{\text{max}}(808 \text{ nm}) = 4.85 \text{ cm}^{-1}$). This is the positive role of high Ω_2 parameter. At the same time for excited state absorption (ESA) at the ${}^4\text{F}_{3/2} \rightarrow {}^4\text{G}_{5/2}$ transition where $U^{(2)}=0.483$ the high value of Ω_2 can be drawback of the $\text{PbGa}_2\text{S}_4:\text{Nd}^{3+}$ crystal, because of parasitic losses.

Let us consider the reason of high emission radiative rate from the ${}^4\text{F}_{3/2}$ level in $\text{PbGa}_2\text{S}_4:\text{Nd}^{3+}$. Usually, there are two ways to increase the radiative emission probability A and an emission cross-section $\sigma_{\text{em}}(\nu)$. One is to increase the line-strength S^{ED} of an electro-dipole RE ion electronic transition. This can be arranged by choosing appropriate crystal matrix with large Ω_k . The influence of Ω_k parameters on radiative probability and, hence, on emission cross-section of the ${}^4\text{F}_{3/2} \rightarrow {}^4\text{I}_{11/2}$ and ${}^4\text{F}_{3/2} \rightarrow {}^4\text{I}_{9/2}$ transitions is described above. And the second way is to increase an index of refraction n in order to increase the photon density of states and to modify the polarizability of the surrounding medium.

New low phonon sulfide PbGa_2S_4 crystal matrix doped with Nd^{3+} has very high refractive index $n \cong 2.51$ and, hence, high photon density of states and high polarizability of surrounding medium. To compare emission cross-section of the ${}^4\text{F}_{3/2} \rightarrow {}^4\text{I}_{11/2}$ and ${}^4\text{F}_{3/2} \rightarrow {}^4\text{I}_{9/2}$ transitions for the $\text{PbGa}_2\text{S}_4:\text{Nd}^{3+}$ crystal with those for extensively used $\text{Nd}:\text{YAG}$ and the $\text{PbCl}_2:\text{Nd}^{3+}$ crystals taking into account the index of refraction n of crystal matrix the product

$$a = \left[\frac{(n^2 + 2)^2}{n} \right] S^{\text{ED}} \quad (1.2.8)$$

is analyzed. Again, the line-strength S^{ED} of the ${}^4\text{F}_{3/2} \rightarrow {}^4\text{I}_{11/2}$ and ${}^4\text{F}_{3/2} \rightarrow {}^4\text{I}_{9/2}$ transitions is a function of terms with $k = 4$ and 6, only, because $U^{(2)} = 0$, and only $U^{(4)} = 0.14$ and $U^{(6)} = 0.41$ are nonzero parameters. The values of Ω_k for $\text{Nd}:\text{YAG}$ were taken from Ref. [30]. Their refraction indexes n were taken from Ref. [31]. The a parameters calculated for the ${}^4\text{F}_{3/2} \rightarrow {}^4\text{I}_{11/2}$ and ${}^4\text{F}_{3/2} \rightarrow {}^4\text{I}_{9/2}$ transitions are presented in Table 1.2.8. For the $\text{PbGa}_2\text{S}_4:\text{Nd}^{3+}$ crystal the $a_{11/2}$ parameter is 1.3 times larger than for $\text{PbCl}_2:\text{Nd}^{3+}$ and 2 times larger than for $\text{Nd}:\text{YAG}$. This indicative of the largest integral emission cross-section σ_{em} at the ${}^4\text{F}_{3/2} \rightarrow {}^4\text{I}_{11/2}$ laser transition for the $\text{PbGa}_2\text{S}_4:\text{Nd}^{3+}$ crystals. The measured lifetimes taken from the literature for $\text{Nd}:\text{YAG}$ [32] are depicted in Table 1.2.8 as well as lifetimes for $\text{PbGa}_2\text{S}_4:\text{Nd}^{3+}$ and $\text{PbCl}_2:\text{Nd}^{3+}$ [33, 34]. They are

in correlation with the sum of a_1 and a_2 parameters. The larger is the sum the shorter is the lifetime.

Although Ω_6 parameters is 1.2 times bigger in Nd: YAG comparing to PbGa₂S₄: Nd³⁺ the higher refractive index n is responsible for much larger radiative emission probability A in the latter crystal. Also, the branching ratio coefficients $\beta(^4F_{3/2} - ^4I_{11/2})$ and $\beta(^4F_{3/2} - ^4I_{9/2})$ can be compared for these crystals using spectroscopic parameter given in Ref. [30].

$$X_{Nd}(^4F_{3/2}) = \Omega_4/\Omega_6 \quad (1.2.9)$$

It should be noted (see Table 1.2.8) that the X parameter raises significantly from the Nd: YAG to the PbCl₂: Nd³⁺ and PbGa₂S₄: Nd³⁺ crystals. Using curves of Fig. 3.1 from Ref. [30] one can easily estimate the branching ratio coefficients from $^4F_{3/2}$ to all four 4I_J manifolds. The calculations results to β values for the $^4F_{3/2} \rightarrow ^4I_{11/2}$ and $^4F_{3/2} \rightarrow ^4I_{9/2}$ laser transitions in three crystals are presented in Table 1.2.8, too. The β values found from the calculation with Judd-Ofelt theory and from estimation of Ref. [30] agree well for the studied crystals.

Table 1.2.8. The parameters having influence on the radiative transitions from the $^4F_{3/2}$ manifold in various Nd³⁺ doped laser crystals.

	$\Omega_4, 10^{-20}, \text{cm}^2$	$\Omega_6, 10^{-20}, \text{cm}^2$	n	$a_{11/2}, 10^{-20}, \text{cm}^2$	$a_{9/2}, 10^{-20}, \text{cm}^2$	X	$\beta(^4F_{3/2} - ^4I_{9/2})$	$\beta(^4F_{3/2} - ^4I_{11/2})$	$\tau, \mu\text{s}$
PbGa ₂ S ₄ :Nd	5.39	4.19	2.51	68.8	40.2	1.29	0.47	0.44	60
PbCl ₂ :Nd	4.73	4.269	2.2	51.6	28	1.11	0.45	0.46	115
YAG:Nd	2.7	5.0	1.82	33.7	13.9	0.38	0.31	0.6	230

The peculiarity of PbGa₂S₄: Nd³⁺ and PbCl₂: Nd³⁺ is increased branching ratio coefficient from the initial $^4F_{3/2}$ laser level to the $^4I_{9/2}$ ground level due to larger Ω_4 parameter comparing to Ω_6 ($X > 1$). As a result the values of branching ratio coefficient to the ground level $\beta(^4F_{3/2} - ^4I_{9/2})$ are practically the same or larger in these crystals than those for the $^4F_{3/2} - ^4I_{11/2}$ transition and come

to $\beta(9/2) = 0.45$ in $\text{PbCl}_2: \text{Nd}^{3+}$ and $\beta(9/2) = 0.47$ in $\text{PbGa}_2\text{S}_4: \text{Nd}^{3+}$. In that way it was also found that for $\text{PbGa}_2\text{S}_4: \text{Nd}^{3+}$ and $\text{PbCl}_2: \text{Nd}^{3+}$ the $\beta(^4\text{F}_{3/2} - ^4\text{I}_{11/2})$ parameter is 25% smaller than for Nd: YAG. Large value of Ω_4 parameter together with rather high value of matrix element $U^{(4)} = 0.2293$ results to larger absorption cross-section for the $^4\text{I}_{9/2} \rightarrow ^4\text{F}_{3/2}$ transition as compared to Nd: YAG. For example, in the $\text{PbGa}_2\text{S}_4: \text{Nd}^{3+}$ (0.5 m. %) crystal k_{max} at 880 nm is equal to 1.75 cm^{-1} .

Hence, it may be concluded that the laser crystals in study, with the high value of the X parameter, have higher than usual branching ratio coefficient from the metastable level to the ground level. This allows realize quasi-three level scheme of oscillation at the $^4\text{F}_{3/2} \rightarrow ^4\text{I}_{9/2}$ transition with the wavelength around $0.9 \mu\text{m}$ under usual laser diode pumping at the $^4\text{I}_{9/2} \rightarrow ^4\text{F}_{5/2}$ transition. Besides, such materials also possess higher than usual the absorption cross-section at the resonant $^4\text{I}_{9/2} \rightarrow ^4\text{F}_{3/2}$ transition which allows to realize an effective pumping directly into the metastable level and decrease the nonradiative losses (quantum defect) to as small as 5% of laser radiation energy. This may reduce many times the heat load on laser element.

The fluorescence spectra at the $^4\text{F}_{3/2} \rightarrow ^4\text{I}_{9/2}$ transition in both crystals were recalculated into emission cross-section spectra with the results of Judd-Ofelt analysis (Fig. 1.2.17). One can see that the advantage of the $\text{PbGa}_2\text{S}_4: \text{Nd}^{3+}$ crystal is narrow fluorescence lines of Stark-Stark inter-manifold transitions and the highest intensity of the fluorescence line for the $^4\text{F}_{3/2}(1) \rightarrow ^4\text{I}_{9/2}(5)$ transition to the upper crystal-field level. The emission cross-section for the longest wavelength 911 nm is twice larger in the $\text{PbGa}_2\text{S}_4: \text{Nd}^{3+}$ crystal comparing to $\text{PbCl}_2: \text{Nd}^{3+}$ crystal and reaches $4.8 \times 10^{-20} \text{ cm}^2$. Another advantage of the $\text{PbGa}_2\text{S}_4: \text{Nd}^{3+}$ crystal against the $\text{PbCl}_2: \text{Nd}^{3+}$ one is two times larger the value of the $^4\text{I}_{9/2}$ manifold crystal-field splitting E1 – E5. This decreases the population of the final crystal-field level E5 and allows realize population inversion more easily.

Hence, it can be concluded that the $\text{PbGa}_2\text{S}_4: \text{Nd}^{3+}$ crystal may be considered as a perspective active laser media for one-micron laser generation with short lifetime, high emission cross-section and small heat losses.

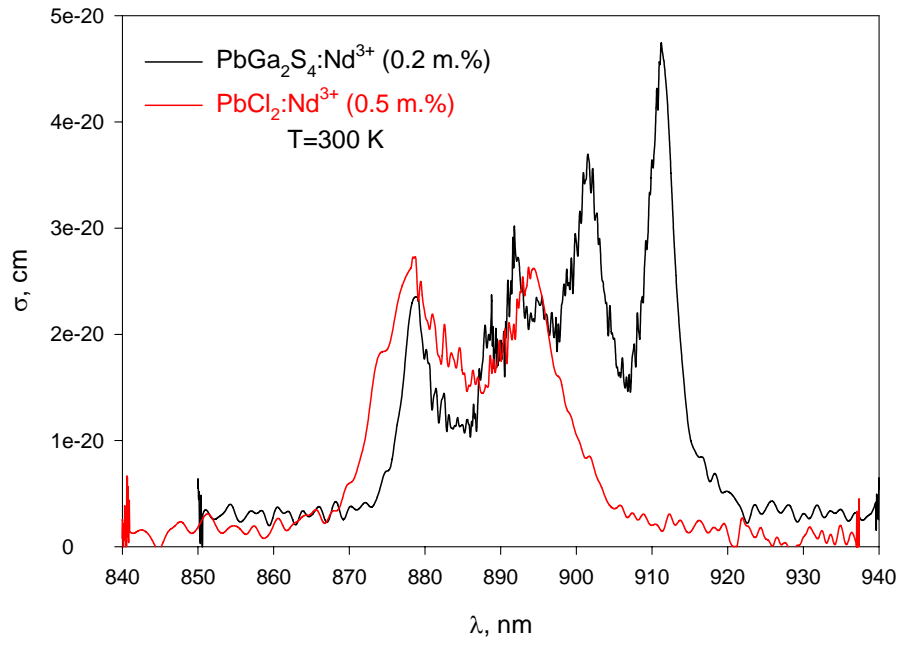


Fig. 1.2.17. Spectral dependence of emission cross-section at $^4\text{F}_{3/2}-^4\text{I}_{9/2}$ transition in $\text{PbGa}_2\text{S}_4:\text{Nd}$ (0.2 m.%) and $\text{PbCl}_2:\text{Nd}$ (0.5 m.%) crystals.

1.2.3. Appendix

Kinetics of mid IR emission

Multiphonon and radiative decay (PbGa₂S₄: Nd³⁺ and CaGa₂S₄: Nd³⁺)

$$\dot{n}_4 = -\gamma_4 n_4, \quad (\text{A.1a})$$

$$\dot{n}_3 = -\gamma_3 n_3 + (W_{43} + V_{43}) n_4, \quad (\text{A.1b})$$

$$\dot{n}_2 = -\gamma_2 n_2 + (W_{32} + V_{32}) n_3 + V_{42} n_4, \quad (\text{A.1c})$$

where

$$\gamma_4 = W_{43} + V_{43} + V_{42} + V_{41}, \quad (\text{A.2a})$$

$$\gamma_3 = W_{32} + V_{32} + V_{31}, \quad (\text{A.2b})$$

$$\gamma_2 = W_{21} + V_{21}, \quad (\text{A.2c})$$

W_{ij} is a probability of nonradiative transition from i -th level to j -th,

V_{ij} is a probability of radiative transition from i -th level to j -th.

We neglected in Eq. (A.1) the terms of the order of W_{42}/V_{42} , W_{41}/V_{41} , and W_{31}/V_{31} , because they are well below 1. Then the values of $\tau_2 = 1/\gamma_2$, $\tau_3 = 1/\gamma_3$, and $\tau_4 = 1/\gamma_4$ can be considered as lifetimes of second, third, and fourth levels, respectively (counting from the bottom). Level one is the background level.

The solution of the set of equations (A.1) with initial conditions $n_4(0) = 1$, $n_3(0) = n_e(0) = n_1(0) = 0$ is

$$n_4(t) = n_4(0) \exp(-\gamma_4 t), \quad (\text{A.3a})$$

$$n_3(t) = -\frac{W_{43} + V_{43}}{\gamma_4 - \gamma_3} [\exp(-\gamma_4 t) - \exp(-\gamma_3 t)] n_4(0), \quad (\text{A.3b})$$

$$n_2(t) = \frac{(W_{32} + V_{32})(W_{43} + V_{43})}{\gamma_4 - \gamma_3} \left[\frac{\exp(-\gamma_4 t) - \exp(-\gamma_2 t)}{\gamma_4 - \gamma_2} - \frac{\exp(-\gamma_3 t) - \exp(-\gamma_2 t)}{\gamma_3 - \gamma_2} \right] n_4(0) - \frac{V_{42}}{\gamma_4 - \gamma_2} [\exp(-\gamma_4 t) - \exp(-\gamma_2 t)] n_4(0) \quad (\text{A.3c})$$

Eq. (A.3a) describes exponential decay of population of the fourth (upper) level from initial value $n_4(0)$ to zero with the characteristic time $1/\gamma_4$. Eq. (A.3b) describes increasing of

population of third level from initial value $n_3(0) = 0$ to a maximum value, after that the population tends to zero. In a similar way the population $n_2(t)$ varies with time.

Normalized infrared intensity $I(t)/I(0)$ is equal to

$$\begin{aligned} I(t)/I(0) &= [\hbar\omega_{43}V_{43}n_4(t) + \hbar\omega_{32}V_{32}n_3(t) + \hbar\omega_{21}V_{21}n_2(t)] / \hbar\omega_{43}V_{43}n_4(0) = \\ &= [C_2 \exp(-\gamma_2 t) + C_3 \exp(-\gamma_3 t) + C_4 \exp(-\gamma_4 t)] / (C_2 + C_3 + C_4). \end{aligned} \quad (\text{A.4})$$

Here

$$C_2 = \hbar\omega_{21}V_{21}a_{22}, \quad (\text{A.5a})$$

$$C_3 = \hbar\omega_{21}V_{21}a_{23} + \hbar\omega_{32}V_{32}a_{33}, \quad (\text{A.5b})$$

$$C_4 = \hbar\omega_{21}V_{21}a_{24} + \hbar\omega_{32}V_{32}a_{34} + \hbar\omega_{43}V_{43}a_{44}, \quad (\text{A.5c})$$

where

$$a_{22} = \frac{(W_{32} + V_{32})(W_{43} + V_{43})}{(\gamma_4 - \gamma_2)(\gamma_3 - \gamma_2)} + \frac{V_{42}}{\gamma_4 - \gamma_2}, \quad (\text{A.6a})$$

$$a_{23} = -\frac{(W_{32} + V_{32})(W_{43} + V_{43})}{(\gamma_4 - \gamma_3)(\gamma_3 - \gamma_2)}, \quad (\text{A.6b})$$

$$a_{24} = -a_{22} - a_{23}, \quad (\text{A.6c})$$

$$a_{33} = -a_{34} = \frac{W_{43} + V_{43}}{\gamma_4 - \gamma_3}, \quad (\text{A.6d})$$

$$a_{44} = 1, \quad (\text{A.6e})$$

Asymptotic behavior

As it follows from Eq. (A.4), the asymptotic equation for function $I(t)/I(0)$ is

$$\lim_{t \rightarrow \infty} I(t)/I(0) \rightarrow A_k \exp(-\gamma_k t), \quad (\text{A.7})$$

where γ_k is smallest among $\gamma_2, \gamma_3, \gamma_4$, and

$$A = C_k / (C_2 + C_3 + C_4). \quad (\text{A.8})$$

Radiative decay ($\text{PbCl}_2: \text{Nd}^{3+}$)

Let us consider the only radiative relaxation of the four-level system when radiative rates V_{ij} are much larger than nonradiative W_{ij} rates, that is

$$V_{ij} \gg W_{ij} \quad (\text{A.9})$$

In this case Eq. (A.1) may be simplified and rewritten Eq. (A.1) as

$$\dot{n}_4 = -\gamma_4 n_4, \quad (\text{A.10a})$$

$$\dot{n}_3 = -\gamma_3 n_3 + V_{43} n_4, \quad (\text{A.10b})$$

$$\dot{n}_2 = -\gamma_2 n_2 + V_{32} n_3 + V_{42} n_4, \quad (\text{A.10c})$$

where

$$\gamma_4 = V_{43} + V_{42} + V_{41}, \quad (\text{A.11a})$$

$$\gamma_3 = V_{32} + V_{31}, \quad (\text{A.11b})$$

$$\gamma_2 = W_{21}, \quad (\text{A.11c})$$

The solution of the set of equations (A.10) is

$$n_4(t) = n_4(0) \exp(-\gamma_4 t), \quad (\text{A.12a})$$

$$n_3(t) = -\frac{V_{43}}{\gamma_4 - \gamma_3} [\exp(-\gamma_4 t) - \exp(-\gamma_3 t)] n_4(0), \quad (\text{A.12b})$$

$$\begin{aligned} n_2(t) = & \frac{V_{32} V_{43}}{\gamma_4 - \gamma_3} \left[\frac{\exp(-\gamma_4 t) - \exp(-\gamma_2 t)}{\gamma_4 - \gamma_2} - \frac{\exp(-\gamma_3 t) - \exp(-\gamma_2 t)}{\gamma_3 - \gamma_2} \right] n_4(0) - \\ & - \frac{V_{42}}{\gamma_4 - \gamma_2} [\exp(-\gamma_4 t) - \exp(-\gamma_2 t)] n_4(0) \end{aligned} \quad (\text{A.12c})$$

In considered case the normalized infrared intensity $I(t)/I(0)$ has the same form as Eq. (A.4)

$$\begin{aligned} I(t)/I(0) = & [\hbar\omega_{43} V_{43} n_4(t) + \hbar\omega_{32} V_{32} n_3(t) + \hbar\omega_{21} V_{21} n_2(t)] / \hbar\omega_{43} V_{43} n_4(0) \\ = & [C_2 \exp(-\gamma_2 t) + C_3 \exp(-\gamma_3 t) + C_4 \exp(-\gamma_4 t)] / (C_2 + C_3 + C_4). \end{aligned} \quad (\text{A.13})$$

with the same form of coefficients C_k :

$$C_2 = \hbar\omega_{21} V_{21} a_{22}, \quad (\text{A.14a})$$

$$C_3 = \hbar\omega_{21} V_{21} a_{23} + \hbar\omega_{32} V_{32} a_{33}, \quad (\text{A.14b})$$

$$C_4 = \hbar\omega_{21} V_{21} a_{24} + \hbar\omega_{32} V_{32} a_{34} + \hbar\omega_{43} V_{43} a_{44}, \quad (\text{A.14c})$$

However, coefficients a_{ik} in Eqs. (A.14) are equal now to

$$a_{22} = \frac{V_{32} V_{43}}{(\gamma_4 - \gamma_2)(\gamma_3 - \gamma_2)} + \frac{V_{42}}{\gamma_4 - \gamma_2}, \quad (\text{A.15a})$$

$$a_{23} = -\frac{V_{32} V_{43}}{(\gamma_4 - \gamma_3)(\gamma_3 - \gamma_2)}, \quad (\text{A.15b})$$

$$a_{24} = -a_{22} - a_{23}, \quad (\text{A.15c})$$

$$a_{33} = -a_{34} = \frac{V_{43}}{\gamma_4 - \gamma_3}, \quad (\text{A.15d})$$

$$a_{44} = 1, \quad (\text{A.15e})$$

Asymptotic behavior of radiative decay

As it follows from Eq. (A.13), the asymptotic equation for $I(t)/I(0)$ function again has a form

$$\lim_{t \rightarrow \infty} I(t)/I(0) \rightarrow B_k \exp(-t/\tau_k), \quad (\text{A.16})$$

where $\tau_k = 1/\gamma_k$ is the longest lifetime among $\tau_2 = 1/\gamma_2$, $\tau_3 = 1/\gamma_3$, $\tau_4 = 1/\gamma_4$ lifetimes, and

$$B_k = C_k / (C_2 + C_3 + C_4). \quad (\text{A.17})$$

References

1. S. R. Bowman, L. B. Shaw, B. J. Feldman, and J. Ganem, IEEE J. Quantum Electron. 32 (1996) 646.
2. S. R. Bowman, S. K. Searles, N. W. Jenkins, S. B. Qadri, E. F. Skelton and J. Ganem, "Diode pumped room temperature 4.6 μm erbium laser," in *Proceedings of Advanced Solid State Lasers Conference*, (Seattle, Wash., 2001), pp.84- 86.
3. Yu.V.Orlovskii, K.K.Pukhov, T.T.Basiev, T.Tsuboi, Optical Materials 4 (1995) 583.
4. M. C. Nostarnd, R. H. Page, S. A. Payne, and W. F. Krupke, Optics Letters 24 (1999) 1215.
5. T.T. Basiev, M.E. Doroshenko, V.V. Osiko, V.V. Badikov, "Mid IR laser oscillations in new low phonon $\text{PbGa}_2\text{S}_4:\text{Dy}^{3+}$ crystal", in *Advanced Solid State Photonics*, February 6-8, 2005, Vienna, Austria, Technical digest, TuB10.
6. Laser Materials and Technologies Research Center of General Physics Institute RAS, Active materials for lasing in the 4 – 5 μm spectral range, Final report, Contract No EOARD F61775-99- WE033 (2000).

7. J.P.Hurrel and V.J.Minkiewicz, Solid State Communications 8 (1970) 463.
8. Yu. V. Orlovskii, T. T. Basiev, K. K. Pukhov, N. A. Glushkov, O. K. Alimov, S. B. Mirov, “Multiphonon relaxation of mid IR transitions of rare- earth ions in fluorite type crystals”, in *the Proceedings volume of the Advanced Solid-State Photonics 2004*, author: Gregory Quarles, (Optical Society of America, Washington, D.C., TOPS Volume 94, 2004), pp. 440-445.
9. K.K. Pukhov, V.P. Sakun, Phys. Stat. Sol.(b) 95 (1979) 391.
10. K.K.Pukhov, Fiz. Tverd. Tela 31 (1989) 144; [Sov. Phys. Solid State, 31 (1989) 1557].
11. Yu.V.Orlovskii, R.J.Reeves, R.C. Powell, T.T.Basiev, K.K.Pukhov, Phys. Rev. B 49 (1994) 3821.
12. T.T.Basiev, Yu.V.Orlovskii, K.K.Pukhov, V.B.Sigachev, M.E.Doroshenko, I.N.Vorob'ev, Journal of Lumin. 68 (1996) 241.
13. T.T.Basiev, Yu.V.Orlovskii, K.K.Pukhov, F.Auzel, Laser Physics, **7** (1997) 1139.
14. W.T. Carnall, Hannah Crosswhite and H.M. Crosswhite, “Energy level structure and transition probabilities in the spectra of the trivalent lanthanides in LaF_3 ”, Aragon National Laboratory, Internal Report (1977).
15. B.Z. Malkin, in *Spectroscopy of Solids Containing Rare Earth Ions*, A.A. Kaplyanskii and R.M. Macfarlane, eds. (North-Holland, Amsterdam 1987), Chap. 2.
16. M.D. Sturge, Phys. Rev. B, **8** (1973) 6.
17. B.R.Judd, Phys.Rev. 127 (1962) 750.
18. G.S. Ofelt, J. Chem. Phys. 37(3) (1962) 511.
19. M.J. Weber, Phys.Rev. 157 (1967) 262.
20. A.A. Kornienko, personal communication.
21. L. A. Riseberg, H. W. Moos, Phys.Rev. 174 (1968) 429.
22. Yu.V. Orlovskii, T.T.Basiev, I.N.Vorob'ev, V.V.Osiko, A.G.Papashvili, A.M.Prokhorov, Laser Physics International Journal, 6 (1996) 448.
23. Yu.V.Orlovskii, T.T.Basiev, S.A.Abalakin, I.N.Vorob'ev, O.K.Alimov, A.G.Papashvili, K.K.Pukhov, Journal of Lumin. 76/77 (1998) 371.
24. Yu.V.Orlovskii, T.T. Basiev, A.G.Papashvili, I.N.Vorob'ev, O.K.Alimov, V.V.Osiko, J.Heber, Journal of Lumin. 99/3 (2002) 233.

25. Yu.V.Orlovskii, T.T.Basiev, K.K.Pukhov, I.N.Vorob'ev, A.G.Papashvili, F.Pelle, V.V. Osiko, *Journal of Lumin.* 94/95 (2001) 791.
26. B.Eisenmann, M.Jakowski, W.Klee, H.Schafer, *Revue de Chimie Minerale* 20 (1983) 255.
27. A. Abraham and B. Bleany, "Paramagnetic resonance of transition ions", Claredon Press, Oxford (1970)
28. K. Nitsch, M. Dusek, M. Nikl, K. Polak and M. Rodova, *Prog. Crystal Growth and Charact.* 30 (1995) 1.
29. T. T. Basiev, A. Yu. Dergachev, Yu. V. Orlovskii, A. M. Prokhorov, "Multiphonon nano- and subnanosecond relaxation from high- lying levels of Nd^{3+} ions in laser fluorides and oxides," in *Proceedings of General Physics Institute*, (Moscow, Nauka, 1994) v. 46, pp.3-64.
30. A.A.Kaminskii, B.M.Antipenko, *Multilevel operating schemes of crystalline lasers*, Moscow, Nauka, 1989, pp. 270 (in Russian)
31. *Handbook of lasers with selected data on optical technology*, Ed. R.J. Pressley, Chemical Rubber Co, Cleveland, 1971
32. W.Koechner, *Solid- State Laser Engineering*, Fifth revised and updated edition, Springer, p. 73.
33. T.T.Basiev, Yu.V.Orlovskii, I.N.Vorob'ev, L.N.Dmitruk, T.D.Efimenko, V.N.Skvortsov, V.A.Konyushkin, V.V.Osiko, *Relaxation of mid- IR transitions of Nd^{3+} in laser crystals with "short" phonon spectra*, NATO Science Series, Proceeding of the NATO Advanced Research Workshop on Physics of Lasers Crystals, J.-C. Krupa and N.A.Kulagin (eds.), Kluwer Academic Publishers, v. 126, p. 51-61 (2003)
34. Annual report (2nd year), *Active Laser and Raman materials for 1.3 – 5 μm spectral range*, Contract No ISTC 2022p/ EOARD 207042 (2004)

2. Research and development of laser ceramics

2.I. Oxide Ceramics.

2.1.1. Introduction.

This report summarized our experiments on yttria laser ceramic.

The optically transparent ceramics are known for several decades (see [1-3]). Transparent laser-quality ceramics comparable with single crystals is an achievement of recent years (Fig.2.1.1), though the first publication on a ceramic laser is dated 1966 and refers to $\text{CaF}_2:\text{Dy}$ [4]. The announcement of transparent ThO_2 -doped Y_2O_3 ceramics (“Yttralox”) designed by General Electric and the creation of polycrystalline ceramic lasers using this ceramics appeared in 1973 [5,6].

The series of publications about obtaining and investigation of yttrium oxide laser TR ion-doped ceramic, $\text{Y}_3\text{Al}_5\text{O}_{12}$ YAG ($\text{Nd}^{3+}:\text{YAG}$, $\text{Cr}^{4+}:\text{YAG}$, and $\text{Nd}:\text{Y}_3\text{Sc}_x\text{Al}_{5-x}\text{O}_{12}$) as well as samples of $\text{Nd}^{3+}:\text{YGdO}_3$, $\text{Nd}^{3+}:\text{Lu}_2\text{O}_3$, $\text{Yb}:\text{Sc}_2\text{O}_3$ are currently available [7-22].

Compared to single crystals, the ceramic laser materials have several advantages, namely, ease of fabrication, lower cost, fabrication of large size elements, large concentration and homogeneous distribution of dopants, possibility to obtain a new composition as an optical media, which is difficult or impossible to prepare in the form of single crystals. In 1990s, a new stage in the laser ceramics development started. After several unsuccessful attempts, the yttrium aluminum garnet laser ceramics was first synthesized by A. Ikesue’s group [7]. The synthesis was carried by classical ceramic technology.

In 2000, the group of Prof. Kenichi Ueda presented laser study on ceramics developed by Konoshina Ltd (Japan) by completely different technology, based on the patents [23, 24]. High-power and highly efficient lasers with laser-diode pumping were performed on the basis of $\text{Nd}:\text{YAG}$ ceramics. The ceramics is produced from nanoparticles in a manner of self-energy-driven formation process. Fig. 2.1.2 shows the fabrication process of nanocrystalline $\text{Nd}:\text{YAG}$ laser ceramics.

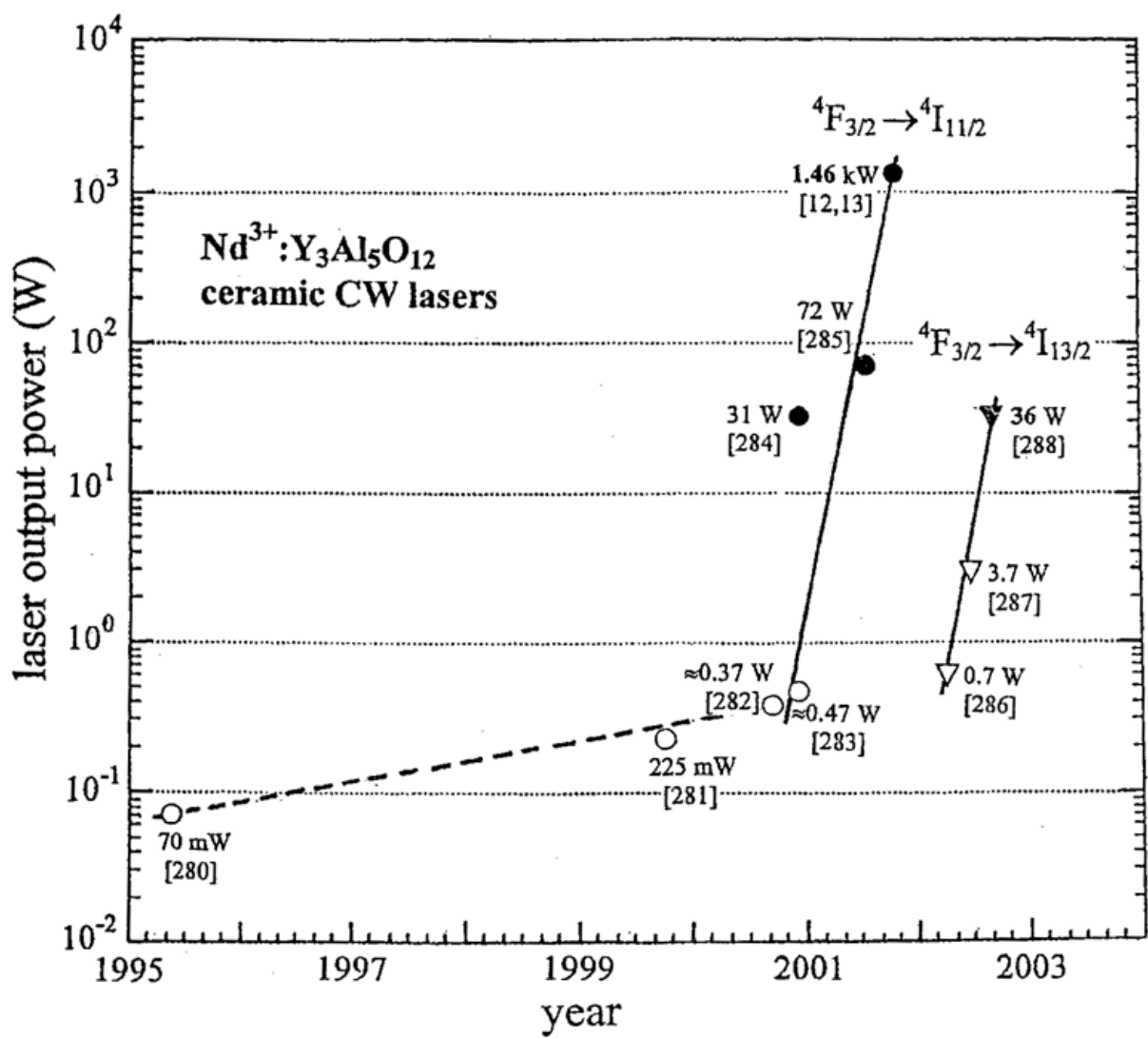


Fig. 2.1.1. Development of ceramic YAG lasers. (Kaminskii, 2004)

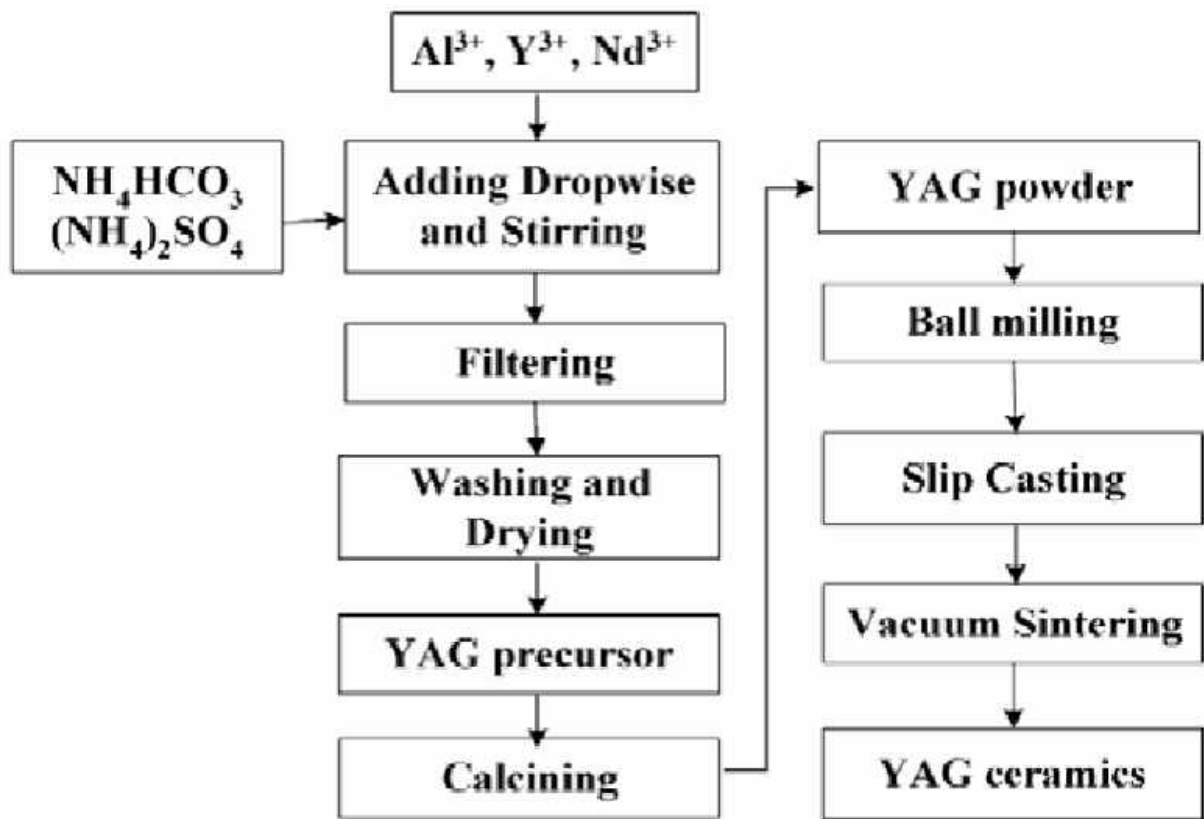
The obtaining possibility of 100% nominative density ceramics was realized by fundamental systematic researches of agglomeration kinetics mechanisms and respective theory of agglomeration [25, 26]. The technology of obtaining of optical oxide ceramics was created in other scientific centers past years too [27-30].

Almost zero porosity is the essential but not sufficient requirement for preparing of laser ceramic materials. In particular, the quality of Yttralox products is not sufficient for creation of the effective laser elements in spite of very low pore concentration. Our investigation by electron microscopy (see previous report) doesn't reveal any chemical inhomogeneity, which considered as reason of preventing efficient laser oscillation. It seems that mutual orientation of nanoparticles due to casting process (Fig. 2.1.2) leads to crystallographic orientation of grains in ceramic, the special organization of grains interface and very small optical losses.

Project goals and tasks:

Experimental study of physicochemical processes leading to preparation of laser grade ceramics doped with neodymium or another rare-earth elements, based on selforganization of nanoparticles. Yttrium oxide (yttria), Y_2O_3 and $Y_3Al_5O_{12}$ garnet (YAG) were selected as main object. The following tasks were decided :

- preparation of precursor in wet processes
- preparation of nanoparticles
- preparation of green compact
- sintering of ceramic without external pressure



Forming by simple casting

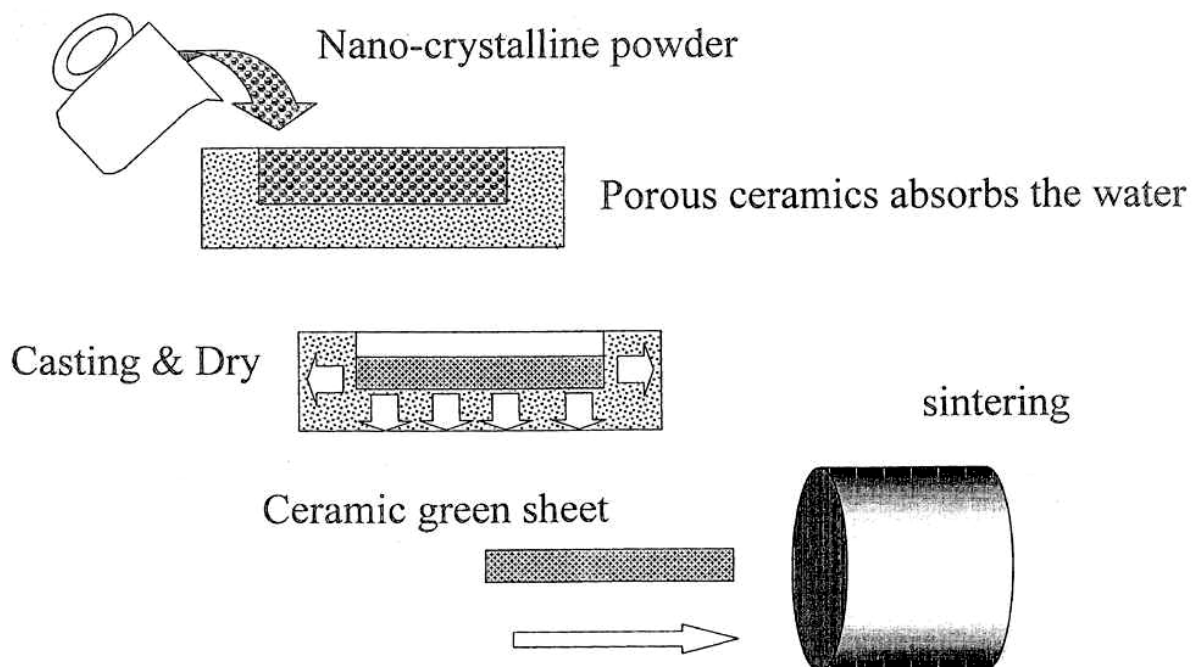


Fig. 2.1.2. Scheme of preparing of YAG ceramic lasers by Konoshima Chemical Corp.
(Kaminskii, 2004)

2.1.2.Experimental

We used yttrium oxide (yttria), Y_2O_3 , and oxides of rare-earths (Nd_2O_3 , Yb_2O_3) with 99,99% content of basic component as initial reagent. $Al(NO_3)_3 \cdot 9H_2O$, nitric acid, ammonium hydroxide and other reagent analytical grade were used. The electron micrograph of yttria powder is presented on Fig. 2.1.3.

To avoid moisture and carbon dioxide the Nd_2O_3 was calcinated at 750 °C for several hours before the using.

We carried out 125 experiments on precipitation of yttria and garnet precursor from water solution. General scheme of experimental set up is presented on Fig. 2.1.4.

The samples were characterized by the X-ray diffraction (DRON-2 diffractometer, $Cu\ K\alpha$ radiation) and the electron scanning microscopy (JEOL 59/10). The thermogravimetry technique (Q-1500 Derivatograph and Netsch Thermoanalyser) was used to study the processes of thermal decomposition of yttria and garnet precursors. IR spectroscopy (Bruker) in 2000-500 cm^{-1} range were used also. Raman spectra of the samples were investigated at 300 K with Spex–Ramalog-1403 spectrometer using conventional back scattering geometry under Ar (488 nm) excitation.

The size of particle (coherent scattering regions, CSR) and microdeformations were calculated from the broadening of the reflexes at X-ray powder diagrams according to Ref. [31]. The X-ray peak parameters (the peak position, area, and width) were determined using a «Microcal origin» program.

Primary data processing was done using an ARX-63 program: we subtracted background, separated the $K\alpha_1$ lines, and determined the width of the peak at half height ($2w$) and the integral width of the peak (β). The standard (no broadened) profile was obtained by recording a polycrystalline silicon etalon at the same parameters of X-ray pattern.

It is assumed that the profile of the X-ray diffraction line is described by the Voigt function, which is a combination of the Cauchy and Gauss functions. The measured experimentally profile h is a combination of the structurally broadened profile f and the standard profile g . The standard profile is used for the account of the instrumental broadening. Hence, we have

$$h_c = g_c * f_c \text{ and } h_G = g_G * f_G,$$

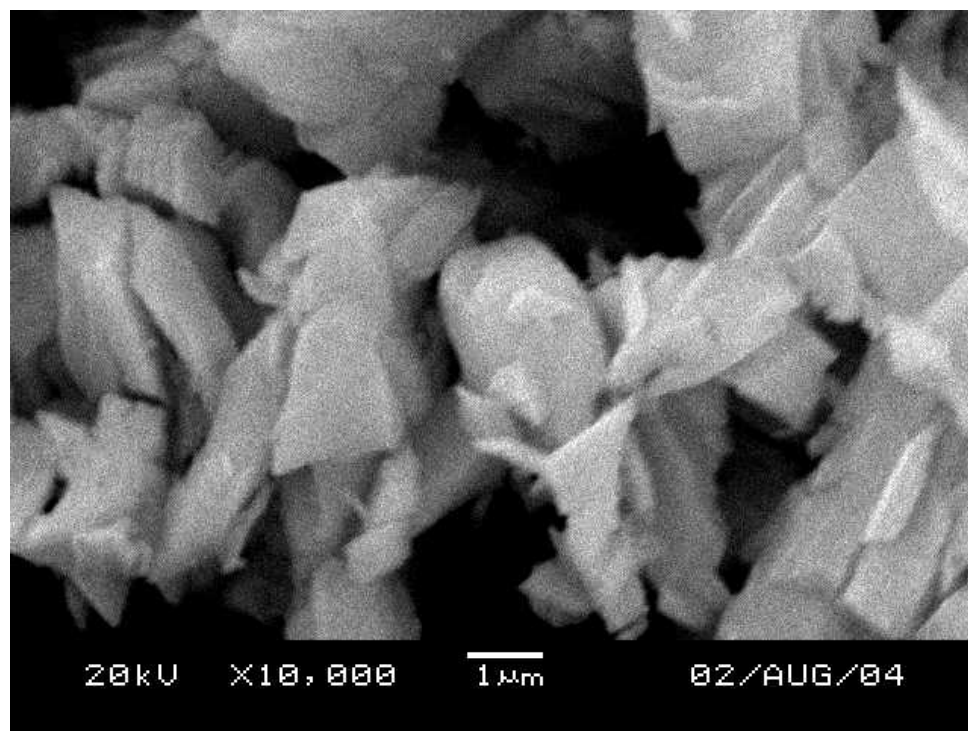


Fig. 2.1.3. Scanning electron microscopy, initial Y_2O_3 powder.

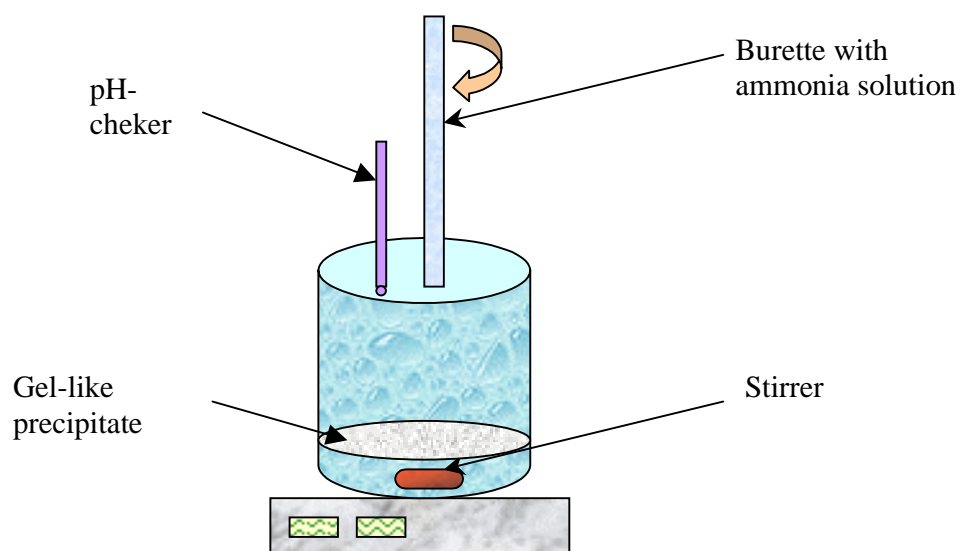


Fig.2.1.4. The scheme of precursor precipitation from water solution

where C and G are the Cauchy and Gauss components of the Voigt profile and $*$ is the symbol of convolution operation. From this, it follows that the integral widths (β_C^f, β_G^f) for the f profile after correction for the instrumental broadening are given by the expressions

$$\beta_C^f = \beta_C^h - \beta_C^g \text{ and } (\beta_G^f)^2 = (\beta_G^h)^2 - (\beta_G^g)^2.$$

The Cauchy and Gauss components can be found from β and the ratio $2w/\beta$ for h and g profiles, where $2w$ is the width at the half height of the X-ray peak and β is the integral width. We derived the following empirical equations:

$$\beta_C = \beta[2.0207 - 0.4803(2w/\beta) - 1.7756(2w/\beta)^2]$$

$$\beta_G = \beta\{0.6420 + 1.4187[(2w/\beta) - 2/\pi]^{1/2} - 2.2043(2w/\beta) + 1.8706(2w/\beta)^2\}.$$

Then, the sizes of CSR (grain size D) and of microdeformations (e) can be found from the expressions

$$D = K \lambda / \beta_C^f \cos \theta, \quad e = \beta_G^f / 4 \tan \theta,$$

where $K = 0.9$.

Precipitation and thermal decomposition of yttria precursor

We studied the precipitation of yttria precursor from chloride, acetate, and nitrate solutions.

The chloride technology systematically gives stable colloidal solutions or very fine sediments, which requires a special filtration technique. We revealed a complicated chemical composition of precipitates, which requires additional studying. It is known that full removing of chlorine ions from the precipitates by many stages of water washing is a difficult task. The pyrohydrolysis reaction decreases the chlorine ions portion during the agglomeration of ceramics or at thermal treatment. However, this process not ending and so the specimens had includes of second phase i.e. scatter centers [32]. The acetate precursor has no obvious advantages in comparison with the nitrate precursor. It is known that thermal decomposition of acetates with oxide formation requires the oxygen atmosphere. In other cases the carbon particles forms, which may violated optical transparency.

For this reason we leave out both chlorine and acetate processes. So, we made emphasis on nitrate technology for preparing yttria precursor.

Yttrium oxide was dissolved in nitric acid, and the solution was ammonia titrated. We varied the temperature ($4 - 60^\circ \text{C}$) and concentration of initial solution (from 0.0085 to 0.253 mol/l).

A typical titration curve is presented in Fig. 2.1.5.

The X-ray powder pattern of precipitates varied from practically amorphous to series of well-formed, although broaden, reflexes (Fig. 2.1.6).

This pattern is similar, but not identical to ones of compound $Y_2NO_3(OH)_5 \cdot 1.5H_2O$ according to JCPDS card number 49-1107 and basic yttrium nitrate hydrates according to ref. [33].

Table I. X-ray pattern of yttria nitrate precursors ($\lambda = CuK\alpha$).

2Θ	$I/I_0, \%$	$d, \text{\AA}$
9.6	73	9.2
19.6	37	4.53
28.2	50	3.16
28.7	100	3.11
29.6	30	3.02
36.0	15	2.493
40.9	17	2.205
44.7	18	2.026
50.4	31	1.809
51.5	29	1.773
58.5	7	1.577
59.7	11	1.548

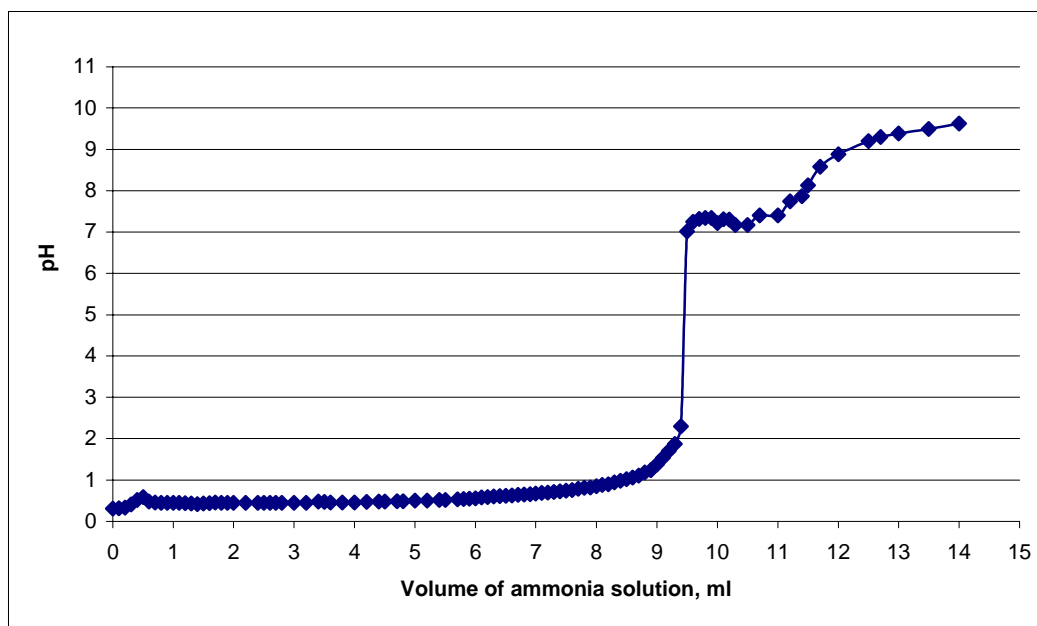
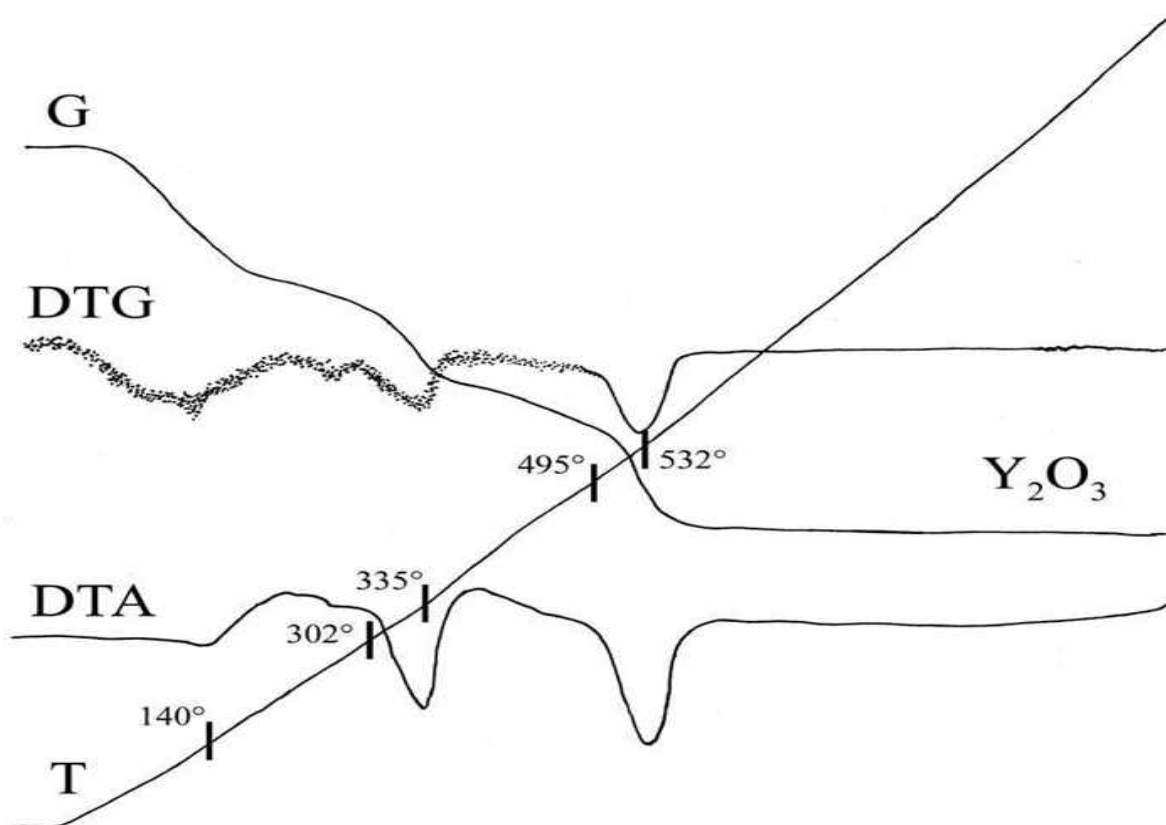
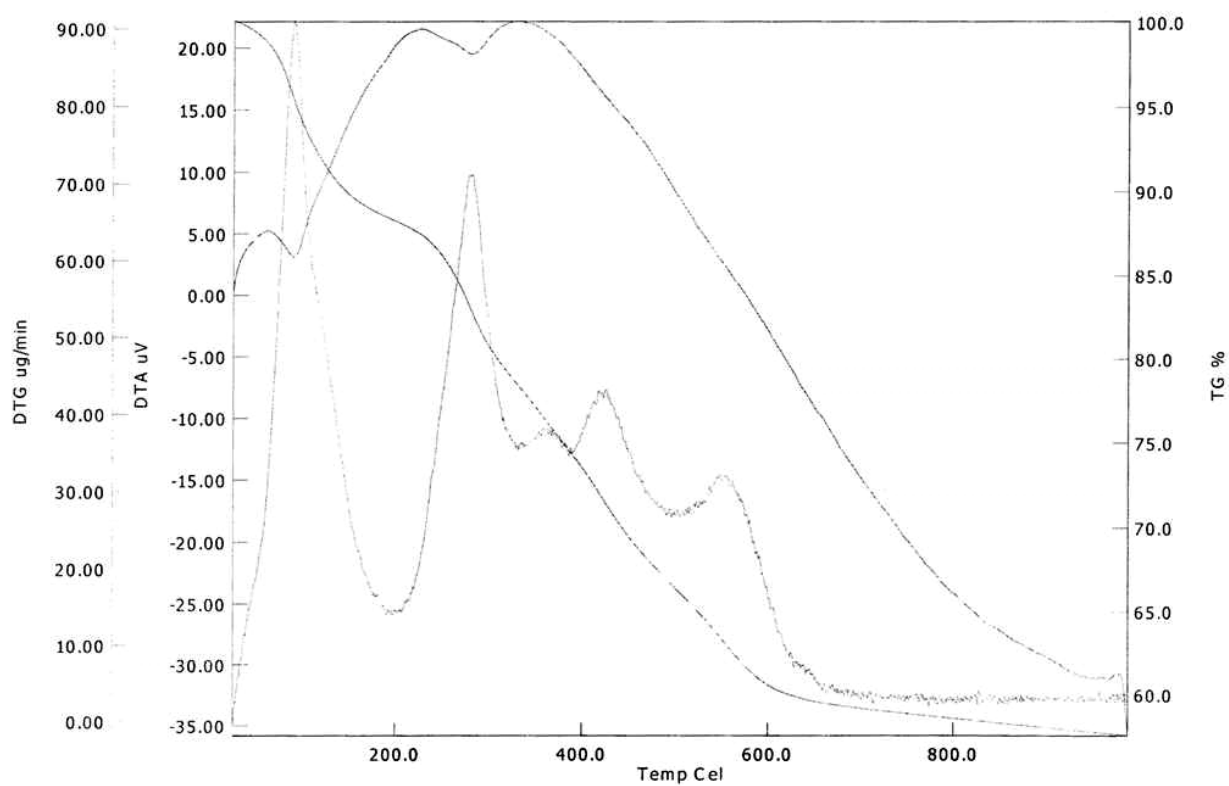


Fig. 2.1.5. Variation of pH during precipitation of yttria from nitrate solution (experiment 11).



a



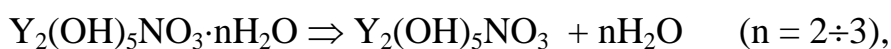
b

Fig. 2.1.6. Thermogram of the yttria nitrate precursor. T–temperature-time curve, DTA – differential temperature-time curve, G –mass- time curve, DTG – differential mass-time curve. (a) Sample № 18, initial mass 0.544 g. (b) Sample 33, initial mass 10 mg.

Yttria nitrate precursors precipitated from nitrate solutions loss weight in three main steps (Fig. 2.1.6a). The first step: from room temperature to 150 °C, the weight loss is 10-13 %. The second step finishes at 340 °C, the weight loss is 12 ± 0.5 %. Third step finishes at 540 °C, the weight loss is 15 ± 1 %. The weight loss of about 5% is observed during following heating up to 800 °C.

According to our weight loss measurements and the literature data [33], the first step corresponds to removal of hydrate water, the second step corresponds to removal of water from hydroxyl ions, and the last step corresponds to removal of nitrate ions.

The following scheme of consecutive chemical reactions, corresponding to stepwise weight loss, is proposed:



The decrease of the mass of samples leads to some change of the decomposition scheme (appearance of two small additional effects between the second and third steps), see Fig. 2.1.6b.

It is important that the temperatures mentioned above correspond to the heating rate 10 degree/min. In a static regime, the temperatures of finishing of decomposition steps is lower. The X-ray patterns of the samples after thermal treatment in the static regime show that the Y_2O_3 structure forms at 500 °C (Fig. 2.1.7).

It is clear that the yttria precursor should be annealed before sintering in order to remove volatile components.

We tried to eliminate the nitrogen ion from yttria precursor by многократной water washing of precipitate. However, according to IR transmittance date, NO_3^- content slightly decreases.

We investigated the influence of oxalate and carbon ions to the yttria precursor precipitation. There were no positive effects both in forms of precipitation particles or in temperature of destruction. Thus we leave out these technologies variants.

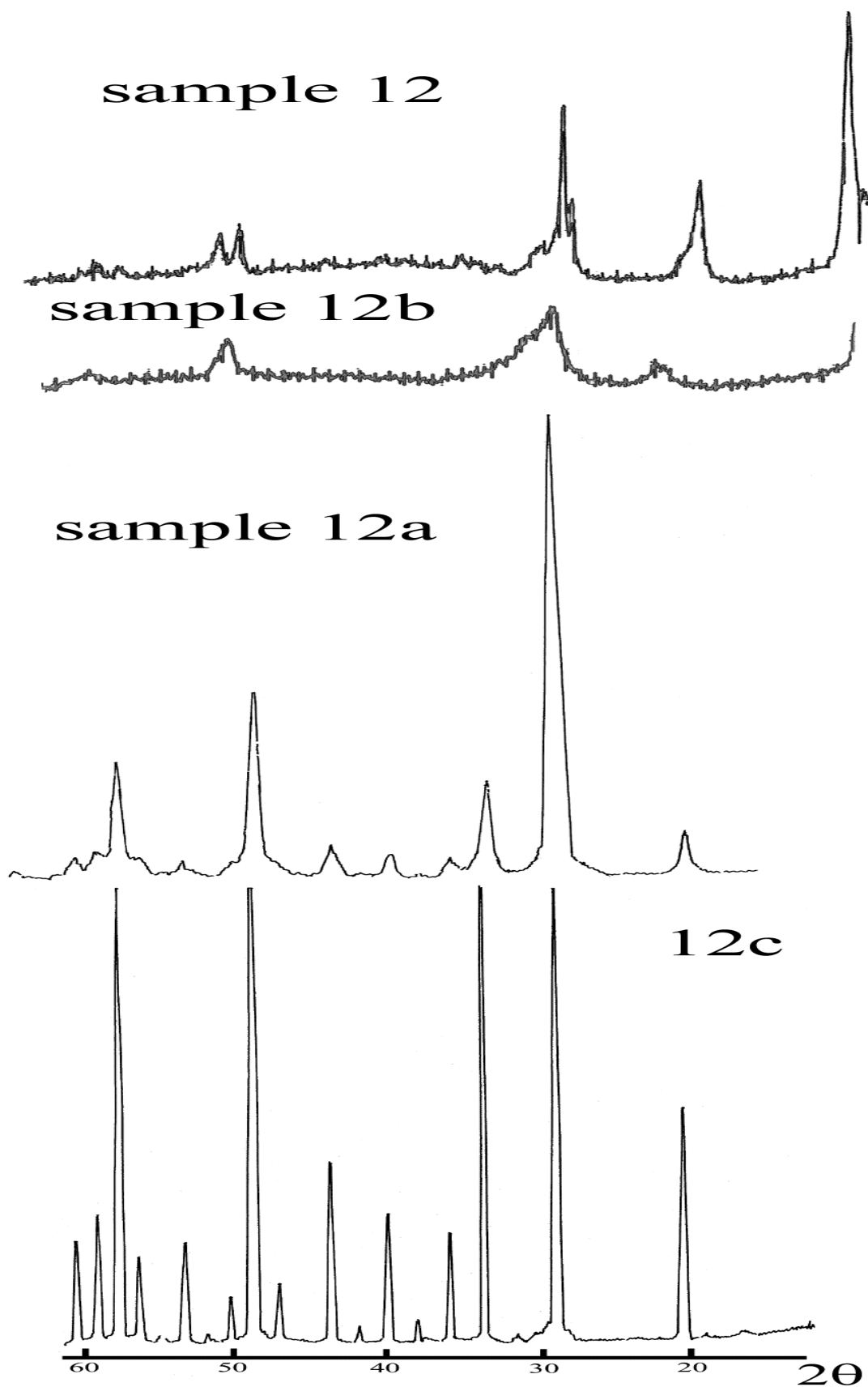


Fig 2.1.7. X-Ray powder data, Cu K_α radiation for sample 12 as precipitated and after thermal treatment at 300 °C (sample 12b), 500 °C (sample 12a, yttria nanoparticles) and 1200 °C (sample 12c, crystalline yttria powder).

Influence of different factors on the shape of precursor particles

According to the electron microscopy data and measurement of particle sizes by the X-ray technique, the formation of yttria precursor from water solution may be described as formation of agglomerated nanoparticles (“druses” of nanocrystals). This agglomeration takes place immediately in the process of yttria precursor formation by chemical reaction. The agglomerates are hardly destroyed under thermal decomposition with the loss of water and nitrogen oxide (stages 1-3).

We studied the influence of different factors on precipitation processes, shape, and agglomeration of nanoparticles, in particular:

- the effect of concentration of the initial yttrium nitrate solution;
- the effect of surfactants additives;
- the effect of strong ultrasonic treatment and cavitations phenomena.

We proposed that the formation of an adsorbed thin film of surfactants on the surface of nanoparticles will lead to isolation of nanoparticles from each another.

An increase of the concentration of the initial solution leads to easy sedimentation and filtration of the precipitate. The concentration we used was 0.06 - 0.08 M.

Three organic surfactants were chosen: cement super plasticizer (trade mark C-3, produced by URAL-PLAST, Sverdlovsk region), polyvinyl alcohol (PVA), and polyvinyl pyralidon (PVP). Cement super plasticizers or high-range water-reducing admixtures (HRWRAs) [34] are the dispersants, which are adsorbed at the liquid-solid interface between the oxide particles and the aqueous phase and induce a repulsive interparticle force, thus reducing or eliminating adhesion between neighboring particles. PVP is a popular surface active reagent in nanotechnology. The action of ammonium sulphate $(\text{NH}_4)_2\text{SO}_4$ on the morphology of yttria precursor, which was described in [27], was studied also.

The 0.5 - 1 wt % of C-3, PVA, or PVP was added to the nitric solution of yttria before ammonia titration. The additives slightly change the values of pH corresponding to the sedimentation of yttria precursor. The data of electron scanning microscopy are the following (see Fig. 2.1.8, 2.1.9):

Addition of C-3 leads to formation of rounded particles with a characteristic dimension of about 100 nm. Thermal treatment at 800 °C leads to a spread of particle structure.

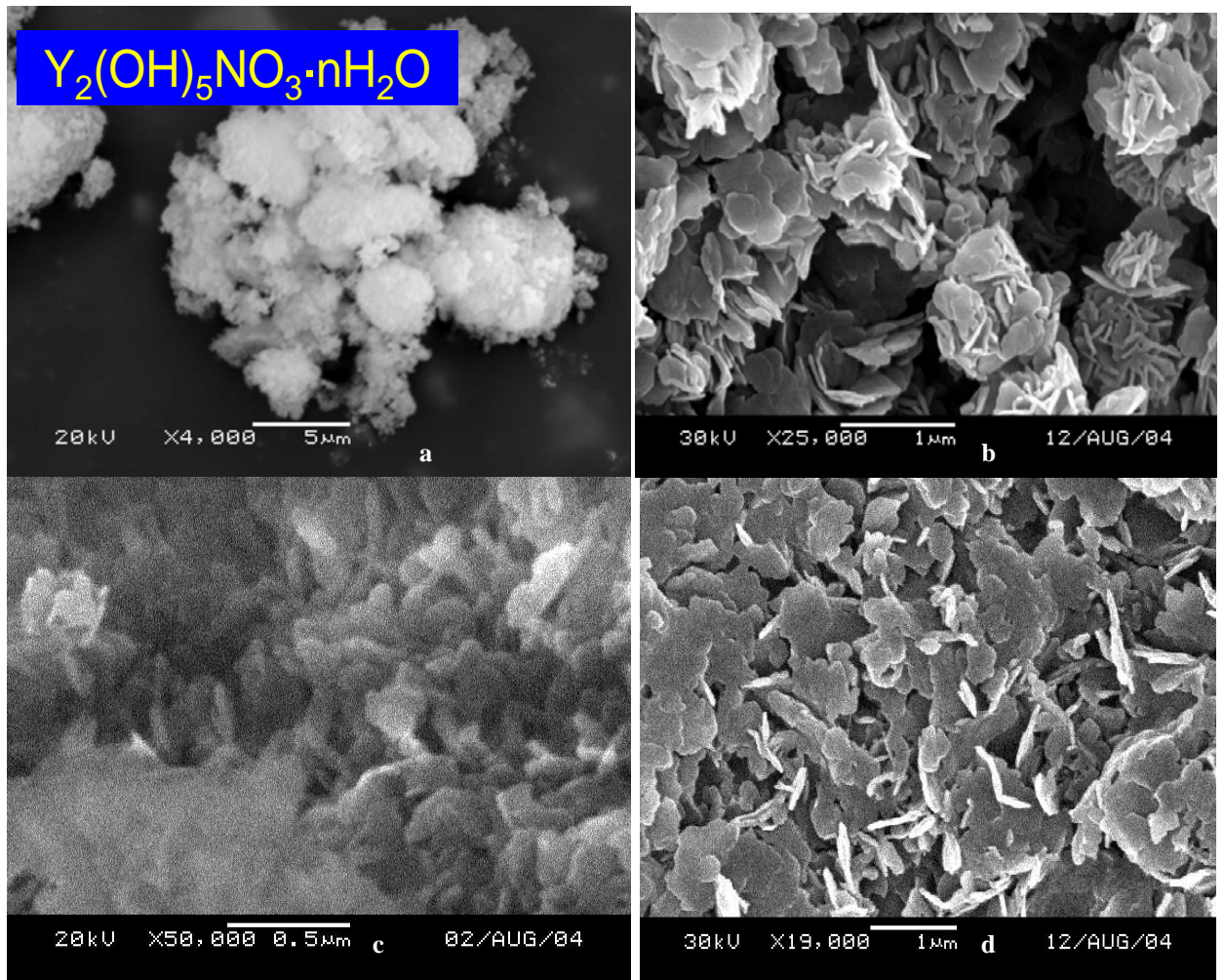
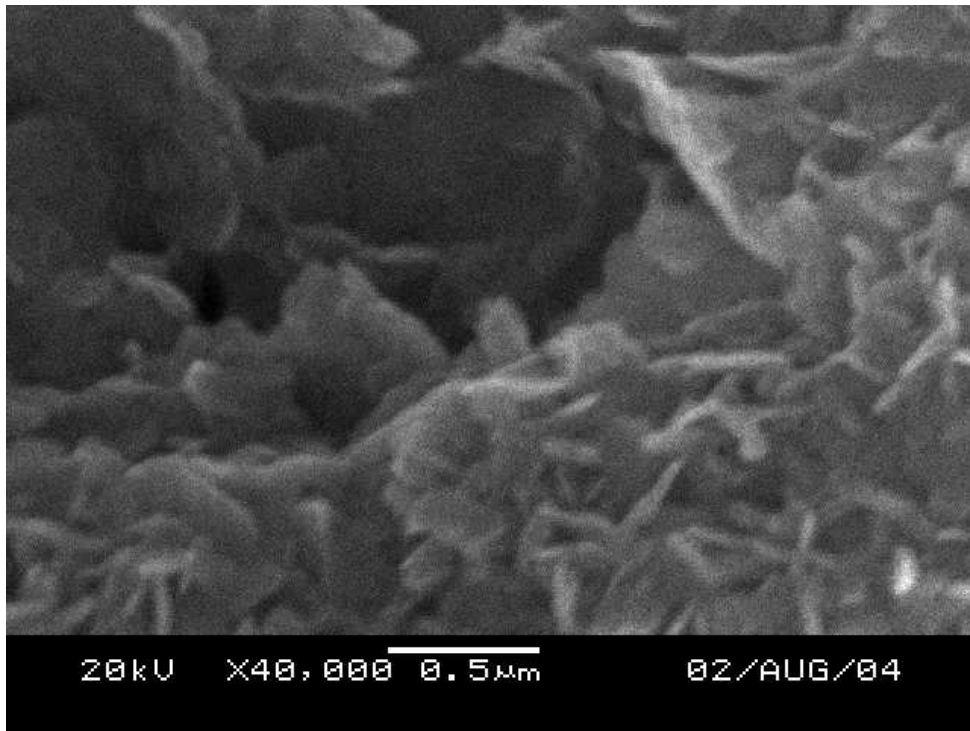


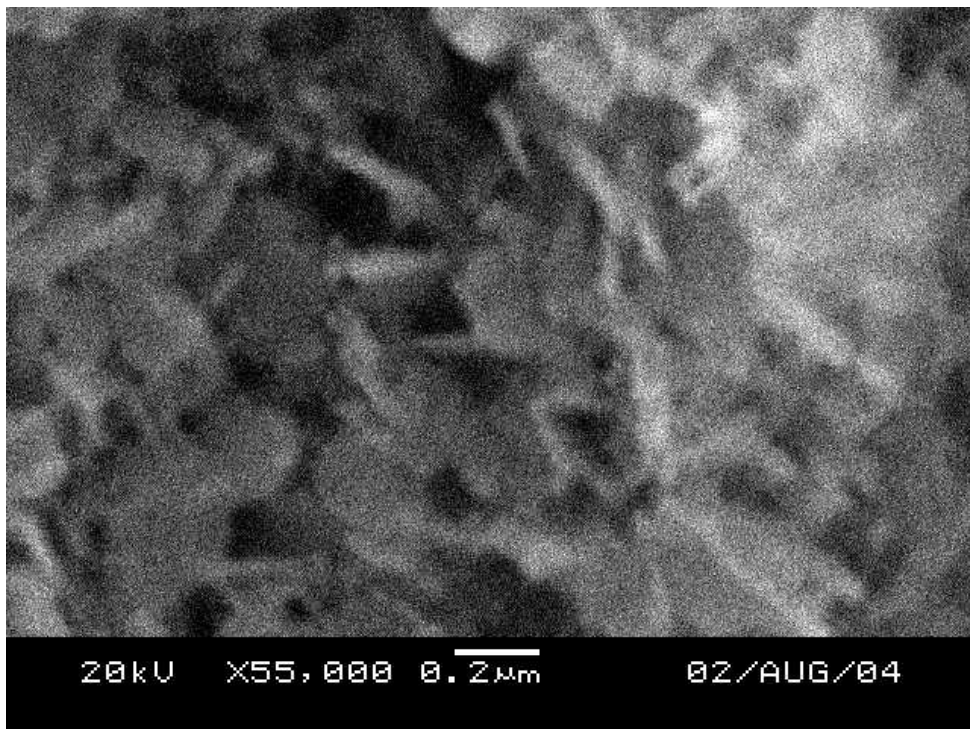
Fig. 2.1.8. Electron scanning microscopy.

The effect of different factors on morphology of yttria nitrate precursor

(a) sample 12a; (b) sample 33 (precipitated under ultrasonic action); (c) sample 27 (precipitated with 0.5% superplastifier C-3 additive); (d) sample 34 (precipitated with 0.5% superplastifier C-3 additive under ultrasonic action).



a- yttria nitrate precursor, precipitated with 0.5% polyvinyl alcohol additive (sample 28);



b- the same after thermal treatment at 800 °C (sample 28a).

Fig. 2.1.9. Scanning electron microscopy. The phenomenon of shape memory.

Addition of PVA, PVP, or $(\text{NH}_4)_2\text{SO}_4$ to initial solutions leads to formation of agglomerates of plate-like particles (“card-dome” structure) after ammonia titration. The morphology of particles does not change substantially after thermal treatment up to 800 °C.

In order to destroy the aggregates of yttria precursor nanoparticles, we tested the strong ultrasonic treatment with cavitations phenomena in the reaction area during sedimentation. We used an ultrasonic dispergator UZD-01/22 (produced by NTK-16, S-Petersburg), frequency 22 KHz, the maximum power (100 W) being employed.

In contrast to the initial proposition, the ultrasonic action does not prevent the agglomeration of particles. The large (up to $1 \times 1 \mu\text{m}$) but thin (about 20 nm) two-dimensional sheet-like particles form. It seems that the ultrasonic treatment stimulates the crystallization processes. The additives of PVA don't affect the morphology of particles of yttria precursor forming under ultrasonic action. The additive of C-3 decreases the agglomeration of particles under the same conditions.

Formation of yttria nanoparticles due to thermal decomposition of the precursor.

Measurements of average size of particle D (coherent scattering regions) by X-ray technique after revealed the dependence of D from temperature of thermal treatment, see Fig. 2.1.10. However, the detail analysis leads to more complicated and interesting pattern.

It is found that the precursor morphology corresponds to the morphology of yttria particles, obtained in the process of thermal decomposition of precursor and heating up to 800 °C (see Fig. 2.1.9). Such interesting effect is known as “effect of shape memory” [35]. According to this observation, we at first focused on the preparation of rounded small particles of precursor, which are formed with C-3 additives. However, after the thermal treatment, the rounded particles of yttria are implanted into non differentiated media. It seems that separation of such particles from media is impossible.

An interesting unexpected effect was discovered, namely, the plate – like particles transform to spherical ones at a certain temperature. This process is illustrated in Fig. 2.1.11 (experiment 59). The samples of precursor were heated in alundum crucibles and taken out from the furnace after 5- minute annealing at 700, 800, 900, 1000, 1100 °C. The ‘card-dome’ morphology of yttria precursor particles, formed with addition 1% PVP to the initial solution (Fig. 2.1.11a), do not changes after thermal

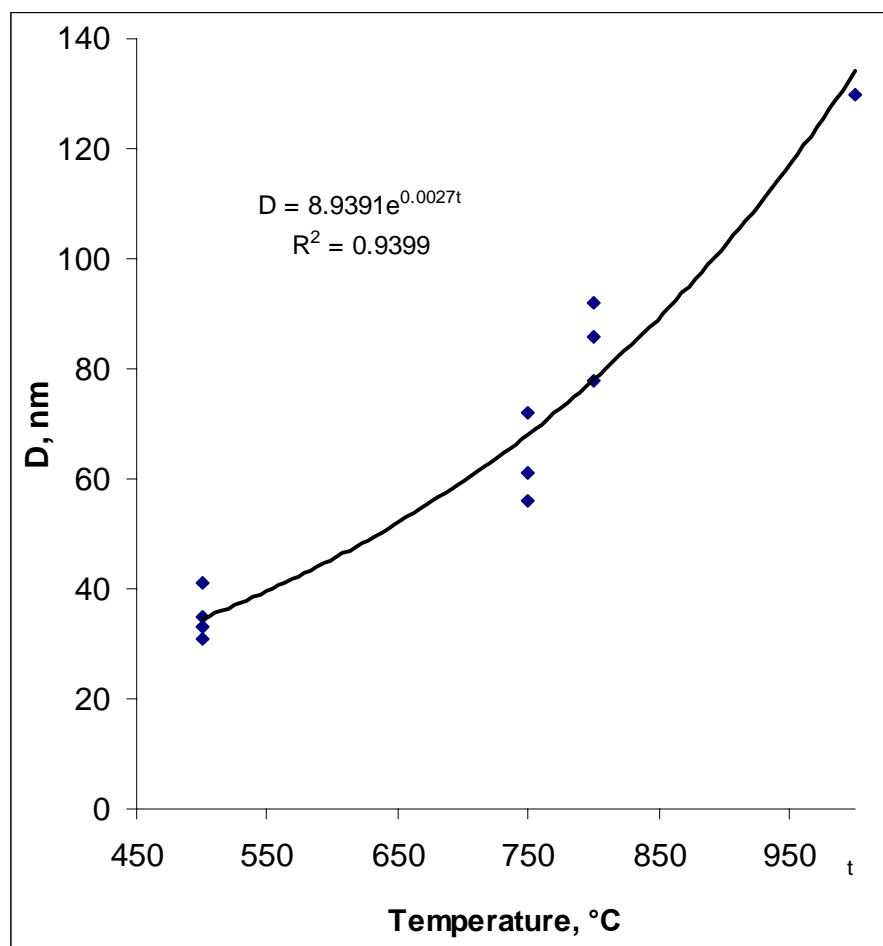


Fig.2.1.10. Dependence of particle size D (coherent scattering regions, nm) versus the temperature of thermal treatment

decomposition and heating up to 800 °C (Fig. 2.1.11, b-c). At 900 °C no visible change takes place, but it is clear that at 1000 °C the plates are destroyed (breakdown into the small spherical particles). At 1100 °C the size of spherical particles increases.

One can see quantitative description of the process in Table 2 and in Fig. 2.1.12.

Table 2. The parameters of yttria particles according to X-ray measurements. Experiment 59.

Composition	Reflec-tion	$2w, ^\circ$	$\beta, ^\circ$	D , nm	e , 10^{-3}	<i>a</i> , Å
Si	(111)	0.110	0.141	-	-	
Y ₂ O ₃ № 59a 600 °C	(222)	0.629	0.871	16	6.3	10.641
Y ₂ O ₃ № 59B 700 °C	(222)	0.600	0.788	22	7.2	10.649
Y ₂ O ₃ № 59c 800 °C	(222)	0.557	0.732	24	6.6	10.634
Y ₂ O ₃ №59d 900 °C	(222)	0.453	0.586	13	0.06	10.642
Y ₂ O ₃ № 59e 1000 °C	(222)	0.291	0.373	13	0.08	10.627
Y ₂ O ₃ № 59f 1100 °C	(222)	0.203	0.369	24	0.02	10.637

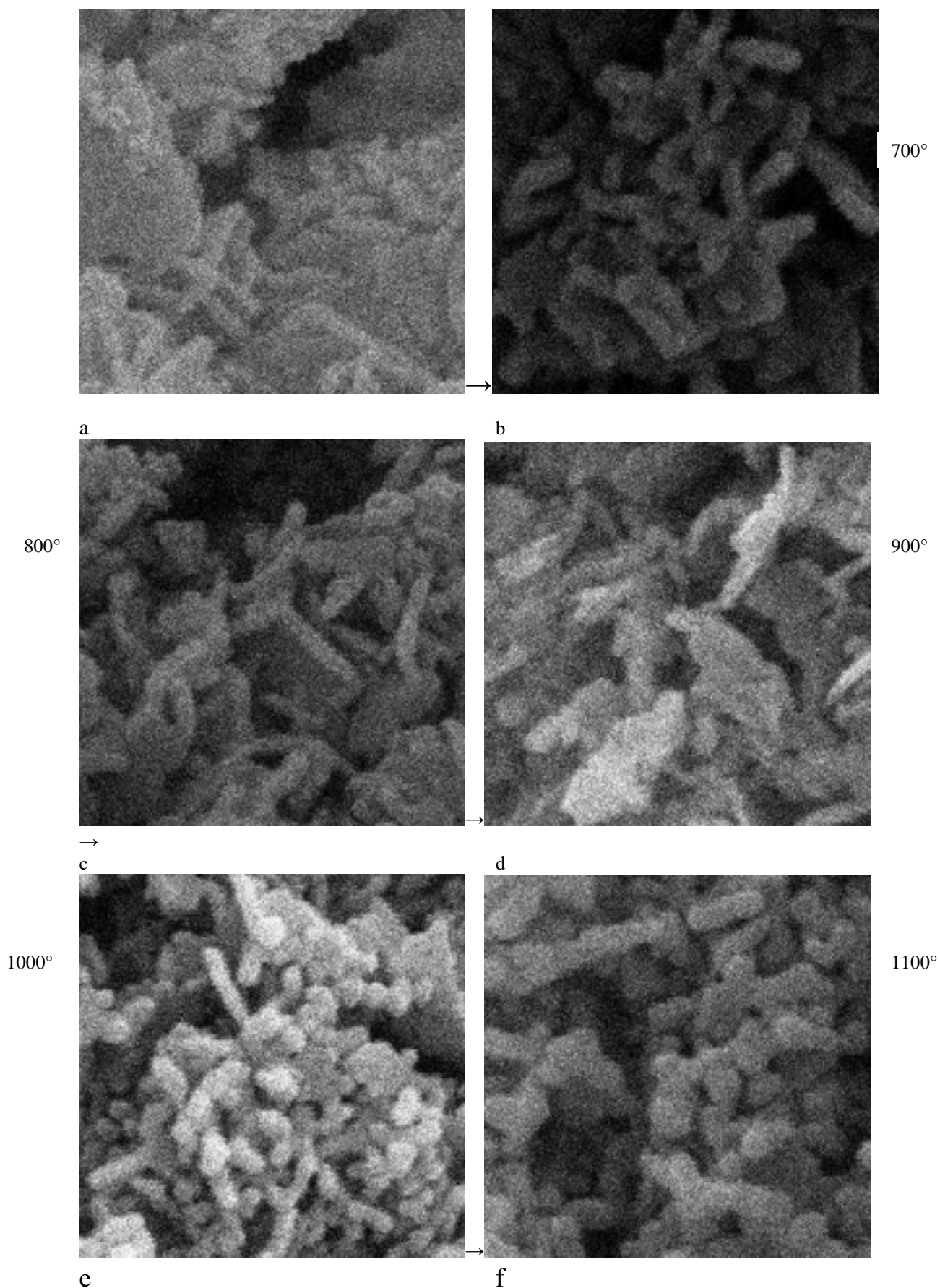


Fig.2.1.11. Scanning electron microscopy. The size of the square is 1×1 μm². Transformation of plates to spherical nanoparticles. Experiment 59. (a) precursor, precipitated with 1% PVP additive; (b) the same after heating to 700 °C, (c) 800 °C, (d) 900 °C, (e) 1000 °C (f) 1100 °C.

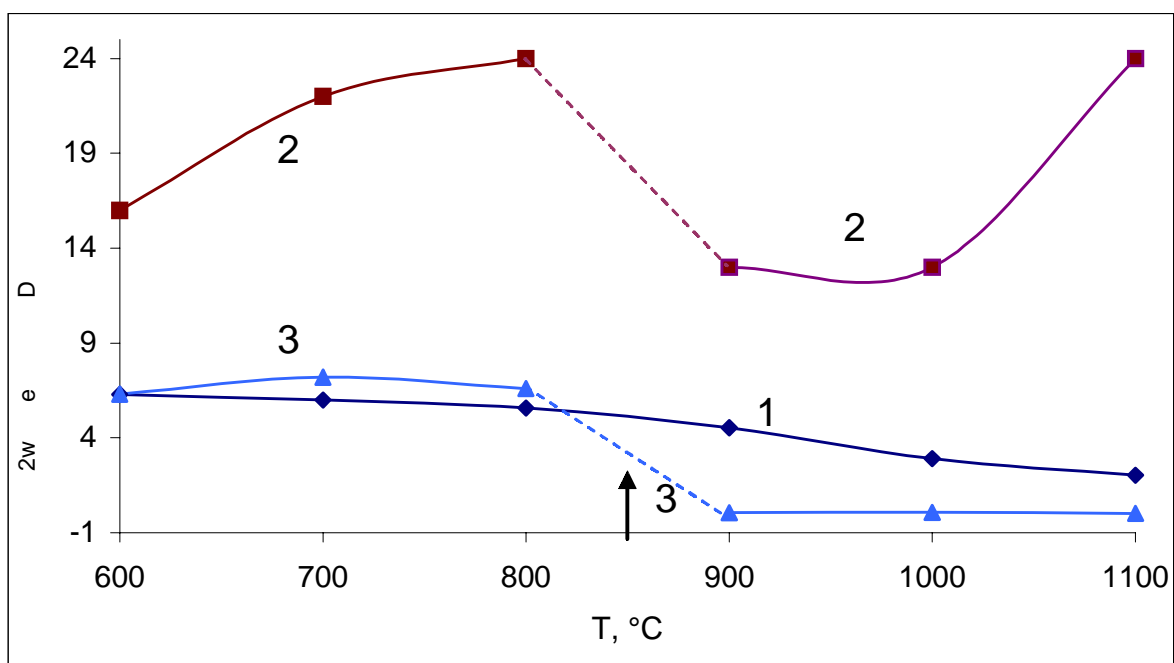


Fig. 2.1.12. Variation of the values of the width of the X-ray peak at half height $2w$ (1), the size of yttria particle (coherent scattering regions), D , nm (2) and microdeformations e (3) with temperature in experiment 59.

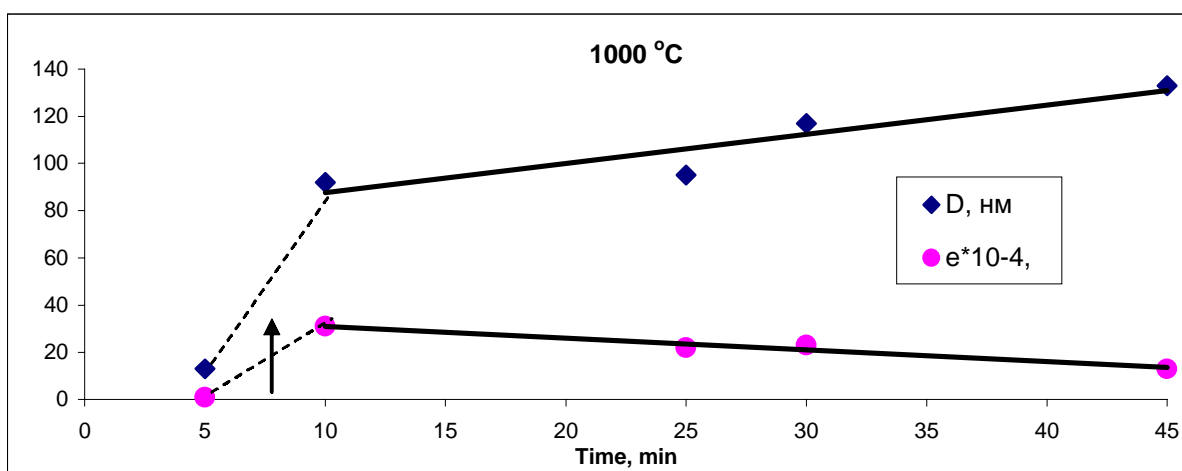


Fig.2.1.13. Variation of the size of yttria particle (coherent scattering regions, D , nm) and microdeformations e with time of annealing at 1000 °C

According to the X-ray data, the values of the width of the peak at half height (2w) smoothly decrease with increasing of temperature. However, the shape of the peak transforms sharply between 800 and 900 °C. Both the size D of particles and the mechanical deformation ϵ fall down.

So, the yttria particles with a non-equilibrium plate-like form inherited from precursor particles, which is characterized by a large concentration of defects (due to thermal decomposition and mass losses) and mechanical stresses, sharply transforms to a nonstressed nanoparticles with an equilibrium form. It seems that D values correspond to the average thickness of plates for the samples heated to 600-800 °C, and diameter of nanoparticles for the samples heated to 1000-1100 °C.

The transformation of form of the yttria nanoparticles has the character of the first-order phase transition.

We studied evolution of nanoparticles during annealing at 1000 °C in experiment 63. The results are presented in Fig. 2.1.13. It seems that the primary nanoparticles sharply transform to considerably larger particles (secondary nanoparticles). We propose that the process of coalescence of nanoparticles (similar to the first-order phase transition) takes place. The mechanical deformations sharply increase due to the coalescence and then slowly relax with increasing size.

The electron microscopy patterns of the samples, annealed at 1100 °C (see Fig. 2.1.14) demonstrate the different stage of coalescence of 100 nm particles to larger ones. It seems that strong variation of transformation order and effective size of particles take place at the same nominal parameters of process.

We examined correction of spherical particles size determination by X-ray. This checking was made by thermal desorption of nitrogen and argon with gas analyzer GH-1. The drying of samples was made at temperature 120 or 300 °C. We calculated results by BET-method. Fig. 2.1.15 showed scanning electron microscopy and nitrogen adsorption isotherm for the sample № 63/64a. For this sample $P_0 = 206,9$, $C=98$, $a_m = 100,3 \text{ } \mu\text{mol/g}$, $\sigma = 0,166 \text{ nm}^2$, $S = 10,0 \text{ m}^2/\text{g}$, $S_{\text{stand}} = 10,04 \text{ m}^2/\text{g}$. The calculation by the $S = \frac{6}{\rho d}$ formula gives particles mean diameter $d = 120 \text{ nm}$ if density of Y_2O_3 , is equal $\rho = 5.03 \text{ g/cm}^3$. This value was in good agreement to the scanning electron microscopy, see fig 1.14. However, the same diameter by X-ray phase analyse was equal $D = 230 \text{ nm}$. Thus, we see only qualitative agreement of two methods but this discrepancy was usual for fractal structure in nanotechnology.

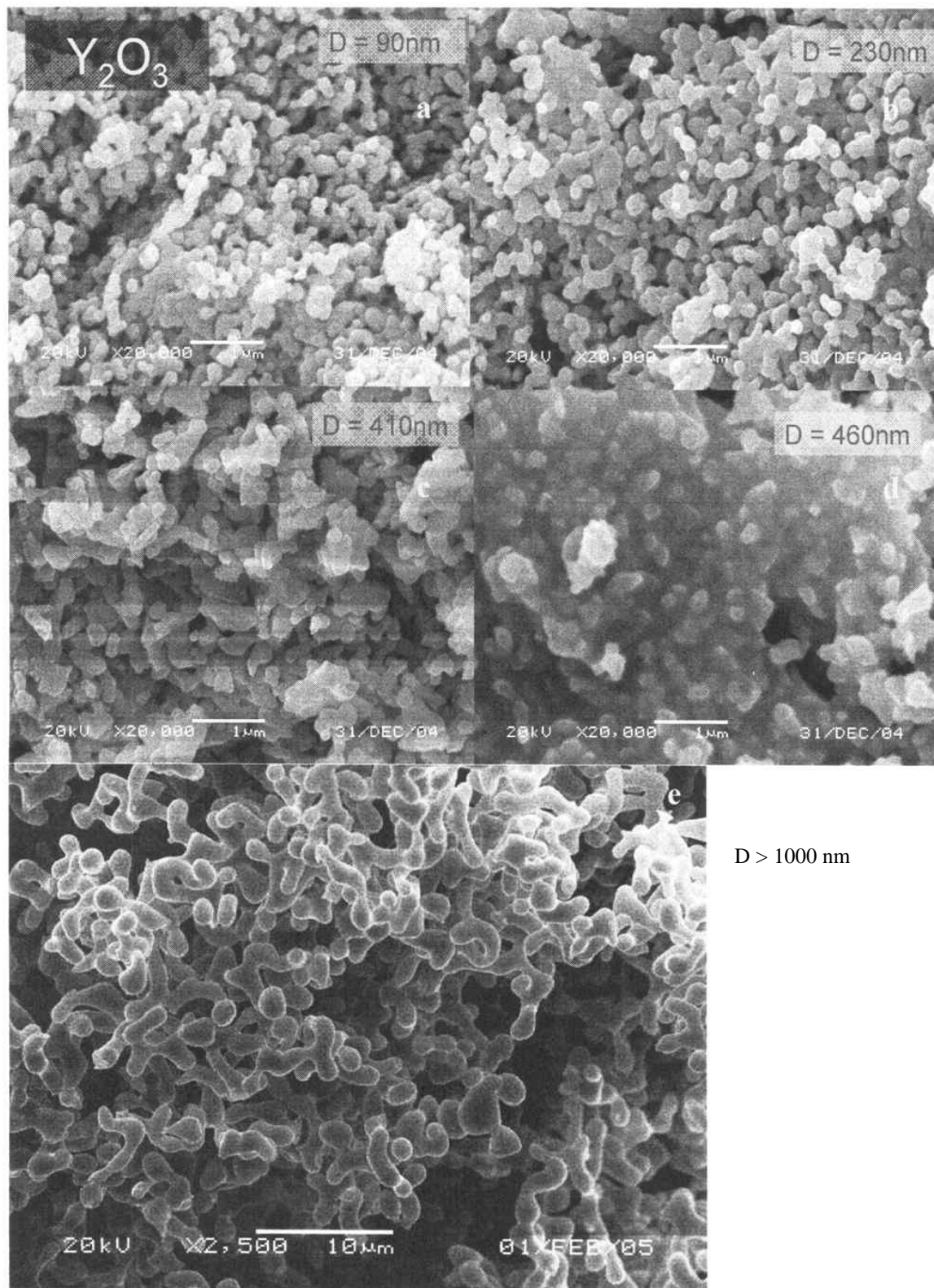


Fig. 2.1.14. Scanning electron microscopy for several yttria samples annealed at 1100 °C. (a) sample 41 b, (b) sample 25a, (c) sample 32b, (d) sample 31b, (e) sample 59g. The values of coherent scattering regions D are indicated.

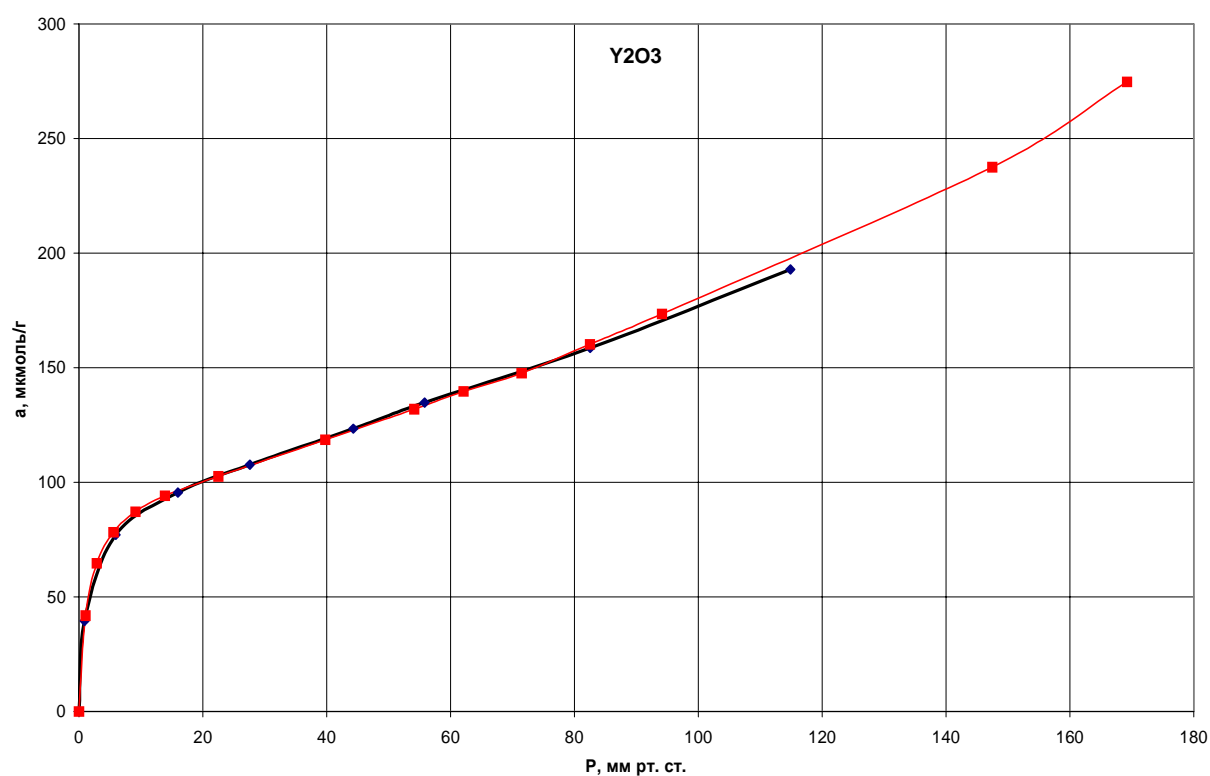
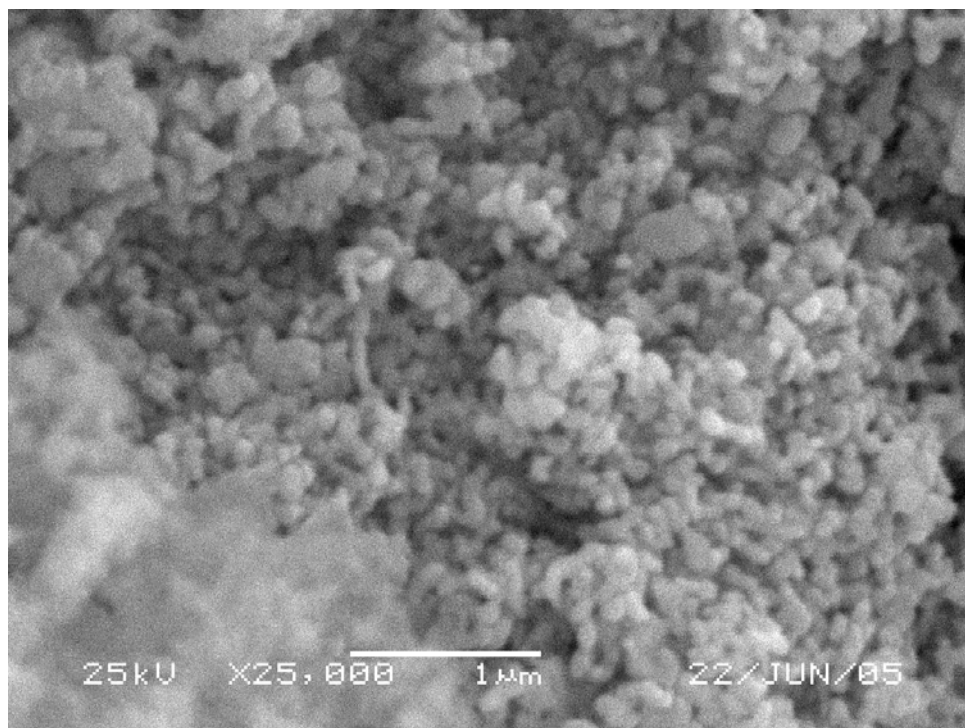


Рис. 2.1.15. Scanning electron microscopy of yttria powder and the graph of argon absorption in sample 63/64b.

Yttria samples with obtained nanoparticles which were found by electron microscopy or X-ray photos, needed disintegration. These samples were white clay-like compact pieces of Y_2O_3 (typical linear size was several mm) with low density (15-20 %) and large porosity.

For these experiments we used samples, prepared by standard technique, which leads to formation of spherical nanoparticles with ~ 100 nm size: thermal heating of precursor with plate-like particles morphology (precipitated with addition of surfactant polyvinyl pyralidon) up to $950^\circ C$ under air (samples numbers 62/68a, 71a, 74a, 75a). According to results of X-ray and electron scanning microscopy measurements such pieces consists from agglomerated nanoparticles. The main idea is they following: before sintering it is necessary to disintegrate these agglomerates and give possibility nanoparticles for close packing.

We tested 3 variants of disintegration: dry milling, liquid milling and ultrasonic treatment. Dry milling was carried out by handle in sapphire mortar. Liquid milling was carried out by handle in sapphire mortar or by FRITSCH PULVERIETTE equipment with agate mortar. We used ethanol for liquid milling.

Ultrasonic action was carried out in two geometries (see Fig.2.1.2). In geometry Fig.2.1.16a we used ultrasonic dispergator UZD-01/22 (produced by NTK-16, S-Petersburg), frequency 22 KHz. We varied amplitude and time of treatment. The solid-water ratio was 1:10.

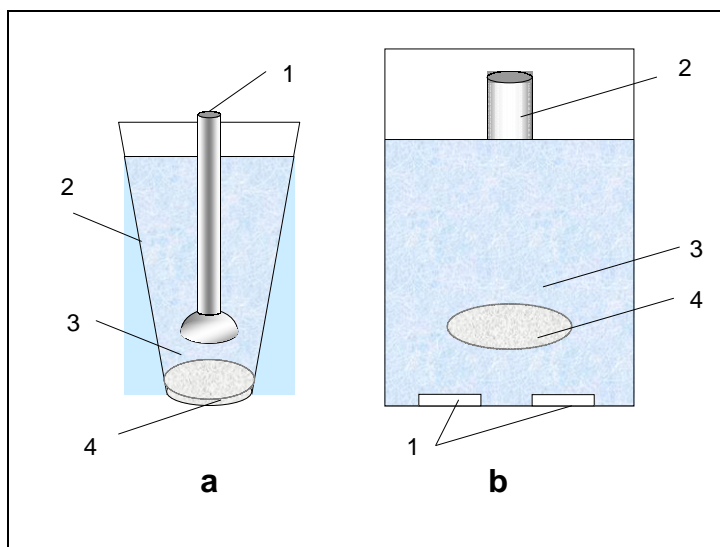


Fig.2.1.16. The scheme of two variants of ultrasonic dispergation of yttria nanoparticles in water; a – ultrasonic zoned, b - ultrasonic bath.

1- source of US, 2- glass, 3 – suspension, 4- yttria powder.

In geometry Fig.2.1.16b we used ultrasonic bath UZB2-0.16/18 (produced by NTK-16, S-Petersburg), frequency 21 KHz.

No surfactants were added to system.

The particle size distribution was analyzed with FRITSCH PARTICLE SIZER ANALYSETTE 22 equipment. The standard measurement procedure includes ultrasonic treatment of water-powder system in order to separate particles, connected by Van der Waals forces. Some typical pictures are presented on Fig. 2.1.17-2.1.20. The main results are the following.

1. One can see two-or three-mode distribution of particle fraction versus size of particles, with maxima at approximately 1; 5-10 and more μm . No nanoscale particles are observed by this analytical technique.

It is clear (in comparison with X-ray and electron microscopy data) that these maxima correspond to agglomerates of small particles with dimensions less than a micron. The occurrence of several maxima on such curves indicates the existence of hierarchy of organization levels of particles.

2. The dry and liquid mechanical milling is not effective and leads to formation of large agglomerates only.

3. The large agglomerates are easily disintegrated by ultrasonic action. However, small (micron scale) agglomerates are stable. The forces between nanoparticles in agglomerates are strong. It is not Van der Waals forces.

4. An optimal time of US treatment exists. The increasing of time leads to reverse agglomeration processes.

5. It seems that small amplitude of US treatment is preferable for breaking of agglomerates.

The geometry Fig.2.1.16b leads to positive results in comparison with geometry Fig.2.1.16a. The amount of solid phase on the bottom of the flask decreases with increasing of time of treatment (up to 1 hour). The stable suspension was formed. In spite of the particle size distribution analysis did not performed yet, it is clear that geometry, corresponding to Fig. 2.1.16b has several advantages:

- easily of process looking out;
- easily of regulation solid: liquid ratio;
- natural separation of small particles from large agglomerates particles and extraction it to the liquid phase.

We also tested the ultrasonic bath (geometry Fig.2.1.2b) with frequency 700 KHz. No visible effects were observed (the solid yttria did not transport to suspension).

2	05-01-2005	00:41	FA.FRITSCH	UserID LAB/22	SerNo. SN3165
---	------------	-------	------------	---------------	---------------

62/68a

Measuring Range	0.10 [μm] - 300.74 [μm]	Pump	10 [rpm]
Resolution	62 Channels (9 mm / 114 mm)	Stirrer	0 [rpm]
Absorption	3.00 [%]	Ultrasonic	10
Measurement Duration	20 [Scans]		

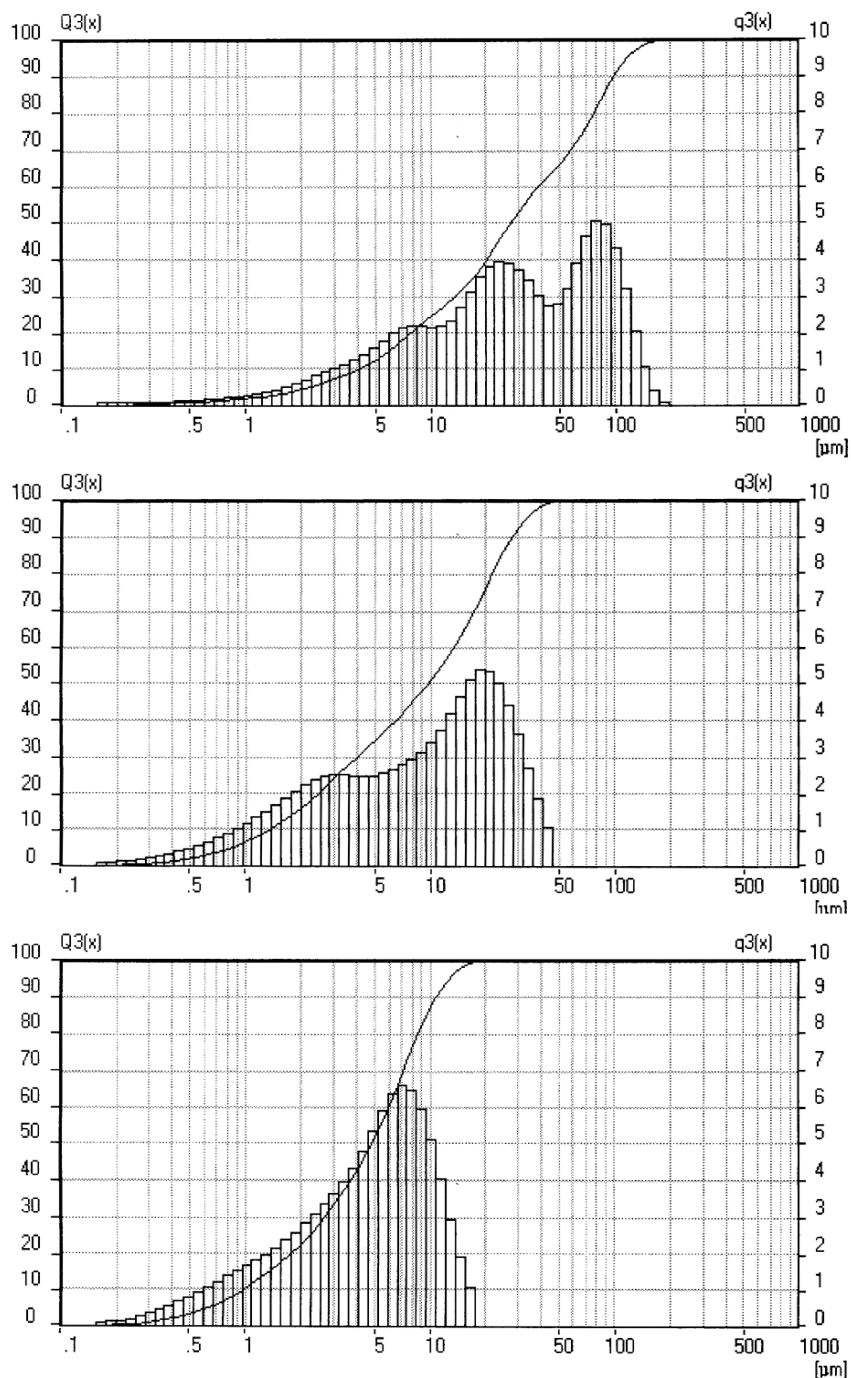


Fig. 2.1.17. Particle size distribution, sample 62/68a. a-after dry milling., b- after 1 min of additional ultrasonic treatment, c- after 7 min of additional ultrasonic treatment

2	05-01-2005	01:12	FA.FRITSCH	UserID LAB/22	SerNo. SN3165
---	------------	-------	------------	---------------	---------------

74a

Measuring Range	0.10 [µm] - 501.24 [µm]	Pump	10 [rpm]
Resolution	62 Channels (9 mm / 190 mm)	Stirrer	0 [rpm]
Absorption	1.00 [%]	Ultrasonic	10
Measurement Duration	20 [Scans]		

Modell Independent
Fraunhofer Calculation selected.

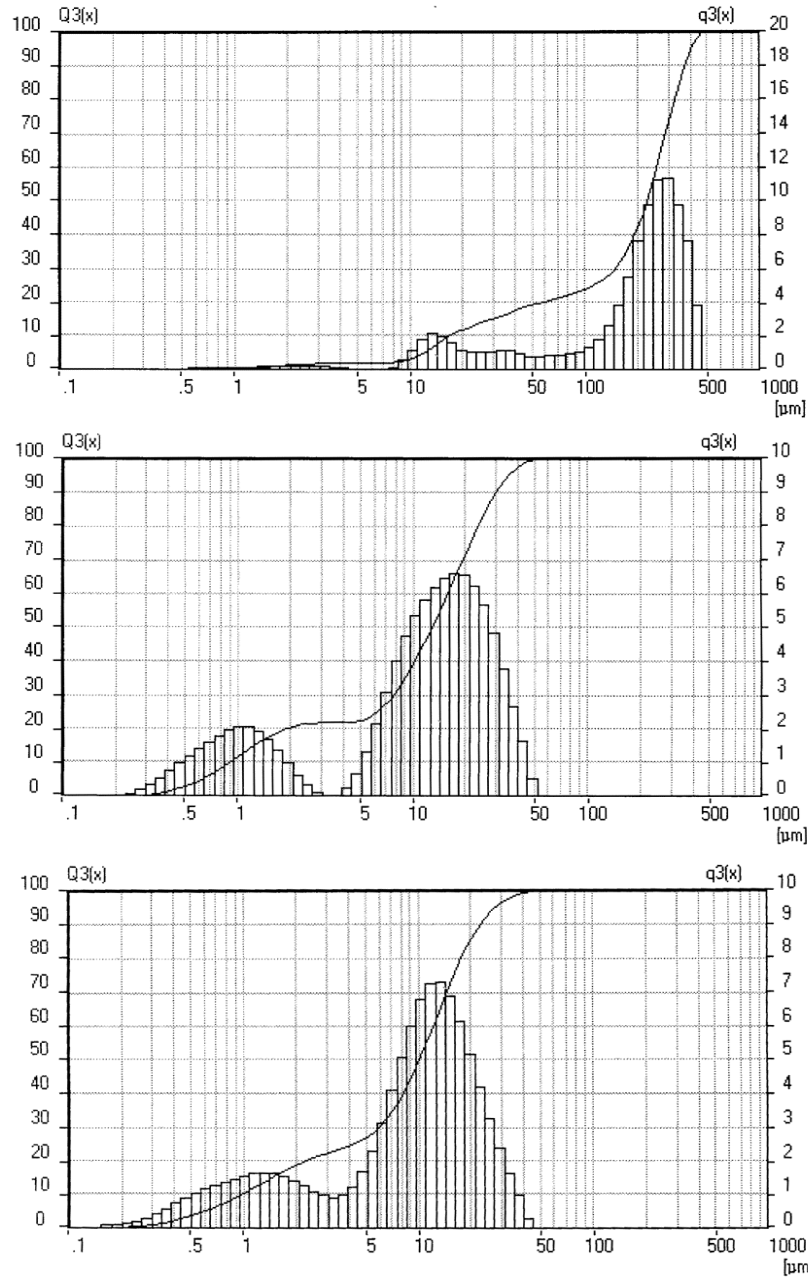


Fig. 2.1.18. Particle size distribution, sample 74a. a- after handle liquid milling, b- after 1 min of additional ultrasonic treatment, c- after 7 min of additional ultrasonic treatment

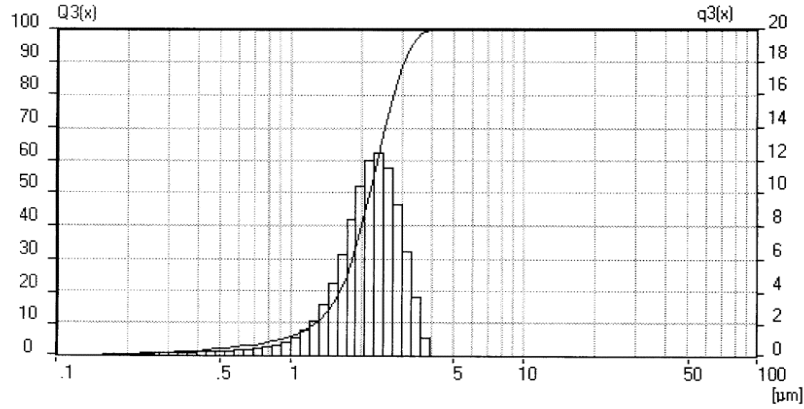
FRITSCH PARTICLE SIZER ANALYSE TTE 22

2	05-01-2005	00:18	FA.FRITSCH	UserID LAB/22	SerNo. SN3165
---	------------	-------	------------	---------------	---------------

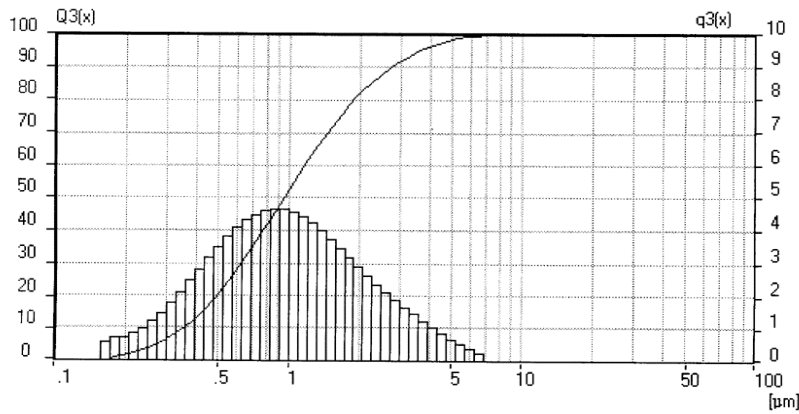
5

Measuring Range	0.10 [μm] - 50.12 [μm]	Pump	10 [rpm]
Resolution	62 Channels (9 mm / 19 mm)	Stirrer	0 [rpm]
Absorption	9.00 [%]	Ultrasonic	10
Measurement Duration	20 [Scans]		

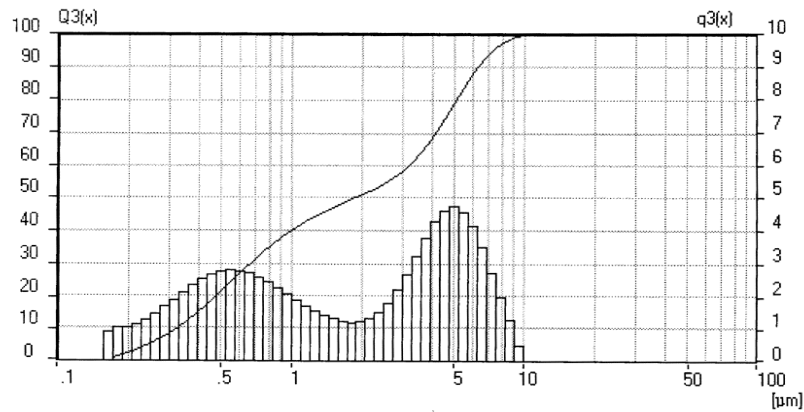
Modell Independent
Fraunhofer Calculation selected.



a



b



c

Fig. 2.1.19. Particle size distribution, sample 71a. a- after ultrasonic dispergation in geometry 2a (amplitude -15 a.u., time 10 min.), b - after 1 min of additional ultrasonic treatment, c- after 3 min of additional ultrasonic treatment

The next planning step of our experiments include ultrasonic disintegration with using of surface active substances for isolation of nanoparticles.

Formation of $Y_2O_3 - Nd_2O_3$ solid solution by co-precipitation and thermal treating.

Since the aim of our work is to study preparation of laser ceramic on the base of ceramic yttria we tested the possibility of yttria doping by Nd ions in the processes of precursor precipitation.

The system $Y_2O_3 - Nd_2O_3$ was not studied in the literature in details. Only a few data are given in [36].

We performed experiments on co-precipitations of neodima (experiments number 15-17, 20-23, 52, 77-83, 103-112, 115-118, 120-123) with yttria precursors in order to estimate the concentration limits of solid solutions of $Y_2O_3-Nd_2O_3$, and the possibility of synthesis of the $(Y_{1-x}Nd_x)_2O_3$ solid-solution transparent ceramic.

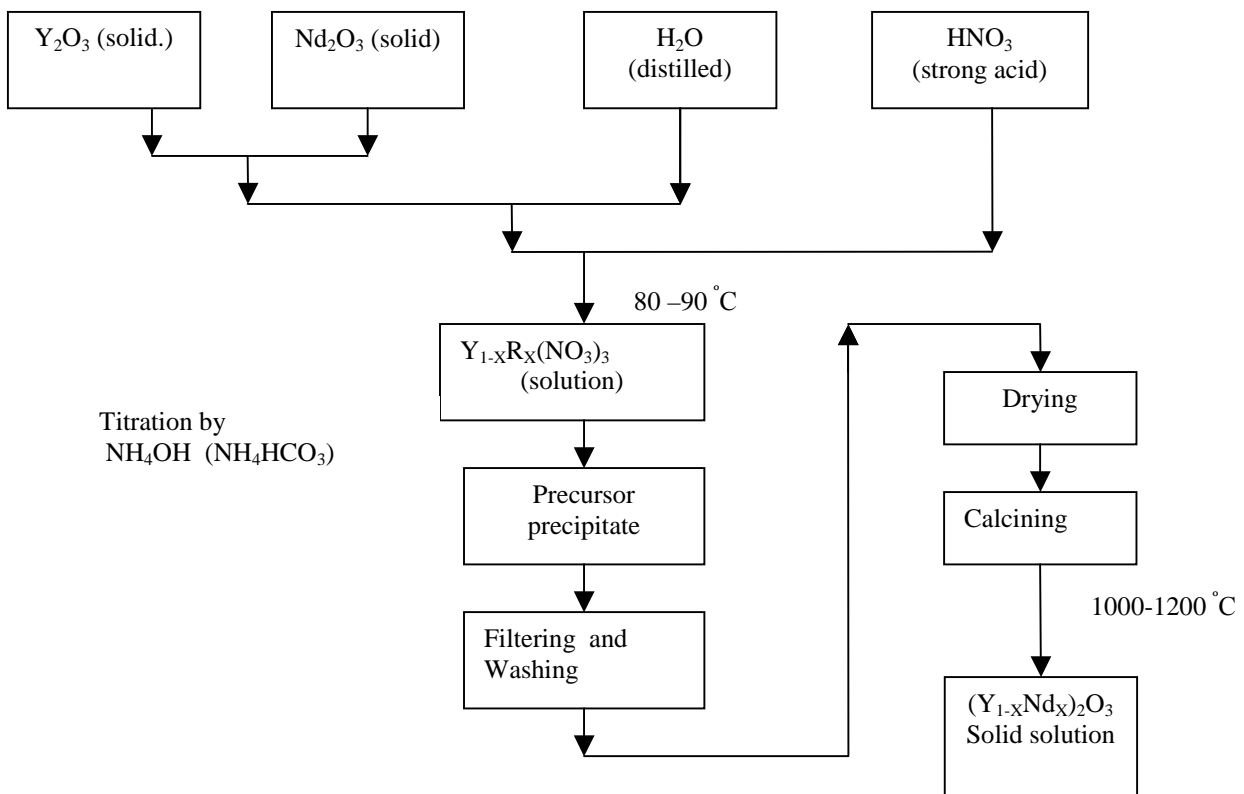


Fig. 2.1.20. The scheme of preparation of $(Y_{1-x}Nd_x)_2O_3$ solid-solution.

We expected complete co-precipitation of yttrium and neodymium and formation of solid solutions $(Y_{1-x}Nd_x)_2O_3$ after thermal treatment.

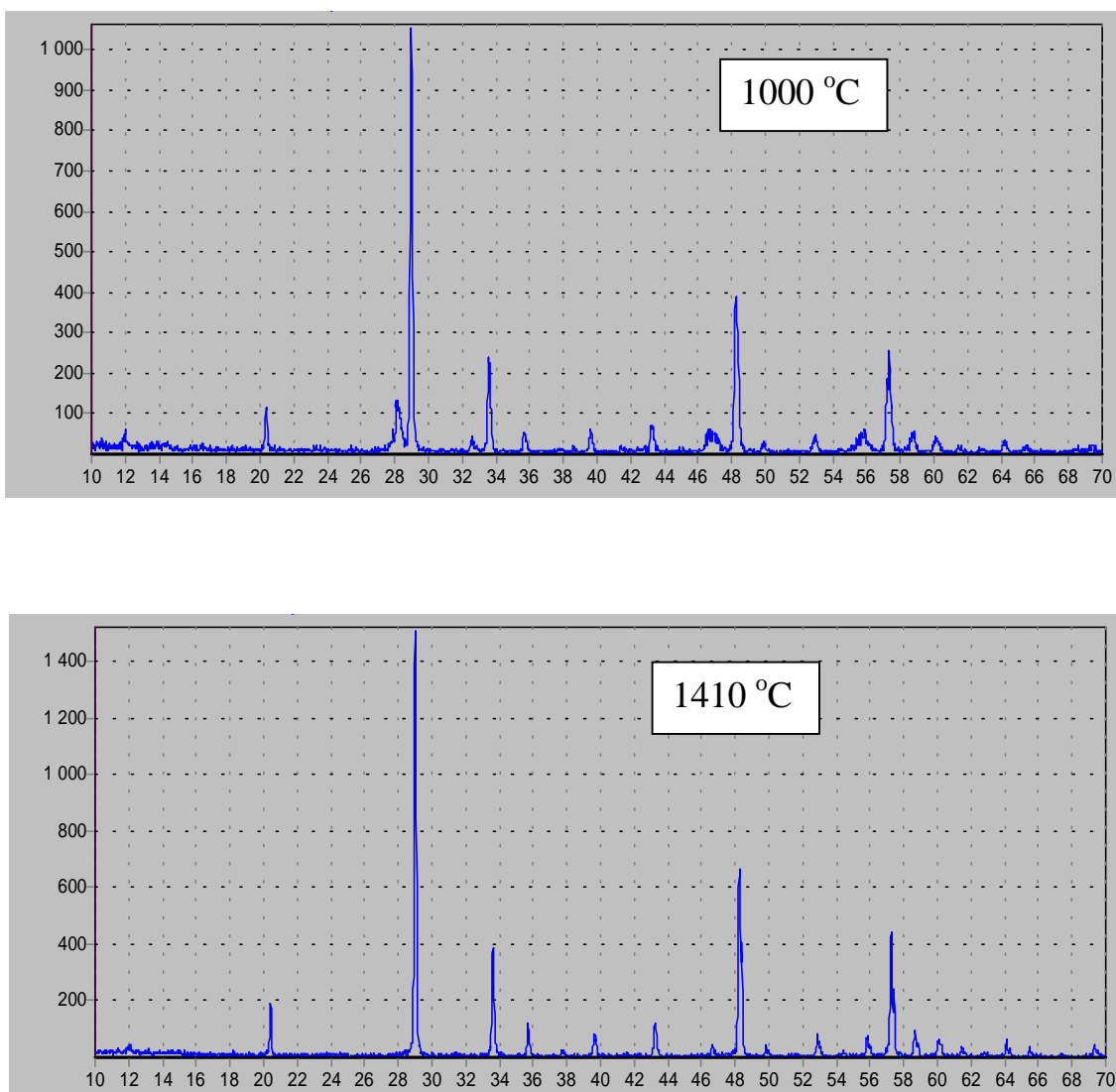


Fig.2.1.21. X-Ray powder pattern of the sample $0.75\text{Y}_2\text{O}_3 \cdot 0.25\text{Nd}_2\text{O}_3$, annealed at $1000\text{ }^\circ\text{C}$ (10 h) and $1410\text{ }^\circ\text{C}$ (3 h).

First experiments indicated that the values of pH corresponding to precipitation of neodima precursor from nitric solutions (experiment number 52), do not differ substantially from ones, corresponding to yttria precipitation. However, we found out as the result of careful experiments, precipitation of neodima was ending after the same of yttria (at $\text{pH}=9$). Therefore particles of precursor were obtained in co-precipitation are heterogeneous. Their surface enriched by neodima. After heating of precursors at the temperatures $500 - 900\text{ }^\circ\text{C}$ we observed the broadened lines at X-ray patterns, which correspond to cubic yttria. No other phases, different from yttria, were observed.

Annealing at 1200 °C leads to well-formed solid solution for $x \leq 0.11$. This is quite sufficient for preparing elements for laser ceramic. The lattice constant of $(Y_{1-x}Nd_x)_2O_3$ solid solution increase with Nd_2O_3 content.

To investigate the kinetics of solid solution synthesis we investigated high content neodima samples. X-Ray powder pattern at the same time increased sensitivity and self-descriptiveness. Figs.2.1.21 and 2.1.22 showed typical X-Ray powder pattern.

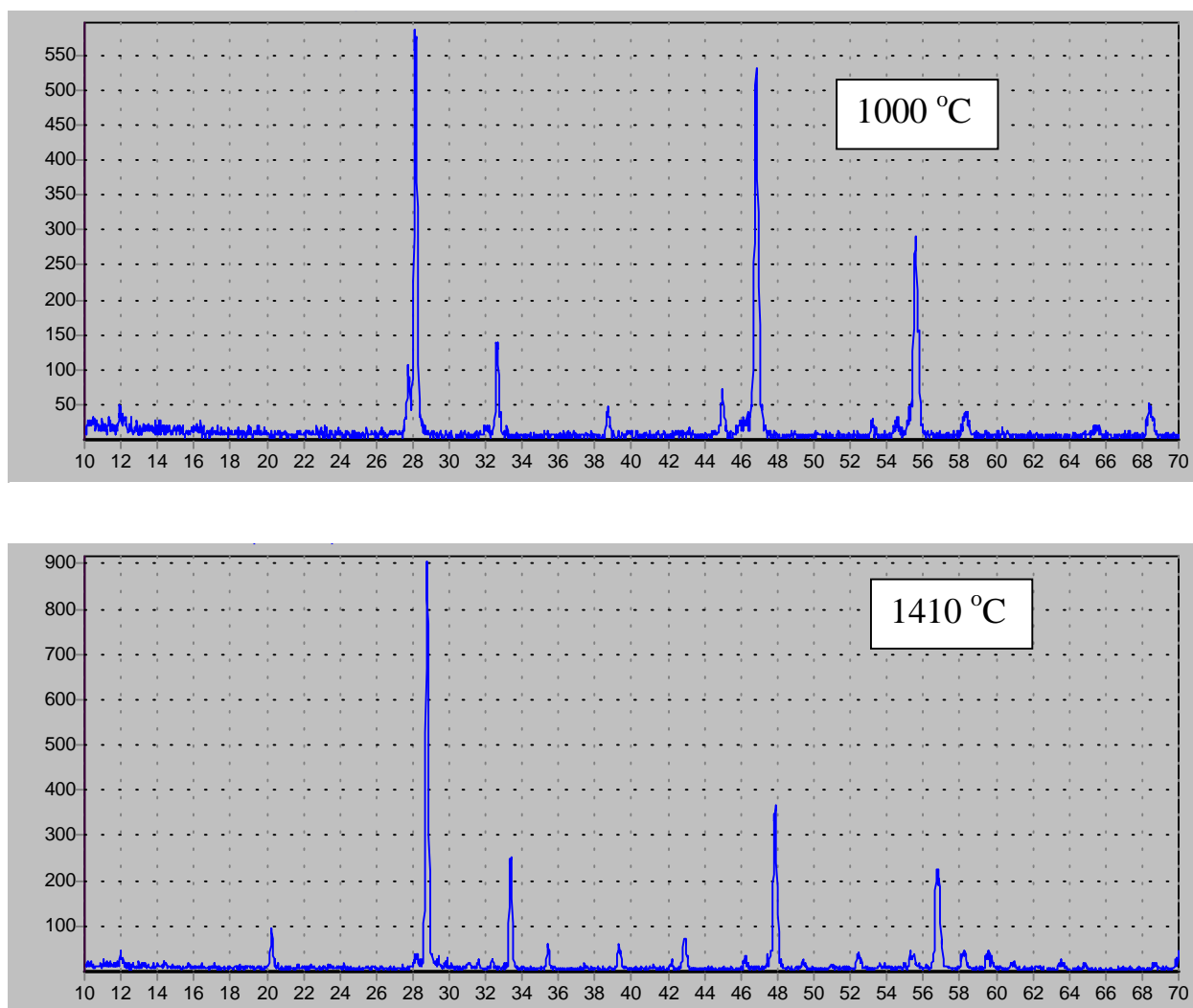


Fig. 2.1.22. X-Ray powder pattern of the sample $0.5Y_2O_3 \cdot 0.5Nd_2O_3$, annealed at 1000 °C (10 h) and 1410 °C (3 h).

The samples with 25% and 50% Nd_2O_3 after annealing at 1400 °C realized solid solution yttria oxide (sp.gr.Ia3) of cubic syngony with lattice parameters $a=10,6599 \pm 0,0015 \text{ \AA}$, $a = 10,7434 \pm 0,0035 \text{ \AA}$. The X-Ray powder patterns allowed to good interpret. The 50% mol. Nd_2O_3 sample has single additional reflex near the 28 degrees 2θ (see fig.2.1.22). This fact confirm the existence of secondary phase of several percents.

The 25% mol. Nd_2O_3 sample X-Ray powder patterns (after 10-hours annealing at 1000 °C) shown cubic solid solution lines of type Y_2O_3 with lattice parameters $a=10,6587\pm0,0034$ Å. In addition to we see the secondary train of peaks caused by cubic phase with lattice parameters $a=10,99$ Å. This parameter too much then the same in Y_2O_3 . (10, 596 Å). Thus, the additional phase has enrich neodima oxide.

X-Ray powder patterns of the 50% mol. Nd_2O_3 sample (after annealing at 1000 °C) could not interpret as two-phases mixture. This pattern indicates regulating of solid solution with YNdO_3 compound. The calculated trigonal lattice parameters are: a 3.869(3), c 9.701(9) Å.

Thus, followed experiments indicate that the formatting of solid solution $(\text{Y}_{1-x}\text{Nd}_x)_2\text{O}_3$ takes place at the temperature over 1000°C i.e. at the stage of formation micro- not nano-particles.

Yttria green compact preparation and sintering experiments.

Series of experiments on ceramic sintering process in high-temperature vacuum furnace has been carried out. For sintering, we reconstructed and adjusted a special high-temperature vacuum furnace Sapphire-2M produced by the Institute of Crystallography Russian Academy of Science for crystal growth of refractory materials. It has a tungsten resistance heater and a system of molybdenum radiation shields (heat screens).

The process was controlled using the heater voltage and current. The temperature was measured with an optical pyrometer. The special experiments for correction of radiation temperature were carried out. In the temperature interval from 500 to 1500 C, the real temperature of ceramic samples was measured by a Pt/PtRh thermocouple and compared the pyrometer measurements. The reflection coefficient of the heater was evaluated.

More than 50 different pellets, including garnet ones, have been prepared.

Effective sintering of pellet from yttria nanoparticles takes place at 1600 – 1700 °C in vacuum.

Two problems appear after first experiments on sintering: black color of yttria pellet after sintering under vacuum and macro cracks observed in sintered pellets.

We supposed the black color was formed due to tungsten impurities and (or) oxygen deficit in yttria (color center formation).

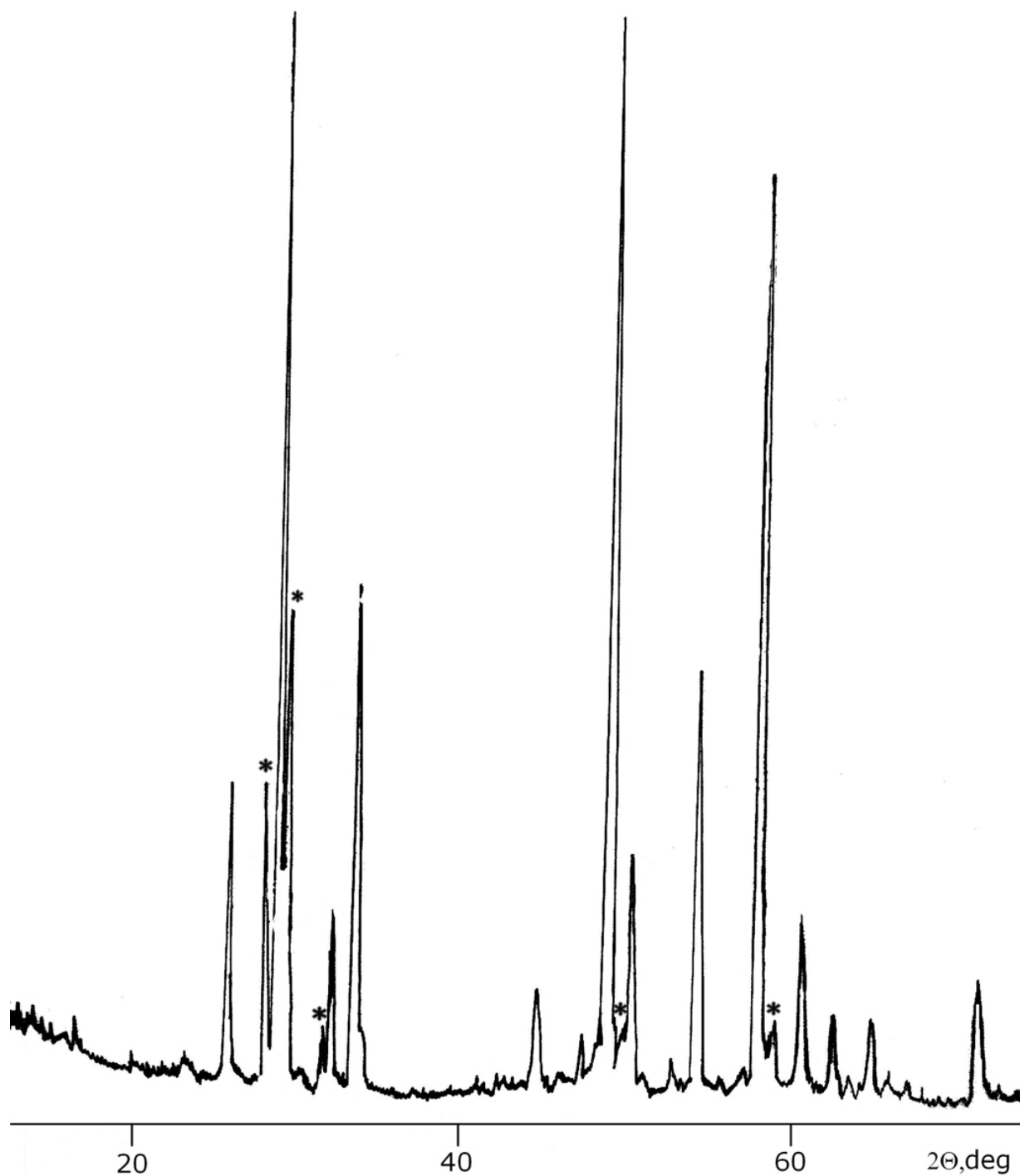


Fig. 2.1.23. X-ray powder data ($\lambda=\text{Cu}_{K\alpha}$) from surface of Y_2O_3 pellet.

Main lines belong to cubic Y_2O_3 ; * – lines of $\text{Y}_{30}\text{W}_8\text{O}_{69}$, JCPDS file # 15-0559.

We observed the black color of yttria ceramic surface and yellow color in the body of pellet, color intensity being decreasing from surface to volume. Black surface has high electric conductivity. The results of electron microanalysis indicate that color is connected with tungsten impurity. X-ray powder data indicate formation of low-valence

yttrium tungstenate (see Fig.2.1.23). The source of tungsten is the material of heater in the high-temperature vacuum furnace. The evaporation of W in form of volatile oxide WO_3 is probable.

Heating of the samples in the melt of mixture of KNO_3 and $NaNO_3$ leads to tungsten removing, but accompanied with erosion of pellet surface. Heating of ceramic under air leads to effective samples purification from tungsten without it destroying.

The dipping of green yttria compact into crumb from yttria particles was sufficient for coloring prevent.

Obviously macro cracks forms due to too high heating rate of initial compact. It was found that the 6 hour-heating from room temperature to temperature of sintering is sufficient for the absence of macro cracks in pellets.

Starting from cotton-like precursor, preliminary annealed at 500 °C or even 300 °C, with 26% density of pressed green compact, we observed a strong shrinkage of the yttria pellet. After several stages we obtained the ceramic with 92 % density. The microstructure studying (Fig. 2.1.24) reveals the formation of large porous with size about 1 μm .

We have been succeeded in fabrication of the pure yttria ceramic having nominal density (comparing with theoretical density of yttria single crystal) with 99 - 100%, and consequently, almost zero porosity. We used complicated technique of precursor with “card-dome” structure preparing and annealing of compact, see Fig. 2.1.25-2.1.27.

1% of surface active reagent polyvinyl pyrrolidone (PVP) was added to initial yttrium nitrate solution according to our previously experiments in order to form plate-like yttria precursor particles.

TEOS (tetra ethoxy silan) additive was introduced to slip for following formation of silica film on grain boundaries. The ball milling was carried out in ethanol medium in order to prevent hydrolysis of TEOS. The average of size of particles yttria press-powder was equal to 50 nm according to X-ray powder measurements, see Fig.2.1.15a.

The operation of pressing (see Fig.2.1.25) was introduced because of the ingot after casting did not keep the form and destroyed to powder.

The sintering of pellet consisted from 3 cycles of annealing for 4 hours (Fig.2.1.26). The rate of heating was large, that leads to formation of macro cracks in sintered pellet, see Fig.2.1.27.

The surface of ceramic consists from grains with 1-5 microns, packing closely without pores (Fig.2.1.28). However, there are small amount of large (up to 5 microns) pores (Fig.2.1.29) in volume of pellet, which make the samples non transparent.

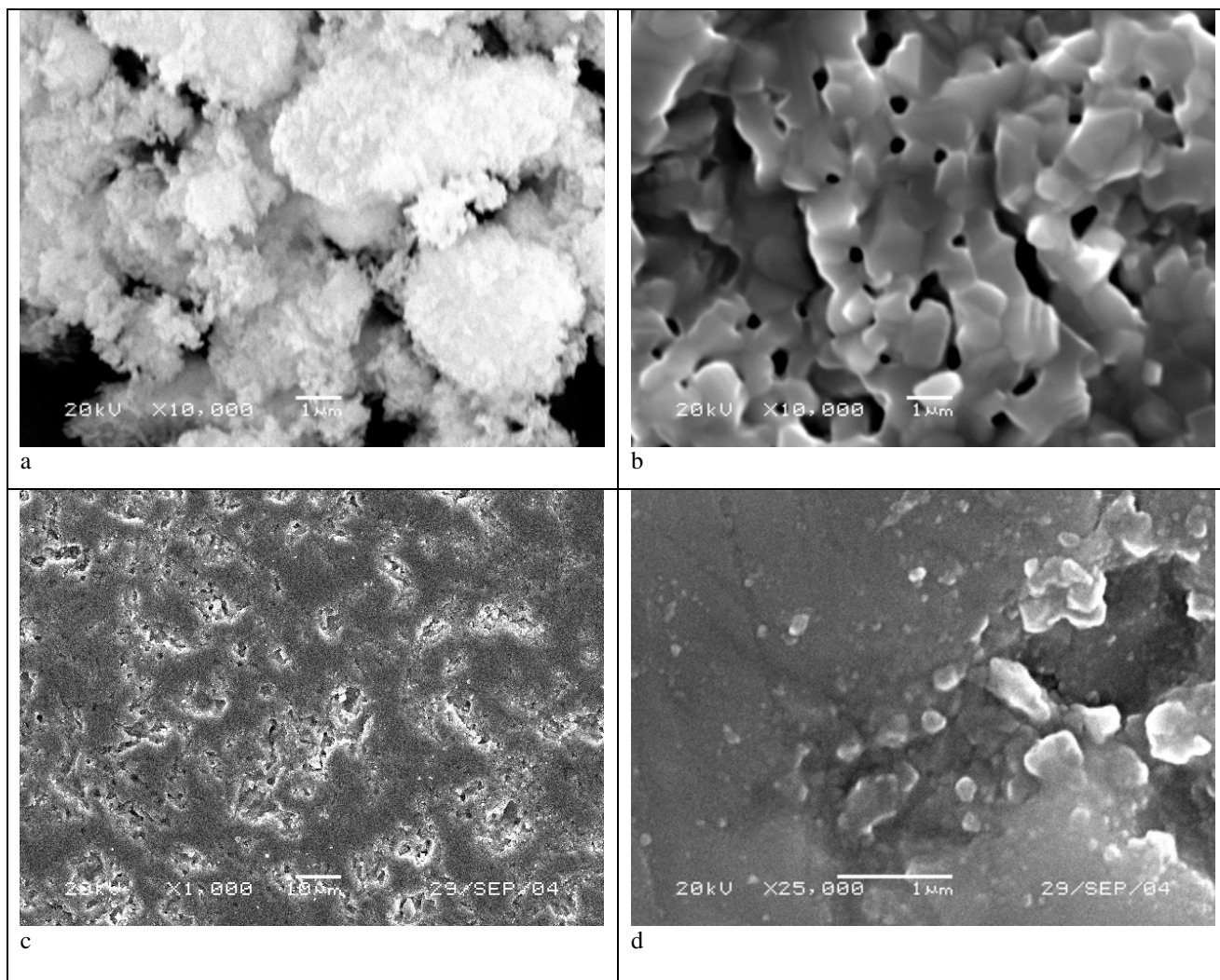


Fig.2.1.24. Electron scanning microscopy. Pellet number I. (a) – precursor, heated up to 500 °C (sample 12a), (b)- sintering at 1600 °C under vacuum, (c, d)- additional sintering at 2000 °C under vacuum (92 % density)

The intermediary stage of pellet sintering process is presented on Fig.2.1.30. It is interesting that grain boundaries form before the compact pellet body forms.

Obviously large pores form into ceramic volume due to too high heating rate of initial compact.

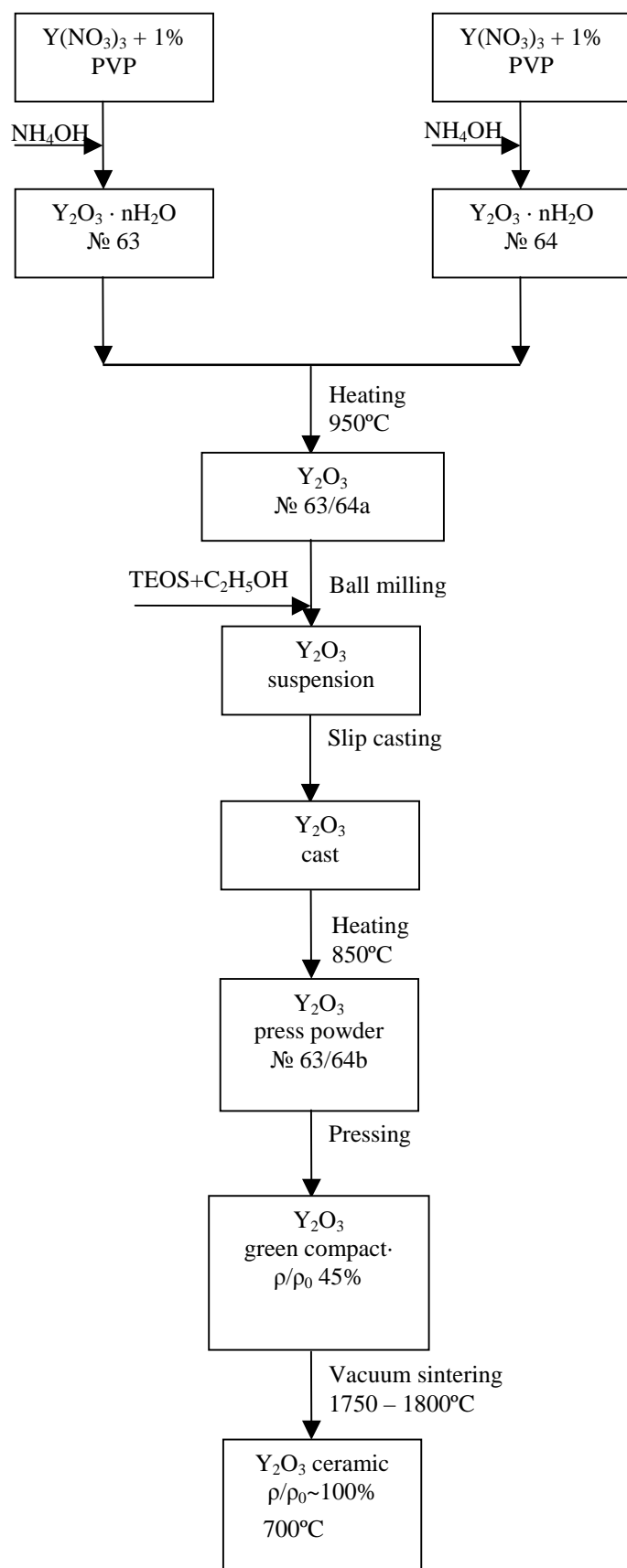


Fig. 1.25. The scheme of preparing of yttria pellet with ~ 100% relative density (pellet XX)

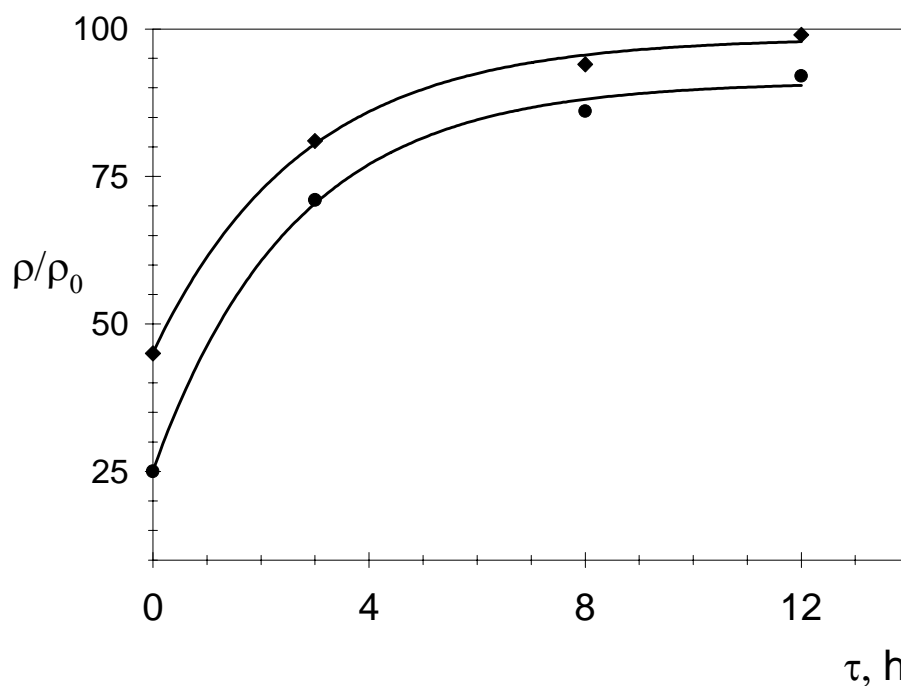


Fig. 2.1.26. Relative density of Y_2O_3 ceramic pellets during sintering at 1750 – 1800°C. ● – pellet number I; ♦ – pellet number XX



Fig. 2.1.27. Hath of yttria pellet (number XX) with nominal 100% density (20 mm diam.). Mechanical treatment (polishing) of the surface. Black part - tungsten deposition on the crack; yellow part – tungsten impurity in pellet body.

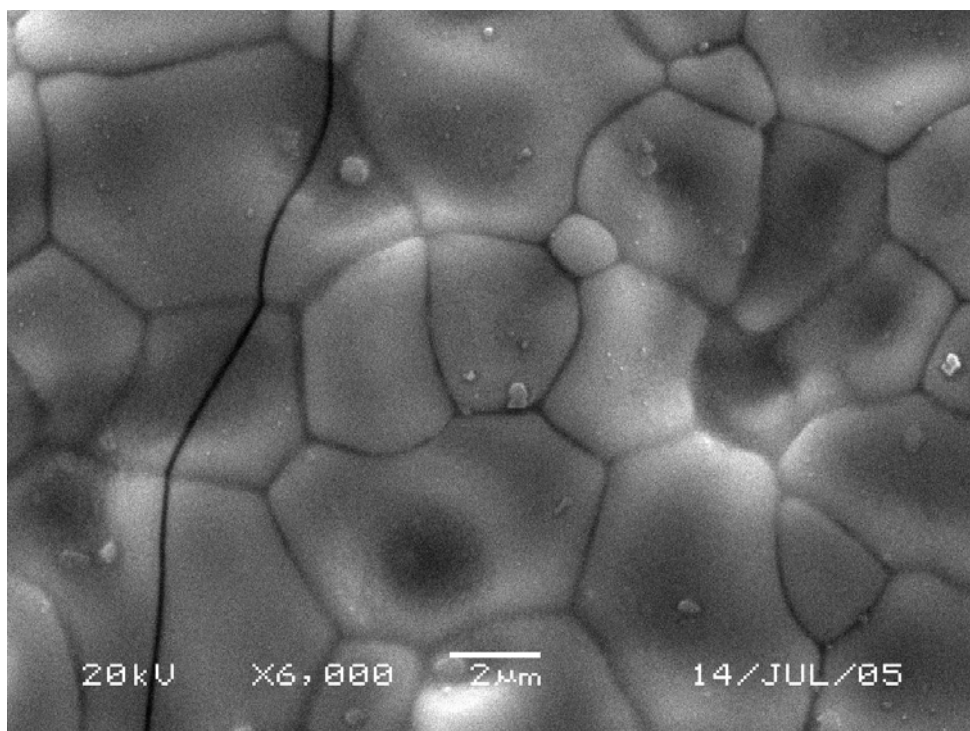
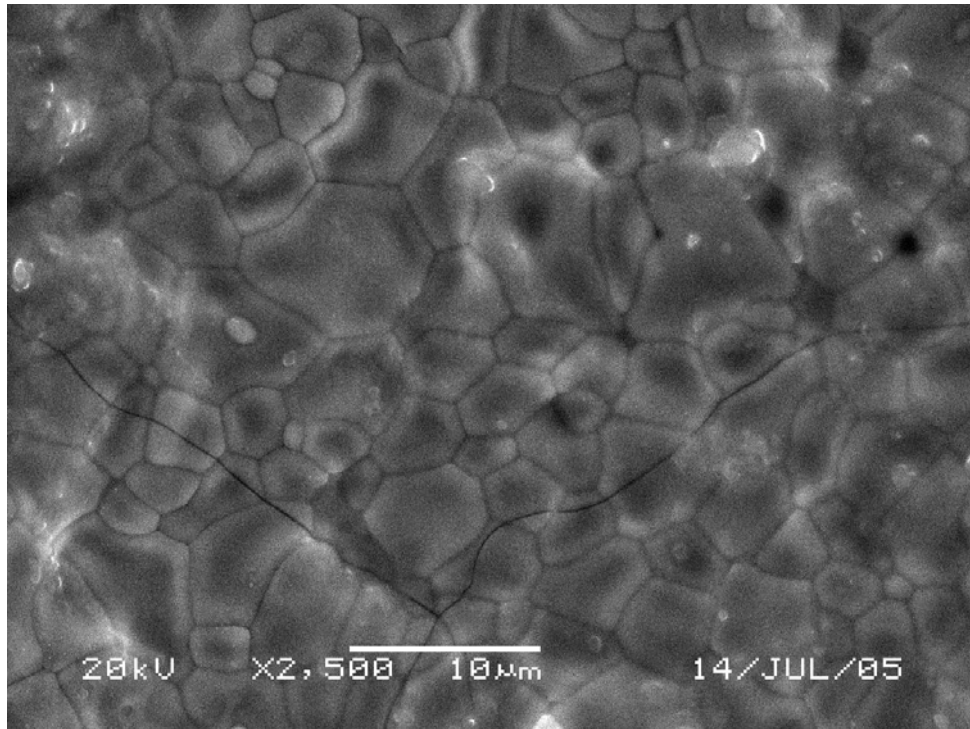


Fig.2.1.28. Scanning electron microscopy of surface of yttria pellet (number XX) with nominal 100% density.

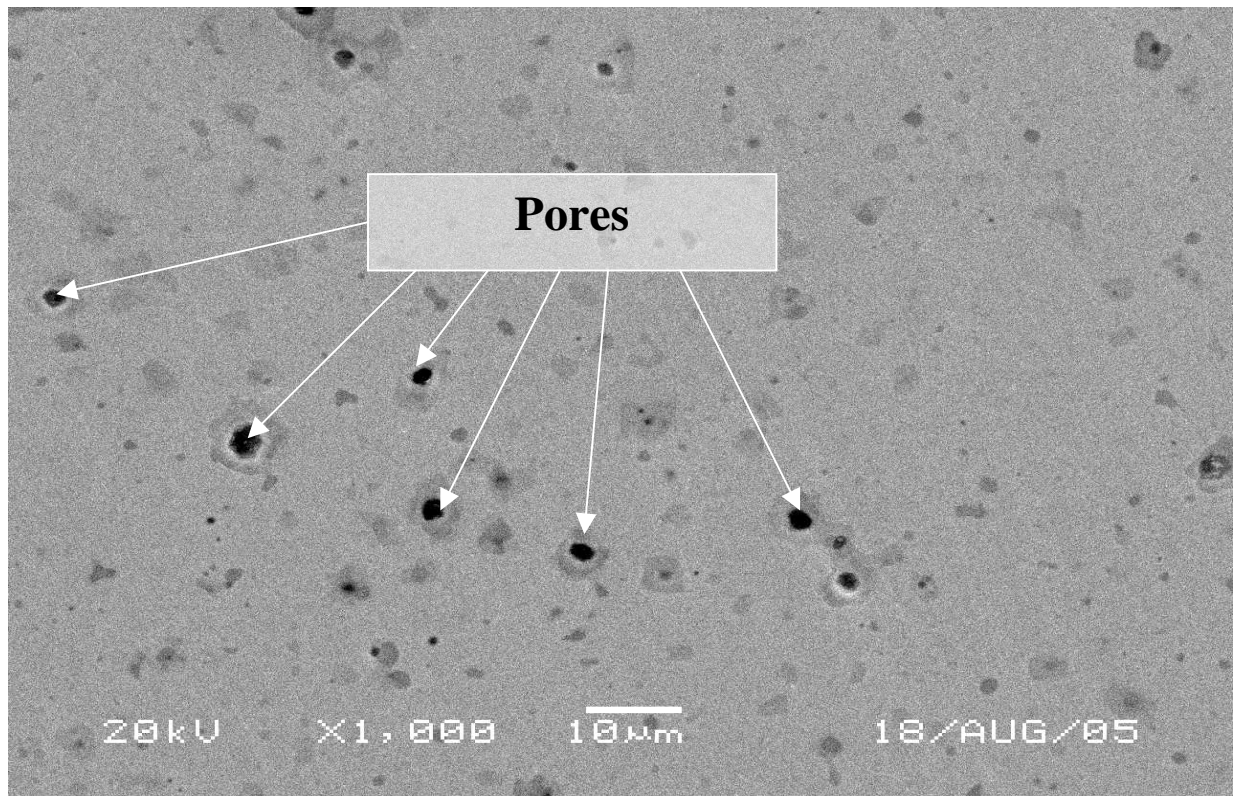


Fig.2.1.29. Scanning electron microscopy microstructure of abraded and polished yttria pellet (number XX) with nominal 100% density.

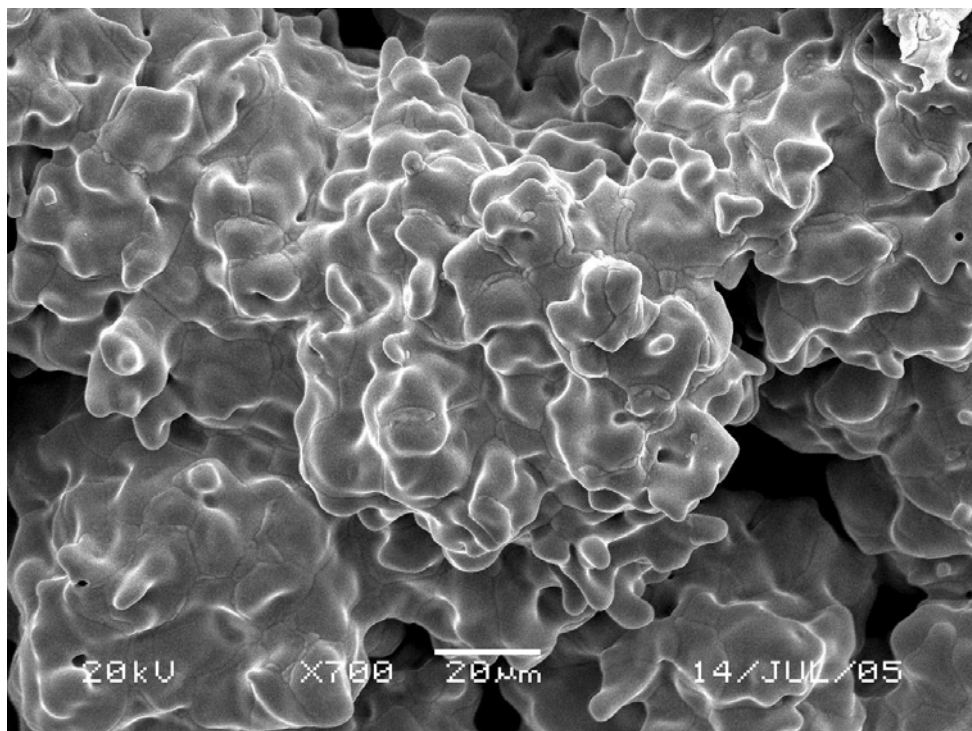
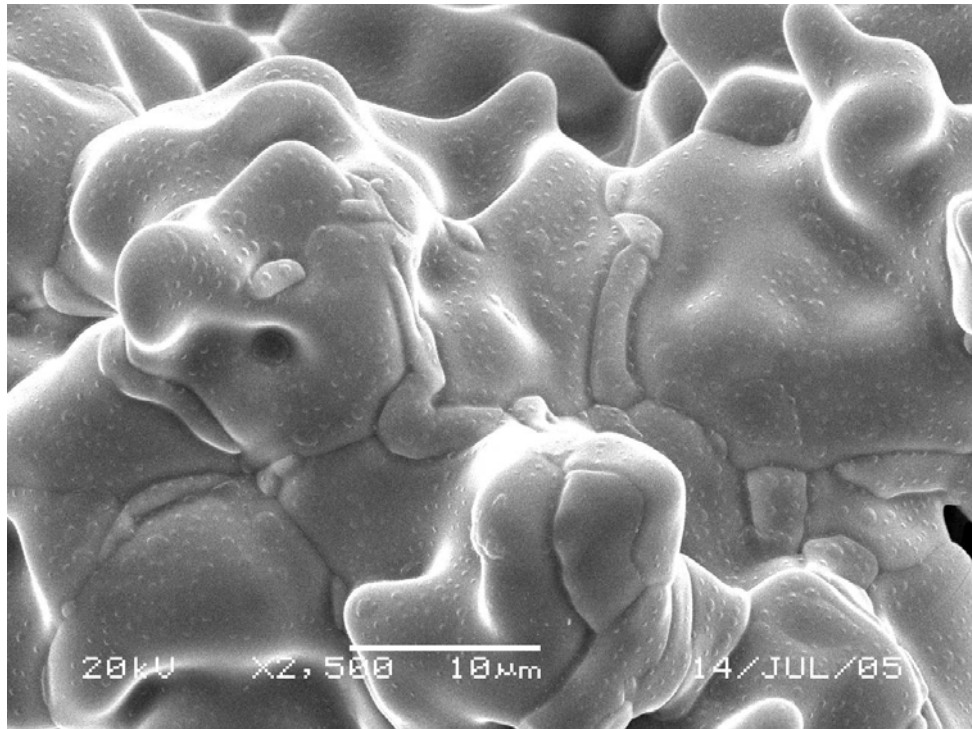


Fig.2.1.30. Scanning electron microscopy .
Process of sintering of yttria pellet (surface).

We studied possibility of decreasing sintering temperature by using some additives with low melting temperature.

Mechanical addition of 1-3 % YF_3 to initial yttria was made in experiments 55-56. The pressured pellets don't shrink at 1200 °C on the air.

Addition of 1, 3, 5 mol % of bismuth oxide to yttria by co-precipitated process was made in experiments 48-50. It is known that Bi_2O_3 forms solid solution with yttria easily and has very low melting temperature. We propose that Bi_2O_3 went out from pellet during sintering due to high vapor pressure. Effective sintering of the pellets takes place at 1200 °C on the air.

Synthesis of YAG garnet materials

We started the investigations for of aluminum – yttrium garnet $\text{Y}_3\text{Al}_5\text{O}_{12}$ (YAG) - ceramics because of lower garnet melting temperature in compare with Y_2O_3 and, consequently, lower sintering temperature. We studied preparation of YAG material by precipitation of precursor from water solutions with following thermal treatment.

Formation of aluminum – yttrium garnet precursor was studied by details. We used acid nitrate solutions and ammonia NH_4OH solution or ammonium bicarbonate NH_4HCO_3 as (titrant agent) precipitant.

Precipitate samples transform into the gel under drying. Garnet gel is solid and transparent at the water content being about 60-70 wt %. Following gel drying leads to formation of fine amorphous (according to X-ray data) powders.

DTA analysis shows (Fig. 2.1.31, 2.1.32) that the dehydration processes of YAG precursor is complicate. Mass losses take place up to ~ 900 °C. Exoeffect on thermogram occurs at ~930 °C.

X-ray powder diffraction data (Fig.2.1.33) showed that exoeffect mentioned above corresponds to formation of yttrium-aluminum garnet structure (crystallization from amorphous state). Measured by X-ray powder diffraction method garnet particles sizes (after DTA at 1000 °C) are 25 nm. So, YAG precursor transforms to $\text{Y}_3\text{Al}_5\text{O}_{12}$ nanoparticles by heating to temperature about 950 °C.

Partial substitution of yttrium by Yb or Nd don't change parameters of synthesis substantially and leads to preparation of single-phase materials (garnet solid solutions) after heating to 950 °C.

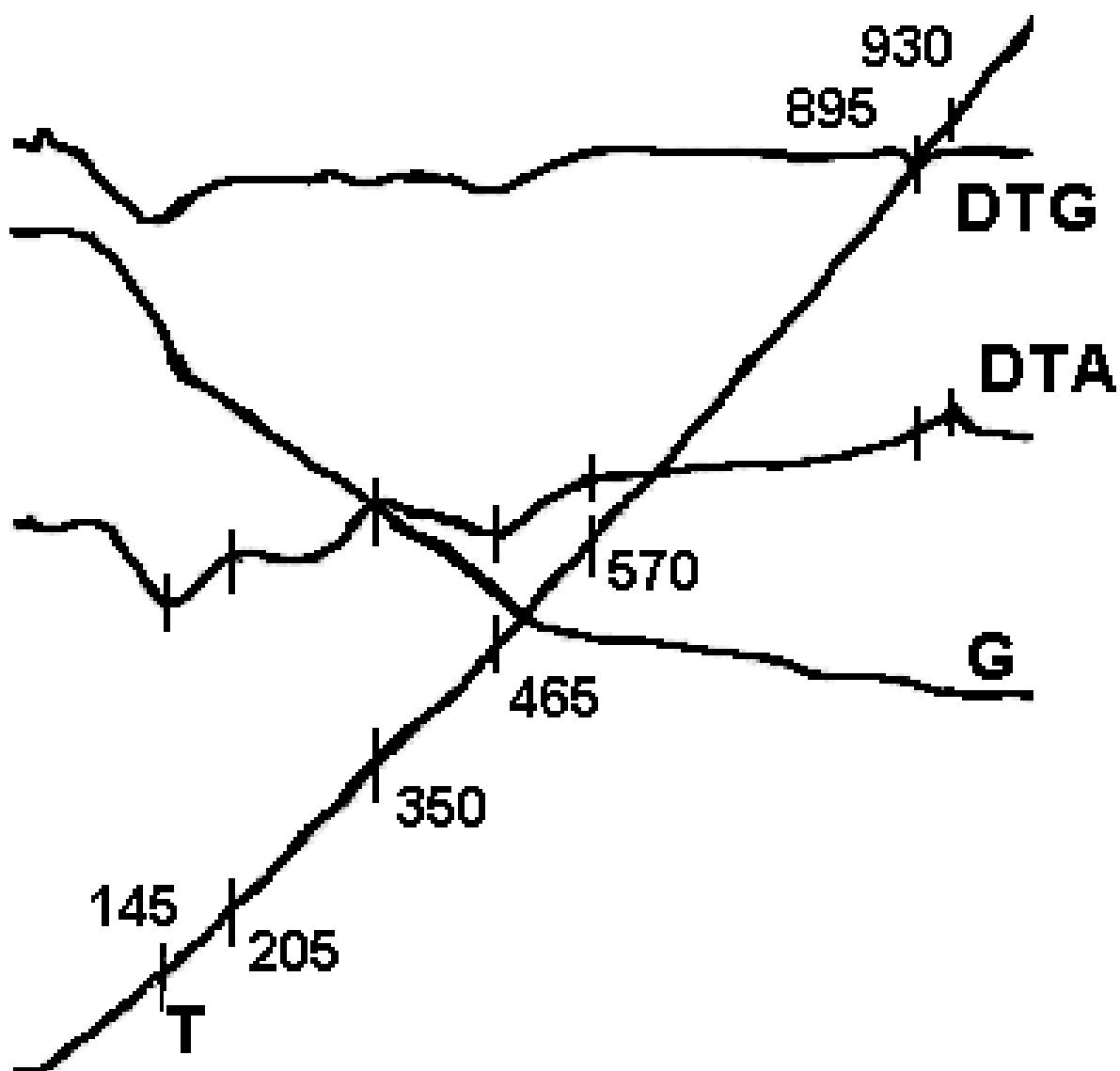


Fig.2.1.31. DTA of garnet precursor (experiment # 95).

Precipitation with NH_4OH solution.

Initial mass 441 mg, total mass loss 49.2 %.

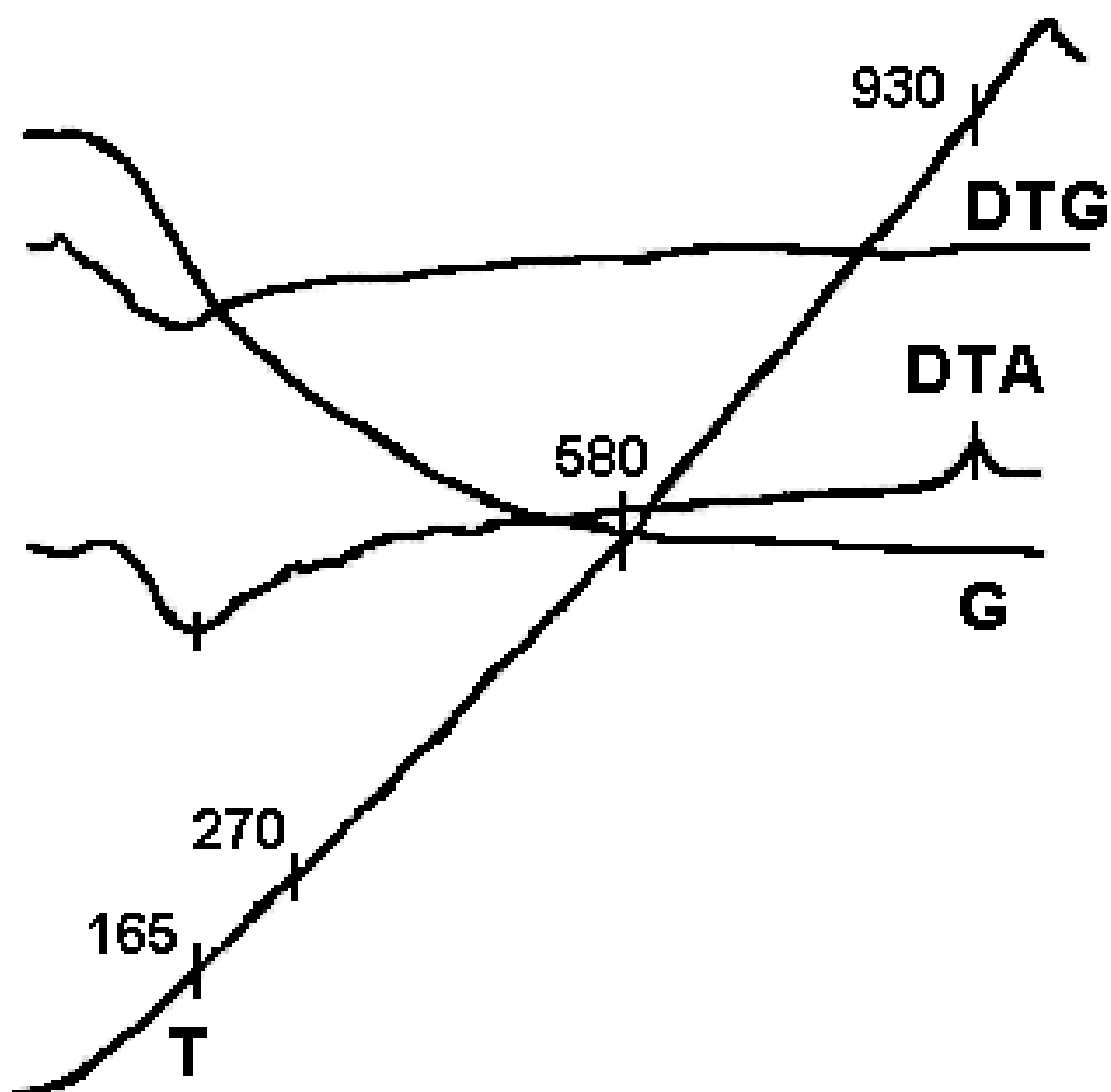


Fig.2.1.32. DTA of garnet precursor (experiment # 96).

Precipitation with NH_4HCO_3 solution.

Initial mass 379 mg, total mass loss 50.7% .

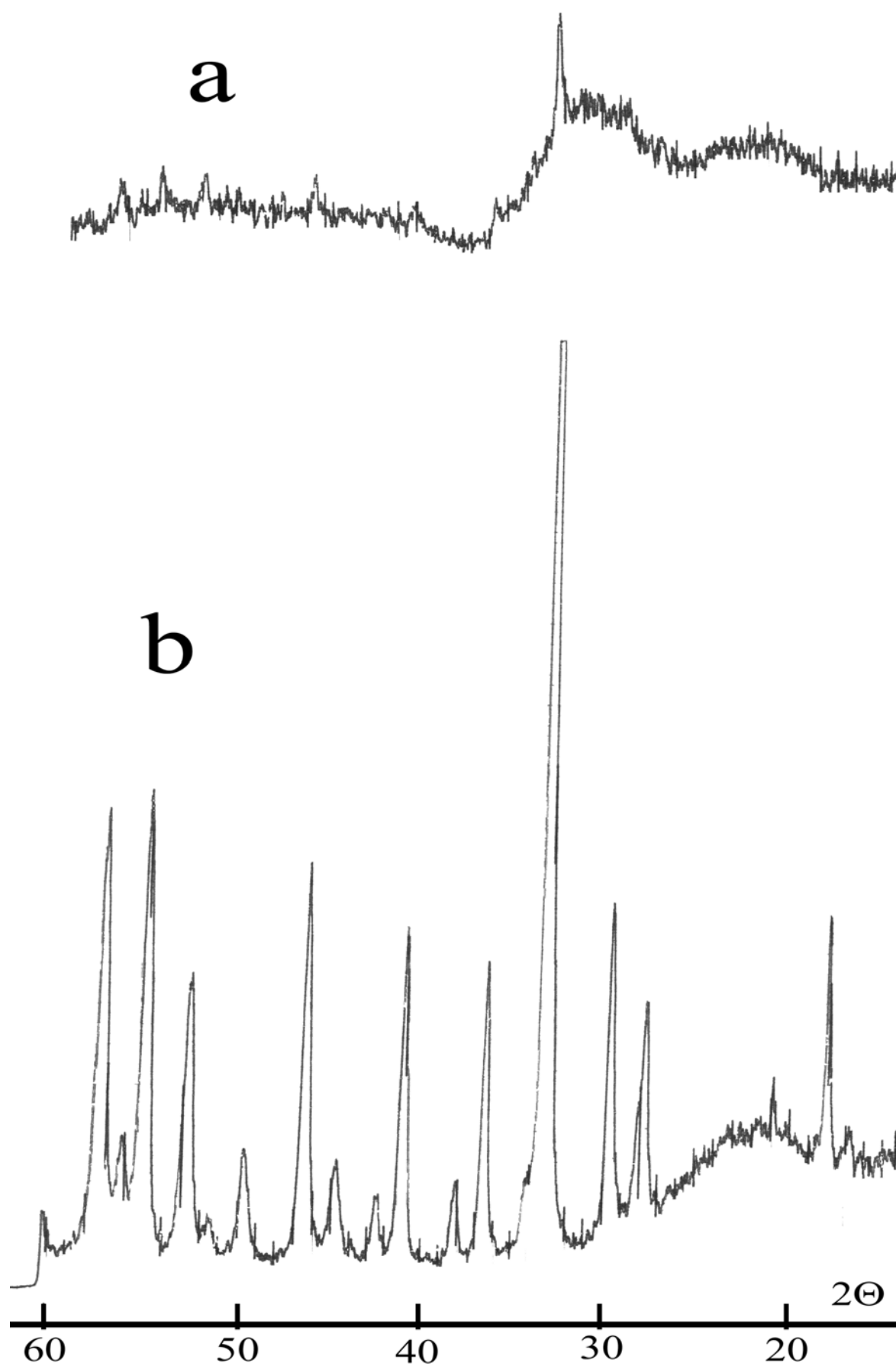


Fig.2.1.33. X-ray powder data of sample #95 after DTA: a – heating up to 870 °C; b- heating up to 1000 °C (cubic garnet structure, average size of particles – 25 nm).

The samples of YAG prepared by thermal treatment of precursor have a consistency similar to clay. They are milled in an agate mortar to powder. It was easier than milling of Y_2O_3 samples, prepared in analogous way. The powder was pressed in a stainless press-form 20 mm in diameter. The Teflon film between the powder and the press-form was used to eliminate possible contamination with metallic particles. The pressure was 3000 atm. The initial relative density ρ/ρ_0 (here ρ_0 is the YAG theoretical density) of green compacts varied from 0.29 to 0.52.

The typical temperature regime of sintering is shown in Fig.2.1.34.

After the first step of sintering at 1650 C, strong shrinkage of YAG powder compact was observed and the value 90 % of relative density was achieved. The microstructure of broken pellets after the first step of sintering is presented in Fig.2.1.35. It is interesting that sintering of garnet had occur through the μ -dimension stage, in contrast to yttrium oxide sintering, see Fig.2.1.30.

The temperature of the second step was up to 1750 C. It was sufficient to achieve almost 100 %-density translucent ceramic (see Fig.2.1.36). However, light scattering of this samples is still rather high and need more detail study and technology experiments.

No coloring of pellets due to tungsten contamination was observed.

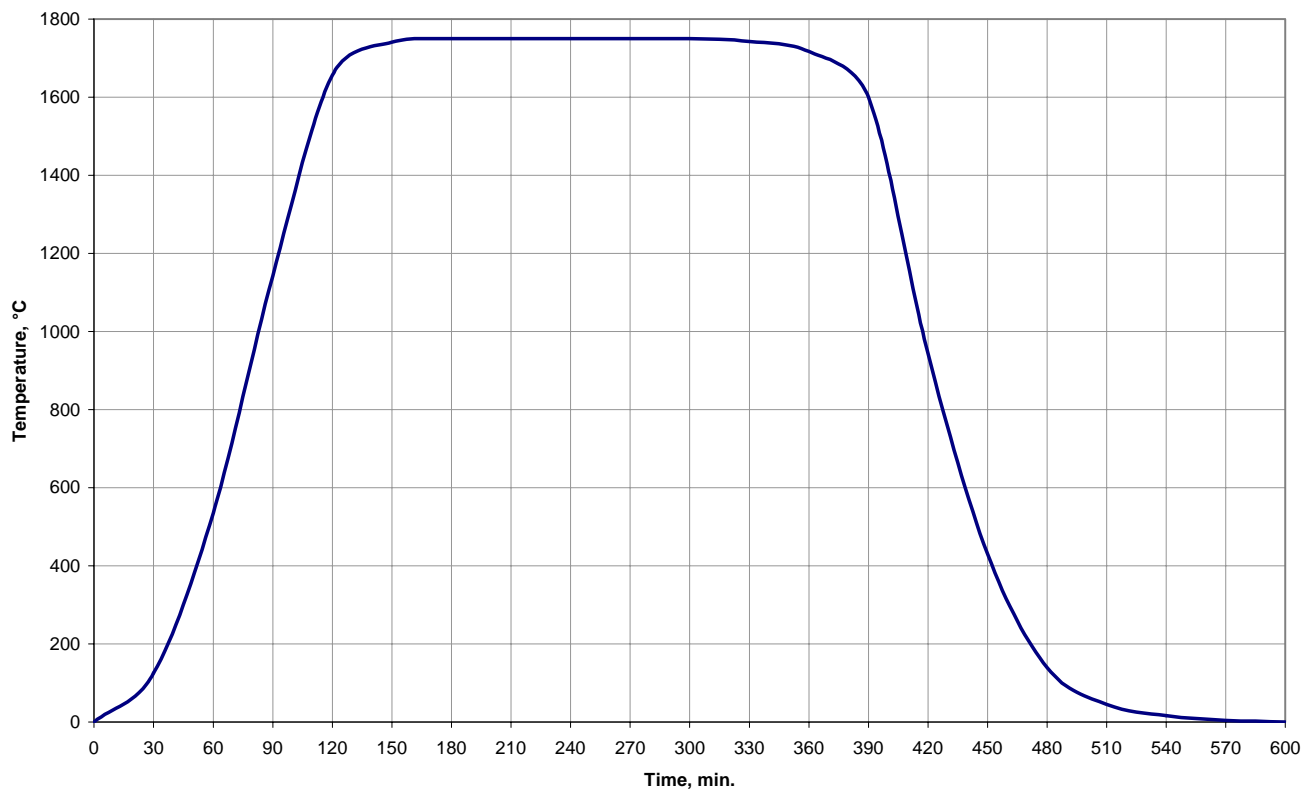


Fig.2.1.34. Temperature regime of sintering of YAG ceramic.

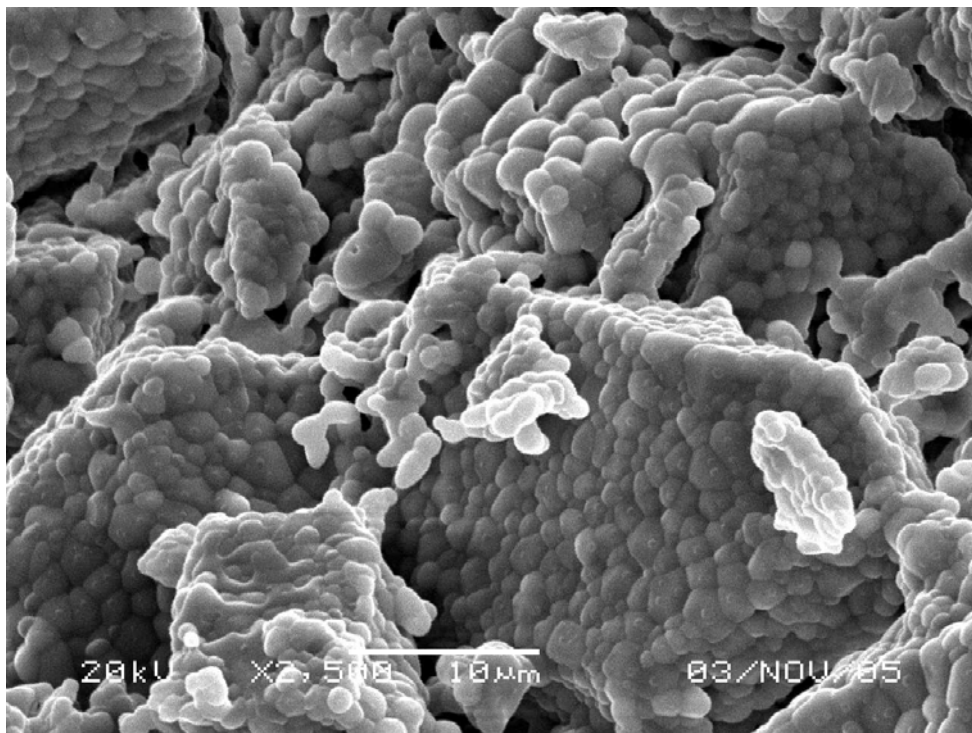
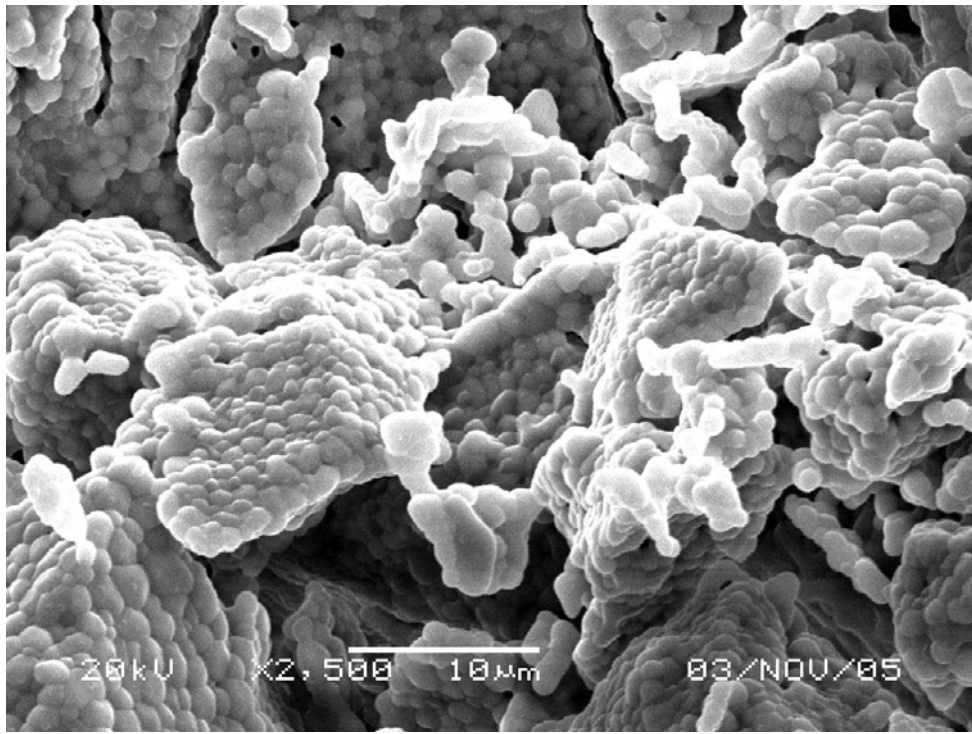


Fig.2.1.35. Electron scanning microscopy of YAG ceramic after first step of the sintering (pellet number XXXIV).

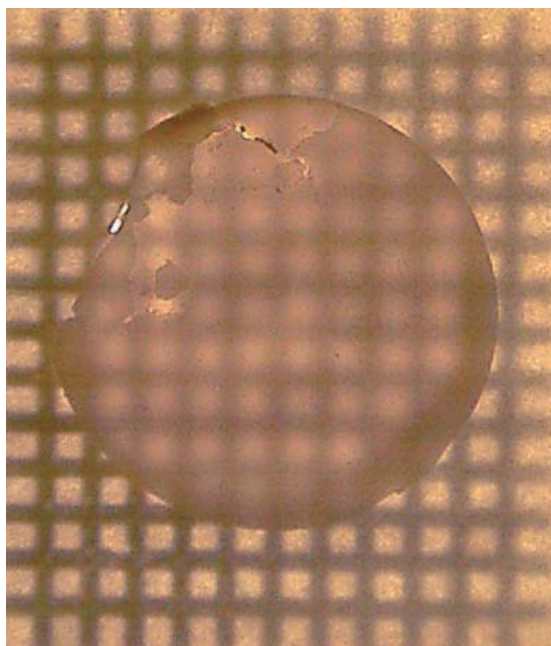


Fig.2.1.36. YAG:Nd ceramic pellet (XLII) with nominal 100% density (\varnothing 15 mm). Mechanical treatment (polishing) of the surfaces. Thickness 0.5 mm.

2.1.3. Conclusions.

1. A technique of precipitation of yttria precursor $Y_2(OH)_5NO_3 \cdot nH_2O$ from nitric solution has been developed. The plate-like particles aggregated in the “card-dome” structure are formed with presence of surface-active particles or under ultrasonic action.

Nitrate precursor loss weight and formation of yttria occur in three main steps. The last step finishes at 500 -500 °C.

The effect of shape memory takes place.

2. The processes of formation of yttria nanoparticles were studied. Heating of plate-like precursor particles up to 900 C leads to mechanical relaxation with transformation of plates to primary isometric nanoparticles with a size about 13 nm. Increasing of temperature or time of annealing leads to transformation of small primary nanoparticles to large secondary ones (coalescence processes). Secondary nanoparticles are characterized by size about 100 nm and mechanical deformation. The problem of preparing of yttria nanoparticles was decided.

3. Co-precipitation of yttria with neodima with following calcinations lead to formation of solid solution $(Y_{1-x}Nd_x)_2O_3$ with $x \leq 0.11$. It is quite sufficient for preparing elements for laser ceramic.

4. Sintering of nanoparticles is effective process at 1600-1700 C in vacuum. Additive of Bi_2O_3 gives possibility to decrease the sintering temperature down to 1200 C

(in air). However, up to day we cannot prepare (neither by pressing nor by slicker technique) the green yttria compact with high density (above 65 %), which can lead to practically 100 % density of ceramic. We have found the regimes of thermal treatment, eliminate macro crakes and color centers in yttria ceramic.

X-ray powder diffraction data showed that thermal treatment of YAG precursors at 950 °C leads to synthesis of $Y_3Al_5O_{12}$ nanoparticles.

The next planning step of our experiments include ultrasonic disintegration with using of surface active substances for isolation of nanoparticles.

References.

- 1 Volynetz F.K. // Opto-mechanical industry , 1973, №9.p.48-60 (in Russian).
2. G.A.Vidrik, T.V.Solov'eva, F.V.Kharitonov. Transparent ceramics. Moscow, Energiya, 1980, 96p. (in Russian)
3. Fine technical ceramics. Edited by Kh. Yanagida. Translated from Japanese. Moskva, Metallurgia, 1986.
4. Jr. Carnall, S.E.Hatch, W.F.Parson.Materials Science Research, ed. W.W.Kriegel, H. Palmor. Plenum Press, New York. 1966 V. 3.
5. C. Greskovich, K.N. Woods.//Amer. Ceram. Soc. Bulletin. 1973. V. 52. № 5. P.473.
6. C. Greskovich, J.P.Chernoch. // J. Appl. Phys. 1974.V. 45, № 10 P. 4495.
7. A. Ikesue, T. Kinoshita, K. Kamata, K. Iosida. // J. Amer. Ceram. Soc. 1995. V. 78. P. 1033.
8. A. Ikesue, K. Yoshida. // J. Materials Science. 1999.V.324. P. 1189-1195.
9. I. Shoji, S. Kurimura, Y. Sato, T. Taire, A. Ikesue, K. Yoshida. // Appl. Phys. Letters. 2000. V.77.P.939.
10. A. Ikesue, T. Taira, Y. Sato, K. Yoshida. // J. Ceram. Soc. Jpn. 2000. V. 108. P. 428.
11. J. Lu, M. Prabhu, J. Xu, K. Ueda, H. Yagi, T. Yanagitani, A. Kaminskii. // Appl. Phys. Lett., 2000. V.77. P. 3707.
12. J. Lu, M. Prabhu, J. Song, C. Li, J. Xu, K. Ueda, A. Kaminskii, H. Yagi, T. Yanagitan. i // Appl. Phys. B. 2000. V. 71. P. 469.
13. J. Lu, T. Murai, K. Takaichi, T. Uematsu, K.Misawa, M. Prabhu, J. Xu, K. Ueda, H. Yagi, T. Yanagitani, A. Kaminskii, A. Kudryashov, // Appl. Phys. Lett. 2001. V. 78. P. 3586.
14. J. Lu, K. Ueda H. Yagi, T. Yanagitani, Y. Akiyama, A. Kaminskii, // J. Alloy and Compounds. 2002. V. 341. P. 220.

15. J. Lu, M. Prabhu, K. Ueda, H. Yagi, T. Yanagitani, A. Kudryashov, A. Kaminskii. // Laser Physics. 2001. V.11. P. 1053.
16. J. Lu, K. Takaichi, A. Shirakawa, M. Musha, K. Ueda, H. Yagi, T. Yanagitani, A. Kaminskii. // Jpn. J. Appl. Phys. 2002. V.41. P. L1373.
17. J. Lu, K. Takaichi, A. Shirakawa, M. Musha, K. Ueda, H. Yagi, T. Yanagitani, A. Kaminskii. // Appl. Phys. Lett. 2002. V. 81. P. 4324.
18. A. Kaminskii, M. Akryryn, et. al., // Crystallography Reports. 2003. V.48.P.515.
19. J.Lu, J.F.Bisson, K.Takaichi, e.a. // Appl. Phys. Lett. 2003. V.83. P.1101
20. A.A.Kaminskii, K.Ueda, A.F.Konstantinova, e.a. // Crystallography Reports. 2003. V.48. P.1041.
21. Yu.N.Baranenkov, S.N.Ivanov, A.V. Taranov, e.a. // JETP Lett. 2004. V.79. P.342.
22. A.A.Kaminskii, M.Sh.Akchurin, R.V.Gainutdinov. // 11 National Conference on Crystal Growth. Moscow, Dec. 14-17, 2004. Abstracts P. 497.
23. T. Yanagitani, H. Yagi, M. Ichikawa, // Japanese patent: 10-101333 (1998).
24. T. Yanagitani, H. Yagi, Y. Hiro, // Japanese patent: 10-101411 (1998).
25. Ya.E.Geguzin. // Agglomeration physics. Moscow, Nauka, 1967, 360 p. (in Russian)
26. P.J.Reijnen. Unstehiometry and agglomeration of ionic solids. In coll. "The problems of unstehiometry". Ed.A.Rabenau. Moscow, Metallurgia, 1975, p.239-261 (in Russian)
27. L. Wen, X.Sun, Z.Xiu, S.Chen, Chi-Tay Tsai. // J. European Ceramic Soc. 2004. V. 24. P. 2681-2688.
28. Xia Li, H. Liu, J. Wang, X. Zhang, H. Cui. // Optical Materials. 2004. V.25. P. 407-412.
29. T. Feng, J. Shi, J. Chen, D. Jiang. // J. Opt. Soc. Amer. 2005. V. 22B. P. 2134-2137.
30. M. Dubinskii, L. D. Merkle, J.R.Goff, e.a. // Proc. of SPIE. V. 5792. P.1-9.
31. H.G.Jiang, M.Ruhle, E.J. Lavernia. // J. Mater. Res. 1999. V. 14. P. 459.
32. C.-Z. Huo, Z.Q. Liu, Z.-F.Liang, X.-Y. Li. // J. Guangdong Non-Ferrous Metals. 2005. V. 15. N. 2-3.P. 265 - 271.
- 33.C.E.Holcombe. // J. Amer. Ceram. Soc. 1978. V. 61. P. 481.
34. R.J.Flavy, N.Martys, L. Bergstrom. // MRS Bulletin. May 2004. P. 314.
35. N.N.Olejniov. // Russian Chem. Journal. 1995. V.39. P.85.
36. M. Yoshimura, Xiao-Zheng Rong. // J. Mater. Sci. Letters. 1997.V.16. P.1961.

2.2 Fluoride ceramics

In order to get deeper understanding of problems related to the optical laser ceramics, we studied a natural transparent ceramic material in comparison with a single crystal material of the same composition. As the objects of our investigation, we chose the natural fluorite from the Suranskoe Deposit and single crystals of fluorite grown artificially.

Artificial polycrystalline optical materials transparent in the IR and visible spectral ranges are known for several decades [1]. In recent years, the technology of so-called laser ceramics was developed for YAG (yttrium-aluminum garnets) and rare-earth oxides [2-4]. The optical losses, as well as the spectral and lasing characteristics of these ceramic materials are not poor than that for single crystals [2-4]. It should be noted, that the first Dy - doped fluorite ceramic laser action was obtained long ago, in 1966 [5].

The translucent colorless (optical) fluorite from the Suranskoe Deposit [6, 7] is a quite interesting material, which has a latent crystal structure and is a natural analog of optical ceramics. This fluorite, characterized by a high homogeneity and a good purity with respect to isomorphous cation admixtures [8, 9], can be found in the sellaite-fluorite body of the deposit, where it forms isometric clusters and fibers, filling cracks in sellaite (MgF_2) blocks splintered by tectonic shearing.

A specific feature of the Suranskoe cryptocrystalline optical fluorite (SCOF) is its high “impact resistance”, which is easily seen when crushing the material. This feature encouraged us to study the mechanical properties of SCOF, which is the goal of this paper. For comparison, we also measured the corresponding characteristics for a sample of artificial single-crystal fluorite, grown by the method of directional crystallization.

The ceramic samples for investigations were cut out by a diamond saw, grinded, and polished mechanically. The mechanical tests of the single crystals were carried out on the chips along the [111] cleavage. Deformations were made by a diamond Vickers pyramid at room temperature. Identification was carried out by a

microhardnessmeter PMT-3; for the sclerometric tests, we used a Martens sclerometer. The load for the indenter was chosen so that not only the impressions themselves but also the radial cracks from them were reliably detected.

While radial cracks in single crystal are well distinguished even at $P=0.2\div0.3$ N, destructions in the natural CaF_2 ceramics are reliably detected only at $P\geq 1$ N. That is why the microhardness and toughness single crystals and CaF_2 ceramics were measured at $P=1$ N. Taking into account a rather high homogeneity of ceramic samples, we made 50 impressions both on ceramic samples and single crystals, the diagonals of the impressions lying along the direction $\{110\}$, which has the maximum hardness.

The microhardness H was calculated by the well-known formula $H=KP/d^2$, where P is the load to the indenter, d is the impression diagonal, and K is a coefficient dependent on the indenter shape ($K=1.854$ for the Vickers pyramid). The toughness K_{1c} was determined by measuring the linear sizes of radial cracks (C) (appearing close to the point of the load application) as a function of the load and estimated by an approved formula taking into account the elastic and strength characteristics of the material studied [10]. For the Vickers indenter, $K_{1c}=0.016 (E/H)^{1/2}P/C^{3/2}$, where E is Young's modulus. For fluorite, $E = 8.73\times 10^{11}$ dyne/cm² [11].

The morphology of the surfaces of breaks in the samples was studied by the atomic-force microscopy (AFM) in a contact regime, using an atomic-force microscope Solver P47. The samples were broken by three-dot bending, before which the sample was scratched with a scratch of a definite length, serving as a stress concentrator. The cathode luminescence CL of the samples was studied with a scanning electron microscope JSM-6460-LV.

The samples studied are shown in Fig. 2.2.1. The transmission spectrum of SCOF in the IR spectral region is virtually identical to the spectrum of the single crystal. The X-ray powder diffraction analysis (a DRON-2 diffractometer, CuK_α radiation) of the SCOF samples has shown almost complete disorientation of their grains. Investigations with the CL revealed that the SCOF samples, in contrast to the CaF_2 single crystals, consist of the differently oriented blocks with sizes from several to tens of micrometers, the grains having mainly a layered structure (Fig. 2.2.2a).

Chemical etching of the SCOF sample showed that the large grains contain smaller grains, 50-200 nm in size (Fig. 2.2.2b).



Fig. 2.2.1. The samples of (left) artificial monocrystalline fluorite and (right) Suranskoe cryptocrystalline optical fluorite (SCOF).

Our study disclosed that the microhardness of the ceramic samples only slightly (by 10÷12%) exceeds the microhardness of CaF_2 single crystals, but the crack resistance is considerably better: the toughness (K_{IC}) is approximately fourfold higher (see table).

Table 2.2.1.

Material	H (GPa)	K_{IC} ($\text{MPa}\cdot\text{m}^{-1/2}$)
Single crystal	200 ± 7	1.5 ± 0.15
Ceramics	225 ± 5	6.3 ± 0.60

Sclerometric tests of ceramic samples (the scratches were drawn from the center of a circle along radii each 15 degrees) revealed no hardness anisotropy, while the hardness of CaF_2 single crystals is higher in the directions $\langle 110 \rangle$.

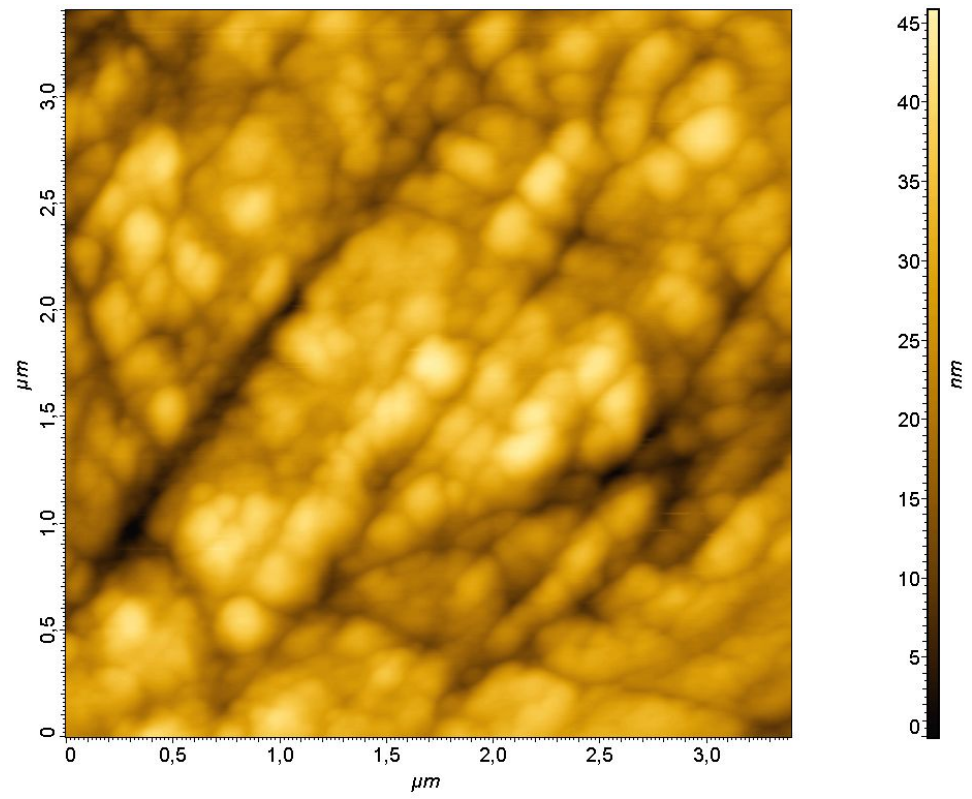
It was found that CL of separate SCOF grains in the vicinity of the relaxed exciton band (280 nm) is 20-30% higher than that of CaF_2 single crystals, while the CL radiation at the grain boundaries is noticeably weaker. The VE and CL images of the impression on the CaF_2 ceramics and the CL spectrum of a separate grain are shown in Fig. 2.2.3. The quenching of CL from the bottom of impressions and scratches relates to the distortion of the crystal structure till the crystal amorphization [12, 13].

It is well known that the hardness of crystals is determined by the dispersion energy [13, 14]. It is also known that, with decreasing size of the crystal, its structure becomes more perfect (it is energetically unfavorable for defects to be created and stay

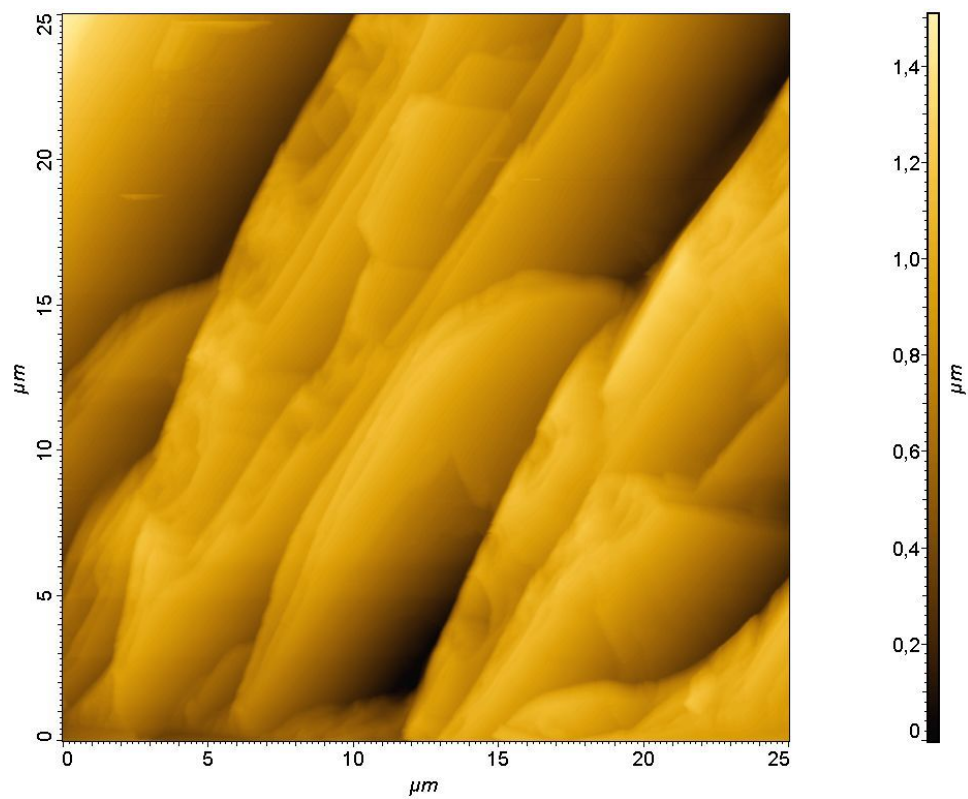
in small volumes, and they are moved to the boundaries by the image forces) and its mechanic properties improve (as, for example, in whiskers). The higher exciton luminescence of separate SCOF grains in comparison with CaF_2 single crystals points to their more ideal structure, which can explain the higher microhardness of investigated polycrystalline CaF_2 samples in comparison with single crystals.

The abnormal toughness of polycrystalline samples of SCOF evidently relates to the problems in the formation and expansion of cracks. First, the more perfect structure of separate grains suggests the presence of a smaller amount of stress concentrators (seeds for microcracks). Second, the layered structure and the intergrain boundaries may prevent the development of cracks. The layered structure of grains in the natural polycrystalline optical material is similar to the layered structure of grains in the Y_2O_3 -based laser ceramics [15]. The morphological analysis of the AFM image in Fig. 2.2.2a allows us to suppose that the mechanism of the LCOF formation is based on twinning.

Thus, abnormally high toughness of polycrystalline optical fluorite from Suranskoe Deposit (the South Ural) was found. Our investigation proved that one of advantages of ceramics in comparison with single crystals is the better mechanical properties, which is important for further research in the field of laser ceramics technology.

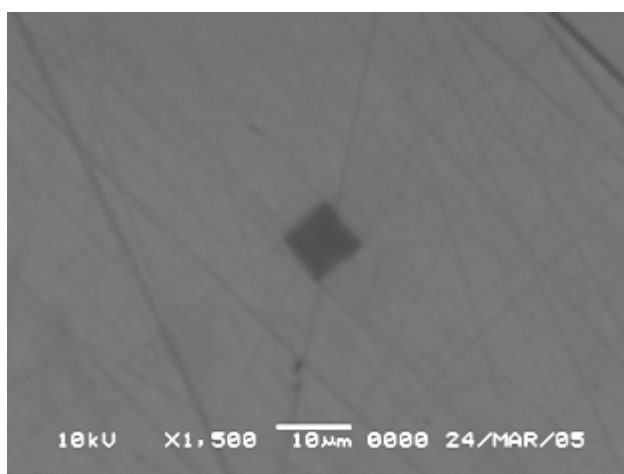
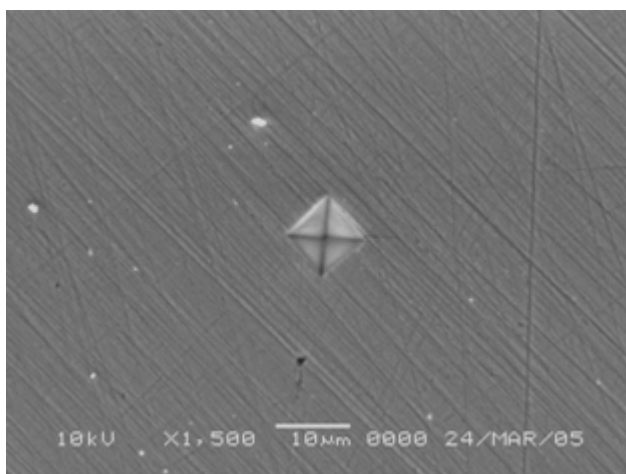


a)



b)

Fig. 2.2.2. AFM images of (a) a break in the SCOF sample and (b) the fine structure of separate grains on the SCOF surface after chemical etching.



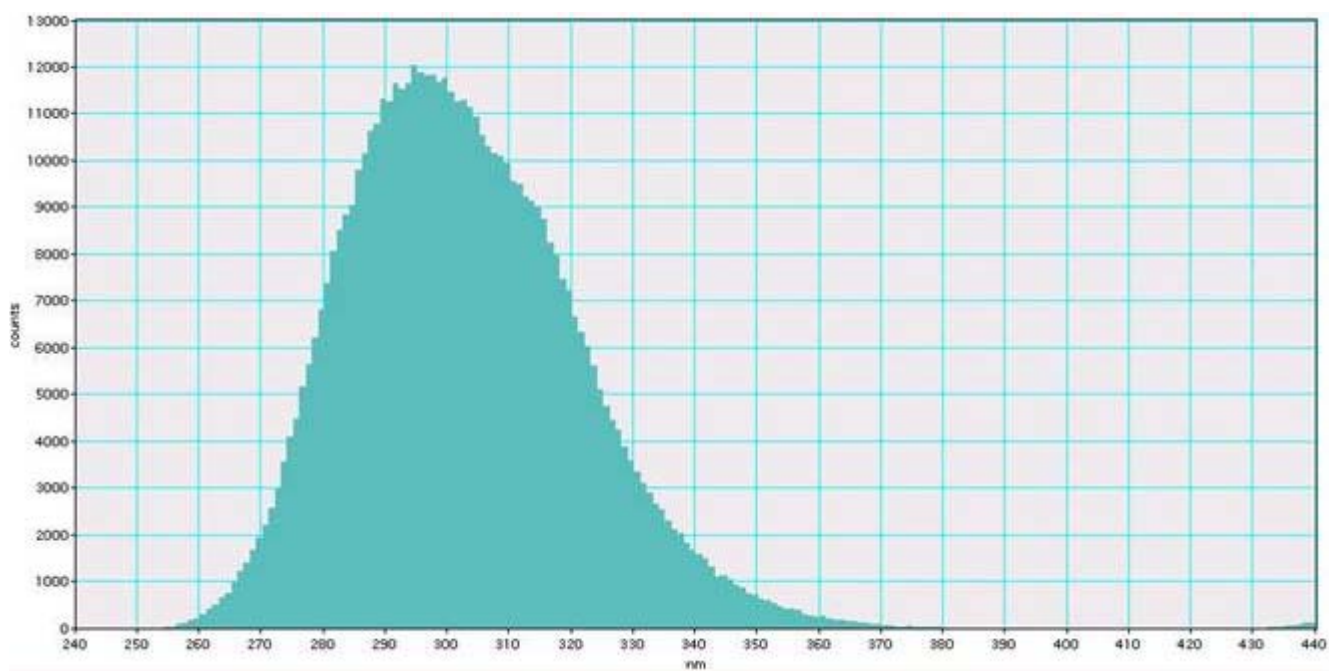


Fig. 2.2.3. Impressions of the indenter on the polished surface of the SCOF sample, observed in the regimes of (a) secondary electrons and (b) cathode luminescence. (c) CL Spectrum of a separate grain in the SCOF sample.

2.2.2 A $\text{CaF}_2:\text{Er}^{3+}$ fluoride ceramics

Fluoride ceramics $\text{CaF}_2:\text{ErF}_3$ (5 mol. %) have been prepared by hot-pressing process. CaF_2 and ErF_3 powders were used as initial reagents. CaF_2 high purity powder produced by “Stella” Corp. (Japan) was used. The electron microscopy of this powder is presented in Fig.

2.2.4

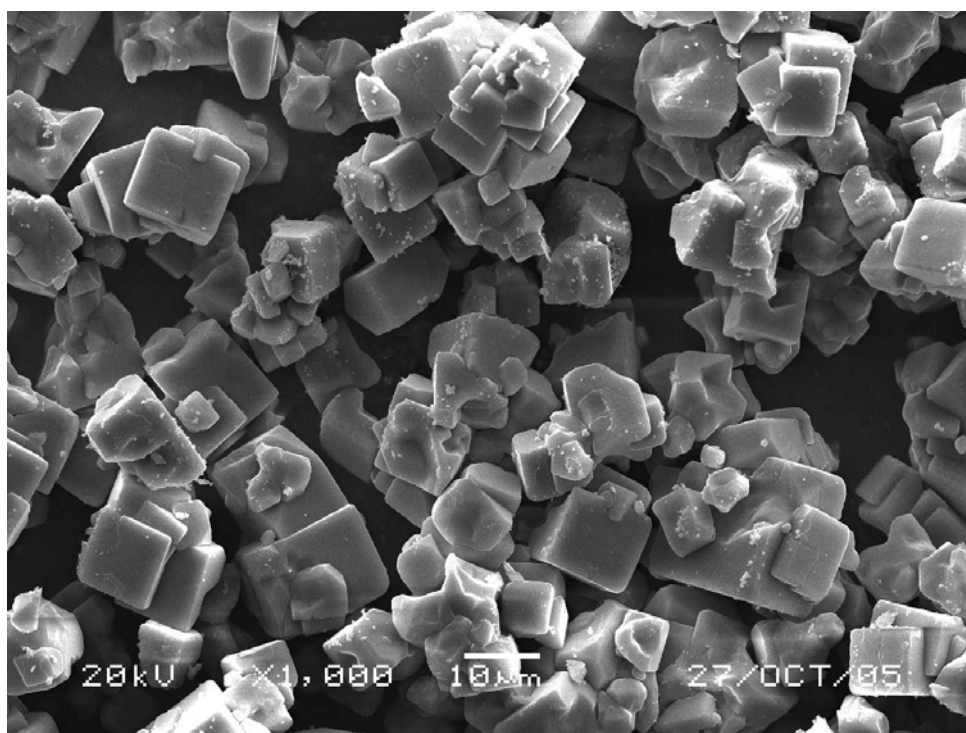


Fig.2.2.4. Electron microscopy of CaF_2 powder produced by corporation “Stella”, Japan.

The ErF_3 fluorides “chemical pure” grade was melted under reactive fluorinating CF_4 atmosphere in order to eliminate oxygen-containing impurities. The CaF_2 and ErF_3 powders were carefully mixed. Hot pressing process was carried out at 1100°C , 200 MPa, during 1 h. under vacuum $10^{-2} - 10^{-3}$ Torr.

For pure CaF_2 such process results in preparing of transparent ceramics (Fig.2.2.5). The mixture of CaF_2 and ErF_3 transforms into transparent, but inhomogeneous ceramics pellet (Fig. 2.2.6).

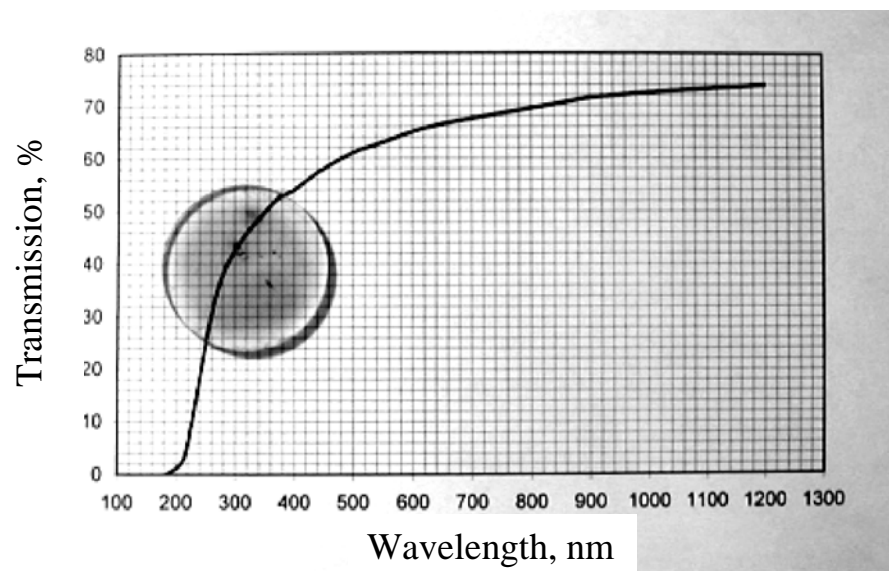


Fig. 2.2.5 CaF_2 hot- pressed ceramics (sample thickness 2 mm).

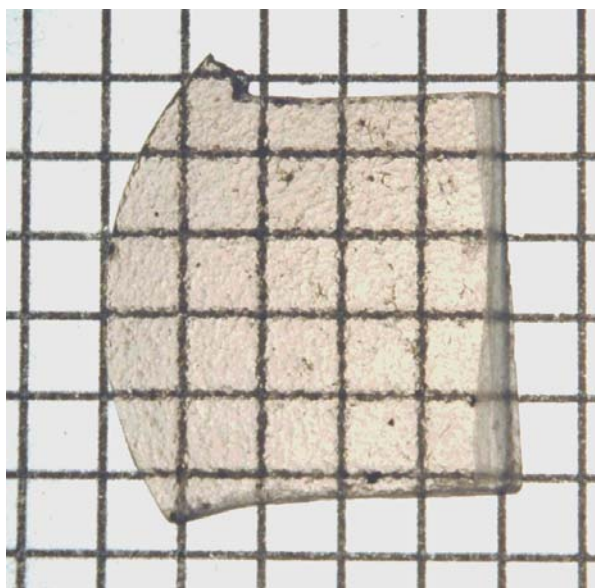


Fig.2.2.6. $\text{CaF}_2:\text{Er}^{3+}$ hot-pressed ceramics (sample thickness 2 mm).

X-ray diffraction data corresponds to fluorite-type structure with widening of reflexes. Electron microscopy (Fig. 2.2.7) reveals inhomogeneous distribution of Er^{3+} .

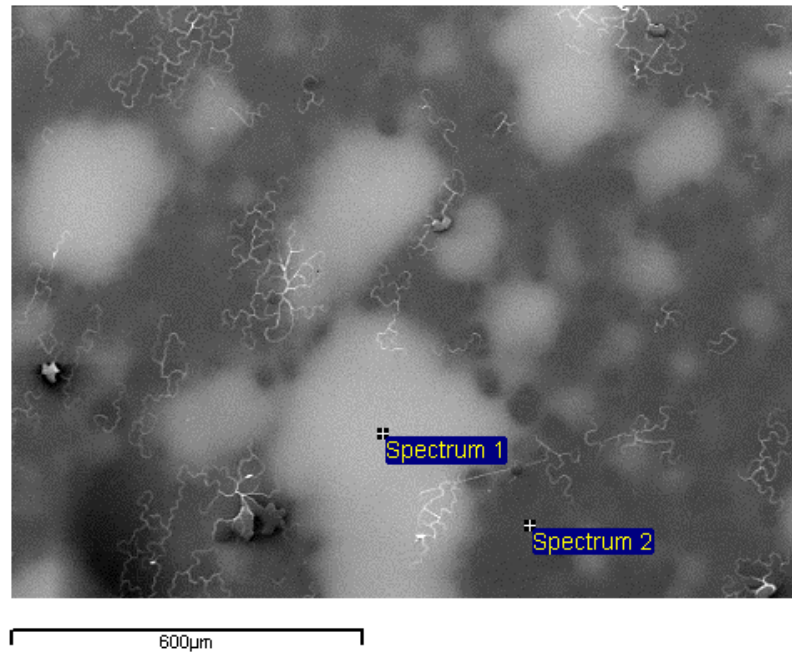


Fig. 2.2.7. Electron microscopy of $\text{CaF}_2:\text{Er}^{3+}$ hot-pressed ceramics in Er^{3+} emission.

The bright spots in the figure correspond to solid solution with high erbium concentration, while the dark spots correspond to lower calcium fluoride concentration. The picture corresponds to diffusion process of erbium fluoride into CaF_2 matrix. The characteristic distance of diffusion is about 50 μm . The difference in erbium concentration in solid solution $\text{Ca}_{1-x}\text{Er}_x\text{F}_{2+x}$ leads to variations of both cell parameters a , which reflects in the mechanical stresses and refraction index n , which gives rise to optical scattering.

For solid solution of $\text{Ca}_{1-x}\text{Er}_x\text{F}_{2+x}$ the following relations are known [Fedorov, 1991]:

$$a = 5.463 + 0.176x \text{ [\AA]},$$

$$n = 1.434 + 0.181x + 0.0285x^2.$$

where x is the molar fraction of ErF_3 in solid solution.

The absorption spectra in the $\text{CaF}_2:\text{Er}^{3+}$ (5 mol. %) ceramic sample were measured at $T=300 \text{ K}$ in the visible and near IR spectral ranges using Shimadzu UV – 3101 PC UV – VIS – NIR spectrometer (Fig. 2.2.8). High value of the absorption coefficient ($k = 2.6 \text{ cm}^{-1}$) for the laser diode pumping at 980 nm was obtained.

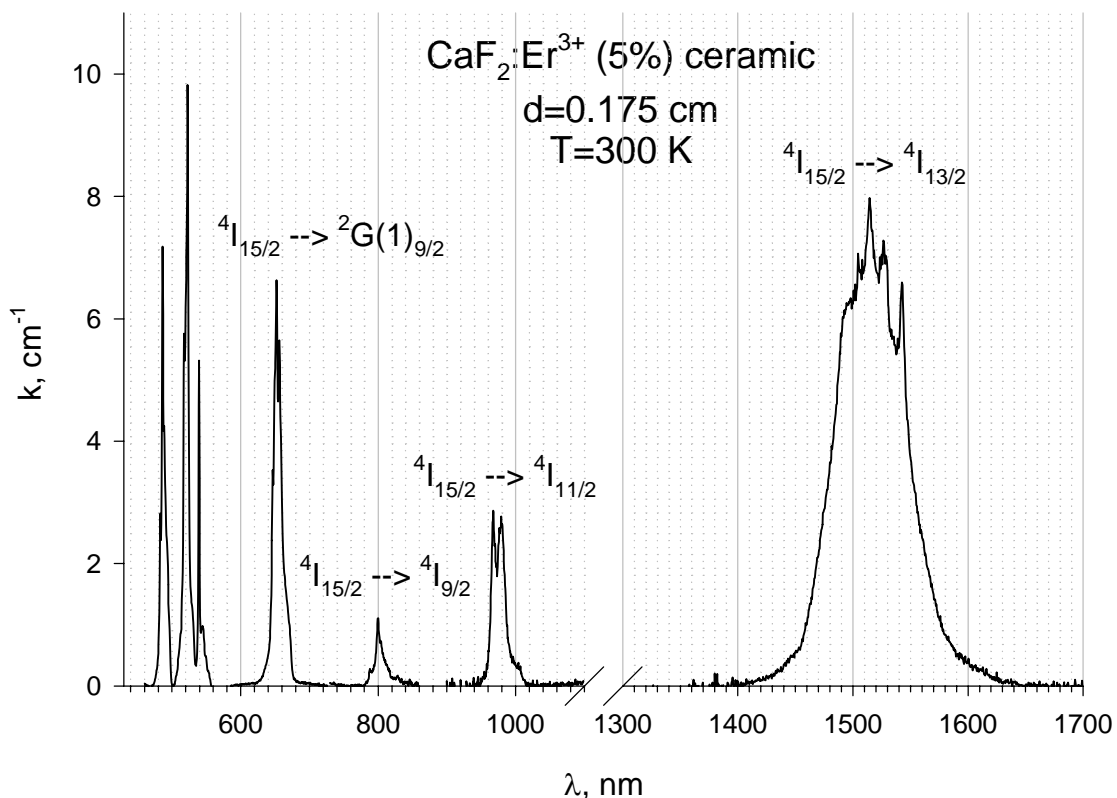


Fig. 2.2.8. Absorption spectra in the $\text{CaF}_2:\text{Er}^{3+}$ (5%) ceramic sample measured at $T=300$ K.

Fluorescence spectrum at the $^4\text{I}_{11/2} \rightarrow ^4\text{I}_{15/2}$ transition was measured under 810 nm CW laser excitation at $T=300$ K in the $\text{CaF}_2:\text{Er}^{3+}$ (5 mol. %) ceramic sample and the powdered ceramic sample (Fig. 2.2.9a). Comparison of the fluorescence spectra in the ceramics and in the $\text{CaF}_2:\text{Er}^{3+}$ (5 %) crystal (Fig. 2.2.9a) shows small spectral shift and some variation in spectral shape in the $\text{CaF}_2:\text{Er}^{3+}$ (5 mol. %) ceramic sample, but the difference is not significant. There is no any difference observed in spectral shape for the ceramic sample and the powdered ceramics prepared from a part of ceramic sample, which is an indication of no fluorescence trapping.

Fluorescence kinetics decay of the $^4\text{I}_{11/2}$ manifold was measured under 987 nm pulsed $\text{LiF}: \text{F}_2 \rightarrow \text{F}_2^+$ laser excitation and 980 nm detection in the $\text{CaF}_2:\text{Er}^{3+}$ (5 %) and $\text{CaF}_2:\text{Er}^{3+}$ (10 %) crystal, 977.5 nm laser excitation and 974 nm detection in the $\text{CaF}_2:\text{Er}^{3+}$ (5 mol. %) ceramic sample and the powdered ceramic sample, and 968 nm laser excitation and 981.5 nm detection in the ErF_3 raw material (Fig. 2.2.9b).

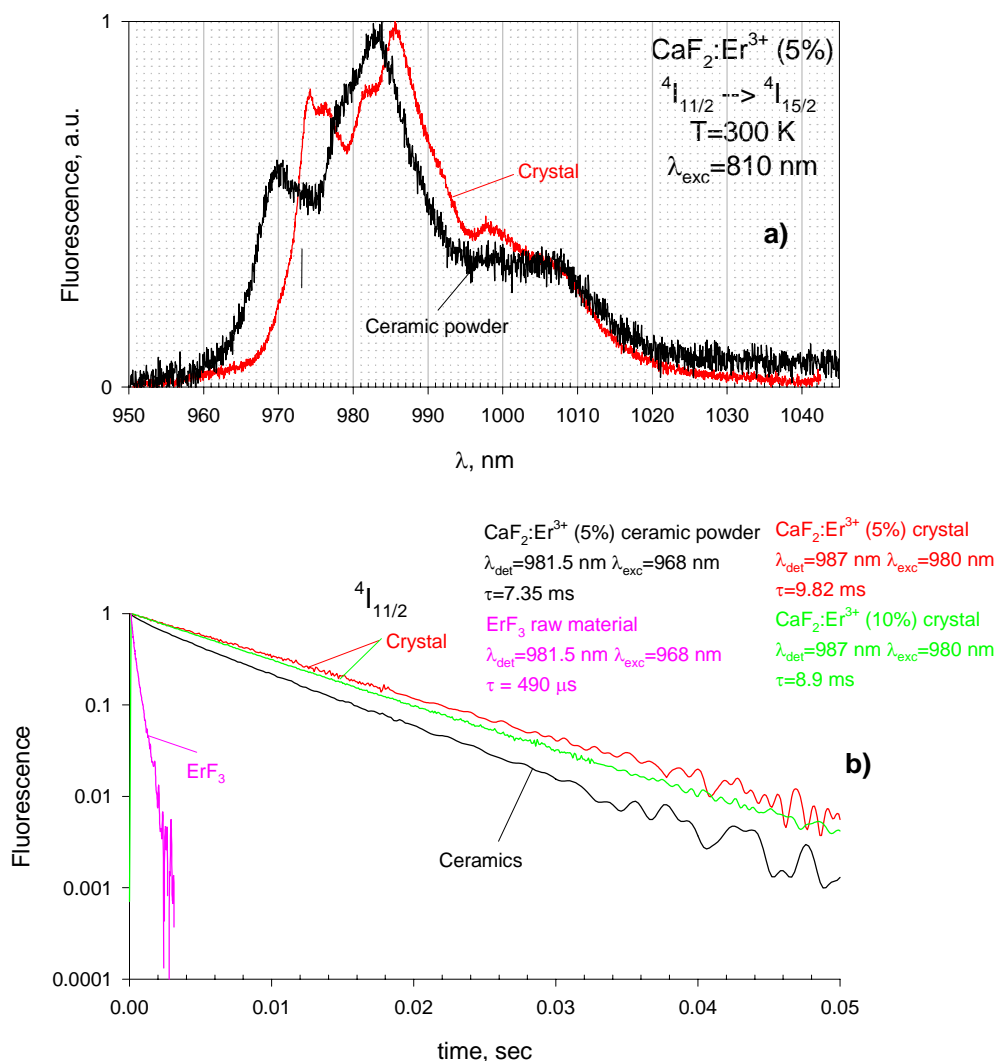


Fig. 2.2.9. Fluorescence spectra at the $^4I_{11/2} \rightarrow ^4I_{15/2}$ transition measured under 810 CW laser excitation – a, and kinetics decay of the $^4I_{11/2}$ manifold measured under pulsed laser excitation – b in the ErF_3 raw material (pink), in the $\text{CaF}_2:\text{Er}^{3+}$ (5%) ceramic sample (black), in the $\text{CaF}_2:\text{Er}^{3+}$ (5%) crystal (red) and $\text{CaF}_2:\text{Er}^{3+}$ (10%) crystal (green) at $T=300$ K.

As was stated before the electron microscopy of the $\text{CaF}_2:\text{Er}^{3+}$ (5 mol. %) ceramic sample shows that the areas exist, where the Er^{3+} ions concentration is higher (brighter areas) and where the concentration is smaller (darker areas) (Fig. 2.2.7). Strong acceleration of fluorescence decay was observed for ErF_3 raw material in comparison with the ceramic samples and especially with the crystals. No difference was found between ceramic sample and the powdered ceramics, which confirms the absence of fluorescence trapping. Acceleration of fluorescence kinetics decay can be explained with the fluorescence quenching by uncontrolled impurities as a result of direct transfer and/or energy migration over the donors (Er^{3+} ions). Analysis of the disordered stage of energy transfer kinetics for ceramics and ErF_3 powder gives us the sum of

two mechanisms of interaction between the energy donors (erbium ions) and the acceptors (uncontrolled impurities), i.e. quadrupole – quadrupole and dipole- quadrupole. In frame of just one of the mechanisms of donor – acceptor interaction we found the averaged relative concentration of erbium in the ceramics samples, considering 100 % concentration of Er^{3+} in ErF_3 . For $s = 10$ it is 14.4 % and for $s = 8$ it is 10.9 %. This is more than two times higher than in the raw materials for the ceramic samples and in agreement with the results of electron microscopy.

Fluorescence spectrum at the $^4\text{I}_{13/2} \rightarrow ^4\text{I}_{15/2}$ transition in the $\text{CaF}_2:\text{Er}^{3+}$ (5 mol. %) ceramics was measured under 810 nm CW laser excitation (Fig. 2.2.10a). Fluorescence kinetics decay of the $^4\text{I}_{13/2}$ manifold in this sample was measured by pulsed $\text{LiF}:\text{F}_2 \rightarrow \text{F}_2^+$ color centers laser excitation at 974 nm wavelength and 1.53 μm detection at $T=300$ K (Fig. 2.2.10b). A build - up of the fluorescence is observed with the duration of 6 ms. Fluorescence kinetics decay at the long time scale is exponential with the decay time $\tau_{\text{final}} = 15.7$ ms. The powdered ceramic sample exhibits exponential decay with $\tau = 6.7$ ms which is ~ 3 times shorter than for the ceramic sample and indicates the fluorescence trapping for the latter one.

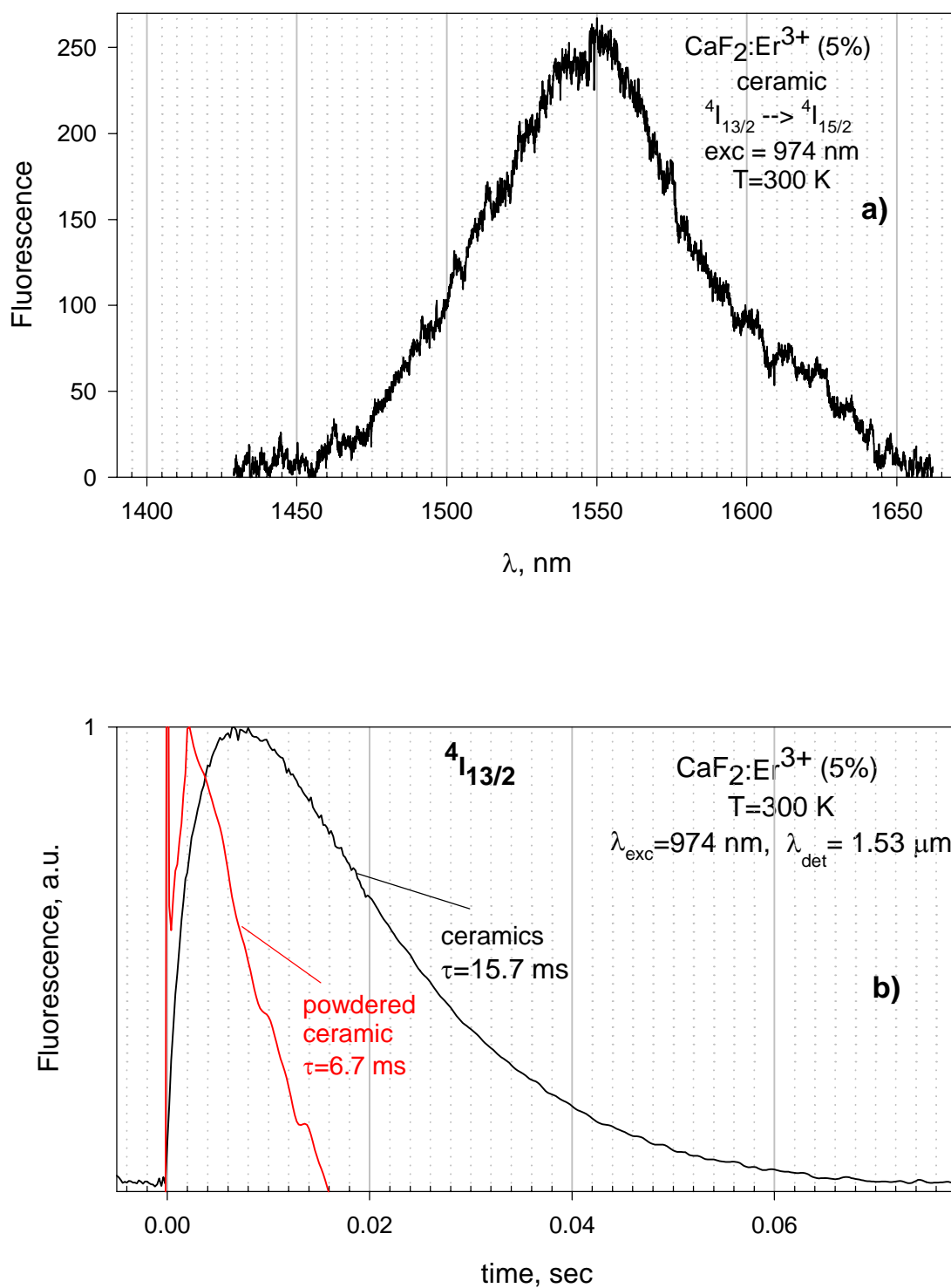


Fig. 2.2.10. Fluorescence spectra at the $^4\text{I}_{13/2} \rightarrow ^4\text{I}_{15/2}$ transition measured under 810 CW laser excitation – a, and kinetics decay of the $^4\text{I}_{13/2}$ manifold – b measured under 980 nm pulsed laser excitation in the $\text{CaF}_2:\text{Er}^{3+}$ (5%) ceramic sample and the powdered ceramic sample at $T=300\text{ K}$.

References

1. Volynets F.K.//Optical-mechanical Industry. 1973. № 9. P. 48 – 60 (in Russian)
2. Yanagitani T., Yagi H. /Japanese Patent 10-101333. 1998
3. Kaminskii A.A., Eichler H.J., Ueda K. et al.// Phys. Status Solidi (a). 2000. V.181. № 2 P. R19
4. Kaminskii A.A., Akchurin M.Sh., Alshits V.I., e.a.// Crystallography Reports 2003. V.48. № 3. P. 562-566(in Russian)
5. Carnall Jr., Hatch S.E., Parson W.F. Materials Science Research. Ed. W.W.Kriegel, H. Palmor. Plenum Press, N.Y. 1966. V.3
6. Smolyansky P.L., Nastasienko E.V., Malakhov D.A. // In:”Mineralogy, Crystallography , Syktyvkar: KOMI Acad.Sci.. 1990. P. 58-59(in Russian)
7. Smolyansky P.L. // Zapiski VMO. 2003. № 4. P. 96-112 (in Russian)
8. Krupenin M.T., Meller P., Dul’ski P. // Geochemistry, 1999. №11. P. 1165-1177 (in Russian)
9. Smolyansky P.L.. // Zapiski VMO.. 2002. № 4. C. 70-84(in Russian)
10. Lan B.R., Evans A.G., Marshall D.B. // J. Amer. Ceram. Soc. 1980. V. 63. № 2. P. 576
11. Voronkova E.M., Grechushnikov V.M., Distler G.I., Petrov I.P. Optical IR Materials. M.: Nauka. 1965. (in Russian)
12. Enomoto Y., Yamanaka K.// Mater. Sci. 1982. V.17. P. 3288 - 3292
13. Akchurin M.Sh., Regel V.R.// Chem. Rev. 1998. V. 23. P. 59
14. Rebinder A.P.// Proc. Acad. Sci. USSR. 1936. V.5.P. 639(in Russian)
15. Kaminskii A.A., Akchurin M.Sh., Gainutdiniv R.V., e.a.// Crystallography Reports. 2005. V.50. (in Russian)

3.1 Comparative study Yb-lasers and LiF:F_2^- color center laser under LD pumping

3.1.1. Introduction

In the frames of the research project the comparative study of the Yb-doped crystals and LiF crystal with F_2^- color centers have been carried out. The spectroscopic characterization of the crystals has included absorption and luminescence spectroscopy of the pump and laser transitions, and luminescence lifetime measurements.

Important feature of the $\text{Yb}^{3+}:\text{PbMoO}_4$ crystal is a short radiative lifetime (210 μs , one of the smallest among known Yb-doped crystals). Another interesting property of $\text{Yb}^{3+}:\text{PbMoO}_4$ crystal is low quantum defect and flat-top shape of the fluorescence spectrum. This feature is important for realization of laser wavelength tuning as well as for short-pulse laser oscillations. The $\text{Yb}^{3+}:\text{CaF}_2$ fluoride crystal is currently considered as one of the most promising laser materials for LD pumping near 970 nm wavelength. In contrast with $\text{Yb}^{3+}:\text{PbMoO}_4$ crystal, the $\text{Yb}^{3+}:\text{CaF}_2$ crystal demonstrates one of longest lifetimes of $^2\text{F}_{5/2}$ excited Yb^{3+} level, which is as long as 2500 μs .

The LiF crystal with F_2^- color centers is a new laser medium for LD pumped lasers. Main advantages of the LiF:F_2^- crystal as a medium for high-power lasers are broad band luminescence and absorption in near-IR (line widths about 140 nm), very high absorption and stimulated emission cross sections ($7 \cdot 10^{-17} \text{ cm}^2$), high thermal conductivity ($14 \text{ W} \cdot \text{m}^{-1} \cdot \text{K}^{-1}$ at 300 K, even higher than that of YAG crystal), availability of large size crystal samples (up to $\varnothing 400 \times 200 \text{ mm}$).

The laser characteristics of the Yb-doped and LiF:F_2^- crystals were evaluated using computed simulation. Mathematical model of two-manifold LD pumped laser was developed on a basis of rate equations for the laser medium and transport equations for the radiation. The mathematical model is described and results of the crystals comparative evaluation are presented in the section 3.1.2 of the report.

The results of the laser experiments with Yb-doped crystals are presented in the section 3.1.3. In the section 3.1.4 the laser characteristics of the LiF:F_2^- color center crystals are discussed in detail and experimental results on the LD pumped LiF:F_2^- crystal laser oscillations are presented. To our knowledge, the QCW and CW lasing of LiF:F_2^- crystal under direct LD pumping have been demonstrated for the first time.

3.1.2. Comparative study of laser characteristics of Yb-doped crystals and LiF:F_2^- under LD pumping

Mathematical model of two-manifold LD pumped laser

The standard approach to the modeling of various kinds of lasers is use of rate equations for the laser medium and transport equations for the radiation. A number of models of a two-manifold laser including rather rigorous have been discussed in the literature [1, 2, 3]. For our analysis we will use a simplified model based on a following assumptions:

- Use of steady state approximation
- Averaging of the radiation and the laser medium parameters over transverse cross-section of the laser beam. Thus, two-dimensional problem for one spatial co-ordinate and the time will be solved.
- Pump and laser radiation will be considered in terms of photon fluxes.

Schematic of two-manifold system is shown in the Fig. 3.1-1. The pump photon $h\nu_p$ absorption causes the transition from lower manifold with population N_0 to upper manifold with population N_1 . Lasing occurs between (1) and (0') sublevels of upper and lower manifolds. The upper manifold spontaneously decays with the characteristic time τ . Thermalization within manifolds occurs in picosecond timescale and populations of the 0' and 1' laser levels are given by

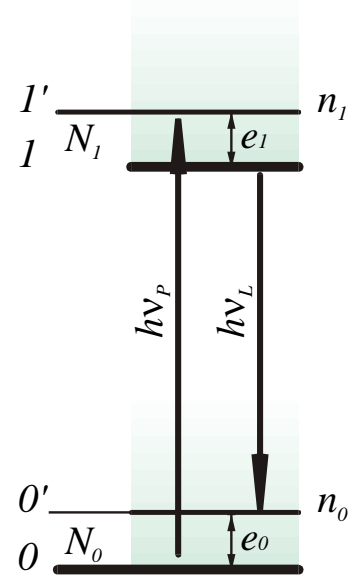


Fig. 3.1-1

$$\begin{aligned} n_0 &\sim N_0 \cdot \exp(-e_0/kT) \\ n_1 &\sim N_1 \cdot \exp(-e_1/kT) \end{aligned} \quad (1)$$

where $e_{0,1}$ are energies of the levels, k is the Boltzman factor, and T is the temperature. If $e_{0,1} \sim kT$, then the stimulated emission at the pump wavelength and ground state absorption at the laser wavelength have to be taken into account. Thus, one can write out the rate equations for the laser crystal in the following form:

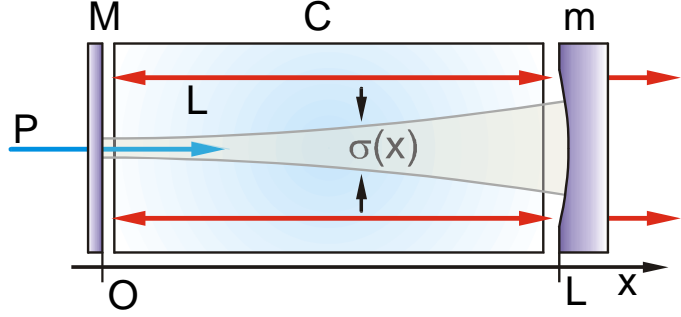


Fig. 3.1-2

$$\frac{dN_1}{dt} = (N_0\sigma_P^{(a)} - N_1\sigma_P^{(e)})F_P + (N_0\sigma_L^{(a)} - N_1\sigma_L^{(e)})F_L - \frac{N_1}{\tau}, \quad (2)$$

$$N = N_1 + N_0 = \text{const}$$

where N_0 and N_1 are levels populations [cm^{-3}]; N is the active centers concentrations in the laser crystal [cm^{-3}]; F_P , F_L are the pump or laser photon fluxes [$\text{photon} \cdot \text{s}^{-1} \cdot \text{cm}^{-2}$]; $\sigma_{P,L}^{(a)}$, $\sigma_{P,L}^{(e)}$ are the absorption and emission effective cross sections at pump and laser wavelengths [cm^2]; τ is the characteristic time of spontaneous emission [s].

Schematic of the laser is illustrated in the Fig. 3.1-2. The flat mirror M and concave mirror m form the laser cavity. The laser crystal C is pumped through the dichroic mirror M . We assume that the pump beam distribution matches perfectly the laser mode spatial distribution. The variation of the laser beam transverse size along the laser cavity could affect considerably at the radiation intensity and hence at the laser output parameters. The “geometrical” constituent of phonons flux variation could be expressed in a following form:

$$\frac{\partial^{(Geom)}}{\partial x} F = -F \frac{\sigma'(x)}{\sigma(x)} = -F \cdot \Sigma(x), \quad (3)$$

where $\sigma(x)$ is the beam cross-section area (see Fig. 3.1-2).

The transport equations, which describe the evolution of the pump and laser photon fluxes in the laser cavity, are following:

$$\begin{aligned}
\left(\frac{1}{c} \frac{\partial}{\partial t} + \frac{\partial}{\partial x}\right) F_p &= \left(-N_0 \sigma_p^{(a)} + N_1 \sigma_p^{(e)} - k\right) F_p - \Sigma F_p \\
\left(\frac{1}{c} \frac{\partial}{\partial t} \pm \frac{\partial}{\partial x}\right) F_L^\pm &= \left(-N_0 \sigma_L^{(a)} + N_1 \sigma_L^{(e)} - k\right) F_L^\pm + \omega \frac{N_1}{\tau} \mp \Sigma F_L^\pm
\end{aligned} \tag{4}$$

Where F_p is the pump photon flux in positive direction [$\text{photon} \cdot \text{s}^{-1} \cdot \text{cm}^{-2}$]; F_L^\pm are laser photon fluxes in positive and negative directions [$\text{photon} \cdot \text{s}^{-1} \cdot \text{cm}^{-2}$]; k is the parasitic losses in the laser crystal [cm^{-1}]; ω is the spontaneous seeds for laser oscillations; c is the light velocity [$\text{cm} \cdot \text{s}^{-1}$]. Symbol F_L in the rate equations (2) denotes the total laser intensity in both directions $F_L = F_L^+ + F_L^-$. Relations between positively and negatively directed photon fluxes are given by boundary conditions at the laser cavity mirrors:

$$\begin{aligned}
F_L^+(x=0) &= F_L^-(x=0) \\
F_L^-(x=L) &= R F_L^+(x=L) \\
F_p(x=0) &= F_p^{(0)}
\end{aligned} \tag{5}$$

where R is the output mirror m reflectivity; L is the laser crystal (cavity) length [cm] and $F_p^{(0)}$ is the pump photons flux at the input crystal end [$\text{photon} \cdot \text{s}^{-1} \cdot \text{cm}^{-2}$].

In steady state approximation the rate equation (2) could be resolved algebraically and substituted in to transport equations (4) this yields to the following form of equations, which describe the two manifold laser:

$$\begin{aligned}
\frac{df_p}{dx} &= +D \left(-G f_L^{(\Sigma)} - G_0 - df_p \right) - \Sigma f_p \\
\frac{df_L^\pm}{dx} &= \pm D \left(+G f_L^\pm + \omega G_0 - df_L^\pm \right) - \Sigma f_L^\pm \\
f_p(0) &= 1 \quad \begin{aligned} f_L^-(0)/f_L^+(0) &= 1 \\ f_L^-(L)/f_L^+(L) &= R \end{aligned}
\end{aligned} \tag{6}$$

where following nondimensional variables and designations were introduced:

$$\begin{aligned}
G &= \frac{(\tilde{s}\sigma - s\tilde{\sigma})f_p - sf_0}{\tilde{\sigma}f_p + \sigma f_L^{(\Sigma)} + f_0} & G_0 &= \frac{(\tilde{s}f_p + sf_L^{(\Sigma)})f_0}{\tilde{\sigma}f_p + \sigma f_L^{(\Sigma)} + f_0} \\
f_p &= F_p/F_p^{(0)} & f_L^{\pm} &= F_L^{\pm}/F_p^{(0)} & f_L^{(\Sigma)} &= f_L^+ + f_L^- \\
D &= N\sigma_L^{(e)} & d &= k/N\sigma_L^{(e)} & f_0 &= 1/F_p^{(0)}\tau\sigma_L^{(e)} \\
\sigma &= \frac{(\sigma_L^{(a)} + \sigma_L^{(e)})}{\sigma_L^{(e)}} & s &= \frac{\sigma_L^{(a)}}{\sigma_L^{(e)}} & \tilde{\sigma} &= \frac{(\sigma_p^{(a)} + \sigma_p^{(e)})}{\sigma_L^{(e)}} & \tilde{s} &= \frac{\sigma_p^{(a)}}{\sigma_L^{(e)}}
\end{aligned} \tag{7}$$

Here terms G and G_0 comprise effective steady state gain and saturation of the pump transition, term d represents the parasitic losses and the variable Σ describes “geometrics” of the laser (we suppose it is the same for the pump and laser fields).

The Fig. 3.1-3 illustrates the approximation that we have used to describe the variation of the pump beam transverse size along propagation for the case of fiber coupled LD pumping. The output of the fiber F with the core radius r_0 and numerical aperture N.A. is focused by lens appliance L to the spot with the radius r . At that the geometrical divergence of resulting beam changes in direct proportion to the r_0/r ratio. The beam size variation in vicinity of the focal point and the term Σ in equations (6) could be described by hyperbolic functions as following:

$$\begin{aligned}
\sigma(x) &= \pi(kx)^2 + \pi r^2 \\
\Sigma(x) &= \frac{\sigma'(x)}{\sigma(x)} = \frac{2x}{x^2 + r^2/k^2} \quad , \\
k &= \tan \alpha \approx \sin \alpha = N.A. \times (r_0/r)
\end{aligned} \tag{8}$$

where $x = 0$ corresponds to the waist position. From the (8) could be also derived an expression for the waist radius $r^{(\text{opt})}$ that corresponds to the most intensive pumping of the crystal with the thickness L :

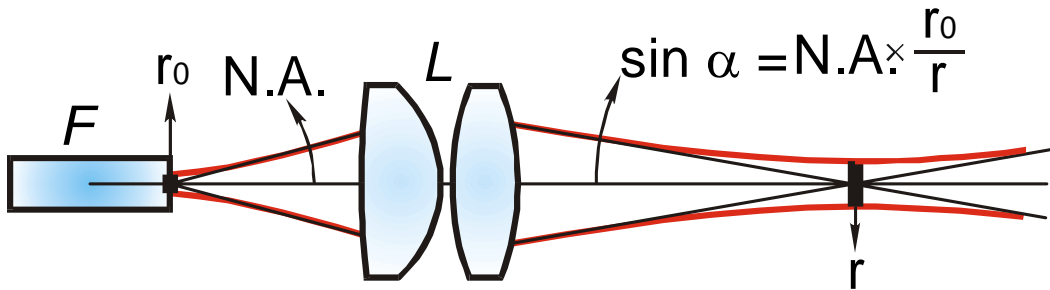


Fig. 3.1-3

$$\frac{d}{dr} \left(\int_0^L \sigma(x) dx \right) = 0 \Rightarrow r^{(opt)} = \sqrt{(N.A.) r_0 L / \sqrt{3}}. \quad (9)$$

As an illustration in the Fig. 3.1-3 are shown pump distributions near the focal point for 100 μ fiber with numerical aperture of 0.16. As follows from the figure, the optimal pump spot size for 3 mm thick crystal is approximately 2.5 times larger than the fiber core diameter.

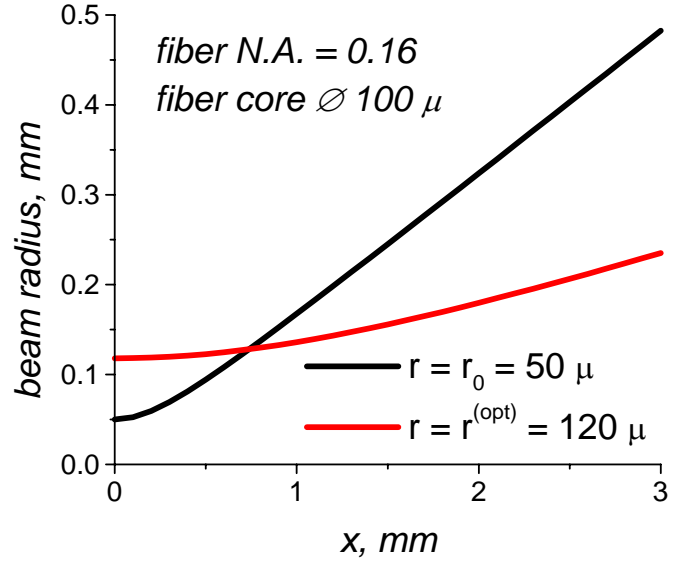


Fig. 3.1-4

Comparative study Yb-lasers and LiF : F₂⁻ color center lasers under LD pumping

The developed mathematical model of two-manifold laser was used for evaluation of new gain media for LD pumped lasers with LD emission wavelength between 900 and 1000 nm. The evaluation was made for two host crystals CaF₂ and PbMoO₄ doped with Yb³⁺ ions. Besides, we have included in our study the LiF crystal with F₂⁻ color centers since the recent progress in development of high power high brightness LD pump sources allows considering this material as a very potential for LD pumped laser applications. To make comparisons, the same modeling and optimizations were carried out for well known Yb³⁺ : YAG and Yb³⁺ : KYW laser crystals.

The standard starting point for laser medium evaluation is extraction of some key laser parameters from the spectroscopic data (absorption and emission cross-sections and radiative lifetime). This is especially useful since the Yb-based lasers as well as color center lasers are subject to quasi-three-level pumping and lasing constraints.

There are several figures of merit for quasi-three-level medium. Among these the maximum extraction efficiency

$$f^{(\max)}(\lambda) = \frac{\sigma_L^{(e)}}{\sigma_L^{(e)} - \sigma_L^{(a)}} \quad (10)$$

or maximum fraction of stored energy that can be extracted under most favorable conditions. The saturation intensity parameter

$$I_P^{(sat)} = \frac{hc}{\lambda_P} \frac{1}{\tau \sigma_P^{(a)}} \quad (11)$$

depicts the ratio between the accumulation of the populations inversion in the laser medium and spontaneous decay of the upper laser level. In quasi three-level systems the substantial excited state population is required in order to achieve the gain, which overwhelms the ground state absorption losses at laser transition. This could be described by the “minimum pump intensity parameter” $I_P^{(\min)}$ specifying pump intensity needed (in each point of the laser medium) to achieve the laser threshold in a lossless oscillator [4].

$$I_P^{(\min)} = I_P^{(sat)} \frac{\sigma_L^{(a)}}{\sigma_L^{(e)} + \sigma_L^{(a)}}. \quad (12)$$

Another useful parameter for quasi-three-level medium evaluation is the effective gain cross-section $\sigma^{(gain)}$, which is defined by formula:

$$\sigma^{(gain)}(\lambda) = n\sigma^{(e)}(\lambda) - (1-n)\sigma^{(a)}(\lambda), \quad (13)$$

where $\sigma^{(e)}$ and $\sigma^{(a)}$ are absorption and emission cross-sections at the specific wavelength and $n = N_1/N$ is the populations inversion (fraction of excited laser centers). The expression for the populations inversion in steady state approximation could be derived from the rate equations (2) as following:

$$n = \left(\frac{\sigma_P^{(a)} + \sigma_P^{(e)}}{\sigma_P^{(a)}} + \frac{I_P^{(sat)}}{I_P} \right)^{-1}, \quad (14)$$

where $I_P^{(sat)}/I_P$ is the ratio of saturation intensity (see (11)) to the pump intensity. The gain cross-section parameter comprises as the quasi-three-level characteristics of the medium (stimulated emission at the pump wavelength and ground state absorption at the laser wavelength) as well as the pump transition saturation. Thus, for given pumping conditions (wavelength λ_P and intensity I_P) both the laser tuning range and laser medium gain could be simultaneously estimated.

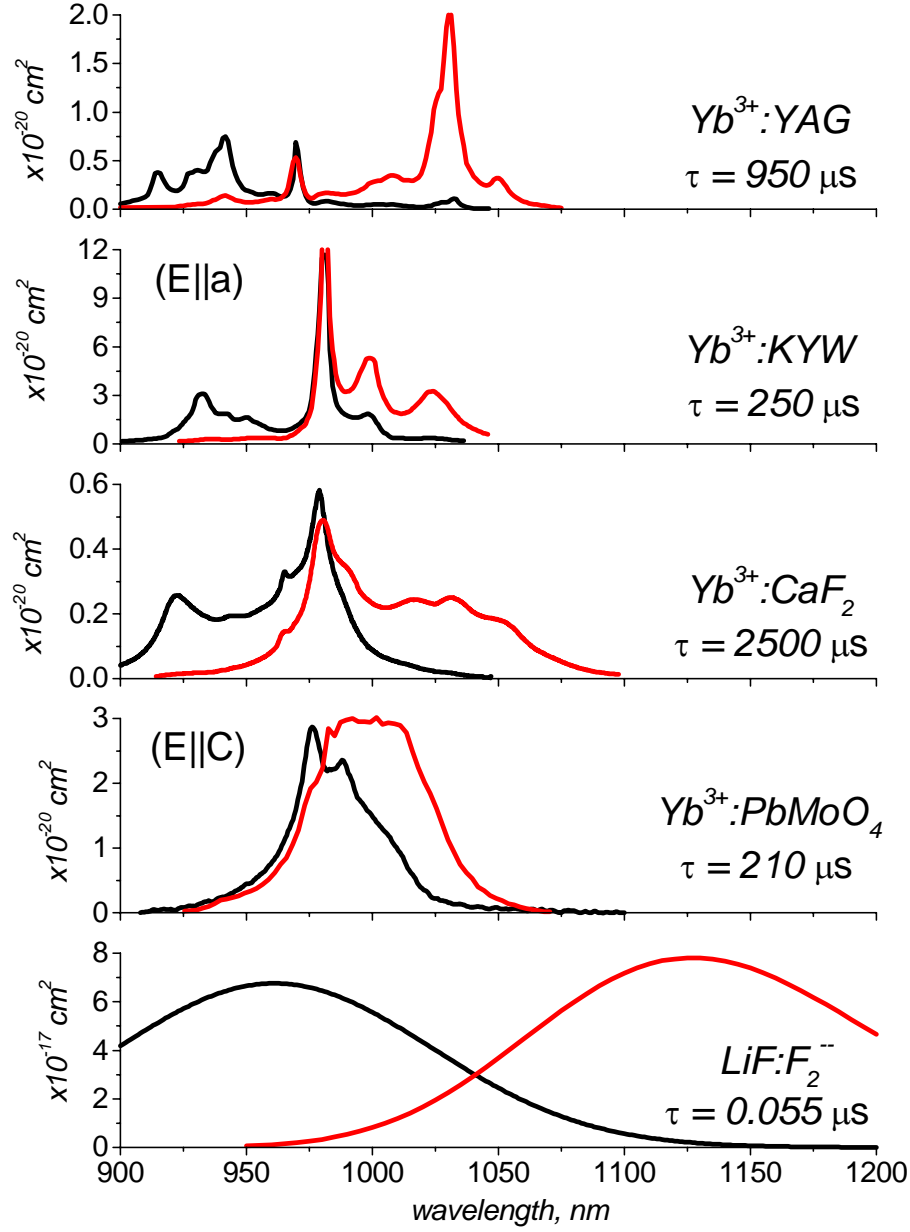


Fig. 3.1-5

The spectroscopic parameters of $\text{Yb}^{3+}:\text{YAG}$, $\text{Yb}^{3+}:\text{KYW}$, $\text{Yb}^{3+}:\text{CaF}_2$, $\text{Yb}^{3+}:\text{PbMoO}_4$, and LiF:F_2^- compared in the Fig. 3.1-5. In the figure are shown the room-temperature absorption (black lines) and emission (red lines) cross-section spectra and radiative lifetimes. The spectral data for $\text{Yb}^{3+}:\text{YAG}$ and $\text{Yb}^{3+}:\text{KYW}$ crystals were acquired from the papers [4, 5]. Measurements of absorption and emission cross-section spectra and radiative lifetimes for $\text{Yb}^{3+}:\text{CaF}_2$, $\text{Yb}^{3+}:\text{PbMoO}_4$, and LiF:F_2^- crystals were carried out in LMTRC.

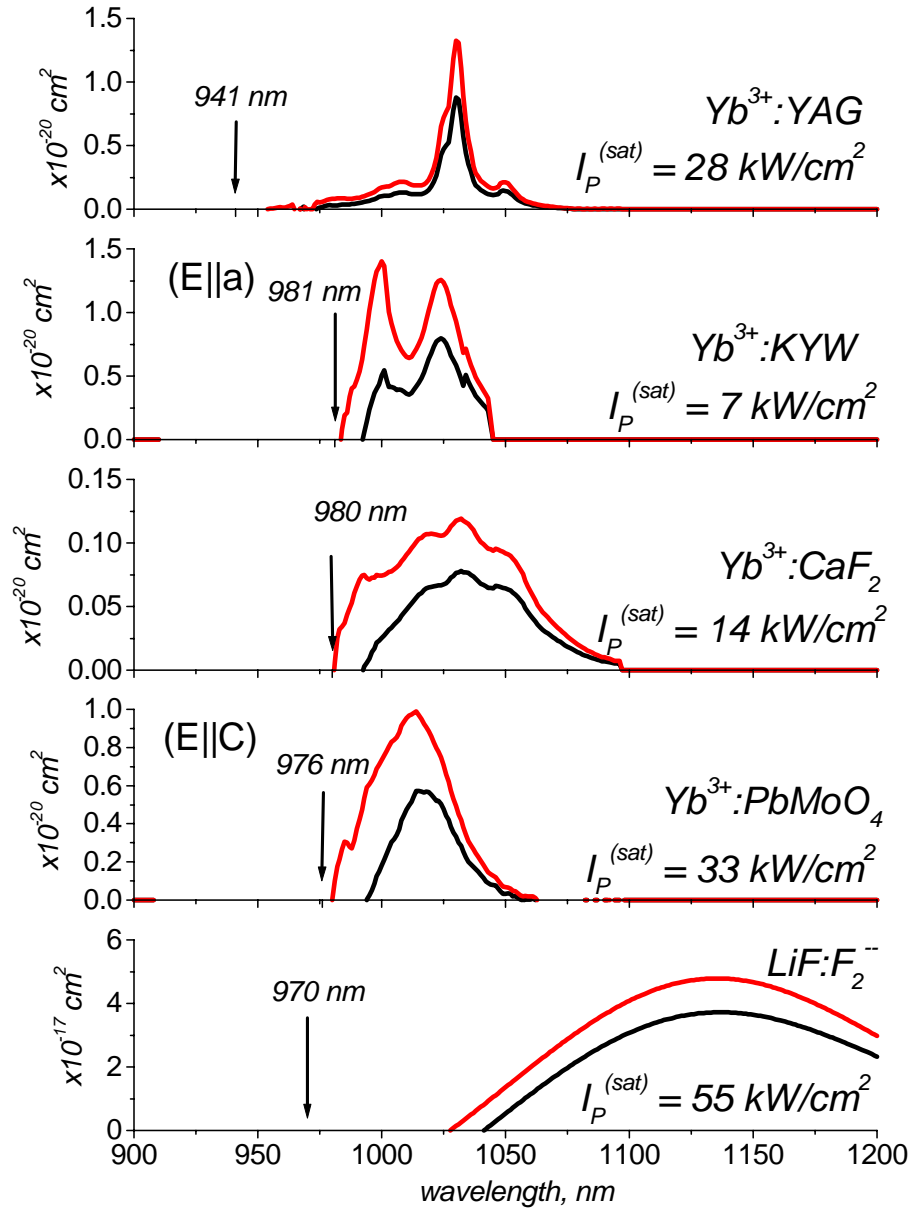


Fig. 3.1-6

Common feature for $\text{Yb}^{3+}:\text{CaF}_2$ fluoride and $\text{Yb}^{3+}:\text{PbMoO}_4$ oxide crystals is a broad and smooth emission spectra that correspond to the multi-site, inhomogeneous broadening nature of these laser mediums. The $\text{Yb}^{3+}:\text{CaF}_2$ crystal has a longest lifetime of 2500 μs and lowest peak cross-sections, while the $\text{Yb}^{3+}:\text{PbMoO}_4$ crystal demonstrates record short lifetime (210 μs) and cross-sections comparable with these of $\text{Yb}^{3+}:\text{YAG}$ and $\text{Yb}^{3+}:\text{KYW}$.

The $\text{LiF}:\text{F}_2^-$ color center crystal exhibits essentially different characteristics in comparison with Yb-based laser materials. It has three – for orders of magnitude higher cross-

	YAG	KYW	CaF ₂	PbMoO ₄	LiF:F ₂ ⁻
Pump wavelength, nm	941	981	980	976	970
Pump transition cross section, $\times 10^{-20} \text{ cm}^2$	0.8	12	0.58	2.9	6800
Radiative lifetime, μs	950	250	2500	210	0.055
Pump saturation intensity, kW/cm^2	28	7	14	33	55
Laser wavelength, nm	1030	1024	1034	1020	1135
Laser transition cross section, $\times 10^{-20} \text{ cm}^2$	2.1	3.2	0.25	2.1	7800
Ground state absorption cross section, $\times 10^{-20} \text{ cm}^2$	0.12	0.3	0.014	0.4	140
Gain cross-section ($I_p = I_p^{(\text{sat})}$), $\times 10^{-20} \text{ cm}^2$	0.9	0.8	0.08	0.6	3700
$I^{(\text{min})}$, kW/cm^2	1.5	0.6	0.7	5.3	1.0

Table 1

sections and proportionally lower lifetime. Another important feature of the LiF:F₂⁻ crystal is very broad absorption and emission lines and large Stokes shift. This enables the use of LiF:F₂⁻ crystal as in quasi-four-level as well as in quasi-three-level laser schemes.

The gain cross-section spectra (see (13), (14)) were calculated for two pumping intensities $I_p = I_p^{(\text{sat})}$ and $I_p = 100 \text{ kW/cm}^2$ that is achievable for present-day LD modules. The pump wavelengths, which were used for calculations, have corresponded to the maximum pump absorption cross-sections. The gain cross-section spectra are shown in the Fig. 3.1-6. Black curves correspond to the $I_p = I_p^{(\text{sat})}$ pump intensity and red curves correspond to the $I_p = 100 \text{ kW/cm}^2$ pump intensity. Vertical arrows show the pump transition. Laser parameters of the crystals are summarized in the Table 1.

Relatively large shift between pump and laser wavelengths leads to the high gain cross-section of Yb³⁺:YAG crystal, which is only twice lower than the emission cross-section at the lasing wavelength. Pumping of Yb³⁺:KYW and other Yb-doped crystals in vicinity of the zero-phonon line results in much higher decrease of the gain cross-section with respect to the peak emission cross-section. In spite of very different properties of Yb³⁺:KYW and Yb³⁺:CaF₂ hosts these crystals have low saturation intensity and relatively low ground state absorption at the laser transition. As a result, the minimum pump intensity parameter $I_p^{(\text{min})}$ is smallest for Yb³⁺:KYW and Yb³⁺:CaF₂ crystals, besides very small shift between pump and laser wavelengths is achievable for these crystals at intensive pumping. The Yb³⁺:PbMoO₄ crystal has smallest radiative lifetime and high ground state absorption. This leads to the relatively small gain cross-section and to the high value of the minimum pump intensity parameter.

The LiF:F₂⁻ crystal has a large shift between absorption and emission lines. Therefore, at 970 nm LD pumping this medium tends to operate in quasi-four-level scheme with low ground

	YAG	KYW	CaF ₂	PbMoO ₄	LiF:F ₂ ⁻
LD pump type 1:	12 W, 100 μ fiber, N.A. = 0.16				
LD pump type 2:	12 W, 200 μ fiber, N.A. = 0.22				
Pump wavelength λ _p , nm	941	981	980	976	970
Laser wavelength λ _L , nm	1030	1024	t.	1023	t.
Pump absorption coefficient k _p , cm ⁻¹	o.	o.	o. (9)	o. (12)	2 or 4
Laser crystal length L _C , cm	0.3	0.3	0.3	0.3	o.
Minimum pump spot diameter d ₀ , μ	o.	o.	o.	o.	o.
Output coupler reflectivity R _{OC} , %	o.	o.	o.	o.	o.

Table 2

state absorption at laser transition and low stimulated emission at pump transition. In spite of nanosecond scale of radiative lifetime the LiF:F₂⁻ crystal has reasonable saturation intensity, which is only twice higher than that of Yb³⁺:YAG. As a result, the minimum pump intensity parameter for LiF:F₂⁻ crystal is surprisingly low (1 kW/cm² vs. 1.5 kW/cm² for Yb³⁺:YAG).

* * *

Further laser mediums evaluation was carried out using developed model of two-manifold laser. The laser parameters, which were used for modeling, are summarized in the Table 2. Two types of fiber coupled LD pump were considered. The first, high brightness LD pump with characteristics corresponding to the new IPG Laser GmbH PLD-10-975 module: the maximum power of 12 W, 100 μ fiber core diameter, fiber numerical aperture N.A. = 0.16, and maximum intensity about 100 kW/cm². The second, standard LD pump module with the output power of 12 W, 200 μ fiber core diameter, N.A. = 0.22, and maximum intensity of 40 kW/cm². Parameters of Yb³⁺:YAG, Yb³⁺:KYW and Yb³⁺:PbMoO₄ crystals were investigated for fixed wavelengths of laser operation, while for Yb³⁺:CaF₂ and LiF:F₂⁻ crystals the laser tuning ranges were also evaluated (symbols “t.” in the table).

The YAG and KYW crystals allow very high Yb concentrations therefore pump absorption for these laser mediums was optimized to achieve maximum laser efficiency at given pumping conditions (symbols “o.” in the table). The Yb³⁺:CaF₂ and Yb³⁺:PbMoO₄ crystals allow Yb ions concentration as high as 10 % and 5 % respectively that corresponds to the pump absorption coefficients of 9 cm⁻¹ and 12 cm⁻¹. Thus, the pump absorption coefficient for Yb³⁺:CaF₂ and Yb³⁺:PbMoO₄ crystals was optimized taking into account this limitation.

The LiF:F₂⁻ crystal is also concentration limited laser medium. High quality LiF:F₂⁻ crystals have absorption as high as 4 cm⁻¹ at 970 nm, while the absorption of standard LiF:F₂⁻

crystals is twice lower. During the calculations the absorption coefficient of LiF:F_2^- crystal was fixed and the crystal length was optimized to achieve maximum laser efficiency, while for Yb-doped crystals the fixed parameter was crystals length (0.3 cm). The minimum pump spot diameter and output coupler reflectivity were optimized for all crystals. The parasitic losses of 0.02 cm^{-1} were assumed for Yb doped crystals and for LiF:F_2^- crystal with 2 cm^{-1} pump absorption, and 0.05 cm^{-1} parasitic losses were assumed for LiF:F_2^- crystal with 4 cm^{-1} pump absorption.

The numerical simulations results for type 1 high brightness LD pump are shown in the Fig. 3.1-7. The

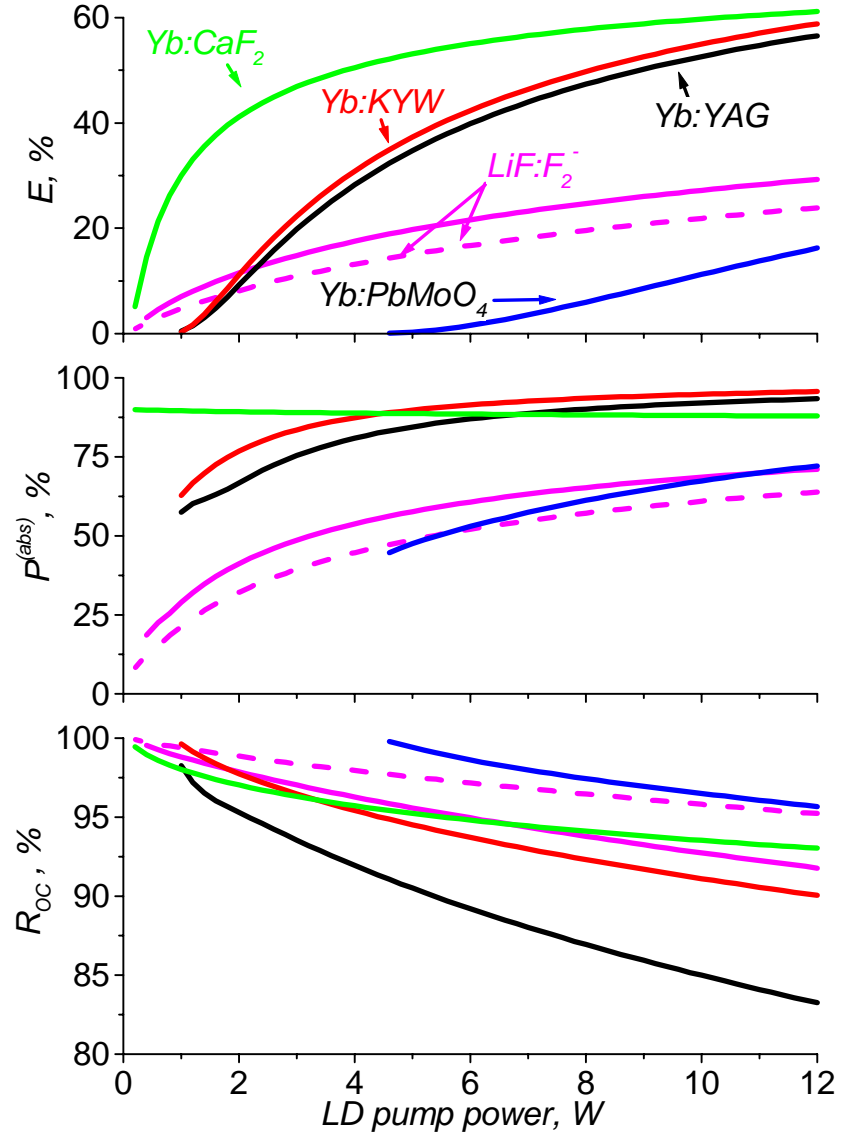


Fig. 3.1-7

plots show (from top to bottom) the maximum laser efficiency, optimal pump absorption and optimal output coupler reflectivity as functions of the LD pump power. The optimal diameters of LD pump beam (not presented on the Fig. 3.1-7) were close but little lower than the analytical estimation (see formula (9)) at the pump power above 5 W. At lower pump power narrower LD focusing was found to be optimal. Results for $\text{Yb}^{3+}:\text{YAG}$, $\text{Yb}^{3+}:\text{KYW}$, $\text{Yb}^{3+}:\text{CaF}_2$, and $\text{Yb}^{3+}:\text{PbMoO}_4$ crystals are shown by black, red, green, and blue colors respectively. Results for LiF:F_2^- crystal are shown by magenta color; solid lines correspond to the high pump absorption coefficient 4 cm^{-1} and dash lines correspond to the standard 2 cm^{-1} pump absorption.

As can be seen from the Fig. 3.1-7 the $\text{Yb}^{3+}:\text{KYW}$ crystal, which is pumped in zero-phonon-line near 980 nm, exhibits a little higher efficiency and the same threshold than these of $\text{Yb}^{3+}:\text{YAG}$ crystal, which is pumped at 941 nm. However, higher output coupler reflectivity is required to achieve maximum $\text{Yb}^{3+}:\text{KYW}$ laser efficiency. The $\text{Yb}^{3+}:\text{CaF}_2$ crystal demonstrates very low threshold and high efficiency in all range of LD pump powers. The advantage in efficiency for $\text{Yb}^{3+}:\text{CaF}_2$ crystal is especially high at low and medium pump powers ($< 5 \text{ W}$), while at the maximum pump the difference

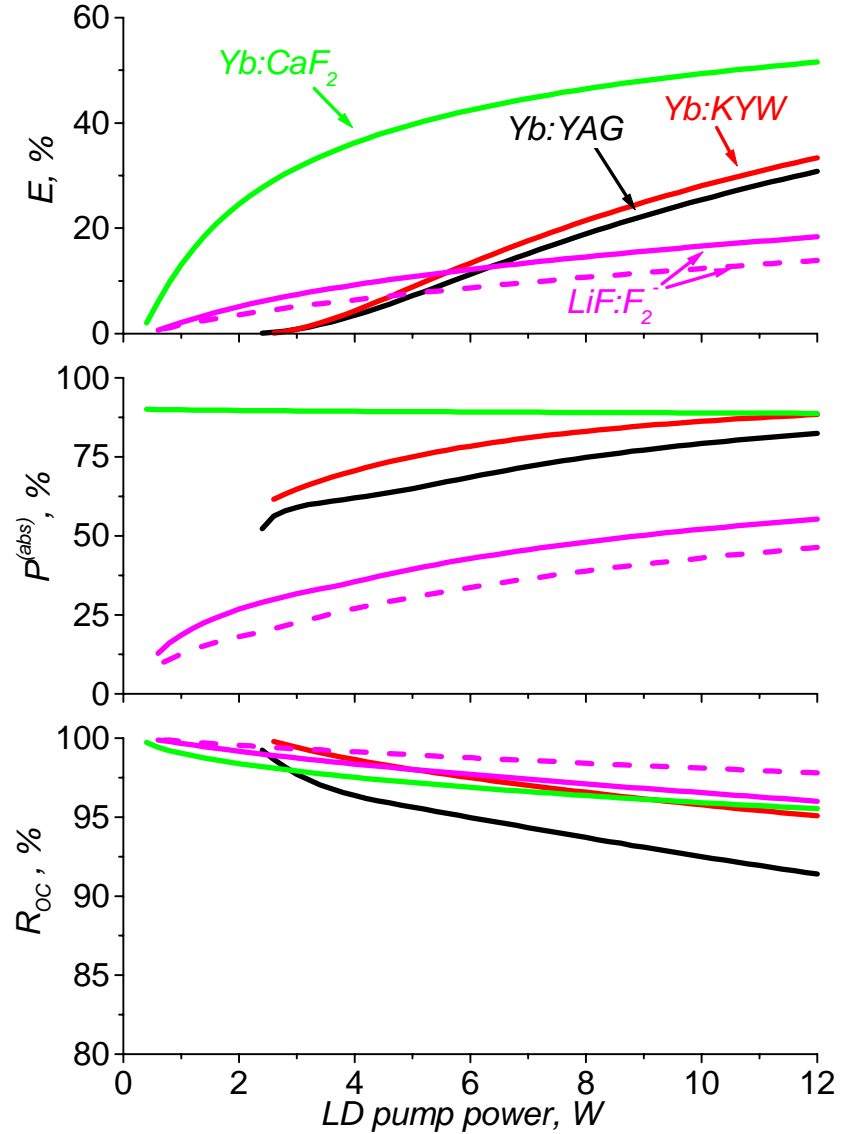


Fig. 3.1-8

between $\text{Yb}^{3+}:\text{CaF}_2$ and $\text{Yb}^{3+}:\text{KYW}$ crystals became insignificant. Due to the low cross-section of the laser transition the $\text{Yb}^{3+}:\text{CaF}_2$ crystal requires higher output coupler reflectivity even at high LD pump intensities, if compared with $\text{Yb}^{3+}:\text{YAG}$ and $\text{Yb}^{3+}:\text{KYW}$ crystals.

On the other hand, the $\text{Yb}^{3+}:\text{PbMoO}_4$ crystal demonstrates higher threshold and lower efficiency than these of $\text{Yb}^{3+}:\text{KYW}$ crystal. That is explained by high values of the saturation intensity $I_p^{(sat)}$ and minimum pump intensity parameters $I_p^{(min)}$ and relatively low gain cross-section of this crystal (see Table 1).

Our calculations have shown that is rather high pump absorption (90 – 95 %) is optimal for Yb-doped crystals at intense LD pumping. However this estimation could be considered as

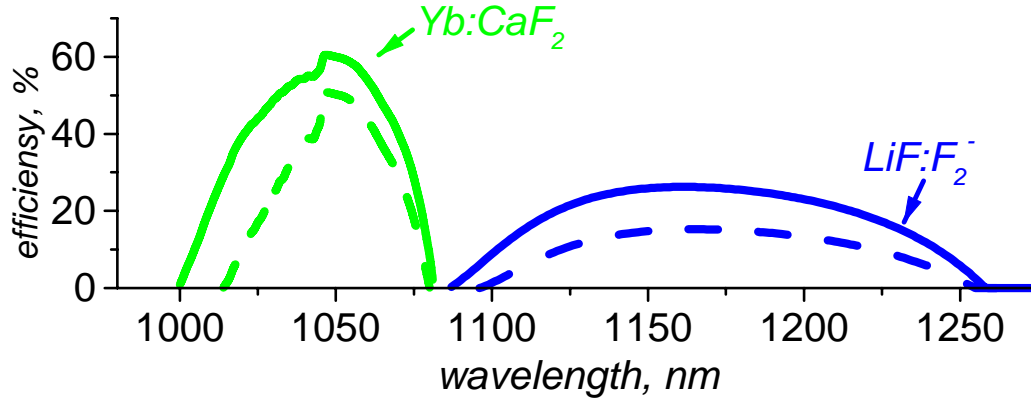


Fig. 3.1-9

too optimistic mostly because the model we use does not take into account various thermal effects, which can suppress laser oscillations or cause the crystal fractures.

In comparison with Yb-doped crystals the LiF:F_2^- crystal exhibits lower efficiency, which caused mostly by limited concentration of active centers in the crystal and hence relatively low pump absorption. Nevertheless the efficiency of LiF:F_2^- laser oscillations crystal reaches 30 % at high power of LD pumping. Another favorable feature of LiF:F_2^- crystal is a low lasing threshold that can be explained by low value of $I_p^{(\min)}$ parameter for this crystal (see Table 1).

The same modeling and optimizations were repeated for type 2 “standard” LD pumping (see Table 2). The modeling results are shown in the Fig. 3.1-8 where all designations are the same as on the previous figure. Reduce of LD pumping brightness have caused almost two times decrease of efficiency for $\text{Yb}^{3+}:\text{YAG}$ and $\text{Yb}^{3+}:\text{KYW}$ crystals and significant decrease of the optimal pump absorption. Drop of efficiency for $\text{Yb}^{3+}:\text{CaF}_2$ crystal is much smaller (25 %) and for the LiF:F_2^- crystal efficiency have reduced by 70 %.

The important feature of $\text{Yb}^{3+}:\text{CaF}_2$ and LiF:F_2^- laser mediums is the possibility of continuous tuning of the laser wavelength. Estimations of the $\text{Yb}^{3+}:\text{CaF}_2$ and LiF:F_2^- lasers tuning ranges were carried out assuming maximum power of LD pumping (12 W) and optimal parameters of the laser cavity (crystal absorption, pump spot size, OC reflectivity, see Fig. 3.1-7 and Fig. 3.1-8). Modeling results for type 1 high brightness pump (solid lines) and type 2 standard LD pump (dash lines) are shown in the Fig. 3.1-9. Green color corresponds to $\text{Yb}^{3+}:\text{CaF}_2$ crystal and blue color corresponds to LiF:F_2^- crystal.

The $\text{Yb}^{3+}:\text{CaF}_2$ crystal has the tuning range from 1000 to 1075 nm while the tuning range for LiF:F_2^- crystal is approximately twice broader (1100 – 1250 nm). It is interesting to notice that more than two times decrease in pump intensity does not reduce strongly the tuning

ranges. The Fig. 3.1-9 also shows that the very short lasing wavelengths below 1000 nm could be achieved for $\text{Yb}^{3+}:\text{CaF}_2$ crystal. However, practical realization of LD pumped $\text{Yb}^{3+}:\text{CaF}_2$ laser with limit low quantum defect will require the use of special pumping schemes (off-axis pumping [6], or end-pumping through resonantly reflecting mirror [7]).

3.1.3. Experimental investigation of Yb-doped crystals under LD pumping

Experimental arrangement

The high brightness fiber coupled IPG Photonics LD-975-10 module with 100 μ fiber core diameter and 0.16 fiber numerical aperture was used for the experiments. The watt-amp characteristic of LD module is shown on the Fig. 3.1-11. The LD pump unit was driven by a power supply, which provided CW and pulsed modes of LD operation with the minimum current pulse duration of 80 μ s and pulses repetition rate up to 10 kHz. The LD temperature and the emission wavelength was adjusted and stabilized by Peltier thermo electric cooler. LD emission spectra at different temperatures are shown in the Fig. 3.1-11.

The LD module focusing system has consisted of collimating lens with 5 mm focal distance and focusing lens with 15 mm focal distance. LD pump intensity distribution in vicinity of the focal point, which was registered by CCD array, is shown in the Fig. 3.1-12 (blue curve). At

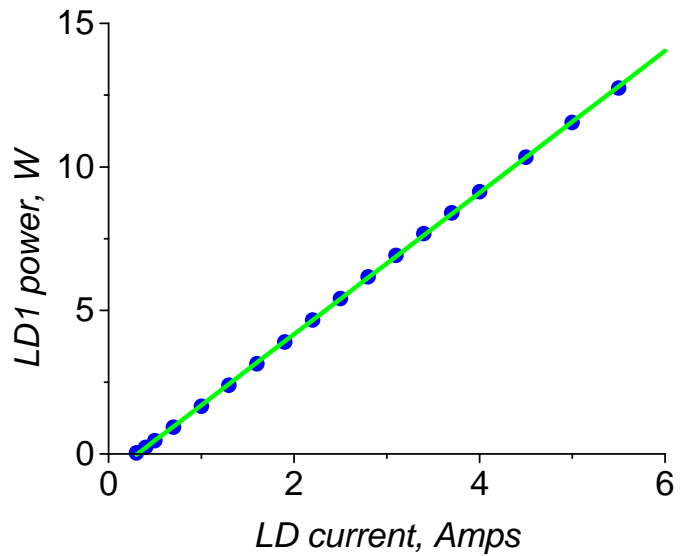


Fig. 3.1-10

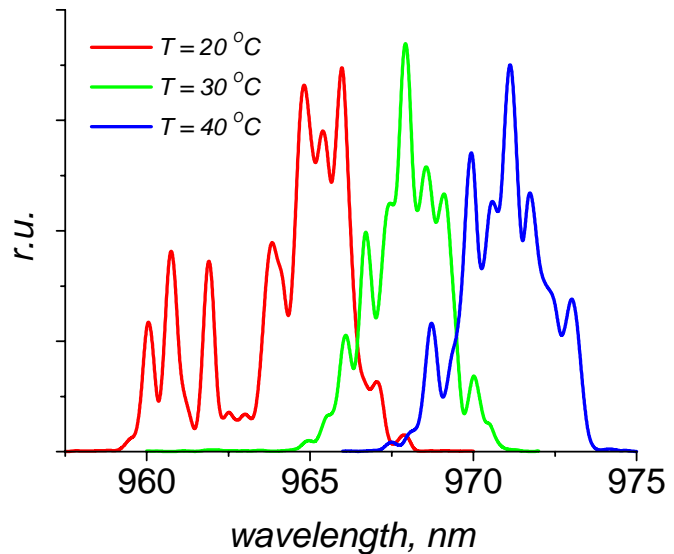


Fig. 3.1-11

the same figure by red color is shown integral LD emission distribution: $I(r) = \pi \int_0^r i(x) \cdot x dx$. As can be seen, pump intensity distribution has near triangular shape, 50 % of LD power concentrated in a $\varnothing 0.3$ mm spot and 75 % of LD power concentrated in a $\varnothing 0.55$ mm spot.

The LD pump distribution lengthwise pump beam axis is shown in the Fig. 3.1-13. The pump spot diameters were defined at the level of 50 % and 75 % of total LD power. As can be seen from the figure, the focusing system that we have used provides almost constant pump beam diameter within 5 - 6 millimeters from the focal point. However, the pump spot was several times larger than the fiber core diameter. The variation of the pump beam transverse size along propagation could be roughly described by hyperbolic function: $d^2(x) = (kx)^2 + d_0^2$.

The laser setup is shown on the Fig. 3.1-14. The laser consists of laser crystal C, dichroic back mirror M, and output coupler (OC) all placed on separately adjustable optical mounts. All experiments were carried out for pulsed LD pumping, therefore no forced crystal cooling was necessary.

The Yb-doped laser crystal samples were plane-parallel cut and uncoated. Curved mirrors with

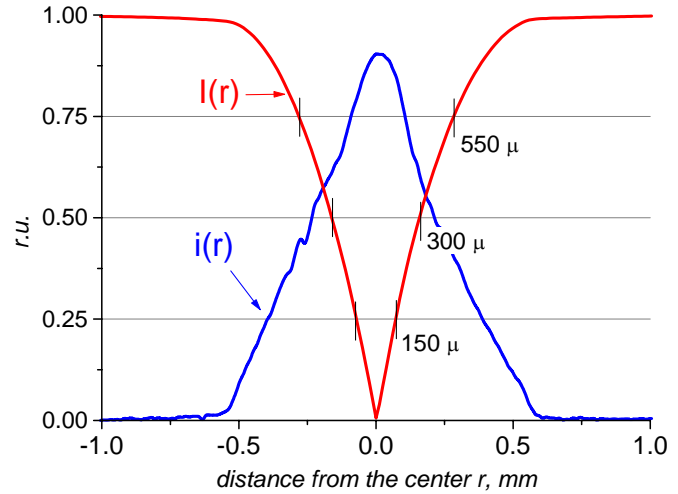


Fig. 3.1-12

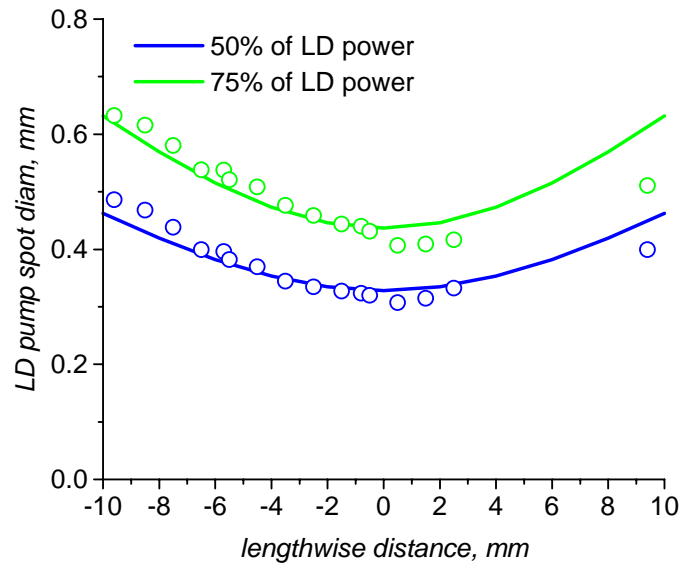


Fig. 3.1-13

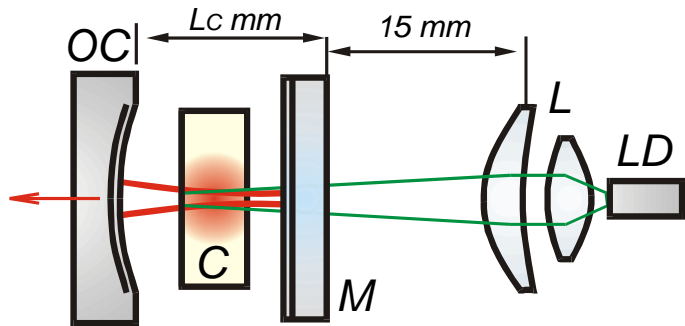


Fig. 3.1-14

reflectivities of about 75, 85 and 95 % and radiuses of curvature (ROC) of 25, 50, and 100 mm were used as output couplers. Reflectivity of the dichroic mirror M as function of the radiation wavelength is shown in the Fig. 3.1-15. Specially optimized 36 layer coating has provided 95 % transmission in the pump wavelengths range (969 nm – 981 nm), >97 % reflectivity starting from 1005 nm wavelength and almost total reflectivity in the 1017 nm – 1200 nm range. Thus, this mirror can be used in a laser experiments with a variety of Yb doped crystals.

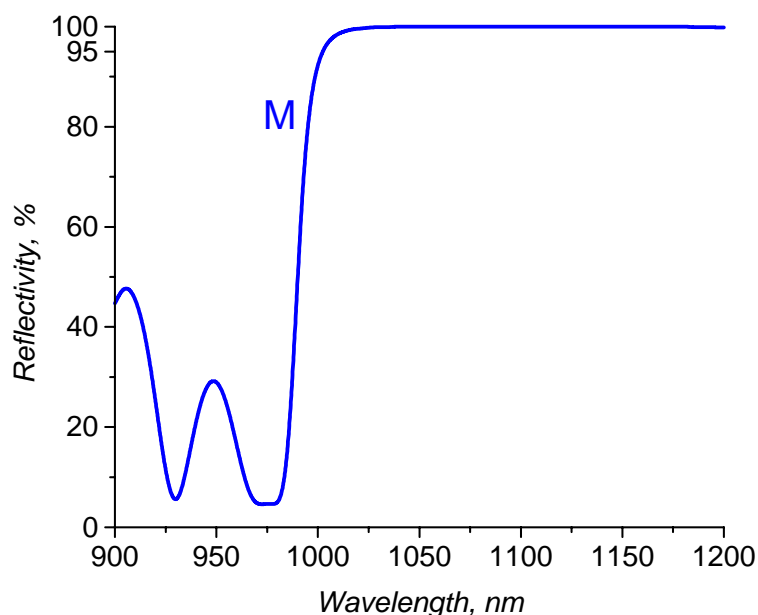


Fig. 3.1-15

Experimental results

Several samples of $\text{Yb}^{3+}:\text{CaF}_2$ crystals with different Yb^{3+} ions concentration (3, 5, 9, and 15 % wt.) and different thicknesses (2 and 4 mm) were prepared for the laser experiments. The $\text{Yb}^{3+}:\text{YAG}$ (10 % wt. Yb) and $\text{Yb}^{3+}:\text{KYW}$ (20 % wt. Yb) were used as a reference crystals.

In the Fig. 3.1-16 are shown pump-to-output characteristics for LD pumped $\text{Yb}^{3+}:\text{YAG}$ crystal. Pump pulse duration was about 2 ms pump at 10 Hz pump pulse repetition rate. Measurements were carried out for different OC reflectivities: 75, 85, and 95 %. OCs ROC was equal to 100 mm and the cavity length (35 mm) was adjusted to achieve maximum laser output power. In accordance with the modeling results, rather low OC reflectivity is optimal for $\text{Yb}^{3+}:\text{YAG}$ crystal (at 75 % OC reflectivity the laser slope efficiency is about 59 %, while the use of OC with 95 % have reduced the slope efficiency to 35 %). Besides, the reduction of OC reflectivity from 95 % to 75 % does not affected noticeably on the laser oscillations threshold (average LD pump power of about 50 mW).

The same dependencies for $\text{Yb}^{3+}:\text{KYW}$ crystal are shown in the Fig. 3.1-17. As can be seen, decrease of OC reflectivity causes increase of the laser slope efficiency and decrease of the laser output power. In contrast with $\text{Yb}^{3+}:\text{YAG}$ crystal the $\text{Yb}^{3+}:\text{KYW}$ crystal has twice higher threshold and demonstrates strong dependence of the threshold pump power on OC reflectivity. Lower laser performance of the $\text{Yb}^{3+}:\text{KYW}$ crystal in comparison with $\text{Yb}^{3+}:\text{YAG}$ crystal could be explained by lower optical quality of $\text{Yb}^{3+}:\text{KYW}$ crystal sample.

Results of the laser experiments with $\text{Yb}^{3+}:\text{CaF}_2$ crystals are illustrated in the Fig. 3.1-18. Measurements were carried out for the 2 mm thick crystal with 3 % wt. Yb^{3+} ions concentration (circles), 4 mm thick crystal with 3 % wt. Yb^{3+} concentration (squares) and 2 mm thick crystal with 9 % wt. Yb^{3+} concentration (triangles in the Fig. 3.1-18). Experimental results corresponding to the 85 % OC reflectivity are shown by the green color and results for 95 % OC reflectivity are shown by blue color.

As can be seen from the Fig. 3.1-18, the laser parameters of LD pumped $\text{Yb}^{3+}:\text{CaF}_2$ crystals depend strongly on Yb^{3+} ions concentration and on crystal thickness. However, all

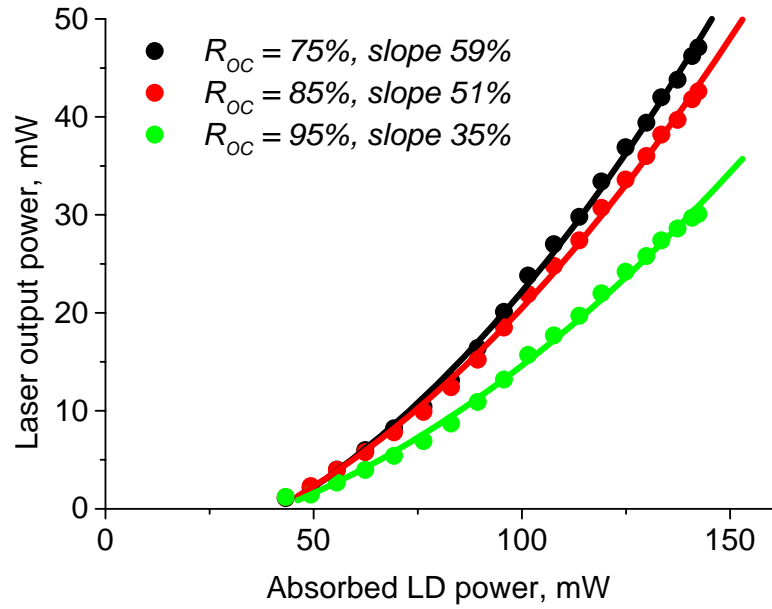


Fig. 3.1-16

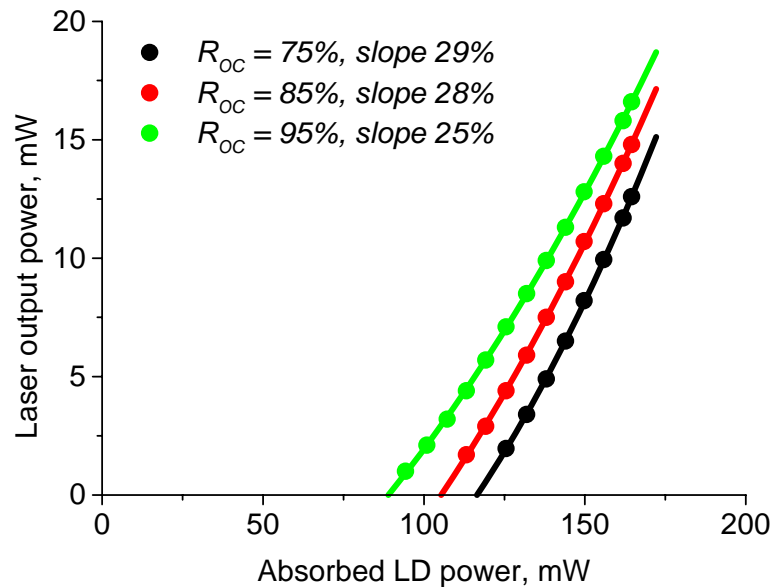


Fig. 3.1-17

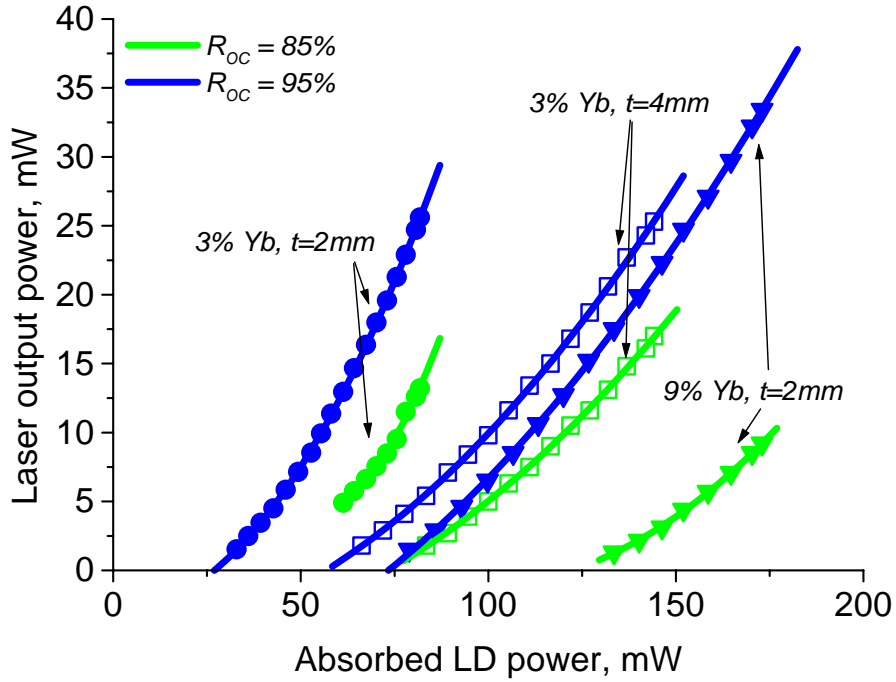


Fig. 3.1-18

Sample	Yb, % wt	thickness, mm	pump absorp, %	max output, mW	slope, %
1	3	2	40	26	68
2	3	4	75	25	38
3	9	2	80	33	42

Table 3

$\text{Yb}^{3+}:\text{CaF}_2$ samples have demonstrate lower threshold, higher laser output power as well as a slope efficiency for the laser cavity equipped with 95 % reflectivity OC.

Experimental results for tested $\text{Yb}^{3+}:\text{CaF}_2$ crystal samples are summarized in the Table 3. As follows, the sample #1 with 40 % LD pump absorption demonstrates the slope efficiency as high as 68 % at 26 mW output power. Two times increase of the crystal thickness (sample #2) has caused significant decrease of the slope efficiency (to 38 %), while the output power for the sample #2 has remained almost the same (25 mW). The 2 mm thick sample #3 with high Yb concentration has demonstrated highest output power (33 mW) but the slope efficiency lower than that for the sample #1 (42 % versus 68%). Thus, in similar experimental conditions, the $\text{Yb}^{3+}:\text{CaF}_2$ crystal demonstrates lower threshold and higher efficiency than the $\text{Yb}^{3+}:\text{YAG}$

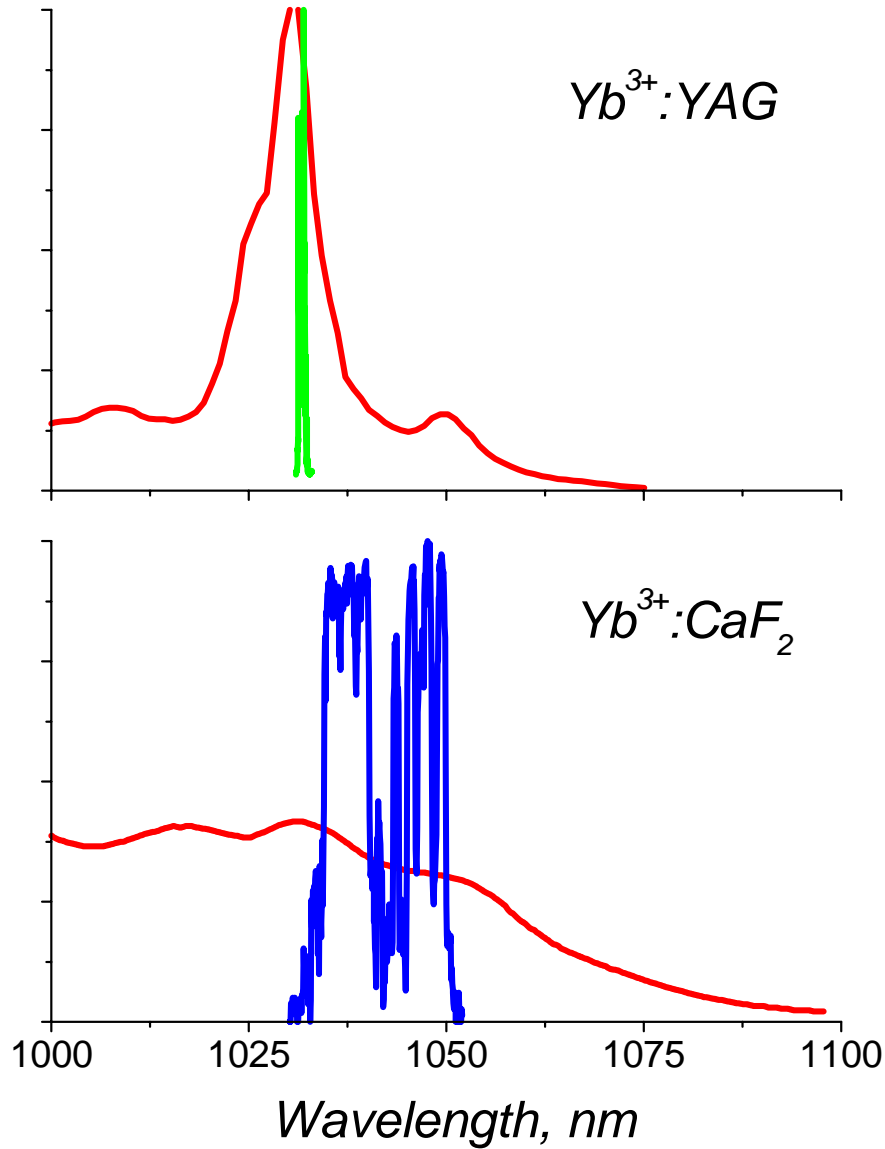


Fig. 3.1-19

crystal. However, in contrast to the $\text{Yb}^{3+}:\text{YAG}$ crystal, rather high OC reflectivity was found to be optimal for the $\text{Yb}^{3+}:\text{CaF}_2$ crystal. These experimental results are in good agreement with the simulation results, presented in the section 3.1.2.

Spectra of the laser emission of the $\text{Yb}^{3+}:\text{YAG}$ and $\text{Yb}^{3+}:\text{CaF}_2$ crystal are compared in the Fig. 3.1-19. Neighboring parts of the crystals' luminescence spectra are shown on the figure by red curves. Laser cavity parameters were the same in both experiments. The non uniform structure of the $\text{Yb}^{3+}:\text{CaF}_2$ laser spectra can be explained by Fabri-Perot effect between the cavity mirrors and uncoated crystal surfaces. As follows from the figure, $\text{Yb}^{3+}:\text{YAG}$ laser

oscillations wavelength is located in vicinity of luminescence spectra maximum. The spectral width of $\text{Yb}^{3+}:\text{CaF}_2$ laser oscillations is much more broader that corresponds to the smooth and broadband luminescence spectra of this crystal.

3.1.4. Experimental study of the laser oscillations in $\text{LiF}:\text{F}_2^-$ color center crystal under direct LD pumping

Introduction

Room temperature color center lasers (CCLs) developed over the last few decades have become a new class of smoothly tunable coherent radiation sources in visible and IR spectral regions [8, 9]. CCLs can operate efficiently in all the modes of oscillation (from continuous wave to sub-picosecond pulse duration) and have a broad continuous tuning range (up to 2500 cm^{-1}). The most widespread and well-studied media for CCLs are alkali-halide crystals. Alkali-halide crystals lattice have a simple cubic symmetry, i.e. they inherently isotropic. The simple and fast Ciropulos technique enables the growth of high quality and large-size crystals (up to $\varnothing 400 \times 200\text{ mm}$) on a large-scale commercial level. Among the alkali-halides crystals LiF crystal has low hygroscopicity, the smallest value of the temperature-derivative refractive index ($-1.2 \times 10^{-5}\text{ K}^{-1}$) and a high thermal conductivity coefficient ($14\text{ W}\cdot\text{m}^{-1}\cdot\text{K}^{-1}$ at 300 K , even higher than that of YAG crystal).

The diagram shown on the Fig. 3.1-20 describes the principle of the CCL operation. Pump radiation is absorbed in the wide band of the electric-dipole electron-vibrational transition $1 \rightarrow 2$. In a period of time of the order of $10^{-12} - 10^{-13}\text{ sec}$, radiationless relaxation $2 \rightarrow 3$ within potential curve of the excited electronic state occurs, accompanied by a mutual rearrangement of the neighboring ions and by phonon emission. Then the radiative electron-vibrational transition $3 \rightarrow 4$ occurs with a probability of $A = 10^7 - 10^8\text{ sec}^{-1}$, followed by another rapid vibrational relaxation $4 \rightarrow 1$ and resetting of the spatial ions configuration. Depending on pumping and lasing

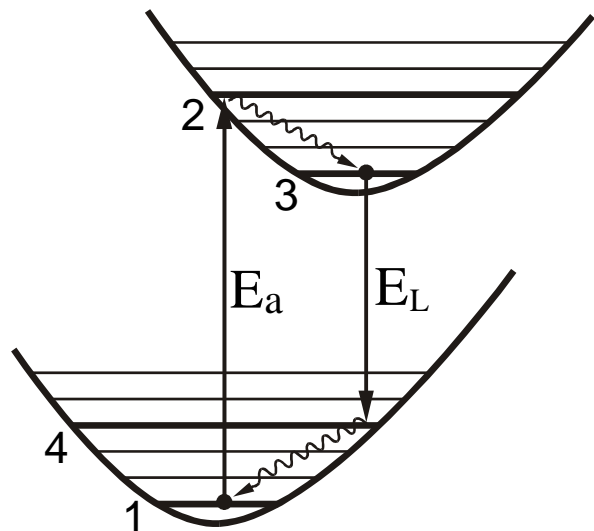


Fig. 3.1-20

wavelengths, the CCL can operate as in quasi-four-level as well as in quasi-three-level schemes.

The LiF:F_2^- color center lasers is an effective tunable source in near-IR spectral region. The technology of LiF:F_2^- crystals fabrication that was developed in LMTRC allows the large-scale production of LiF:F_2^- laser elements with superb characteristics. The main criteria of the LiF:F_2^- laser element quality (figure of merit) is the ratio of the active absorption by laser centers to parasitic losses (so-called contrast ratio). The optimization of the LiF:F_2^- laser crystals fabrication process have allowed to reach the record 1.5 cm^{-1} active absorption at the 1064 nm and the contrast as high as 40, while the typical values are $0.4 - 0.6 \text{ cm}^{-1}$ of active absorption at the contrast about 10 – 20.

On the Fig. 3.1-21 are shown the absorption and emission cross sections of the LiF:F_2^- crystal as functions of the radiation wavelength (blue solid lines, curves 1 and 2 respectively). The maximum value of the cross sections is about $7 \cdot 10^{-17} \text{ cm}^2$ at the bands half-widths of about 140 nm and the Stokes shift of 1500 cm^{-1} . The fluorescence lifetime of the CCs at room temperature is about 55 ns. Among advantages of this laser active medium is negligibly small excited state absorption (ESA). At the room temperature, the laser characteristics of the LiF:F_2^- crystals remain constant for years. However, the overheating above 60°C and UV irradiation

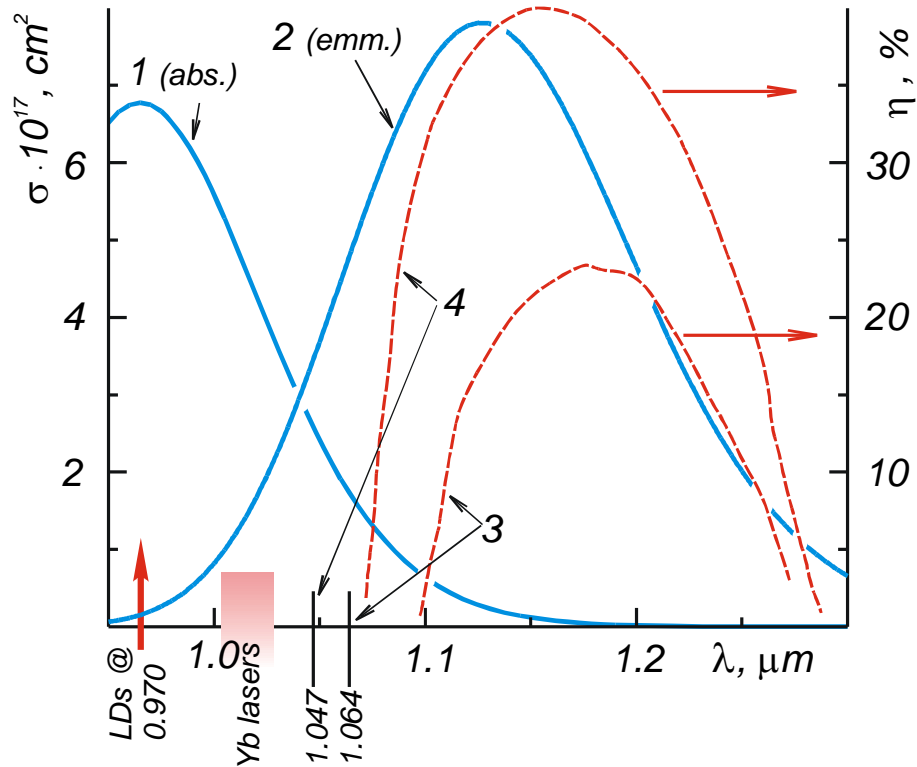


Fig. 3.1-21

could cause the degradation of the laser element performance. Intensive mid-IR radiation can cause the laser centers destruction as well. The probable mechanism of this parasitic effect is the color center ionization at the two-photon excited state absorption. However, at the laser intensity about $100 - 200 \text{ MW}\cdot\text{cm}^{-2}$, the probability of this process is negligible.

By dash red lines on the Fig. 3.1-21 are shown the tuning curves of LiF:F_2^- laser pumped by Nd^{3+} :YAG laser ($\lambda=1.064 \text{ }\mu\text{m}$, curve 3) and Nd^{3+} :YLF laser ($\lambda=1.047 \text{ }\mu\text{m}$, curve 4) [10]. From the figure follows that the 17 nm decrease of the pump laser wavelength causes the increase of the LiF:F_2^- laser efficiency (from 20 % to 40 %) and broadening of the laser tuning range (from $1.09 - 1.027 \text{ }\mu\text{m}$ to $1.065 - 1.29 \text{ }\mu\text{m}$). This allows to expect further improvement of the LiF:F_2^- laser characteristics at the shorter wavelength pumping. Thereupon, the promising source for LiF:F_2^- laser pumping could be the Yb^{3+} :host solid-state lasers operating within $1.01 - 1.03 \text{ }\mu\text{m}$ range. Even more prospective is a pumping of a LiF:F_2^- laser medium by emission of the laser diodes at $0.97 - 0.98 \text{ }\mu\text{m}$ wavelength i.e. directly in maximum of absorption.

As we reported previously, the mathematical model of two-manifold LD pumped laser have been developed. The laser characteristics of LiF:F_2^- crystal were evaluated and compared with these of Yb^{3+} : CaF_2 , Yb^{3+} : PbMoO_4 , Yb^{3+} :YAG, and Yb^{3+} :KYW crystals. The numerical simulations have shown that the short nanoseconds scale radiative lifetime of LiF:F_2^- laser crystal is compensated by high values of absorption and emission cross-sections. As a result, surprisingly low threshold, high (up to 30 %) conversion efficiency, and wide tuning range ($1090 - 1260 \text{ nm}$) were estimated for this laser medium. Presently we report for the first time on experimental demonstration of the laser oscillations in LiF:F_2^- crystal under direct CW LD pumping.

Experimental arrangement

The experiments on direct LD pumping of LiF:F_2^- crystal were carried out using the same set-up as for the laser experiments with Yb-doped crystals (see section 3.1.3). The LD pump source was 12 W fiber coupled module, supplied by IPG Photonics. Schematic of the laser is shown on the Fig. 3.1-22. The same 36 layer dichroic mirror was used for LD pump coupling (see transmission spectrum in the

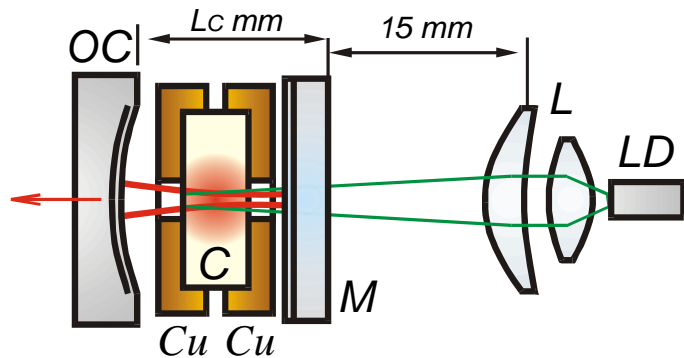


Fig. 3.1-22

Fig. 3.1-15). The LiF:F_2^- laser crystal samples were 10×10 mm square shaped, 5 mm thick and plane-parallel cut with LD pump absorption about 50 - 60 %. Both sides of the laser elements were AR coated at 1064 nm with residual reflectivity at LiF:F_2^- laser wavelengths range of about 1 %. The laser crystal was placed on a water-cooled copper heat sink. The cooling water temperature was stabilized and adjustable. The output coupler OC has declining reflectivity in expected wavelengths range of laser oscillations: 99.5 % at 1145 nm, 95 % at 1155 nm, and 90 % at 1160 nm wavelength. Our computer simulations have shown that rather high OC reflectivity (>95 %) is required to achieve LiF:F_2^- crystal lasing under LD pumping. This roughly defines the “red” wavelengths limit in our laser experiments by 1155 nm.

Experimental results

In the first series of experiments several LiF:F_2^- crystal samples were tested. Measurements were carried out at the room temperature, 80 μs pump pulse duration, and 5 Hz pump pulses repetition rate.

In the Fig. 3.1-23 are shown pump-to-output characteristics for several LiF:F_2^- crystals. In spite of approximately the same absorption, the maximum output and the slope efficiency differs considerably from crystal to crystal. Analysis of the crystals’ absorption spectra has shown the correlation between the laser characteristics of the crystal and its contrast (ratio of pump absorption and parasitic absorption coefficients at the laser wavelength). Sample #1 (9 % slope efficiency) has a contrast about 15, while the contrast of sample #4 (14 % slope efficiency) was about 18. During a testing of a LiF:F_2^- crystal sample with a contrast about 11 the laser oscillations were not detected. In the further experiments the #4 crystal sample with better laser characteristics was used. An extensive study of LiF:F_2^- crystals’ spectral characteristics is planned for the near future to define a quantitative relationship between

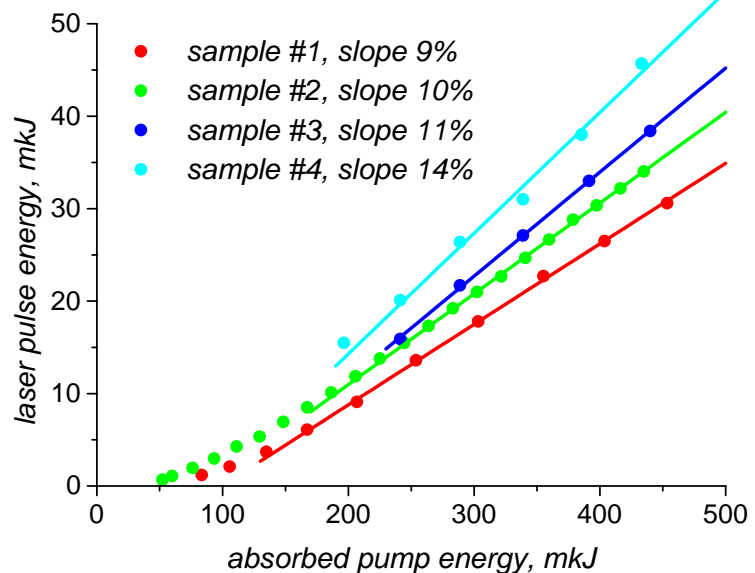


Fig. 3.1-23

LiF:F₂⁻ crystal absorption, contrast, and LD pumped laser performance.

In the Fig. 3.1-24 are shown LD pumped LiF:F₂⁻ laser emission spectra (for sample #4) at different LD pump power. As in previous experiment, the measurements were carried out at the room temperature, 80 μs pump pulse duration, and 5 Hz pump pulses repetition rate. The percentage of the laser cavity output coupler reflectivity is shown on the plots by magenta color (right vertical axis). The midpoints of the LiF:F₂⁻ laser emission are located near the 1149 nm wavelength that corresponds to the 98 % - 99 % OC reflectivity and does not depend strongly on the LD pump power. Presence of the peaks in laser emission spectra is caused, by a weak Fabry-Perot effect between cavity mirrors and a laser crystal

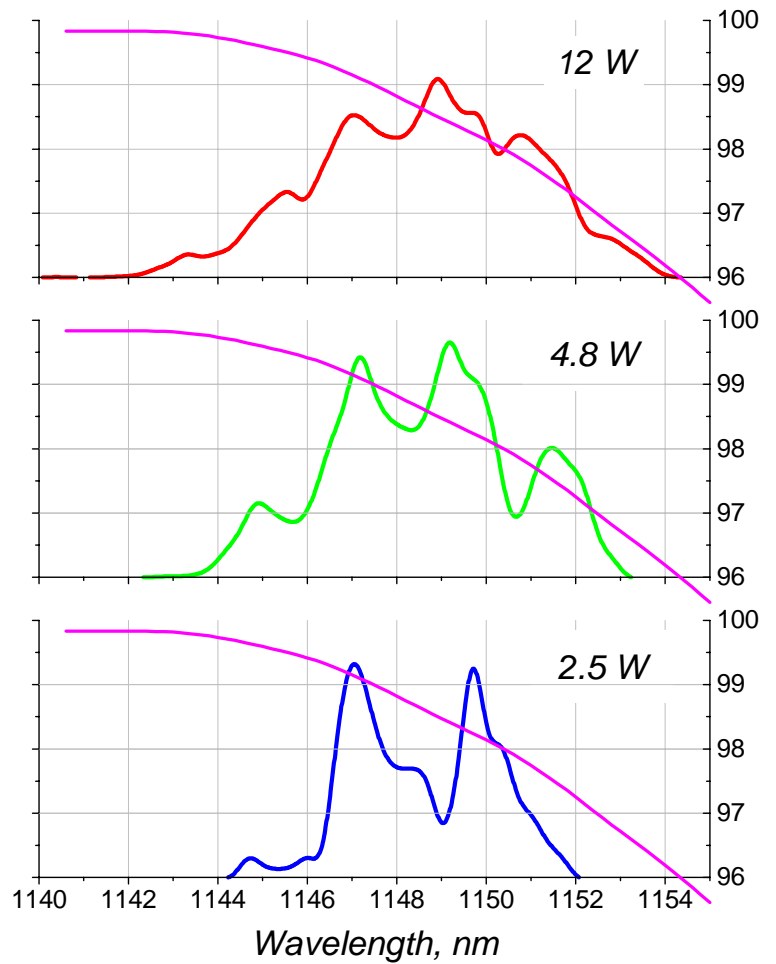


Fig. 3.1-24

surfaces. Full width of the emission spectra decreases from 12 nm at 12 W pump power to 8 nm at 2.5 W pump power. We suppose that the “red” border of the laser emission is determined by insufficient OC reflectivity. Therefore, the use of the output coupler with “flattop” 98 % - 99 % reflectivity curve could allow substantial increasing of the LiF:F₂⁻ laser emission spectral width as well as its output power.

In the next series of experiments the characteristics of LD pumped LiF:F₂⁻ laser oscillations were investigated at different repetition rates of LD pump pulses and at different temperatures of the laser crystal. During these experiments active water-cooling of the LiF:F₂⁻ crystal was used.

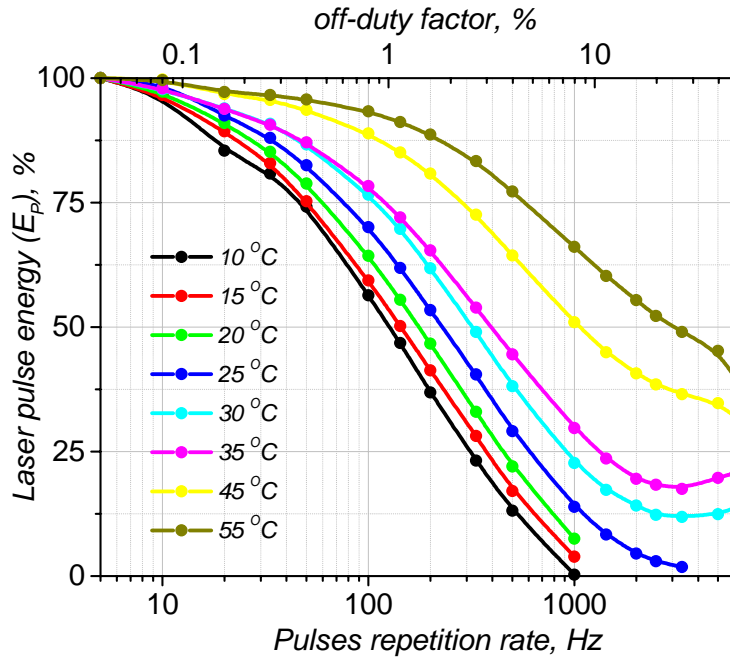


Fig. 3.1-25

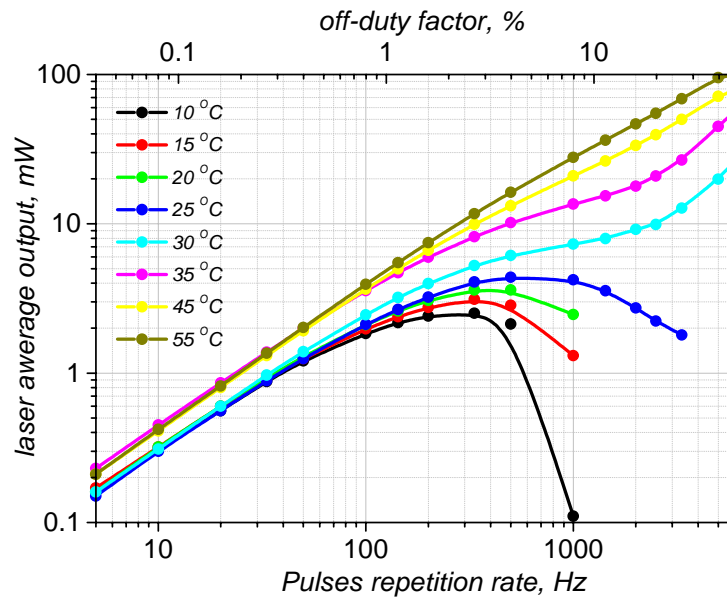


Fig. 3.1-26

The Fig. 3.1-25 shows the dependence of laser pulses energies E_p on pulses repetition rate F (or off-duty factor). The pulses energies are shown as percentage of initial pulse energy at low ($F = 5$ Hz) repetition rate. Measurements were carried out at $80 \mu\text{s}$ pump pulse duration at different temperatures T of the cooling water (from 10°C to 55°C , see plot legend). Respective average powers of the laser output are shown in the Fig. 3.1-26.

At low cooling water temperature ($T = 10^{\circ}\text{C}$, black curves on the plots) the pulse energy decreases monotonously with increase of the repetition rate. Starting from $F = 100\text{ Hz}$ the decline became almost exponential and the laser emission terminates at $F = 1\text{ kHz}$ pumping. With the increase of the cooling water temperature the decline of the pulses energy E_p became slower. At the $T = 30^{\circ}\text{C}$ (cyan curves) the pulses energy decreases to 25 % of initial value at $F = 1\text{ kHz}$, but with further increase of the repetition rate (above 2 kHz) the energy begins to rise. At the cooling water temperatures above of 30°C the pulse energy declines slow enough to provide monotonous grow of the laser average output with the increase of the pulses repetition rate up to 6.25 kHz (50 % off- duty cycle). The average output power exceeds 100 mW for the temperature of 55°C , at that the pulses energy is about 93 % of initial value for $F = 100\text{ Hz}$ and 66 % for $F = 1\text{ kHz}$ repetition rate.

We can explain this rather complex dependence of the LiF:F_2^- laser characteristics on repetition rate and temperature by influence of triplet electronic states of F_2^- color centers, which illustrated in the Fig. 3.1-27. The laser working cycle (pump absorption – picosecond relaxation – stimulated emission) is shown on the figure by a green color. However, population can also be lost from S_1 by the non-radiative process of intersystem crossing to the triplet electronic state T_1 with a characteristic rate W_{ST} . Once a population is in T_1 it can absorb both pump and laser radiation. The relaxation of excited triplet state T_2 occurs partly within triplet system (W_{TT}) and partly with triplet-singlet transition (characteristic rate W_{TS}^*). The population accumulated in T_1 slowly decays to the ground state S_0 by nonradiative thermal relaxation with a rate W_{TS} .

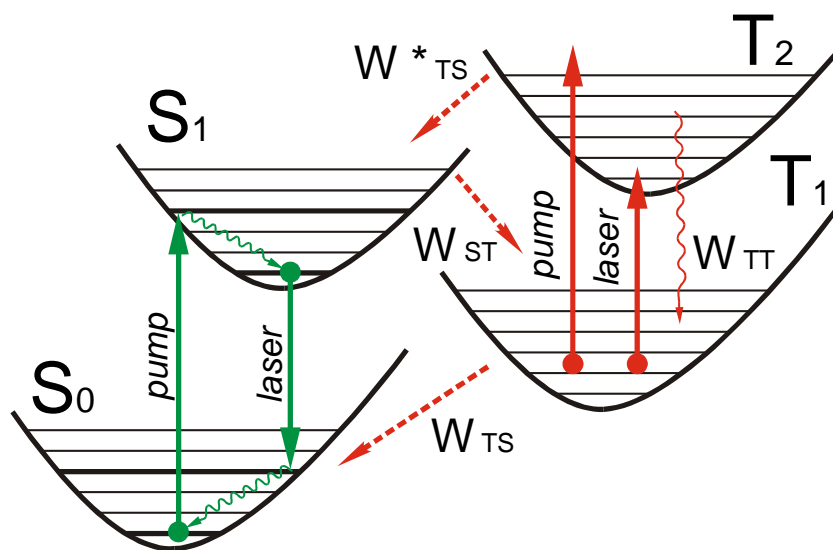


Fig. 3.1-27

The characteristics of LD pumped LiF:F_2^- laser are very sensitive to the cavity losses at the laser wavelength (rather high OC reflectivity is required to achieve laser oscillations). Therefore, even relatively small triplet states population could introduce high enough parasitic absorption to restrain laser oscillations. Among with triplet absorption cross section the characteristics rates of singlet-triplet transitions W_{TS} , W_{TS}^* and W_{ST} are also important limiting parameters, which determine for LiF:F_2^- laser the possibility of CW or high pulses repetition rate operation.

Taking into account described scheme, the experimental results presented on the Fig. 3.1-25 can be explained as following. At periodical pumping with a period comparable or smaller than W_{TS}^{-1} and W_{ST}^{-1} the system shown in the Fig. 3.1-27 reaches quasi-equilibrium with non-zero triplet states population.

Therefore, the laser pulse energy will be reduced in comparison with single pulse pumping due to the triplet state absorption at laser wavelength. With increase of the pulses repetition rate the triplet states population grows and laser pulse energy further reduces. At certain repetition rate the triplet state absorption could became high enough to terminate laser operation (black curve on the Fig. 3.1-25). Obviously, increase of the laser medium temperature changes constants of the nonradiative singlet-triplet relaxations. Specifically the triplet state decay characteristic rate W_{TS} became faster that reduces triplet states population and allows the laser operation at higher pulses repetition rate. Due to the limited

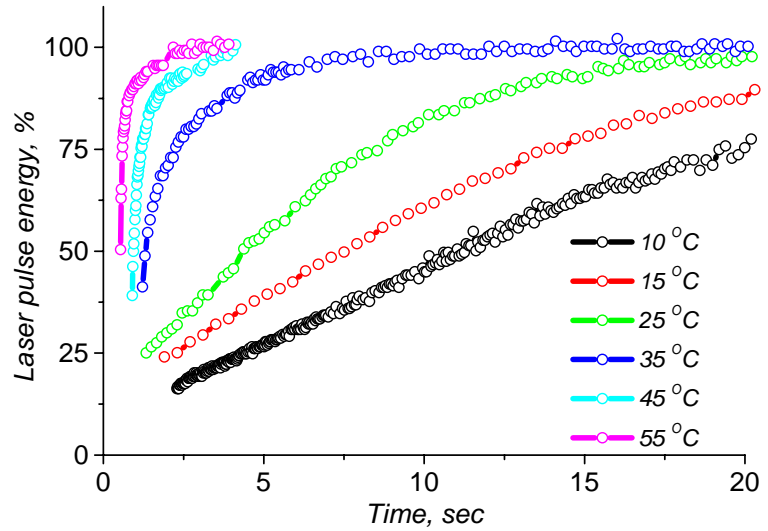


Fig. 3.1-28

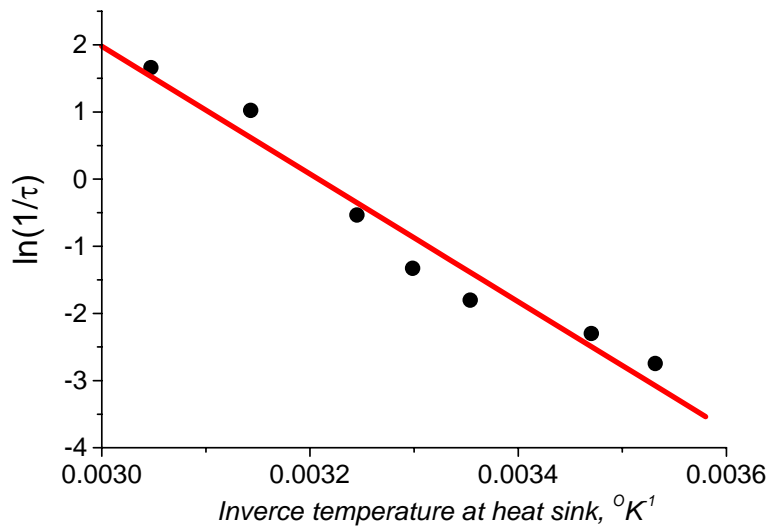


Fig. 3.1-29

thermal conductivity of the LiF:F_2^- crystal the temperature of laser pumped channel could be essentially higher than that at the heat sink. Therefore, an extra heating of the laser active volume by the pump radiation could result in a rise of laser pulses energy with increase of the repetition rate (cyan and magenta curves on the Fig. 3.1-25). However, overheating of the laser medium can introduce some other parasitic effects suppressing the laser oscillations: increase of a ground state absorption, decrease of luminescence lifetime, etc. (see E_P behavior at high repetition rates for a heat sink temperatures of 45 °C and 55 °C).

To evaluate the characteristic nonradiative rate of triplet state decay (W_{TS}) we have investigated the behavior of the laser pulses energy after fast switching of LD pump from high repetition rate (6.25 kHz) to low rate of 5 Hz. Restorations of the of the pulses energies at different heat sink temperatures are shown in the Fig. 3.1-28. Obviously, the pulses energies rise after the LD pump repetition rate switching. However, the time, which required for the laser medium to settle in new quasi-equilibrium, strongly depends on the crystal temperature and differs from minutes for 10 – 15 °C to seconds for 45 – 55 °C. The relaxation dependencies are rather complex due to large number of essential parameters. To estimate roughly the triplet state decay rate a single-exponential constituents of the relaxation curves were extracted. In the Fig. 3.1-29 is shown logarithm of inversed single-exponential relaxation time $\ln(1/\tau)$ vs. inversed temperature $1/T$.

Reduction of the triplet states parasitic absorption with increase of the laser crystal temperature has allowed achieving CW laser operation of LD pumped LiF:F_2^- crystal. Temporal behaviors of LiF:F_2^- laser emission within 4 seconds from LD pump start are shown in the Fig. 3.1-30. As in the case of periodical pumping, the laser characteristics were found to be very sensitive to the crystal temperature. The leading edge of the laser emission could be divided into three parts (see black curve, 20 °C, as example). Within a fraction of second from the pump start the laser output rapidly declines

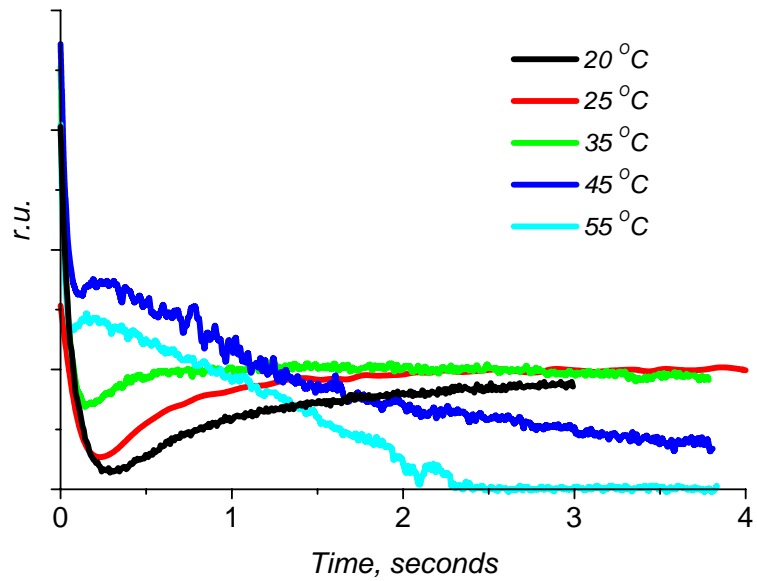


Fig. 3.1-30

due to the grow of triplet levels population (almost to zero at cooling water temperature of 20 °C). Thereupon, the pump radiation increases the temperature of the laser active volume that reduces the triplet states population and the laser output begin to rise. During next few seconds a thermal equilibrium within the laser crystal settles down and the laser output became constant. With increase of the cooling water temperature a gap on a leading edge of a laser emission became smaller and CW laser output groves from ¼ to ½ of its peak value. However, further increase of the cooling water temperature causes overheating of the laser crystal by pump radiation that terminates the laser operation after several seconds (see blue and cyan curves on the Fig. 3.1-30). On the other hand, at the cooling water temperatures below 10 °C, the capacity of the cooling system has not allowed CW laser operation.

Thus, the temperature of the laser pumped channel has to be high enough to suppress triplet absorption and low enough to prevent other thermally induced parasitic effects. Moreover, a temperature not exceeding 50 - 60 °C is required for long-term CW laser operation due to irreversible degradation of F_2^- color centers at higher temperatures. The optimal temperature of the crystal cooler depends on numerous factors: cooling module construction, LD pump power and pump beam geometrics, etc.

3.1.5. Conclusion

Room temperature absorption and emission spectra and radiative lifetimes for new $Yb^{3+}:\text{CaF}_2$, and $Yb^{3+}:\text{PbMoO}_4$ crystals were measured. For $Yb^{3+}:\text{PbMoO}_4$ crystal the measurement were carried out for different polarizations of the radiation ($E \perp C$ and $E \parallel C$). Rather short radiative lifetime of 210 μs and maximum emission cross-section of $3 \times 10^{-20} \text{ cm}^2$ were determined for $Yb^{3+}:\text{PbMoO}_4$ crystal. For the $Yb^{3+}:\text{CaF}_2$ crystal radiative lifetime as long as 2500 μs at the laser emission cross-section of $0.25 \times 10^{-20} \text{ cm}^2$ was measured. Several samples of $Yb^{3+}:\text{CaF}_2$ crystals have been grown and prepared for laser experiments.

Mathematical model of two-manifold LD pumped laser have been developed. The model is based on steady state rate equations for the laser medium and transport equations for radiation. The laser characteristics $Yb^{3+}:\text{CaF}_2$, and $Yb^{3+}:\text{PbMoO}_4$ crystals were evaluated and compared with the characteristics of $Yb^{3+}:\text{YAG}$ and $Yb^{3+}:\text{KYW}$ crystals using developed model and experimental data on cross-sections and radiative lifetimes. The modeling of $Yb^{3+}:\text{YAG}$, $Yb^{3+}:\text{YAG}$, and $Yb^{3+}:\text{CaF}_2$ lasers was carried out for the laser crystals thickness of 0.3 cm. It was

shown that for this condition the $\text{Yb}^{3+}:\text{CaF}_2$ crystal can exhibit lower threshold and higher efficiency than these of $\text{Yb}^{3+}:\text{YAG}$ crystal. The advantage in efficiency for $\text{Yb}^{3+}:\text{CaF}_2$ crystal was found to be especially high at low and medium LD pump intensities powers ($<30 \text{ kW/cm}^2$). Significant heterogeneous spreading of absorption and emission lines and small Stark levels splitting have determined higher threshold and lower efficiency for $\text{Yb}^{3+}:\text{PbMoO}_4$ crystal.

The developed model was also used for evaluation of the laser characteristics of LiF crystal with F_2^- color centers under LD pumping at 960 – 980 nm wavelengths. The nanoseconds scale of radiative lifetime of $\text{LiF}:\text{F}_2^-$ laser crystal (55 ns) is compensated by high values of absorption and emission cross-sections ($7 \times 10^{-17} \text{ cm}^2$ and $8 \times 10^{-17} \text{ cm}^2$ respectively). As a result, surprisingly low threshold and up to 30 % conversion efficiency for this laser medium were estimated.

The experiments on LD pumping of $\text{Yb}^{3+}:\text{CaF}_2$ crystals have been carried out for $\text{Yb}^{3+}:\text{CaF}_2$ crystals samples with various Yb-ions concentrations. To make a comparisons the laser experiments were repeated for $\text{Yb}^{3+}:\text{YAG}$ and $\text{Yb}^{3+}:\text{KYW}$ crystals using the same laser cavity configurations and pumping conditions. Compared with $\text{Yb}^{3+}:\text{YAG}$ crystal the $\text{Yb}^{3+}:\text{CaF}_2$ crystal has demonstrated twice lower threshold, higher slope efficiency (68 % versus 59 %) and much broader linewidth of laser oscillation. Experimental results were found to be in good accordance with computer simulations.

Quasi-CW and CW laser oscillations in LiF crystal with F_2^- color centers have been demonstrated for the first time under direct LD pumping at 965 - 970 nm wavelength. The $\text{LiF}:\text{F}_2^-$ crystal laser parameters were investigated in a wide range of laser pulses repetition rate (from 5 Hz to 10 kHz) and for different crystal temperatures (from 5 °C to 60 °C).

The slope efficiency of the $\text{LiF}:\text{F}_2^-$ crystal laser oscillations up to 14 % was measured at low repetition rates of the laser pulses (5 – 10 Hz). With the use of temperature control and forced crystal cooling stable QCW (at the pulses repetition rate up to 6.3 kHz and 50 % off-duty ratio) and CW $\text{LiF}:\text{F}_2^-$ laser operation were achieved at 7 % slope efficiency.

We expect that the efficiency of LD pumped $\text{LiF}:\text{F}_2^-$ crystal laser oscillations could be increased up to 30 – 40 % by optimization of the laser cavity and crystal parameters.

3.1.6. References

- 1 P. Peterson, A. Gavrielides and P. M. Sharma” CW theory of a laser diode-pumped two-manifold solid state laser” Optics communications v.109, p.282 (1994)
- 2 T. Y. Fan and R. L. Byer, “Modeling and CW operation of a quasi-three-level 946 nm Nd:YAG laser,” IEEE J. Quantum Electron. QE-23, p.605 (1987)
- 3 P. Peterson, A. Gavrielides and M. P. Sharma “Cw theory of a diode pumped solid state laser in a resonant pump cavity” Optics communications v.116, p.123 (1995)
- 4 DeLoach, L.D.; Payne, S.A.; Chase, L.L.; Smith, L.K.; Kway, W.L.; Krupke, W.F. “Evaluation of absorption and emission properties of Yb³⁺ doped crystals for laser applications” IEEE Journal of Quantum Electronics, v.29 p.1179 (1993)
- 5 Krupke, W.F.” Ytterbium solid-state lasers. The first decade”, IEEE Journal of Selected Topics in Quantum Electronics, v.6, p.1287 (2000)
- 6 M. Jacquemet, F. Balembois, S. Chénais, F. Druon, P. Georges, R. Gaumé and B. Ferrand “First diode-pumped Yb-doped solid-state laser continuously tunable between 1000 and 1010 nm” Applied Physics B, v.78, p.13 (2004)
- 7 S.V. Vassiliev, S.B. Kravtsov, T.T. Basiev, V.A. Sychugov, R.R. Gerke, T.G. Dubrovina, I.U. Usypov, S.L. Shevchuk, Y.P. Maishev ”Efficient dielectric diffraction gratings: novel approaches to scaling-up the output of narrowband lasers” Laser Physics v.14, .p.1457 (2004)
- 8 **T.T. Basiev, S.B. Mirov**, *Room temperature tunable color center lasers*, Laser Science and Technology Book Series, Gordon and Breach Sciences Publishers/Harwood Acad. Publishers, Vol. 16, 1994.
- 9 **W. Gellerman, A. Muller, D. Wandt, S. Wilk, F. Luty**, Formation, optical properties and laser operation of F₂⁻ centers in LiF, J. Appl. Phys. Vol. 61, Page 1297, 1987
- 10 **T.T. Basiev, P.G. Zverev, A.G. Papashvilli, V.V. Fedorov**, *Temporal and spectral characteristics of a tunable LiF:F₂⁻ color-center crystal laser*, Quantum Electronics, Vol. 27, Page 574, 1997

3.2 Tungstate and molybdate crystals doped with Nd^{3+} ions for high efficient 1 μm lasers.

3.2.1 Spectroscopic properties of Nd^{3+} ions in tungstate and molybdate crystals.

To evaluate the lasing properties of self Raman capable crystals of tungstates and molybdates doped with Nd^{3+} ions the investigation of spectroscopic properties of neodymium ions was carried out. For investigated crystals of tungstates $\text{BaWO}_4:\text{Nd}^{3+}$, $\text{SrWO}_4:\text{Nd}^{3+}$ and $\text{PbWO}_4:\text{Nd}^{3+}$ and molybdates $\text{SrMoO}_4:\text{Nd}^{3+}$ and $\text{PbMoO}_4:\text{Nd}^{3+}$ absorption spectra, $^4\text{F}_{3/2}$ metastable fluorescent lifetimes and fluorescence spectra were measured.

The absorption spectra of tungstate crystals are shown in Fig.3.2.1. It's necessary to mention that in tested tungstate crystals for crystals synthesized along optical “c” axis ($\text{E} \perp \text{c}$ for all polarizations of incidence light) noticeable dependence of Nd^{3+} absorption and fluorescence spectra on the polarization of incidence or excitation light was not observed. As can be seen from the Fig.3.2.1 the moderate absorption coefficient of 1 cm^{-1} at the laser diode excitation wavelength can be obtained for $\text{BaWO}_4:\text{Nd}^{3+}$ crystal due to small distribution coefficient of Nd^{3+} ions caused by large difference between Ba^{2+} and substituting Nd^{3+} ionic radii. This result in rather low concentrations of neodymium ions of 0.1-0.2 at.% even for crystals with additional charge compensating co-dopants (Na, Nb). The situation is much more promising for $\text{SrWO}_4:\text{Nd}^{3+}$ crystal where difference between Sr^{2+} and Nd^{3+} ionic radii is much less and synthesis of rather heavily doped (up to 1-2 at. %) crystals of high optical quality is possible. Similar situation is realized for lead tungstate crystals doped with neodymium ions ($\text{PbWO}_4:\text{Nd}^{3+}$) which results in 4 times higher absorption coefficient of 4 cm^{-1} for diode laser excitation. Higher absorption coefficients for strontium and lead tungstates allows to use much shorter length of active elements for laser action ensuring about 80% absorption of incidence pump light. This is extremely important for the case of diode pumping where strong focusing of pump radiation inside the crystal with short length of the pump beam waist are usually applied.

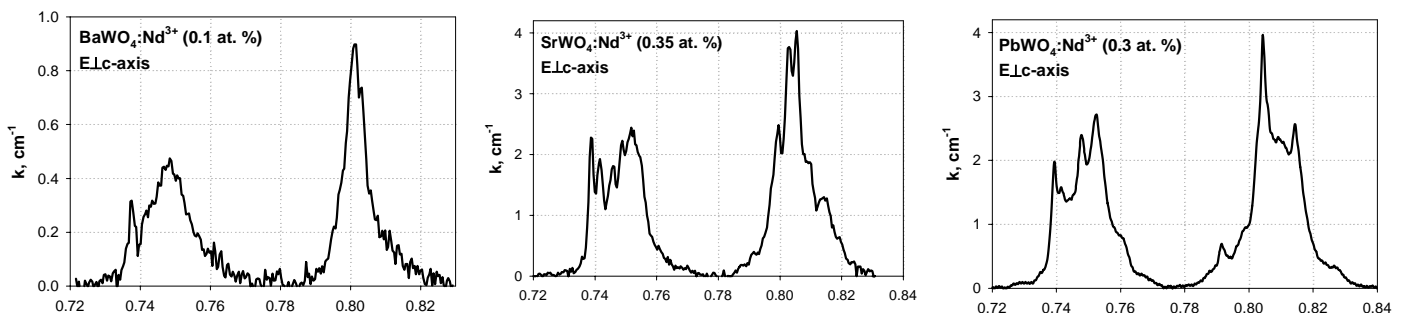


Fig. 3.2.1 Absorption spectra of Nd^{3+} ions in tungstate crystals.

The absorption spectra of the $\text{SrMoO}_4:\text{Nd}^{3+}$ and $\text{PbMoO}_4:\text{Nd}^{3+}$ molybdate crystals with close Nd^{3+} ions concentration of about 1 at. % are shown in Fig.3.2.2. As investigated molybdate crystals are characterized by anisotropic optical properties for the light polarized along different crystallographic axis absorption spectra shown in Fig.3.2.2 were measured for different orientations

of the incidence light polarization with respect to crystallographic c -axis ($E \perp C$ and $E \parallel C$). As follows from Fig.3.2.2, the absorption at diode laser excitation wavelength for $E \parallel c$ orientation for $\text{SrMoO}_4:\text{Nd}^{3+}$ crystal is approximately 4.5 times smaller and for $E \perp c$ orientation ~ 3.5 times smaller than that for $\text{PbMoO}_4:\text{Nd}^{3+}$ crystal. Peak absorption wavelengths for $E \parallel c$ and $E \perp c$ orientations are slightly different: 804 nm for $E \parallel c$ and 806 nm for $E \perp c$ and almost coincide for both crystals. The full width at half-maximum (FWHM) of the absorption peak for $\text{SrMoO}_4:\text{Nd}^{3+}$ crystal in $E \parallel c$ orientation is about 6 nm that is larger than for $\text{PbMoO}_4:\text{Nd}^{3+}$ crystal (4 nm). As can be seen from the figure these crystals should be properly oriented regarding pump light polarization as absorption at laser diode pumping wavelength differs 2.5-3 times for different polarizations. For proper pump light polarization the absorption coefficient as high as 5.5 cm^{-1} for $\text{SrMoO}_4:\text{Nd}^{3+}$ crystal and 17 cm^{-1} for $\text{PbMoO}_4:\text{Nd}^{3+}$ crystal respectively can be realized.

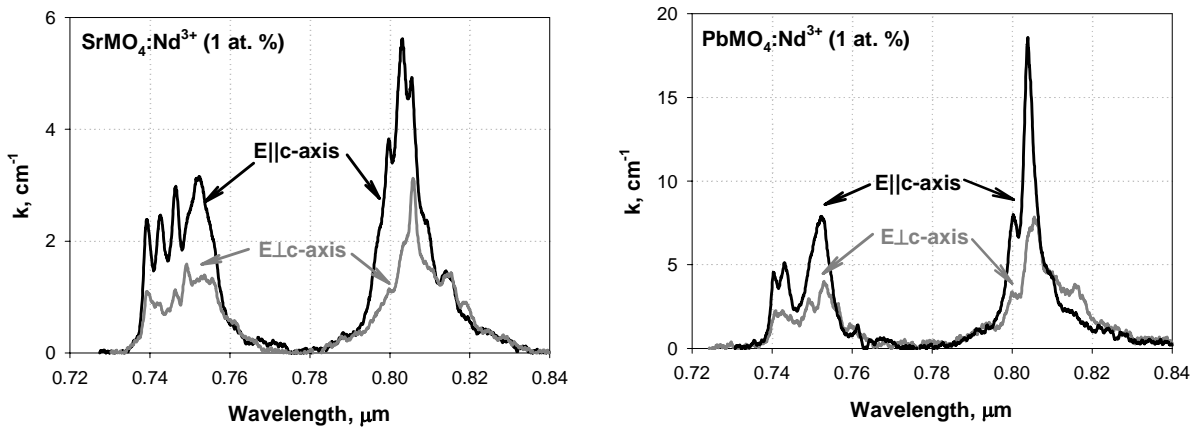


Fig. 3.2.2 Polarized absorption spectra of Nd^{3+} ions in molybdate crystals.

The fluorescence decay time for $^4\text{F}_{3/2}$ metastable level of Nd^{3+} ion in the investigated tungstate and molybdate crystals was measured under resonant excitation of $^4\text{F}_{3/2}$ level by nanosecond pulses of tunable laser based on LiF crystal with F_2^+ color centers ($\lambda=890\text{-}1050 \text{ nm}$) pumped by the second harmonic of $\text{GGG}:\text{Nd}^{3+}$ laser ($0.531 \mu\text{m}$). The measured experimental decay curves for the tested tungstate and molybdate crystals doped with Nd^{3+} ions were single exponential which demonstrates absence of Nd^{3+} optical centers with sufficiently different spectroscopic properties in all these crystals. As an example the decay curves of molybdate crystals are shown in Fig.3.2.3 and all the data on $^4\text{F}_{3/2}$ level lifetimes are summarized in Table 3.2.1. As can be seen from the table the shortest lifetimes of metastable $^4\text{F}_{3/2}$ level can be observed in lead containing crystals both in case of tungstates and molybdates. The shortening of $^4\text{F}_{3/2}$ level lifetime for crystals with practically equal Nd^{3+} ions concentration results from increase in radiative probabilities (and thus integral fluorescence cross-section) for transitions originating from $^4\text{F}_{3/2}$ level as nonradiative decay from this metastable

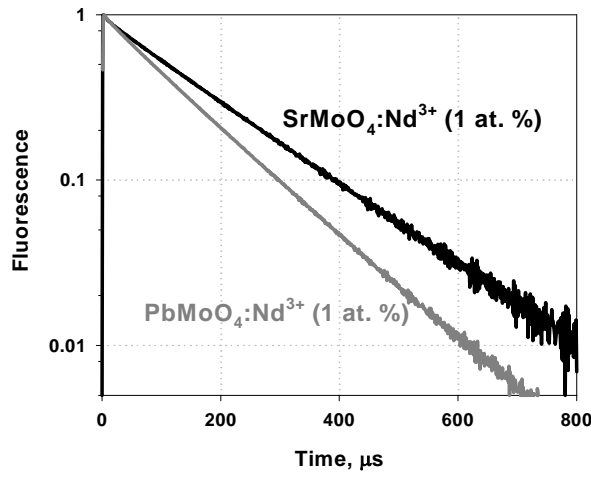


Fig. 3.2.3 Example of measured decay curves for $^4F_{3/2}$ metastable level of Nd^{3+} ions in investigated molybdate crystals.

Crystal	Nd^{3+} ions conc., at. %	$^4F_{3/2}$ level lifetime, μs
$BaWO_4:Nd^{3+}$	0.18	220
$SrWO_4:Nd^{3+}$	1.0	210
$PbWO_4:Nd^{3+}$	0.6	190
$SrMoO_4:Nd^{3+}$	1.0	180
$PbMoO_4:Nd^{3+}$	1.0	140

Table 3.2.1.

level is negligible. As can be also seen from the Table 3.2.1 the shortest radiative lifetime and thus highest fluorescence transition probability were obtained for lead molybdate crystal which demonstrates very good perspectives for using this crystal for laser applications. Though it should be mentioned here that for all investigated molybdate crystals and lead tungstate crystal the lifetime of $^4F_{3/2}$ level is shorter than that for well known YAG: Nd^{3+} oxide crystal.

We observed that the difference in lifetimes for the tested crystals is not as strong as in absorption coefficients. This can be explained by strong variation only for Ω_2 Judd Ofelt intensity parameter, which is responsible for $^4I_{9/2}-^4F_{5/2}$ absorption, while the difference for Ω_4 and Ω_6 intensity parameters, which responsible for $^4F_{3/2}$ level lifetime, is much smaller.

In Fig.3.2.4 the fluorescence spectra of tungstate and molybdate crystals are shown. As can be seen from Fig.3.2.4 the shapes of Nd^{3+} ions fluorescent signal in tungstate crystals is quite similar with smooth shift of fluorescence maximum from 1055 nm for $BaWO_4:Nd^{3+}$ crystal to 1057 nm for $SrWO_4:Nd^{3+}$ crystal and to 1058 nm for $PbWO_4:Nd^{3+}$ crystal. This wavelength shift correlates well

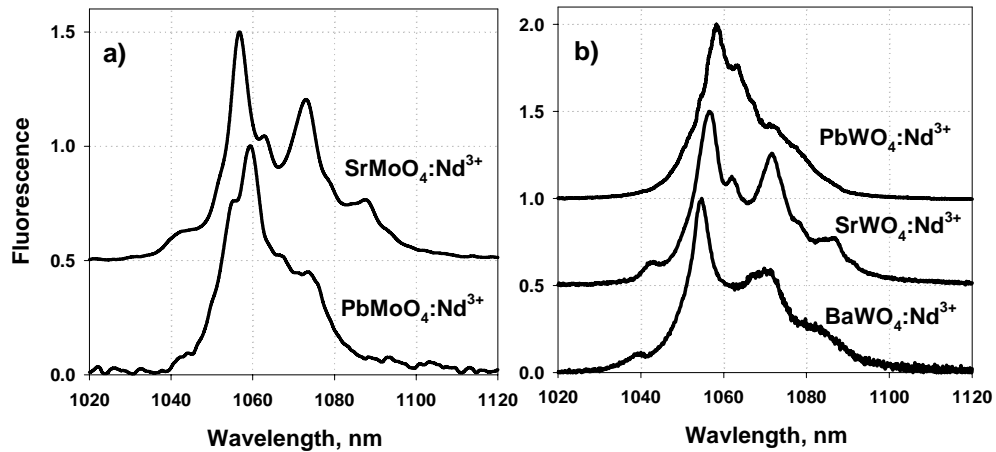


Fig. 3.2.4 Fluorescence spectra of molybdate (a) and tungstate (b) crystals.

with increase of covalent bonding strength for this Ba, Sr, Pb series. The fluorescent maxima in molybdate crystals are similar shifted from 1057 nm to 1059 nm for $\text{SrMoO}_4\text{:Nd}^{3+}$ and $\text{PbMoO}_4\text{:Nd}^{3+}$ crystals respectively.

3.2.2 Laser properties of Nd^{3+} ions in tungstate and molybdate crystals under laser diode pumping.

In lasing experiments the neodymium laser cavity was formed by back flat dichroic mirror with high transmittance at the pumping (800-810 nm) wavelength and totally reflecting at oscillating wavelengths about 1 μm and curved ($r=120$ mm) output mirror with reflectivities 98% and 92% at oscillating wavelengths. The cavity was 100 mm long and was close to hemispherical.

The pumping diode laser was fiber coupled and had special beam forming optical system (FO) at the fiber output end to produce rather prolonged pump beam waist of 4 mm long and beam waist diameter of 400 μm . Due to the fiber, the pumping beam was circular polarized resulting in polarization independence of tested crystals oscillations. For pumping radiation wavelength 805 nm was used and no temperature tuning was applied except of KGW:Nd^{3+} crystal, which was pumped at absorption maximum wavelength of 809 nm. Though in all experiments real absorbed energy was measured for tested sample. All the crystals were pumped with rectangular pulses 350 μs long with repetition rate 100 Hz to avoid thermal effects.

Despite of very low neodymium concentration and thus very low pump absorption the laser oscillations in new $\text{BaWO}_4\text{:Nd}^{3+}$ crystal were obtained under diode pumping for the first time (see Fig.3.2.5). Due to very low absorption (0.49 cm^{-1}), large crystal length ($l=37.7$ mm), and relatively short length of pumping beam waist (~ 4 mm) the oscillation threshold energy was about 1 mJ for both output couplers and slope efficiency of only 6% and 9% was obtained. The input-output

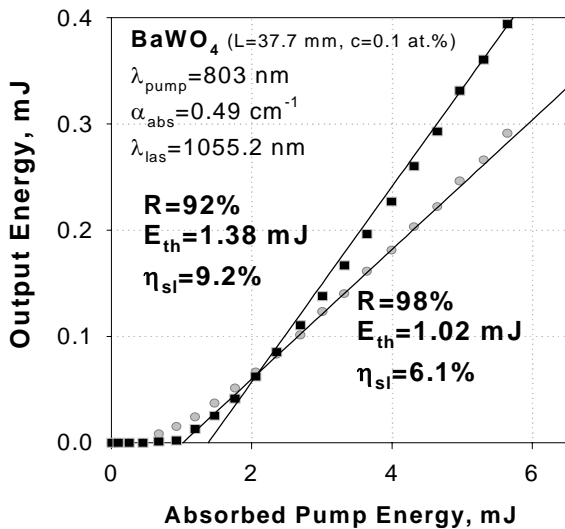


Fig. 3.2.5 Input-output characteristics of $\text{BaWO}_4\text{:Nd}^{3+}$ crystal oscillations under laser diode pumping.

characteristics of $\text{PbWO}_4\text{:Nd}^{3+}$ laser crystal with two different neodymium concentrations of 0.6 at.% and 0.3 at.% were measured and the results are presented in Fig.3.2.6. As can be seen from the Fig.3.2.6 twice higher oscillation threshold and approximately twice lower slope efficiency were obtained for the crystal with lower concentration of Nd^{3+} ions. For PbWO_4 crystal doped with higher concentration of Nd^{3+} 0.6 at.% the oscillation threshold as low as 0.47 mJ and slope efficiency of 13.4% were obtained for the output coupler with reflectivity 98%.

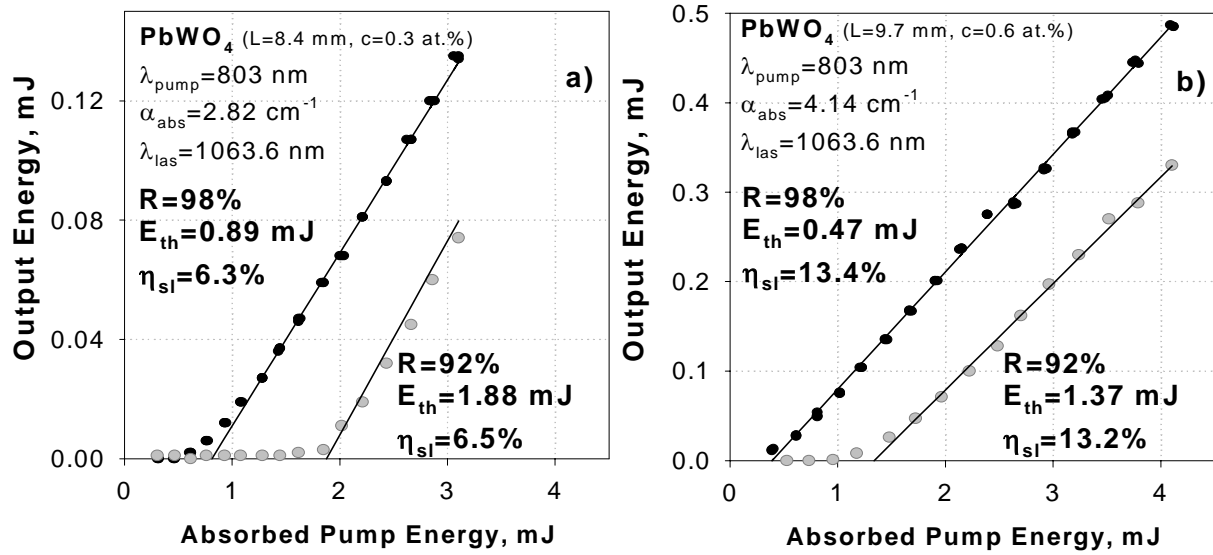


Fig. 3.2.6 Input-output characteristics of PbWO_4 crystal doped with Nd^{3+} ions in concentration 0.3 at.% (a) and 0.6 at.% (b) for different reflectivities of output mirror under laser diode pumping.

As can be seen from the Fig.3.2.7 both investigated molybdate crystals $\text{SrMoO}_4\text{:Nd}^{3+}$ and $\text{PbMoO}_4\text{:Nd}^{3+}$ are characterized by very low oscillation threshold lower than 0.4 mJ (for output coupler reflectivity 98 %). For $\text{SrMoO}_4\text{:Nd}^{3+}$ crystal the slope efficiency of 12.1 % was obtained ($R_{\text{oc}}=92$ %). The $\text{PbMoO}_4\text{:Nd}^{3+}$ crystal demonstrated highest slope efficiency of 21.0 % ($R_{\text{oc}}=92$ %) among the tested crystals despite twice lower Nd^{3+} concentration as compared to lead tungstate.

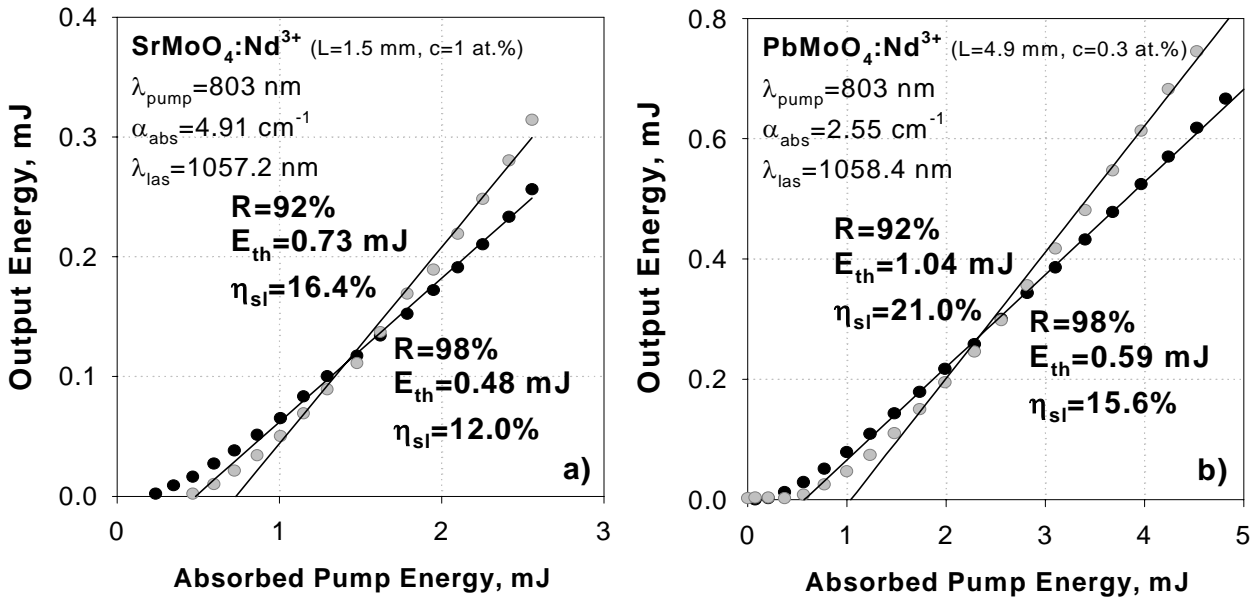


Fig. 3.2.7 Input-output characteristics of $\text{SrMoO}_4\text{:Nd}^{3+}$ (a) and $\text{PbMoO}_4\text{:Nd}^{3+}$ (b) crystals) for different reflectivities of output mirror under laser diode pumping.

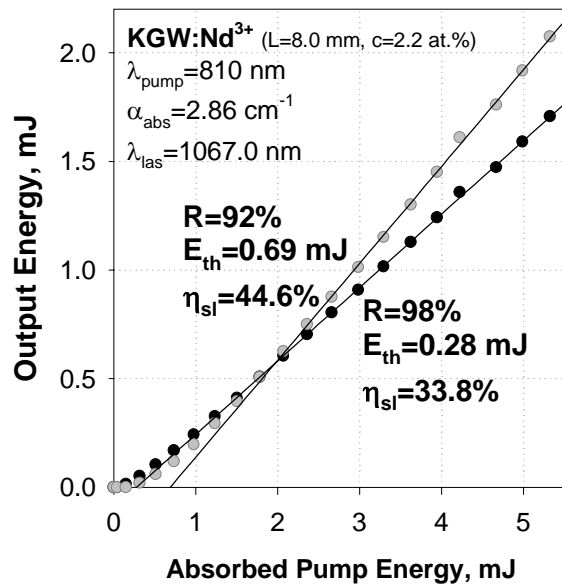


Fig. 3.2.8 Input-output characteristics of KGW:Nd³⁺ crystal for different reflectivities of output mirror

In Fig.3.2.8 the results for well known KGW:Nd³⁺ (2.2 at.%) crystal are also presented for comparison. To get maximum from the crystal the pumping wavelength was tuned to match properly the absorption maximum. Here the oscillation threshold less than 0.3 mJ and slope efficiency of 44.6 % were obtained for output coupler reflectivity of 92 %.

All results on oscillations in tungstate and molybdate crystals are summarized in Table 3.2.2.

Crystal	Length, mm	Concentration	Absorption	Threshold, mJ	η_{slope} , %	η_{tot} , %	Polarization
KGW:Nd	8	2.2%	88%	0.69	44.6	39	⊕
PbMoO ₄ :Nd	4.9	0.3%	69%	1.04	21.0	17	⊕
SrMoO ₄ :Nd	1.5	1%	32%	1.05	16.4	12.3	⊕
PbWO ₄ :Nd	9.7	0.6%	98%	0.47	13.4	12	⊕
BaWO ₄ :Nd	37.7	0.1%	80%	1.38	9.2	7	⊕
PbWO ₄ :Nd	8.4	0.3%	63%	0.89	6.3	4.5	⊕

Table 3.2.2.

3.2.3 Experimental study of LD pumped PbMoO₄:Nd³⁺ and SrMoO₄:Nd³⁺ laser

As can be easily seen from Table 3.2.2 the most efficient oscillations were obtained for PbMoO₄:Nd³⁺ and SrMoO₄:Nd³⁺ molibdate crystals. The evident limitation of the pumping scheme used in the previous section is circular polarization of LD pumping which did not allow to realize most efficient absorption for the molibdate crystals as absorption for E||c case is about 2.5-3 times higher than that for E⊥c case (see Fig.3.2.2). To avoid this drawback a set of experiments with pumping by individual laser diode having linear polarization of output beam was held.

The LD with 200×1 μm² emitting area and 2 W maximum output power was used for the experiments. To minimize the heat generation in the laser crystal the LD unit was driven by pulse power supply with current pulse duration of about 250 μs and 5 Hz repetition rate. The LD temperature and hence the emission wavelength was adjusted and stabilized by Peltier thermo electric cooler with

0.1 °C accuracy. The temperature shift of the LD emission was about 0.22 nm/°C and the LD emission linewidth was about 1.5 nm that is 2.5 times smaller than the $\text{PbMoO}_4\text{:Nd}^{3+}$ crystal absorption linewidth (see Fig.3.2.2). Thus, the efficient LD pumping of the $\text{PbMoO}_4\text{:Nd}^{3+}$ crystal could be achieved in the wide range of LD temperatures.

The LD unit emission was collimated and focused by special optical appliance to form in the laser crystal symmetrically shaped pumping spot. The schematic of spatial distribution of the LD emission in vicinity of the focusing system focal point are shown in Fig.3.2.9. The focal spot is square shaped with the minimum size of $100 \times 100 \mu\text{m}^2$. The focal spot dimensions are about $200 \times 200 \mu\text{m}^2$ at 0.5 mm distance from the focal point and $300 \times 300 \mu\text{m}^2$ at 0.8 mm distance. Thus, for these pumping conditions, the efficient length of the laser active element is limited by few millimeters.

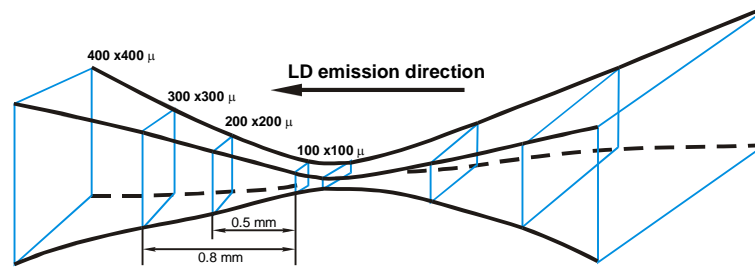


Fig. 3.2.9 Shape of focusing system focal point for individual laser diode pumping

Several samples of $\text{PbMoO}_4\text{:Nd}^{3+}$ and $\text{SrMoO}_4\text{:Nd}^{3+}$ crystals were prepared for the experiments. All samples were cut across *c*- axis, thus, $E \parallel C$ as well as $E \perp C$ LD pumping of the crystal was available. One side of all laser elements was coated by dichroic mirror with high transmission (>95 %) at LD pump wavelength (808 nm) and high reflection (>99.5 %) in the laser operational wavelengths range (1000 – 1200 nm), another side of the laser element was AR coated.

Schematic of the $\text{PbMoO}_4\text{:Nd}^{3+}$ and $\text{SrMoO}_4\text{:Nd}^{3+}$ oscillators optical cavity consisted of laser crystal and output coupler. In major part of the experiments, the concave mirrors with 25 mm, 50 mm, and 100 mm radius of curvature (ROC) and 95 % reflectivity at the laser fundamental wavelength were used as OC's. The cavity length L_C was variable from minimum of 5 - 7 mm (depending on crystal length) to several centimeters.

The Molectron J4-02 pyroelectric detector was used for measurements of the laser energy characteristics. The high precision IMO-2N laser power meter was used for Molectron detector calibration. Temporal characteristics of the laser pulses were registered by avalanche photo diode and Tektronix TDS 3052B digital oscilloscope with temporal resolution of about 1 ns.

3.2.4 LD pumped $\text{PbMoO}_4\text{:Nd}^{3+}$ and $\text{SrMoO}_4\text{:Nd}^{3+}$ crystals parameters in free-running mode of operation

At the first series of experiments the LD pumped $\text{PbMoO}_4\text{:Nd}^{3+}$ and $\text{SrMoO}_4\text{:Nd}^{3+}$ laser crystals parameters in free-running mode of operation were investigated. Large non-uniformity of LD pump near the focal point was obviously unfavorable for correct estimation of the maximum performance of the laser medium (see Fig.3.2.9). Therefore, all experiments were also carried out for well known $\text{YVO}_4\text{:Nd}^{3+}$ and $\text{GdVO}_4\text{:Nd}^{3+}$ vanadate laser crystals using the same optical cavity configurations and pumping conditions as for $\text{PbMoO}_4\text{:Nd}^{3+}$ and $\text{SrMoO}_4\text{:Nd}^{3+}$ molybdate laser elements. Both vanadate crystals were of high optical quality, had the same orientation (*a*-cut), and similar dielectric coatings. The parameters of all laser elements are summarized in the Table 3.2.3.

In Fig.3.2.10 the input-output characteristics of free-running LD pumped $\text{PbMoO}_4\text{:Nd}^{3+}$ oscillator are presented and compared with vanadate crystal characteristics. The oscillator output power (solid curves, left y-axis) and laser efficiency (dash curves, right y-axis) with respect to the total emitted LD power are

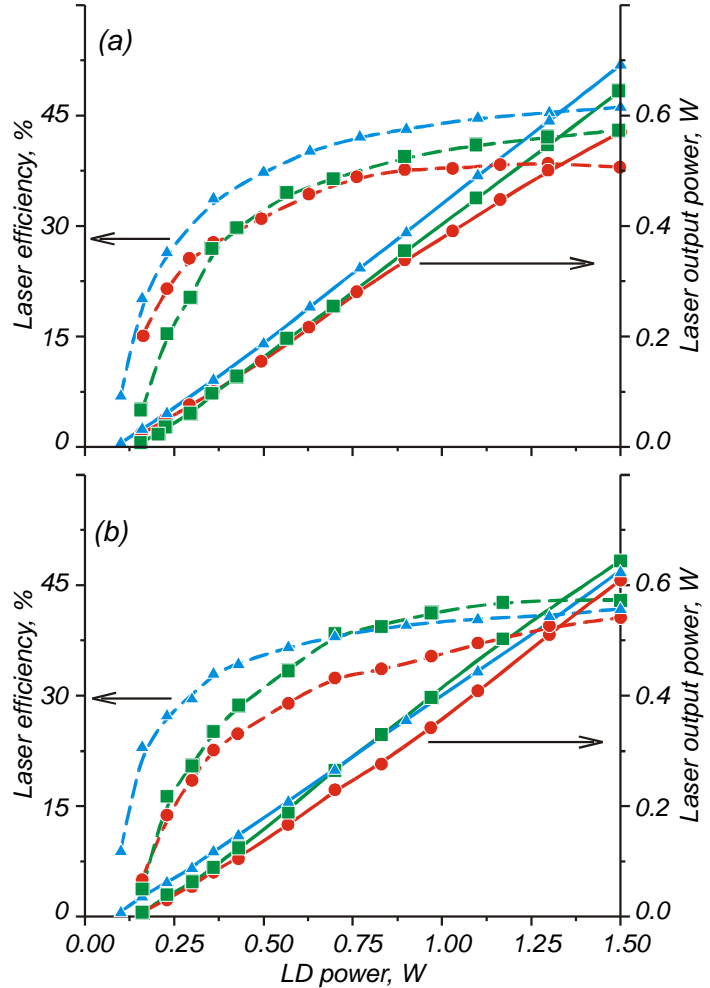


Fig.3.2.10 Input-output characteristics of free-running mode LD pumped $\text{PbMoO}_4\text{:Nd}^{3+}$ oscillator in comparison with vanadate crystal.

#	Crystal	Nd wt., %	Thickness, mm	Absorption (E C), %	Max. output power, mW	Slope efficiency, %
S1	$\text{PbMoO}_4\text{:Nd}^{3+}$	0.3	1	80	570	53
S2		0.3	3	95	610	47
S3		2.0	1	98	645	49
S4		2.0	3	100	644	49
S5	$\text{SrMoO}_4\text{:Nd}^{3+}$	2.0	3	95	673	47
S6	$\text{YVO}_4\text{:Nd}^{3+}$	1.0	1	90	690	55
S7	$\text{GdVO}_4\text{:Nd}^{3+}$	2.5	2.5	100	627	44

Table 3.2.3.

shown in the figure. Upper plot corresponds to 1 mm and lower plot to 3 mm thickness of the crystal. Circles and squares show the experimental results for 0.3 % and 2 % Nd concentration of $\text{PbMoO}_4:\text{Nd}^{3+}$ crystal, while the triangles show results for vanadate crystals. All curves correspond to the 95 % OC reflectivity, 50 mm OC ROC and 5 mm cavity length (i.e. lasers has emitted multiple transverse modes).

Among 1 mm thick crystals the $\text{YVO}_4:\text{Nd}^{3+}$ crystal demonstrates lowest threshold and highest output power and lasing efficiency. However, the vanadate laser slope efficiency calculated with respect to the absorbed LD pump is only slightly higher than that for 0.3 at.% low Nd concentration $\text{PbMoO}_4:\text{Nd}^{3+}$ crystal (55 % vs. 53 %).

Difference in maximum output power is smaller for almost totally absorbing 3 mm thick crystals. Moreover, the $\text{PbMoO}_4:\text{Nd}^{3+}$ crystal demonstrated even higher output and slope efficiency than that of analogous $\text{GdVO}_4:\text{Nd}^{3+}$ crystal: 644 mW vs. 627 mW and 49 % vs. 44 %. Nevertheless, the $\text{GdVO}_4:\text{Nd}^{3+}$ crystal still demonstrated lower lasing threshold and higher output at low LD pump power (< 0.75 W).

The $\text{YVO}_4:\text{Nd}^{3+}$ and $\text{GdVO}_4:\text{Nd}^{3+}$ lasing properties were also measured using curved OC's with 85 % and 75 % reflectivity. It was found that lasers output is the same or a little bit lower than that obtained for OC with 95 % reflectivity.

In Fig.3.2.11 the input-output characteristics of free-running mode $\text{SrMoO}_4:\text{Nd}^{3+}$ oscillator versus absorbed LD pumping are presented. Results in Fig.3.2.11 corresponds to the 3 mm thick $\text{SrMoO}_4:\text{Nd}^{3+}$ crystal with 2 at. % concentration of Nd^{3+} and almost total absorption (95 %) of polarized LD pump. Measurements were carried out for OCs with different reflectivity (see plot legends). The laser cavity lengths were adjusted to achieve maximum laser output.

As can be seen from the figure, the laser slope efficiency as well as its output power grows with increase of the OC reflectivity which can be attributed to high optical quality of the laser crystal and low level of the parasitic losses (including the parasitic losses stimulated by intense pumping and laser emission).

Parameters of $\text{PbMoO}_4:\text{Nd}^{3+}$ and $\text{SrMoO}_4:\text{Nd}^{3+}$ laser crystals operating in free-running mode were compared with the corresponding parameters of $\text{YVO}_4:\text{Nd}^{3+}$ $\text{GdVO}_4:\text{Nd}^{3+}$ vanadate crystals. To make comparison more correct all experiments were

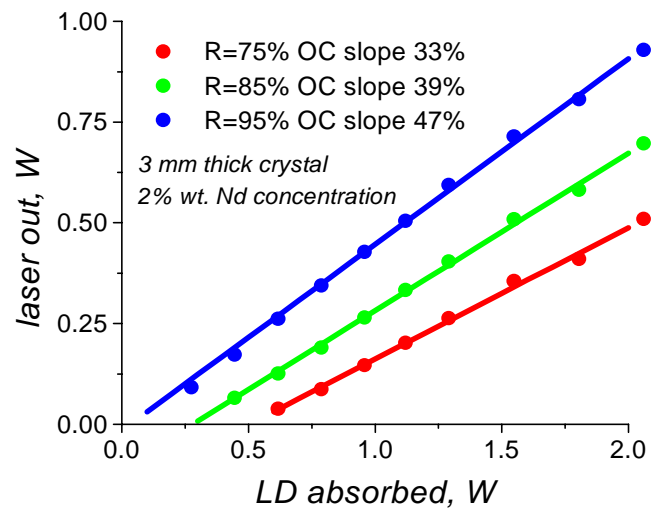


Fig. 3.2.11 Input-output characteristics of free-running mode LD pumped $\text{SrMoO}_4:\text{Nd}^{3+}$ oscillator.

carried out using the same measurements techniques, the cavity configurations, and the pumping conditions (polarized LD up to 1.5 W). Compared with 3 mm thick $\text{PbMoO}_4:\text{Nd}^{3+}$ crystal and 2.5 mm thick $\text{GdVO}_4:\text{Nd}^{3+}$ crystal, the $\text{SrMoO}_4:\text{Nd}^{3+}$ crystal demonstrated highest output power at 1.5 W pump, the slope efficiency higher than that of $\text{GdVO}_4:\text{Nd}^{3+}$, and almost the same slope efficiency as for $\text{PbMoO}_4:\text{Nd}^{3+}$. Applying of 1 mm thick crystals was more favorable for our experimental conditions due to large spatial non-uniformity of the pump beam. However, compared with 1 mm thick $\text{PbMoO}_4:\text{Nd}^{3+}$ crystal with the same Nd^{3+} ions concentration, $\text{SrMoO}_4:\text{Nd}^{3+}$ crystal demonstrated lower slope efficiency but higher output power. Only laser characteristics of 1 mm thick $\text{YVO}_4:\text{Nd}^{3+}$ crystal exceeded those of 3 mm thick $\text{SrMoO}_4:\text{Nd}^{3+}$ crystal (however, we have to mention that the optical quality of the $\text{YVO}_4:\text{Nd}^{3+}$ crystal was outstanding). Thus, the $\text{PbMoO}_4:\text{Nd}^{3+}$ and $\text{SrMoO}_4:\text{Nd}^{3+}$ molybdate crystals demonstrate very favourable almost the same lasing properties in free-running mode of operation which can compete with those of best vanadate laser crystals.

We explain this surprisingly little difference in laser characteristics of $\text{PbMoO}_4:\text{Nd}^{3+}$ and $\text{SrMoO}_4:\text{Nd}^{3+}$ crystals by higher level of various parasitic losses, which occur in the $\text{PbMoO}_4:\text{Nd}^{3+}$ crystal. The parasitic losses arising from up-conversion and excited state absorption processes in Nd^{3+} centers can limit the maximum intensity of LD pumping and hence decrease laser properties of $\text{PbMoO}_4:\text{Nd}^{3+}$ crystal. One may expect, that further enhancement of the $\text{PbMoO}_4:\text{Nd}^{3+}$ crystal synthesis technology will allow to achieve better laser characteristics than for vanadate crystals known as one of the most efficient laser medium for LD pumped lasers.

3.2.5 LD pumped $\text{PbMoO}_4:\text{Nd}^{3+}$ and $\text{SrMoO}_4:\text{Nd}^{3+}$ laser crystals parameters in passively Q-switched mode of operation.

During the experiments it was found out that for our LD pump parameters passively Q-switched mode of the $\text{PbMoO}_4:\text{Nd}^{3+}$ crystal laser operation could be achieved only for “weak” saturable absorbers (SA’s) with initial transmission $T_0 > 85\%$. In contrast, the passive Q-switching of $\text{SrMoO}_4:\text{Nd}^{3+}$, $\text{YVO}_4:\text{Nd}^{3+}$ and $\text{GdVO}_4:\text{Nd}^{3+}$ crystals was observed for SA’s with lower initial transmittance. The experiments on passive Q-switching of $\text{PbMoO}_4:\text{Nd}^{3+}$ laser were carried out using 3 mm thick LiF:F_2^- SA’s with initial transmission $T_0 = 86\%$ and 89% .

Parameters of the passively Q-switched $\text{PbMoO}_4:\text{Nd}^{3+}/\text{LiF:F}_2^-$ laser with 1.5 W LD pumping are presented in Fig.3.2.12. The laser pulse energy E_p , duration τ , repetition rate f , and average output power P are shown as functions of the relative cavity length (L_c/ROC). Measurements were carried out for 1 mm thick $\text{PbMoO}_4:\text{Nd}^{3+}$ crystal, SA with $T_0 = 89\%$, and two OC’s with 95% reflectivity and ROC equal to 25 mm and 50 mm (squares and circles on the plot). The LD pump focusing has corresponded to the maximum laser efficiency in free-running mode.

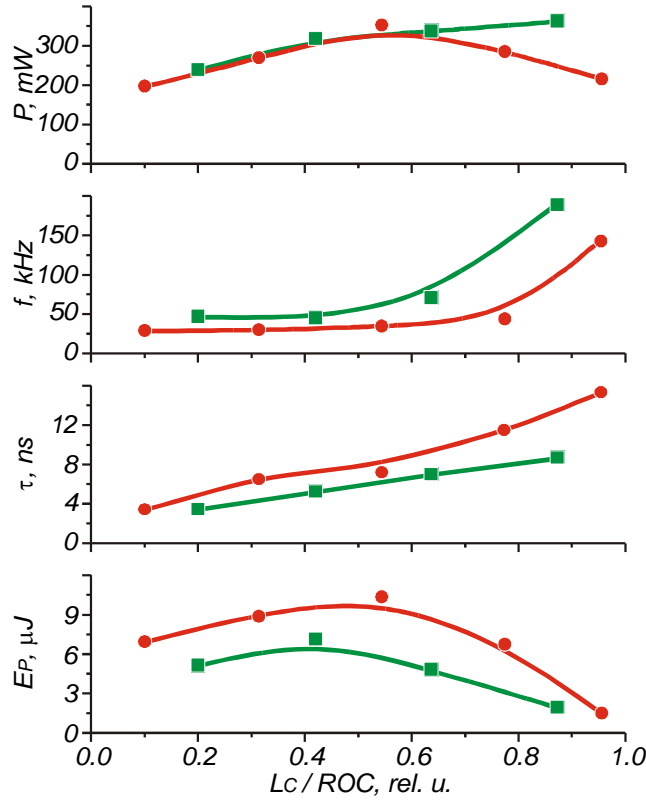


Fig. 3.2.12 Laser pulse energy E_p , duration τ , repetition rate f , and average output power P as function of the relative cavity length (L_c/ROC).

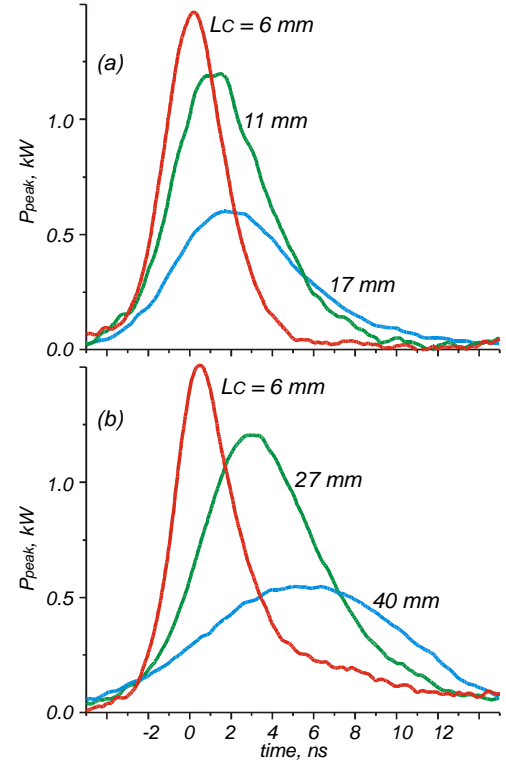


Fig. 3.2.13 Pulse shapes of passively Q – switched $PbMoO_4:Nd^{3+}/LiF:F_2^-$ laser with $T_0 = 89\%$ SA (OC ROC = 25 mm (a) and 50 mm (b)).

The laser pulse energy reaches maximum for $L_c/ROC \sim 0.5$ which corresponds to semi-confocal cavity configuration while the pulses duration increases monotonously with the cavity length. The laser with ROC = 25 mm produces shorter pulses of smaller energy at higher repetition rate. Thus, the laser average output was almost the same for both OC's with different curvature. With further cavity lengthening ($L_c/ROC \rightarrow 1$, semi-concentric cavity) the pulses repetition rate rapidly grows from 30 – 50 kHz to 150 – 200 kHz and the pulses energy goes down. The obtained maximum average power of the Q-switched laser - 360 mW is only 1.8 times lower than free running laser output - 645 mW. Such a decrease could be considered as minor for passively Q-switched lasers.

The nanosecond pulses of a passively Q – switched $PbMoO_4:Nd^{3+}/LiF:F_2^-$ laser with $T_0 = 89\%$ SA are shown in Fig.3.2.13 (OC ROC = 25 mm and 50 mm for part a and part b respectively). Pulses for different cavity lengths are normalized with respect to the pulse energy. As follows, pulses of shortest duration (3.5 ns) and highest peak power are corresponding to the minimal length of the laser cavity (6 mm). The pulses with highest energy ($L_c = 11$ mm on the part a and $L_c = 27$ mm on the part b) are corresponding to the semi-confocal cavity. At that, the pulses peak power is reduced due to increase of the pulses duration.

Parameters of the passively Q-switched vanadate crystal laser were investigated using 1 mm thick $\text{YVO}_4:\text{Nd}^{3+}$ crystal, 5 mm thick $\text{LiF}:\text{F}_2^-$ SA with $T_0 = 78\%$ and OC with 75 % reflectivity and 50 mm ROC. The $\text{YVO}_4:\text{Nd}^{3+}/\text{LiF}:\text{F}_2^-$ laser characteristics were measured as functions of the laser cavity length L_C and of the LD pump focusing.

The characteristics of passively Q-switched $\text{YVO}_4:\text{Nd}^{3+}/\text{LiF}:\text{F}_2^-$ laser were found to be very sensitive to the LD emission focusing. Displacement of LD pump focal point within 1 mm range causes almost 20 times decrease in Q-switched pulses repetition rate and 4 times increase of the pulses energy while the laser pulse duration slightly changes. At the narrowest LD focusing the Q-switched pulses repetition rate have exceeded 300 kHz with the sub- μJ pulses energy. We suppose, that the reason for this behavior is the anomalously high amplified spontaneous emission (ASE) that appears in the vanadate crystal at strong LD emission focusing. The ASE enforces early saturation of the SA and limits accumulation of population inversion in the laser crystal.

In the Fig.3.2.14. The $\text{PbMoO}_4:\text{Nd}^{3+}/\text{LiF}:\text{F}_2^-$ and $\text{YVO}_4:\text{Nd}^{3+}/\text{LiF}:\text{F}_2^-$ passively Q-switched lasers average output power P , pulses energy E_P , and peak power P_{peak} are represented as functions of the pulses repetition rate f . Open circles show the experimental data for $\text{PbMoO}_4:\text{Nd}^{3+}$ laser (for OC ROC equal to 25 mm and 50 mm respectively) and smaller symbols show data for $\text{YVO}_4:\text{Nd}^{3+}$ laser. The solid and dash curves show the data fit for molibdate and vanadate crystals respectively.

As follows from the figure, the $\text{PbMoO}_4:\text{Nd}^{3+}/\text{LiF}:\text{F}_2^-$ laser with higher reflectivity of the OC (95 % vs. 75 %) and smaller optical density of the SA (89 % vs. 78 %) demonstrates higher average output power and pulse energy at pulse repetition rates below 100 kHz. As a first assumption, these results confirm high performance of LD pumped $\text{PbMoO}_4:\text{Nd}^{3+}$ laser in passively Q-switched mode of operation.

To achieve a higher peak power of the passively Q-switched $\text{PbMoO}_4:\text{Nd}^{3+}$ laser oscillations, the laser cavity was equipped with a SA of a higher optical density ($T_0 = 86\%$). The experiments were carried out in the most compact laser cavity ($L_C = 6\text{ mm}$) using 95 % reflectivity OC with 50 mm ROC and the same crystal sample. For such cavity configuration the pulse energy of 11 μJ

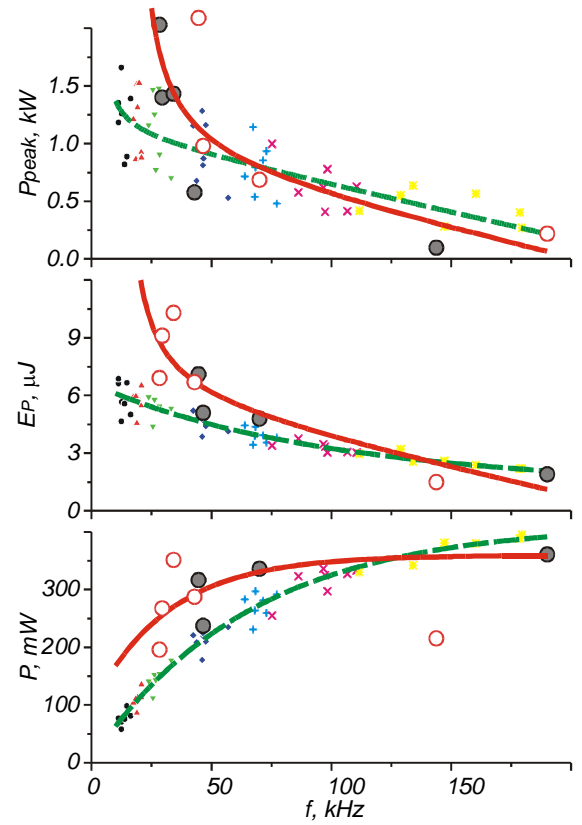


Fig. 3.2.14 Comparison of LD pumped $\text{PbMoO}_4:\text{Nd}^{3+}/\text{LiF}:\text{F}_2^-$ and $\text{YVO}_4:\text{Nd}^{3+}/\text{LiF}:\text{F}_2^-$ passively Q-switched lasers parameters.

and the pulse duration of 1.4 ns at the 7.5 kHz repetition rate were obtained. Hence, 3 % increase of the SAs optical density has caused two times shortening of laser pulses and 3 - 4 times increase of pulses peak power.

Using of the specially designed LiF:F_2^- saturable absorber with gradient concentration of F_2^- color centers and thus variable initial transmission along the crystal length allowed fast and accurate characterization of the passively Q-switched laser oscillations of LD pumped $\text{SrMoO}_4\text{:Nd}^{3+}$ crystal in wide range of the Q-switched pulse energies and repetition rates. In Fig.3.2.15 average power, pulse energy and pulse duration of the Q-switched $\text{SrMoO}_4\text{:Nd}^{3+}$ crystal laser oscillations are shown as function of pulse repetition rate. Measurements were carried out for 3 mm thick $\text{SrMoO}_4\text{:Nd}^{3+}$ crystal with 2 at. % Nd^{3+} concentration and 95 % pump absorption ($E||c$). OCs with ROC = 100 mm and reflectivities of 85 % and 75 % were used in the experiments.

OCs with ROC = 100 mm and reflectivities of 85 % and 75 % were used in the experiments. Green symbols and curves correspond to 85 % OC reflectivity and blue symbols and curves correspond to 75 % OC reflectivity respectively. Dash horizontal lines on the upper plot correspond to the maximum output power in the free-running mode of operation with the same OCs.

As can be seen from Fig.3.2.15, for the repetition rates higher than 30 kHz, the pulse energy and average power of the lasers with 85 % and 75 % reflectivities of OCs are almost the same. The pulse energy decreases monotonously with increase of the repetition rate, while the average power reaches maximum between 50 kHz and 80 kHz. At the maximum repetition rate of 300 – 350 kHz (not shown on the plot) the pulse energy declines to 0.5 – 0.75 μJ , pulse duration rises to 75 – 100 ns, and the average laser power slightly decreases (75 % from its maximum).

The maximum average power of the Q-switched laser with 75 % OC is about 410 mW at 65 kHz that is 80 % of the maximum output average power obtained for laser in free-running mode with the same OC. We consider this difference as very small taking into account the parasitic losses at uncoated ends of the saturable absorber and active losses for its saturation. The maximum average power of the Q-switched laser with 85 % OC was slightly higher than that for 75 % OC (430 mW at

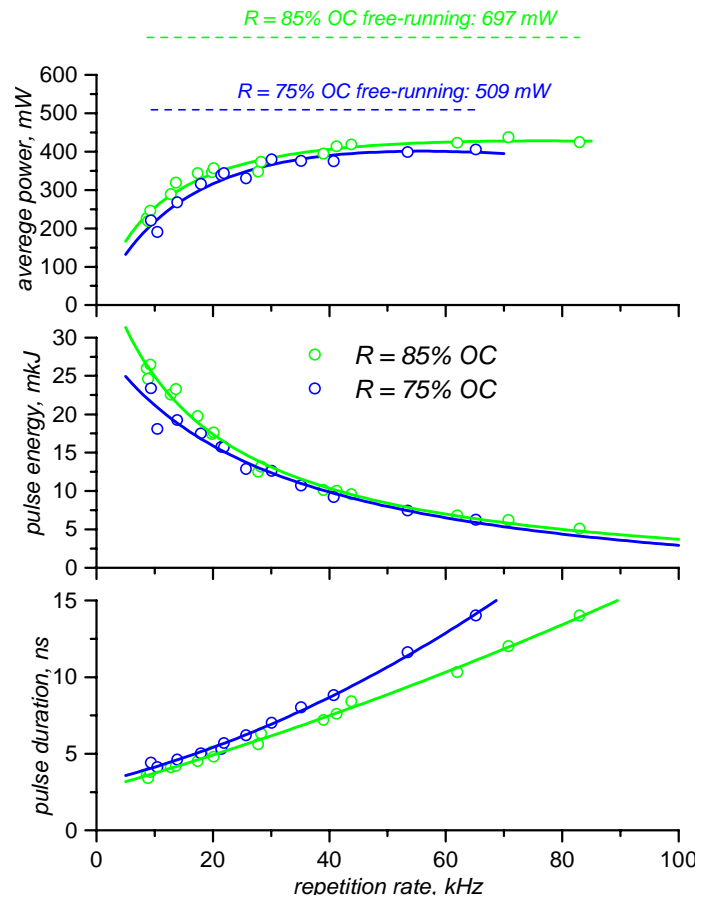


Fig. 3.2.15 Average power, pulse energy and pulse duration of the Q-switched $\text{SrMoO}_4\text{:Nd}^{3+}$ crystal laser oscillations as function of pulse repetition rate.

75 kHz), but much lower in comparison with the free-running laser output (697 mW). The larger difference in efficiency between Q-switched and free-running mode of operation could be explained by higher influence of the intracavity parasitic losses for the laser with higher reflectivity OC. Use of OC with 85 % reflectivity have provided shorter pulse durations (and hence higher peak power) in whole range of repetition rates.

The maximum pulse energies of the Q-switched $\text{SrMoO}_4:\text{Nd}^{3+}$ crystal of about 26 μJ for 85 % OC and 22 μJ for 75 % OC were measured at the repetition rates of 9 – 10 kHz. The average output at low repetition rates was approximately 2 times lower than the maximum output of the Q-switched laser at 65 – 75 kHz. Minimum pulse durations of 3.5 ns for 85 % OC and 4 ns for 75 % OC were measured at low repetition rates. Better performance of a passively Q-switched laser with 85 % OC could be explained by higher intracavity radiation intensity and hence deeper saturation of a laser transition. This leads to faster development of a Q-switched pulse, and more efficient extraction of energy accumulated in a laser medium for the same repetition rate of a Q-switched pulses. On the other hand, further increase of OC reflectivity causes lengthening of a laser pulse trailing edge and increases intracavity losses that reduce the laser efficiency and peak power. Thus, the OC reflectivity about 85 % looks optimal for our experimental conditions.

In Table 3.2.4 the characteristics of LiF:F_2^- passively Q-switched $\text{SrMoO}_4:\text{Nd}^{3+}$, $\text{PbMoO}_4:\text{Nd}^{3+}$, and $\text{YVO}_4:\text{Nd}^{3+}$ crystals are compared. The LD pumping conditions were the same, but experiments with $\text{PbMoO}_4:\text{Nd}^{3+}$ and $\text{YVO}_4:\text{Nd}^{3+}$ crystals were carried out for 1 mm thick samples, SAs were 3 mm thick and AR coated. In spite of use of uncoated SA and 3 times longer laser cavity (15 mm vs. 5 mm), the $\text{SrMoO}_4:\text{Nd}^{3+}$ crystal demonstrated highest pulse energy and efficiency at the comparable pulse duration. Comparison of other experimental data for $\text{SrMoO}_4:\text{Nd}^{3+}$, $\text{PbMoO}_4:\text{Nd}^{3+}$, and $\text{YVO}_4:\text{Nd}^{3+}$ crystals allows confidently estimate better performance of $\text{SrMoO}_4:\text{Nd}^{3+}$ crystal in wide range of Q-switched pulse repetition rates.

CRYSTAL	Thickness, mm	Nd at. %	OC R, %	E_p , μJ	F, kHz	τ , ns
<u>SrMoO₄</u>	<u>3</u>	<u>2</u>	<u>85</u>	<u>26</u>	<u>8.7</u>	<u>3.6</u>
PbMoO ₄	1	2	95	11	8	1.4
YVO ₄	1	1	75	6.9	11.2	3.4

Table 3.2.4.

3.2.6 Self-Raman operation of LD pumped passively Q-switched $\text{SrMoO}_4:\text{Nd}^{3+}$ and $\text{SrMoO}_4:\text{Nd}^{3+}$ laser crystals

To investigate the self-Raman-laser frequency conversion in the LD pumped LiF:F_2^- passively Q-switched $\text{PbMoO}_4:\text{Nd}^{3+}$ laser, output dichroic mirrors with high reflectivity (>99.5%) at the fundamental laser wavelength (1056 nm) and 70 % OC reflectivity at the 1st Stokes SRS wavelength

(1163 nm) were used. The laser cavity was equipped with a SA with initial transmittance of $T_0 = 86\%$ and a 3 mm thick $\text{PbMoO}_4:\text{Nd}^{3+}$ laser crystal to achieve a higher Raman amplification. The laser cavity was set to the minimum length of 8 mm to get a shorter pulse duration and a higher peak power. In the above-mentioned cavity configuration, the self-Raman-laser mode of operation of $\text{PbMoO}_4:\text{Nd}^{3+}$ crystal at the 1163 nm 1st Stokes wavelength was obtained. This regime can be considered as nonlinear cavity dumping when the output coupling fast switched from 0.05% to 30% due to intracavity nonlinear SRS frequency conversion from the fundamental (1056 nm) to the 1st Stokes (1163 nm) operation wavelength. Unfortunately self-Raman laser oscillations in $\text{PbMoO}_4:\text{Nd}^{3+}$ crystal were unstable due to the optical damage of the crystal surfaces.

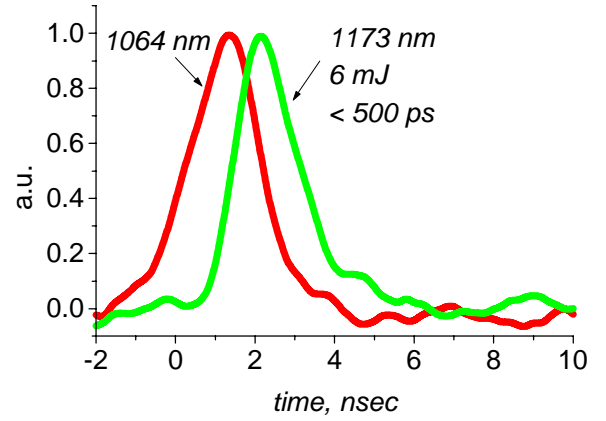


Fig. 3.2.16 Laser pulses at fundamental and Raman wavelengths spectrally resolved by the diffraction grating

In Fig.3.2.16 the laser pulses at fundamental and Raman wavelengths spectrally resolved by the diffraction grating are shown. The Raman laser pulse energy as high as 6 μJ was measured for the OC ROC = 50 mm and the twice lower one for the OC ROC = 25 mm. Thus, the Raman laser pulse energy was only 50 % lower than that of the passively Q-switched $\text{PbMoO}_4:\text{Nd}^{3+}$ laser operating at the fundamental wavelength and approximately twice higher than the pulse energy of the $\text{GdVO}_4:\text{Nd}^{3+}/\text{LiF:F}_2^-$ self-Raman laser of the similar design. The pulse duration of the 1st Stokes SRS radiation in the self-Raman-laser nonlinear cavity dumping mode was measured to be sufficiently shorter (3 – 5 times) than that for Q-switched operation at the fundamental wavelength. Therefore, we can confidently estimate the pulse duration of the $\text{PbMoO}_4:\text{Nd}^{3+}$ self-Raman laser to be shorter than 500 ps, which corresponds to the peak output power of at least 12 kW for 1163 nm 1st Stokes radiation.

The self-Raman-laser frequency conversion in the LD pumped passively Q-switched $\text{SrMoO}_4:\text{Nd}^{3+}$ crystal was investigated using same dichroic mirror (HR at the fundamental laser wavelength and 70 % reflectivity at the 1st Stokes SRS wavelength near 1165 nm), the LiF:F_2^- SA with variable transmission, 3 mm thick $\text{SrMoO}_4:\text{Nd}^{3+}$ laser crystal (2 at.% Nd^{3+} concentration), and 2 W polarized LD pump. The laser cavity was set to the minimum length of 15 mm. In the above-mentioned cavity configuration, the stable self-Raman-laser mode of operation of $\text{SrMoO}_4:\text{Nd}^{3+}$

crystal at the 1163 nm 1st Stokes wavelength was detected. The parameters of the SrMoO₄:Nd³⁺/LiF:F₂ self-Raman laser oscillation were investigated in a range of SA transmissions.

The pulse energy at 1st Stokes wavelength and average power of the self-Raman-laser oscillations are shown in Fig.3.2.17 as a function of pulse repetition rate. Due to the nonlinear nature of the SRS conversion the self-Raman laser demonstrates much stronger dependence of the average power on the pulse repetition rate if compared with the conventional Q-switched laser oscillations at fundamental wavelength (CQ-sw., red curves on the figure). The average power reached maximum of 250 mW at 20 kHz repetition rate and the corresponding peak is more sharp. With increase of the repetition rate the pulse energy drops faster (almost linearly) than that for CQ-sw. and the self-Raman lasing vanishes at the repetition rates higher than 50 kHz.

The maximum measured self-Raman pulse energy was about 21 μ J vs. 26 μ J obtained in CQ-sw. mode. However, the OC transmission at fundamental wavelength in self-Raman mode (<0.5 %) is 30 – 50 times lower than for CQ-sw. mode (15 %). Therefore, the parasitic intracavity reflection losses at uncoated ends of the SA were much more essential in self-Raman mode of the laser operation. Thus, the self-Raman pulse energy as high as 80 % of maximum pulse energy achieved in CQ-sw. mode could be considered as very good result.

We suppose that the use a high quality laser crystal and a high contrast saturable absorber will allow to achieve the self-Raman pulse energy even higher than that for conventional Q-switched mode of operation. One the one hand, high-Q laser cavity at fundamental wavelength provides better extraction of the energy accumulated in the laser medium as populations inversion. On the other hand, nonlinear cavity dumping when the output coupling fast switches from a fraction of percent to 30 – 50 % due to intracavity nonlinear SRS frequency conversion provides an output pulse of the same or even higher energy and 5 – 10 times shorter in duration than for standard Q-switched laser design.

In Fig.3.2.18 laser pulses at 1st Stokes and fundamental wavelengths spectrally resolved by diffraction grating and registered by avalanche photodiodes with temporal resolution of about 1 ns

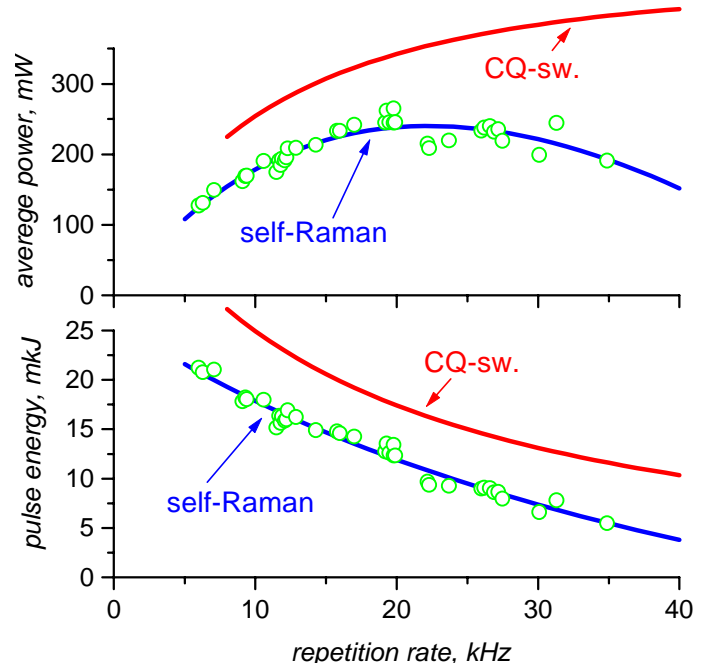


Fig. 3.2.17 Pulse energy at 1st Stokes wavelength and average power of the self-Raman-laser oscillations as a function of pulse repetition rate.

are shown. The averaging of 32 pulses was used to increase signal to noise ratio. Oscillograms correspond (from top to bottom) to the 40 kHz pulses repetition rate (near the self-Raman lasing threshold), 20 kHz (maximum average power), and 7 kHz (maximum self-Raman pulse energy).

With decrease of the repetition rate the laser pulse duration at the fundamental wavelength shortens from 7 ns (at 40 kHz) to 2 ns (at 20 kHz) and to 1.4 ns (at 7 kHz) and delay between Raman and fundamental pulses reduces from 3.6 ns (at 40 kHz) to 1 ns (at 20 kHz) and to 0.6 ns (at 7 kHz). Shortening of the Raman pulse duration takes place as well, however the actual shape of the Raman pulse was not resolved by avalanche photo diode at repetition rates lower than 40 kHz.

To estimate the self-Raman laser pulse duration the results of the self-Raman laser computer simulation were used, which shows that the ratio between pulses duration at fundamental and Raman wavelengths ($\tau^{fund.}/\tau^R$) grows with increase of the Raman pulse energy.

In Fig.3.2.19 experimentally measured pulse durations at fundamental (blue) and Raman (green) wavelengths are shown by circles (dash red line shows resolution limit of our detecting system). Pulse durations at fundamental wavelength were corrected using standard formula: $\tau_{corr} = \sqrt{\tau_{mes}^2 - \tau_{osc}^2}$, where τ_{mes} is a measured pulse duration and τ_{osc} is a resolution of detecting system. Blue solid line is a data fit for a pulse duration at fundamental wavelength. The

$\tau^{fund.}/\tau^R$ ratio is about 5 (was defined at high repetitions rates, near the threshold and above resolution limit). To get an upper estimation for Raman pulse durations the $\tau^{fund.}/\tau^R$ ratio was

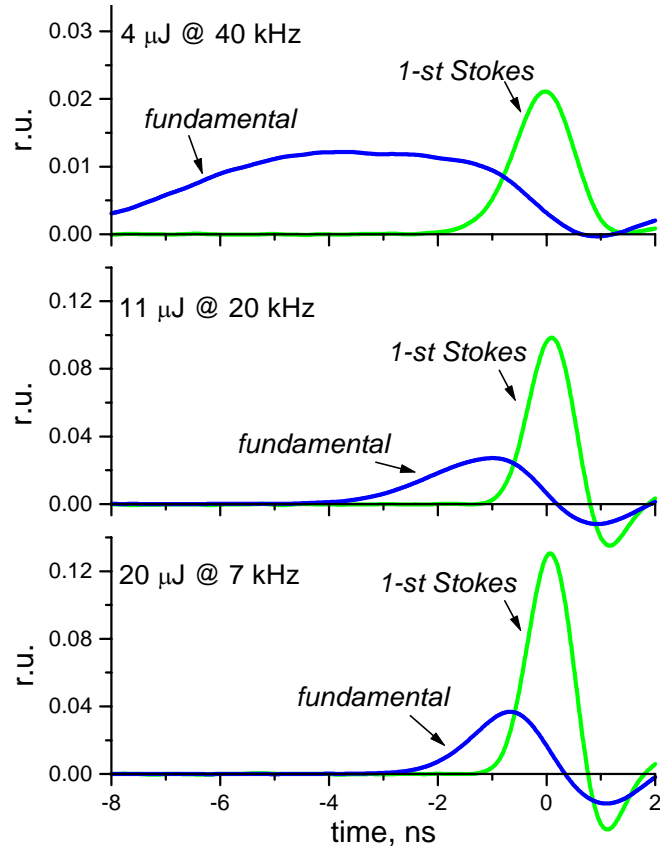


Fig. 3.2.18 Laser pulses at 1st Stokes and fundamental wavelengths spectrally resolved by diffraction grating and registered by avalanche photodiodes with temporal resolution of about 1 ns

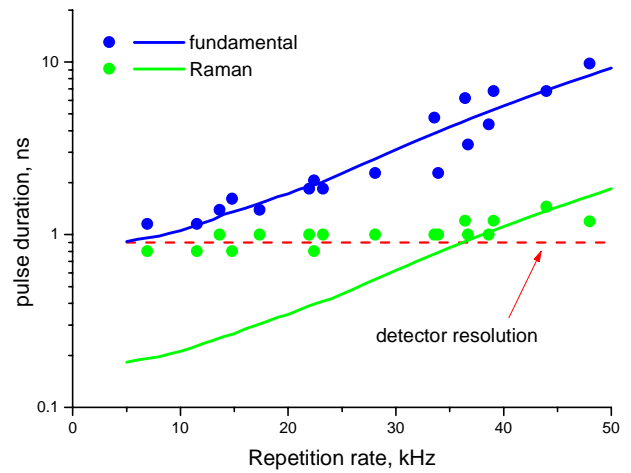


Fig. 3.2.19 Experimentally measured pulse durations at fundamental (blue) and Raman (green) wavelengths (circles). Dash red line shows resolution limit of our detecting system.

supposed to remain constant with decrease of the pulses repetition rate (increase of the Raman pulse energy). Corresponding results of the estimation are shown in the Fig.3.2.19 by green solid line. As can be seen, the estimated Raman pulse duration is about 200 ps at low repetition rates (7 kHz 20 μ J pulses) and about 350 ps at maximum average power of self-Raman laser (20 kHz 11 μ J pulses). As a result, we can estimate rather high peak powers of 100 kW and 30 kW at 7 kHz and 20 kHz repetition rates.

3.2.7 Conclusion

Spectroscopic properties of tungstate ($\text{BaWO}_4\text{:Nd}^{3+}$, $\text{SrWO}_4\text{:Nd}^{3+}$, $\text{PbWO}_4\text{:Nd}^{3+}$) and molybdate ($\text{SrMoO}_4\text{:Nd}^{3+}$, $\text{PbMoO}_4\text{:Nd}^{3+}$) crystals were investigated. Among tested tungstates and molybdates most promising crystals were found out to be those containing lead due to relatively high level of Nd^{3+} ions doping (up to 1-2 at.%), high absorption at laser diode pumping wavelength, comparatively short $^4\text{F}_{3/2}$ metastable level lifetime (high probability of radiative transitions).

The relative lasing properties of tungstate ($\text{BaWO}_4\text{:Nd}^{3+}$, $\text{SrWO}_4\text{:Nd}^{3+}$, $\text{PbWO}_4\text{:Nd}^{3+}$) and molybdate ($\text{SrMoO}_4\text{:Nd}^{3+}$, $\text{PbMoO}_4\text{:Nd}^{3+}$) crystals in free-running mode were investigated for unpolarized LD pumping. All tested crystals were characterized by low oscillation threshold – about 1 mJ of absorbed pump energy. Best oscillation results were obtained for $\text{PbWO}_4\text{:Nd}^{3+}$, $\text{SrMoO}_4\text{:Nd}^{3+}$ and $\text{PbMoO}_4\text{:Nd}^{3+}$ crystals with lasing efficiency comparable with that for well known commercial KGW:Nd^{3+} crystal. For most efficient $\text{PbMoO}_4\text{:Nd}^{3+}$ crystal with neodymium concentration of 0.3 at.% the slope efficiency as high as 21% with total efficiency of 17% were obtained.

Under 2W polarized LD pumping $\text{PbMoO}_4\text{:Nd}^{3+}$ crystal (Nd^{3+} concentration 2 at.%, 3 mm thick) in free-running mode demonstrated maximum output power of 644 mW and slope efficiency of 49 % that exceeded the corresponding results obtained for $\text{GdVO}_4\text{:Nd}^{3+}$ crystal 627 mW and 44 % respectively obtained in the analogous conditions. For 1 mm thick $\text{PbMoO}_4\text{:Nd}^{3+}$ (0.3 at.%) crystal slope efficiency as high as 53% was achieved.

For 2 W polarized LD pumping of $\text{SrMoO}_4\text{:Nd}^{3+}$ laser in free running mode of operation the maximum output power of 928 mW which corresponds to 43 % conversion efficiency (47 % slope efficiency) was obtained. Best results for most efficient molybdate crystals were found to be competitive with that of well-known $\text{GdVO}_4\text{:Nd}^{3+}$ and $\text{YVO}_4\text{:Nd}^{3+}$ vanadate laser crystals for the same cavity configuration and pumping conditions.

At pulse repetition rates below 100 kHz the $\text{PbMoO}_4\text{:Nd}^{3+}/\text{LiF:F}_2^-$ laser with output mirror reflectivity of 95 % and saturable absorber initial transmittance of 89 % demonstrated higher average output power (up to 350 mW) and pulse energy (up to 10 μ J) than $\text{YVO}_4\text{:Nd}^{3+}/\text{LiF:F}_2^-$ laser with higher transmitting output coupler 75 % and lower initial transmittance of SA - 78 %.

Applying of the LiF:F_2^- saturable absorber with variable transmission has allowed fast and accurate characterization of the passively Q-switched laser oscillations of LD pumped $\text{SrMoO}_4\text{:Nd}^{3+}$

crystal. Compared with LiF:F_2^- passively Q-switched $\text{PbMoO}_4\text{:Nd}^{3+}$ and $\text{YVO}_4\text{:Nd}^{3+}$ crystals, the $\text{SrMoO}_4\text{:Nd}^{3+}$ crystal demonstrated higher average power and efficiency in wide range of Q-switched pulses repetition rates. The maximum pulse energy, which was achieved for $\text{SrMoO}_4\text{:Nd}^{3+}$ crystal (26 μJ) is approximately 5 times higher than that for $\text{YVO}_4\text{:Nd}^{3+}$ crystal and 2 times higher than for $\text{PbMoO}_4\text{:Nd}^{3+}$ crystal.

The self-Raman mode of operation of the LiF:F_2^- passively Q-switched LD pumped $\text{SrMoO}_4\text{:Nd}^{3+}$ crystal was demonstrated for the first time. Optimal combination of laser and Raman characteristics of $\text{SrMoO}_4\text{:Nd}^{3+}$ crystal (relatively low laser transition cross-section and long upper level lifetime, high crystal quality, and high enough SRS gain) has allowed to achieve record high self-Raman laser pulse energy (21 μJ) and LD-to-Raman conversion efficiency (13 %) with estimated Raman laser pulse duration of 200 ps. The pulse energy of the $\text{SrMoO}_4\text{:Nd}^{3+}$ crystal self-Raman laser oscillations was 3.5 times higher than for $\text{PbMoO}_4\text{:Nd}^{3+}$ and 7 times higher than for $\text{GdVO}_4\text{:Nd}^{3+}$ self-Raman lasers of similar design.

The self-Raman pulse energy of $\text{SrMoO}_4\text{:Nd}^{3+}$ crystal as high as 80 % of the pulse energy in conventional Q-switched mode at fundamental wavelength. Taking into account relatively high parasitic reflection losses at uncoated ends of the saturable absorber this difference could be considered as very small. Moreover, we suppose that the pulse energy even higher than for conventional Q-switched mode could be reached in self-Raman mode if use a high quality laser crystal and a high contrast saturable absorber. Our preliminary computer simulations confirm that assumption.

4.1 Efficient powerful single-mode Nd:YAG lasers with diffractively coupled self-phase-conjugate and self-phase-locked resonators

In works [1–5] we studied opportunities of development of powerful compact solid-state Nd-lasers based on a principle of lasing via four-wave mixing in the active laser media with self-phase-conjugation (SPC) in a loop configuration of the laser resonator. The high-power laser radiation with the beam divergence close to the diffraction limit was received due to SPC directly in the active laser elements (AE) without use of additional elements. At 30-Hz pump-pulse repetition rate the Nd:YAG-laser radiation average power was up to 50 W – in case of two active laser elements inside the loop resonator [1] and up to 120 W – in case of using the third active element as the single-pass amplifier [2]. The mode of self-Q-switching [4] as the laser giant pulse trains repeating with the pump repetition rate was realized at duration of an individual pulse of about 200 ns and peak power of up to 90 kW. In work [3] there is shown that using the laser passive Q-switch based on LiF:F_2^- crystal allows to increase the peak power and intensity of the laser single-mode radiation up to 17 MW and 130 MW/cm^2 close to a threshold of radiation damage of optical elements of the laser due to decreasing the laser pulse duration up to 20 ns and increasing the laser pulse energy up to 0.35 J.

In this study we investigated principles of construction of loop laser schemes and opportunities of increase of oscillation efficiency of the Nd lasers with loop resonators.

Increasing the oscillation efficiency by change of a configuration of the loop resonator.

In the basic laser scheme (Figure 1) early investigated by us [1–5], a stored energy of AE 2 is incompletely used and only one phase-conjugate mirror writing inside the AE 1 effectively operates. It is caused by that, the beams writing a holographic grating in AE 1 represent the writing beams of AE 2 amplified in AE 2 (at the account only transmitting holograms), i.e. total intensity of radiation in AE 2 less than in AE 1, and also growth of diffraction efficiency of gain hologram in AE 1 overcome growth of efficiency of the phase-conjugate mirror in AE 2.

With a view of more complete use of the stored energy of AE 2 the application of the new scheme of the laser with additional pass of radiation through AE 2 is offered. An optimization of the laser scheme allows increasing the oscillation efficiency, both in a free running and passive Q-switching regime without deterioration of beam quality of the output laser radiation. The increase of the oscillation efficiency was occurred also under pumping by pulses of the larger duration, which we changed from 0.2 up to 4 ms.

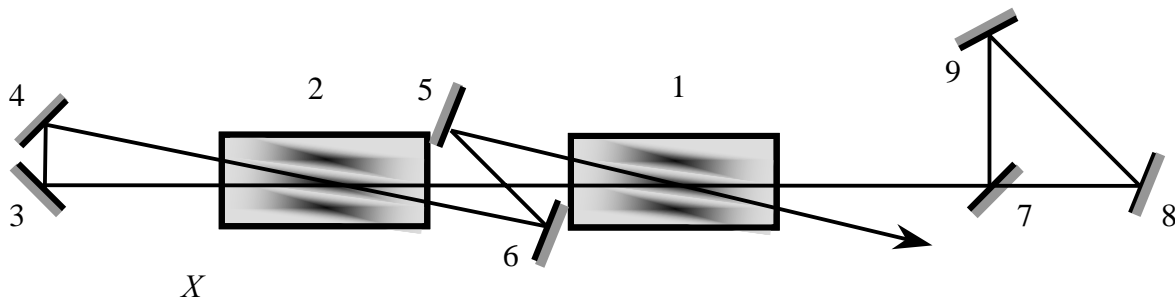


Figure 1. Optical scheme of loop laser resonator

In a Figure 2 the new investigated optical scheme of the laser with additional pass (loop) through AE 2 is submitted. To decrease diffractive losses in view of large length of a loop cavity we applied a concave mirror with 9-m radius of curvature.

At pumping by monopulses with 0.2-ms duration and 63.5-J energy for each AE the laser pulse energy at the output 2 was equal to 2 J that is 26 % higher in comparison with energy at the output 1 corresponding to the previous laser scheme (Figure 1). At pumping by monopulses with 4-ms duration and 1083-J energy for each AE the laser pulse energy at the output 1 was equal to 8.7 J and at the output 2 it was equal to 11 J that is 26.5 % higher.

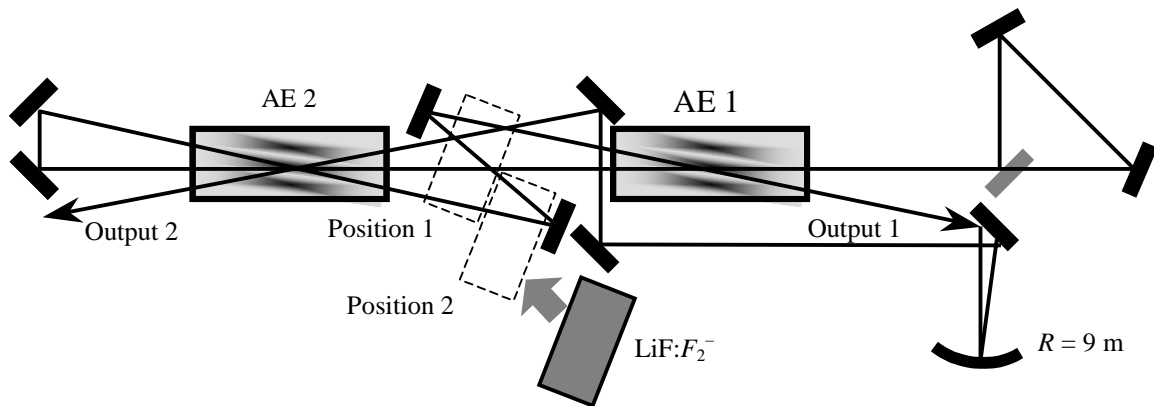


Figure 2. New loop laser scheme

The highest oscillation efficiency is received under pumping by pulses with 0.32 ms duration and 63.5-J energy for each AE. At the output 1 the laser energy of 2.3 J is received, and at the output 2 the laser energy achieved 2.75 J, that is 26 % higher too. Thus the total oscillation efficiency of the phase-conjugated laser on new scheme was increased up to 2.2 %.

We investigated also the laser passive Q-switching by a LiF:F_2^- crystal with 30-% initial transmittance placed at a position 1 and 2 (Figure 2) similarly to earlier our investigation of passive Q-switching of the basic laser [1,3].

At the LiF:F_2^- crystal position 1 and pumping with 0.32-ms duration and 63.5-J energy we observed the laser generation of single-mode radiation as trains of 7 pulses with a pulse train energy of 1.76 J, energy of an individual pulse of 0.25 J, duration of an individual pulse of 30 ns and period of pulse repetition in train of 25 μs . In comparison with results of work [1] at the same position and initial transmittance of LiF:F_2^- crystal, in the scheme of Figure 2 the number of pulses increased from 4 up to 7, and the pulse train energy increased by 76 % at preservation of the individual pulse energy. Thus in this "hard" Q-switching regime the oscillation efficiency was attained to 1.4 %.

To realize a "smooth" Q-switching regime and to increase the Q-switched laser oscillation efficiency we placed the same LiF:F_2^- crystal at the position 2 (Figure 2) as in our work [3]. Thus the individual pulse energy of the single-mode laser radiation decreased down to 0.1 J, the duration of pulses increased up to 40 ns, and the number of pulses in train increased up to 24. However the pulse train energy of output radiation increased up to 2.4 J that corresponds to the oscillation efficiency of 1.9 % and close to optimized free running data.

Our investigation shows that the scheme of Figure 2 is more effective in the Q-switching regime. The oscillation efficiency of the phase-conjugate laser grows by 1.5–2 times without decrease of power parameters of individual pulses of single-mode Q-switched radiation.

Lasing of a phase-locked three-channel laser system based on oscillators with self-pumped phase-conjugate loop cavities. We developed a two-channel laser system (Figure 3) based on loop cavities with phase-conjugation [7], in which the degree of phase locking of the two channels was as high as 0.9. The output radiation of the two channels was formed in one output beam by a beam splitter. We continued our efforts to optimize the previously developed holographic Nd:YAG laser system [7] based on gain gratings so that its total radiation intensity exceeded the intensity of a separate channel radiation by more than three times.

Figure 4 shows the optical scheme of the three-channel Nd:YAG laser system based on oscillators with loop cavities. A separate laser channel is constructed as a loop cavity with a preferential lasing direction, selected using a nonreciprocal Faraday element NE [10]. In such cavities, phase conjugation on the gain gratings in the Nd:YAG laser elements (LE1 – LE3) ensures self-compensation of phase distortions [4,7,10–12]. A Nd:YAG laser element LE4 is a common intracavity amplifier and serves for holographic coupling of different laser channels [9]. A common

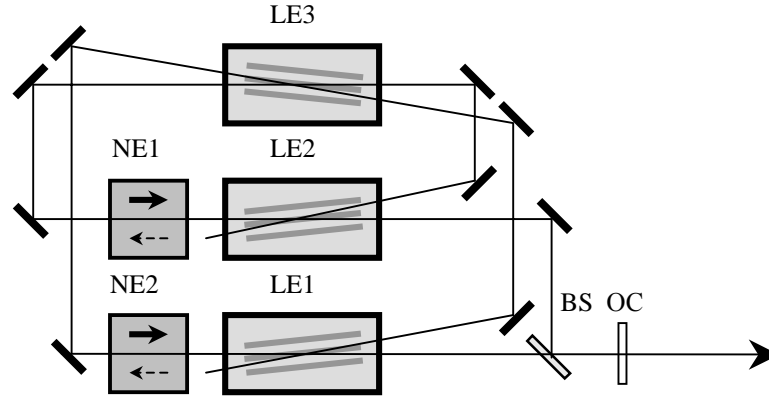


Figure 3. Optical scheme of the two-channel Nd:YAG laser system based on self-pumped phase-conjugate loop cavities. (LE1) – (LE2) active laser elements; (LE3) active element responsible for interchannel coupling; (NE1) – (NE2) nonreciprocal Faraday elements; (BS) beam splitter; (OC) optical coupler;

100% optical coupler OC provides feedback of lasing in each channel via holographic phase-conjugation mirrors recorded by the summed radiation of the three laser channels. For better operation of the new optical scheme, we optimized the construction and parameters of the nonreciprocal Faraday elements NE1–NE3, increasing their contrast from 80 [7] to 170–210.

In the experimental setup, we used active laser elements Nd:YAG with the size

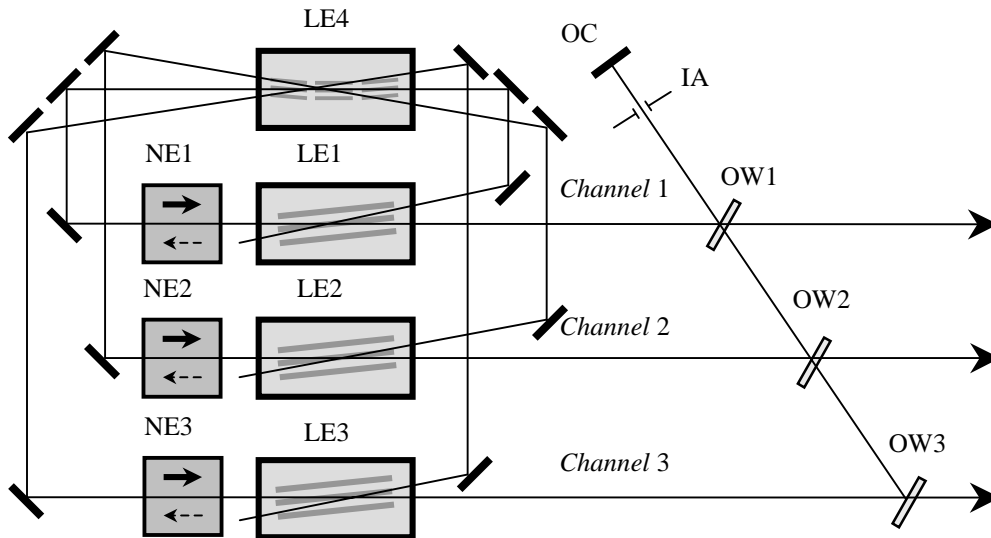


Figure 4. Optical scheme of the three-channel Nd:YAG system based on self-pumped phase-conjugate loop cavities. (LE1) – (LE3) active laser elements; (LE4) active element responsible for interchannel coupling; (NE1) – (NE3) nonreciprocal Faraday elements; (QW1) – (OW3) optical wedges; (OC) optical coupler; (IA) intracavity aperture.

Ø 6.3×100 mm. The laser elements were placed in a K-301V one-lamp pump module with elliptical mirror reflectors and KDNP-6/90A pump krypton lamps. A commercial four-channel power supply 13 GND allowed us to change the pump pulse repetition rate from 1 to 30 Hz at the pump pulse energy of up to 85 J per lamp and the pulse duration of 0.2 ms. Our measurements by the method of maximum losses revealed that the small-signal single-pass gain of the laser elements at the pump energy of 63.5 J were higher than 80.

Using uncoated glass optical wedges OW1 – OW3 with the Fresnel reflection coefficient $R \sim 0.03\text{--}0.1$ (increasing with increasing angle of incidence to the OW), we obtained a sufficient feedback coefficient for each channel, $R^2 \sim 0.001\text{--}0.01$ (at double reflection from OW).

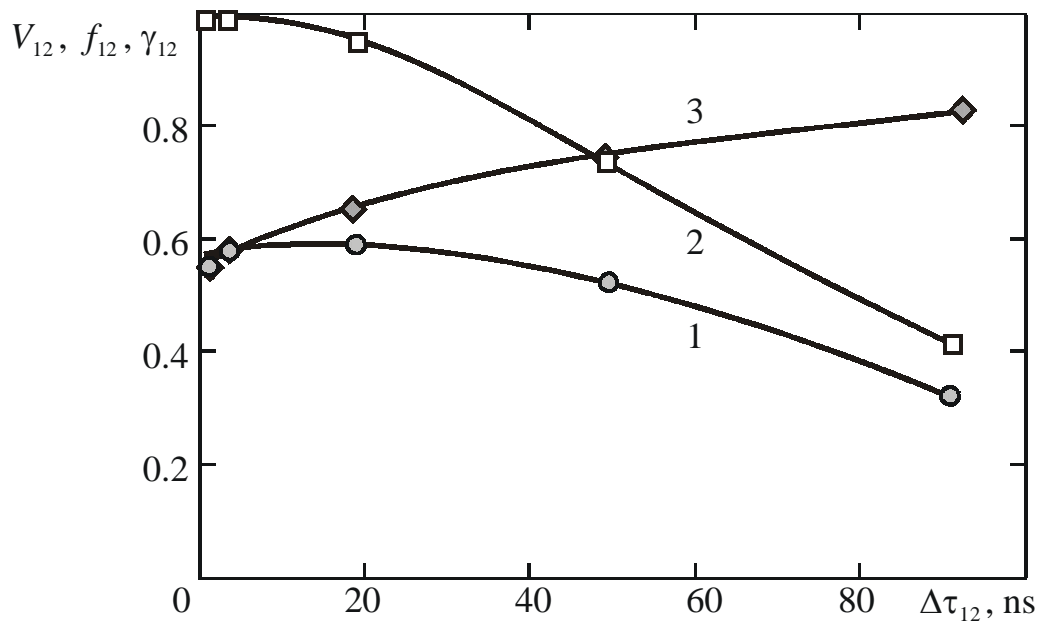


Figure 5. (1) The contrast of the interference between the pulses of the first and second channels, (2) the degree of their time synchronization, and (3) the degree of their phase locking versus the time shift between these pulses.

We have found that the first laser channel, which has the best Nd:YAG element, controls the radiation of the second and third channels. Thus the single pulses of the controlled channels were delayed by 70–100 ns with respect to the pulse of the first channel at synchronized radiation of the controlled second and third channels that predicted by the modeling [13]. The duration of single pulses of a separate channel ($\tau = 60$ ns) exceeded the duration of each channel single pulses ($\tau = 40$ ns) in the absence of lasing of the other channels, which pointed to the formation of a longer collective cavity in the case of the phase-locked operation of the laser system [9]. Our investigation of the phase locking of the second and third channels in the Young scheme [8] has shown a much higher (close to the maximum) contrast $V \rightarrow 1$ of their interference pattern.

With the use of half-wave plates and variable delays, we changed the efficiency of intrinsic lasing of the second and third channels from the near-threshold values to efficiency close to the intrinsic efficiency of the first channel. With increasing efficiency, we observed a decrease in the shift between the pulses of the first and the second (third) channels in the case of their joint operation. At the efficiency of the intrinsic lasing of the controlled channels close to the efficiency of the first channel, all the three laser pulses are synchronized in time. However, our attempts to equalize the intrinsic efficiencies of all the three channels by adjusting the beam splitters OW2 and OW3 (Figure 4) sometimes lead to the violation of the synchronization of the output laser pulses, which we explain by a transverse shift of the optical axes of the laser channels, and, hence, by a poor

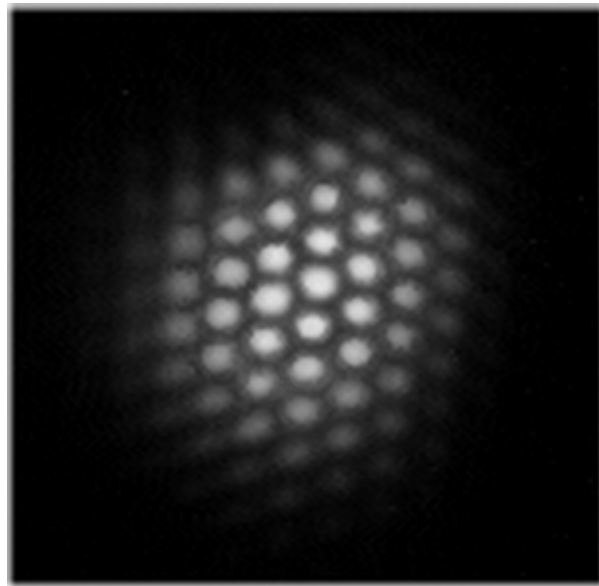


Figure 6. CCD image of interference pattern for interacting beams in the case of three operating channels.

coupling between the channels. To eliminate this effect, we introduce an intracavity aperture between OC and OW1 (Figure 4).

Thus, our study of the interference pattern has shown that the degree of phase locking of the laser channels in the case of perfect time synchronization of their pulses is $\gamma \approx 0.55$, but, as the time shift increases, γ also increases, tending to unity. This is probably related to stronger competition between the intrinsic lasing of the second and third channels with the lasing induced by the first channel in the case of high intrinsic efficiency of the controlled channels. Figure 5 shows the

characteristic dependences of the contrast of the interference between the first- and second-channel beams, as well as of the degrees of their time synchronization and phase locking, on the shift between these pulses.

We can see that, with decreasing shift between the pulses and, hence, increasing degree of their time synchronization, the degree of the phase locking decreases only slightly, and the maximum interference contrast $V \approx 0.5\text{--}0.6$ is observed at $\Delta\tau$ shorter than 0.5τ .

Thus, conditions of reception of the highest contrast of an interference pattern of radiation of the three-channel Nd:YAG-laser system operating in two essentially differing regimes of lasing are determined. The first lasing regime gives perfect time synchronization, but the interference pattern contrast does not exceed 0.5–0.6.

At the second lasing regime the first laser channel controls the radiation of the second and third channels getting increasing degree of their phase locking γ , tending to unity. Therefore contrast of interference between the controlled channel beams tends to unity too. But the controlling first-channel pulse outdistance the controlled second- and third-channel pulse. Thus contrast of interference between controlling and controlled channel beams decreased (see figure 5), which has no crucial importance at the further increase of number N of the controlled laser channels.

References:

1. Basiev T.T., Fedin A.V., Gavrilov A.V., Smetanin S.N. Single-mode Nd:YAG laser with self-phase-conjugation and its application. *Izvestia AN. Seria fizicheskaya* (Russian), 1999, v.9, p.1909–1913.
2. Basiev T.T., Fedin A.V., Gavrilov A.V., Smetanin S.N., Kyalbieva S.A. Single-mode Nd:YAG laser with a self-pumped phase-conjugate loop cavity // *Quantum electronics*, 1999, v.29, p.424–427.
3. Fedin A.V., Gavrilov A.V., Basiev T.T., Antipov O.L., Kuzhelev A.S., Smetanin S.N. Passive Q-switching of a self-pumped phase-conjugate Nd:YAG loop resonator // *Laser physics*, 1999, v.9, №2, p.433–436.
4. Fedin A.V., Gavrilov A.V., Kyalbieva S.A., Smetanin S.N. Self-Q-switching at self-phase-conjugation in active media // *Proceedings of SPIE*, 2001, v.4644, p.312–318.
5. Fedin A.V., Basiev T.T., Gavrilov A.V., Ruliov A.V., Smetanin S.N., Kyalbieva S.A. Powerful neodymium lasers with the self-phase-conjugation // *Proceedings of SPIE*, 2000, v.4353, p.214–220.
6. Svelto O. *Principles of lasers*, 3rd ed. (New York: Plenum, 1989).

7. Basiev T.T., Fedin A.V., Gavrilov A.V., Osiko V.V., Smetanin S.N. Phase locking of optically coupled lasers by gain gratings in an active medium // *Quantum electronics*, 2003, v.33, p.659–670.
8. Born M., Wolf E. *Principles of optics*. (Oxford: Pergamon press, 1964).
9. V.V. Likhanskii, and A.P. Napartovich, *Usp. Fiz. Nauk*, 1990, v.160, p.101-143.
10. Damzen M.J., Green R.P.M., Syed K.S. Self-adaptive solid-state laser oscillator formed by dynamic gain-grating holograms // *Optics Letters*, 1995, v.20, p.1704-1706.
11. Sillard P., Brignon A., Huignard J.-P. Gain-grating analysis of self-starting self-pumped phase-conjugate Nd:YAG loop resonator // *IEEE J. Quantum Electronics*, 1998, v.34, p.465-472.
12. Basiev T.T., Fedin A.V., Osiko V.V., Smetanin S.N. On the influence of reflective gain holograms on the dynamics of lasing in a loop laser cavity. // *Laser physics*, 2003, v.13, p.903-908.
13. Basiev T.T., Fedin A.V., Gavrilov A.V., Osiko V.V., Smetanin S.N. Oscillation dynamics of phase-locked three-channel holographic Nd:YAG laser system // *In technical digest of international conference LAT-2005*, p. 29.

4.2. New cavity schemes for high-power lasers based on dielectric diffractive optics

4.2.1. Introduction

Scaling-up of the laser output power is one of the key topics for laser physics and technology. Among with development of new laser active mediums and new pumping schemes the important direction of research is the development of a new laser cavity schemes and an optical components for high power lasers.

Many current and prospective applications require the laser sources what combine high power and limit high spectral and spatial output quality or, to be short, high-power high-brightness lasers (HPBLs). For various reasons requirements of high power and highly bright output are contradictory for standard laser cavity designs and a usual way for development of HPBLs is a use of master oscillator power amplifier (MOPA) approach with weak but narrow-band master oscillator and a chain of laser amplifiers. More challenging approach is a combining of high power laser performance and perfect spectral and spatial quality of the laser output in a compact single unit device. As a step in this direction we investigate several new laser designs, which based on efficient multilayer dielectric grating diffractive optics.

Diffraction gratings have numerous laser applications. Specifically, gratings are key elements of dispersive laser cavities and pulse compression setups. Commonly used for these applications metal-coated gratings have significant absorption and low radiation damage threshold that restricts the use of metal gratings as a high power laser optics. Restrictions of metal gratings caused by finite conductivity of metals. Therefore, the development of dielectric grating fabrication techniques is of high practical importance. Since the efficiency of simple dielectric gratings (e.g. periodically corrugated border of two semi-infinite dielectric mediums, see Fig. 4.2-1a) is relatively poor, the combination of the dielectric diffraction grating with multilayer dielectric structures seems to be most fruitful approach to design of efficient dielectric diffractive optics (see Fig. 4.2-1b). During past years the rigorous methods for numerical modeling and optimization of these structures have been developed [1, 2, 3, [4]. Specifically, it has been shown that combined grating design allows reaching 100 % diffraction efficiency for given radiation wave-

length and incidence angle. Major part of theoretical and experimental papers on dielectric gratings is focused on development of gratings for pulse compression [5, 6, 7, 8]. However, the use of efficient dielectric gratings in dispersive laser cavities looks very promising as well [9].

Abnormally reflecting mirrors (or resonant grating filters, see Fig. 4.2-1c) represent another relatively new class of dielectric diffractive optics. Diffraction anomalies from gratings were originally observed by Wood in 1902 and have been investigated for many years. The zero-order reflection anomalies from periodically corrugated dielectric thin films were predicted and experimentally observed in [10, 11, 12]. Abnormally reflecting mirrors (ARM's) can exhibit near-ideal characteristics: complete reflection of the incident energy on resonance, narrow response, and high contrast. The resonant nature, fabrication and applications of these structures have been gaining attention in the literature, see refs to [13] and [14]. The advantages of ARM's for laser applications have been discussed as well. However, to our knowledge, the number of publications on experimental demonstration of lasers with the ARM cavities is rather limited.

In this paper we discuss features of abnormally reflecting mirrors, which are favorable for development of HPBLs, present the cavity schemes and experimental results achieved with fabricated samples of dielectric gratings. Proposed cavity schemes are most suitable for medium and high power diode pumped solid-state lasers (LD pumped SSL's). The use of ARM based cavity is especially promising for development of lasers with new types of low quantum defect laser mediums. In absence of high power LD pump source, our preliminary laser experiments

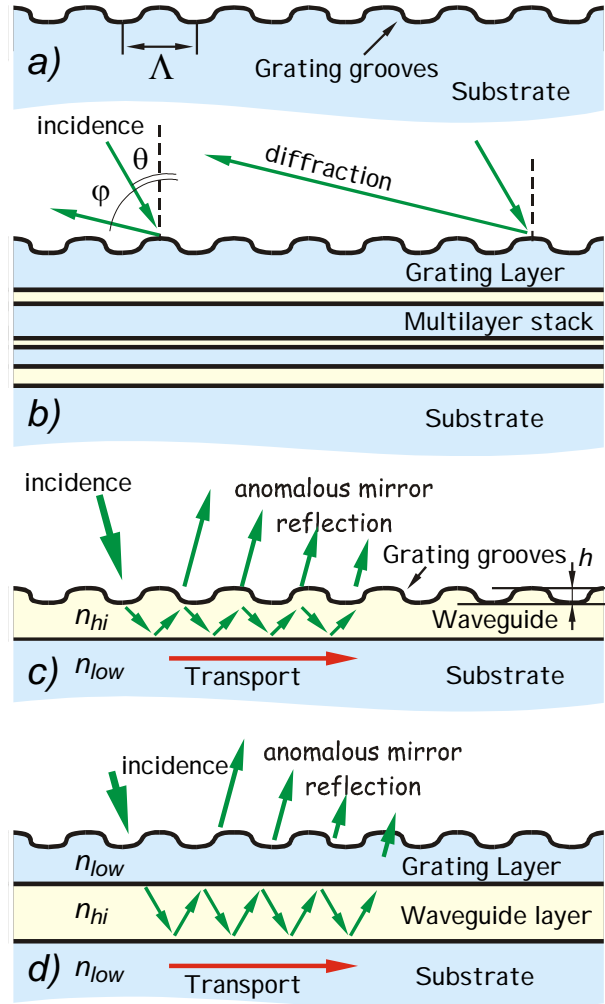


Fig. 4.2-1 Dielectric grating designs

were carried out using LiF crystals with F_2^- color centers as a laser active medium. The optical pump source was passively Q-switched Nd:YLF laser at 1047 nm with 10 mJ pulse energy and 20 ns pulse duration.

4.2.2. Characteristics of ARM dielectric diffractive optics and novel cavity scheme for high-power narrowband lasers

Schematic of simplest abnormally reflecting mirror (ARM) is shown in the Fig. 4.2-1c. The structure represents a periodically corrugated dielectric layer (waveguide) with a refractive index higher than that of substrate. To achieve an abnormal reflection, the grating period Λ has to be chosen in the way to prevent diffraction in upper semi-space and in substrate and provide diffraction in the waveguide:

$$\frac{\lambda}{\Lambda} - \sin \theta > 1 \quad \frac{\lambda}{\Lambda n_{hi}} - \sin \theta < 1 \quad \frac{\lambda}{\Lambda n_{low}} - \sin \theta > 1, \quad (1)$$

where n_{hi} and n_{low} are refractive indexes of the waveguide and the substrate. Thus, the diffraction orders are “locked” in the waveguide due to total internal reflection. If thickness of the waveguide layer satisfies the guiding mode excitation condition the structure exhibits 100 % zero-order (mirror) reflection.

The drawback of the simple single-layer ARM design is considerable off-resonance reflectivity, therefore the contrast of single layer ARM (ratio of peak and sideband reflection) merely exceeds factor of 10. The contrast could be improved by combining the ARM and multi-layer antireflection coating. The double-layer ARM design with low refractive index upper layer is shown in the Fig. 4.2-1d. In the Fig. 4.2-2 reflectances of single- and

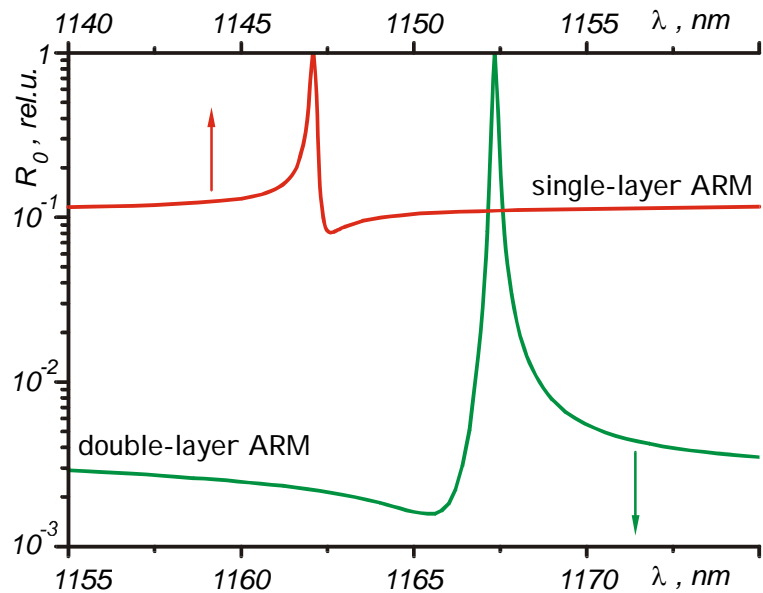


Fig. 4.2-2 Single- and double-layer ARM's reflectances

double-layer ARM's with the same abnormal reflection peak widths are compared. As follows, optimization of double-layer design allows reaching contrast about 500. In [15] have been shown that triple-layer ARM design allows contrast as high as 10000.

In the Fig. 4.2-3 are shown reflectances at normal incidence of double-layer ARM's with different grating depths as functions of radiation wavelength (part a) and angle of incidence (part b). The grating period was 1400 nm^{-1} ; the layers materials were SiO_2 and HfO_2 . As follows, ARM could be very strong spectral and angular selector. Spec-

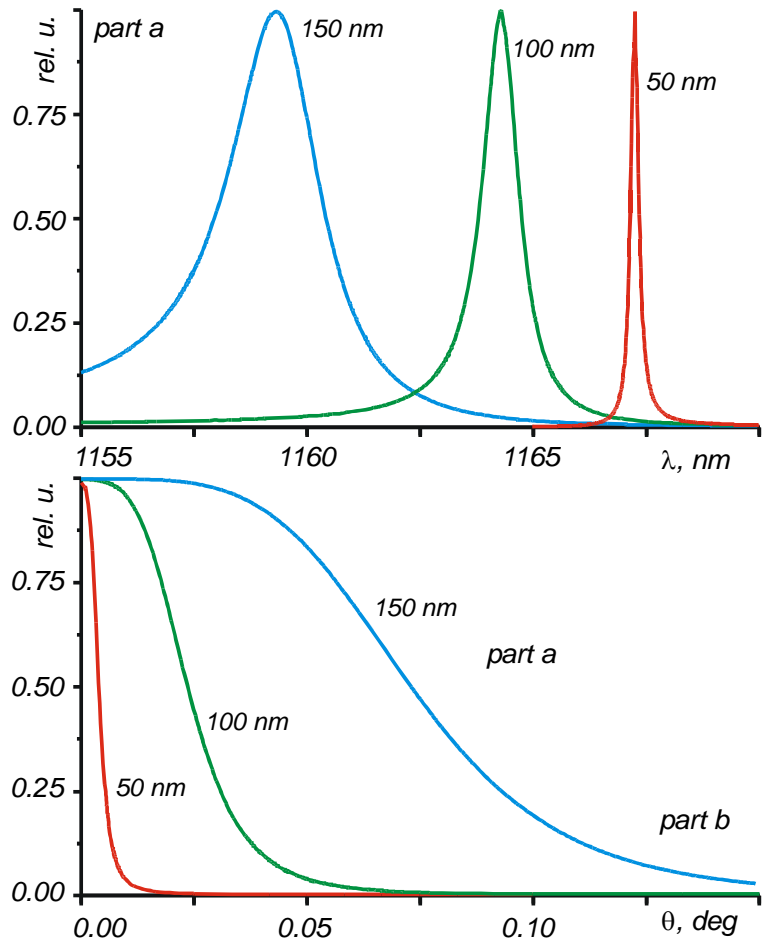


Fig. 4.2-3 Double-layer ARM reflectances

tral and angular width of abnormal reflection peak depends mostly on the grating depth, which determines free-space to waveguide coupling factor. Another important feature of ARM's is the transport of the radiation across incident beam that occurs due to the wave guiding in the structure (see red arrows on the Fig. 4.2-1). Effective length of the transport depends also on grating depth (free space to waveguide coupling). Minimal width of ARM resonant response and maximal waveguide transport length are limited by grating imperfections and losses in the waveguide. Hence, the ARM performance substantially depends on fabrication technology.

We propose a new laser cavity design, which uses advantages of ARM optics and suitable for high-power narrowband LD pumped solid-state lasers and low quantum defect lasers. Design is based on combination of planar (slab) laser active element, end-pumping scheme, and dielectric ARM diffractive optics. Top and side views of the ARM laser cavity are shown in the Fig. 4.2-4. The laser is pumped through the ARM (the ARM itself could be fabricated directly on

the input face of the laser slab). The ARM parameters could be easily selected to provide high transmission at the pump wavelength and abnormal reflection at the laser wavelength even for laser mediums with very low quantum defect. The slab laser active element is end-pumped by LD array. Attractive pumping scheme for high-power laser (shown on the picture) is the use of multiple fiber optics coupled LD arrays. The LD emission from the fibers ends could be focused in the slab by the same cylindrical lens forming strip-shaped laser active volume.

Use of end-pumping scheme allows the efficient heat sink from the slab active element through its lateral sides. Lengthening of the active element in L direction allows proportional increasing of the pump power, volume of the laser active medium and the heat dissipation area. Besides, end pumping allows the perfect match of the laser active volume with the cavity mode geometrics that increases the laser efficiency and reduces heat generation in the laser active element.

Most important feature of proposed cavity scheme is that the phasing of the laser oscillations in whole volume of the laser active medium and hence high coherence of the laser emission is enforced by “strong” interaction of the radiation with ARM diffractive optics. While in conventional mirror-mirror laser cavities the output beam coherence is provided due to “weak” natural divergence of the radiation (that causes fast deterioration of the laser output characteristics with increase of transverse sizes of the laser active volume). The ARM cavity scheme is looks very similar to standard plane-parallel cavity. However, wave-guiding and transport of the radia-

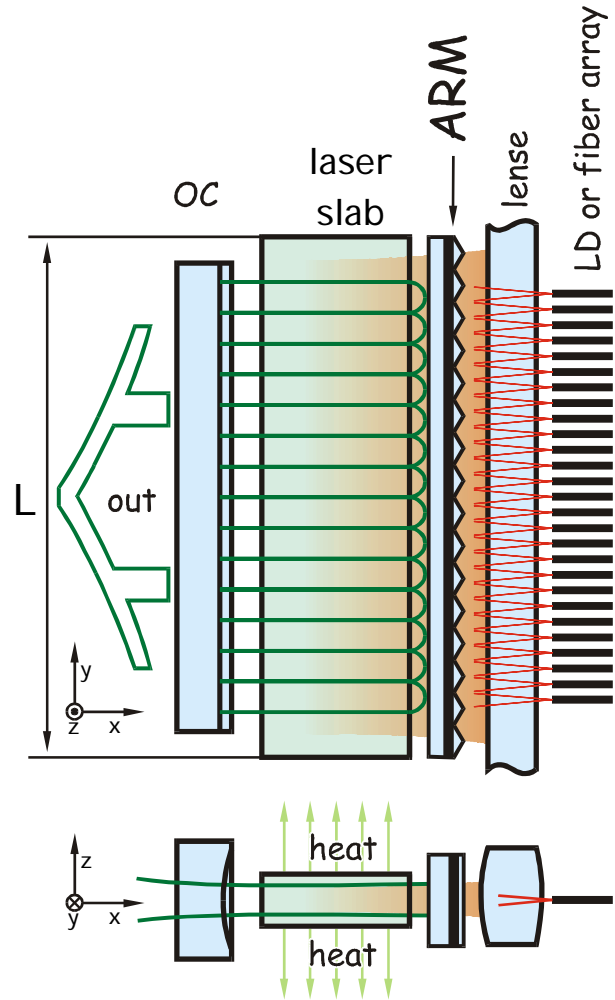


Fig. 4.2-4 ARM cavity high power narrowband laser design

tion in the ARM structure intermixes strongly the laser radiation along L direction at each cavity round-trip what enforces high coherence of the laser oscillations in the whole active volume. Besides, high spectral and angular selectivity of ARM (see Fig. 4.2-3) provide spectrally narrow laser output with high spatial quality.

Thus, proposed cavity scheme combines such a features as large and scalable active medium volume, all the advantages of end-pumping scheme, enough high cavity Q-factor; high spectral and spatial selectivity; and efficient heat sink. These make ARM cavity very attractive for development of HPBLs using various laser active mediums.

4.2.3. Experimental results

The dielectric grating fabrication technology was based on holographic process of the grating recording in chalcogenide glass photoresist followed by anisotropic chemical etching and reactive ion etching. The essential advantages of the technology are vacuum photoresist deposition technique that allows fabrication of large size, highly uniform gratings with minimal number of defects. The holographic and etching facilities characteristics allow gratings recording with a period up to 3600 lines per mm, and 10×10 cm size.

Dielectric ARM diffractive optics for laser experiments was fabricated using high quality polished silica substrates. The ARM has 2 dielectric layers, grooves spacing of 1400 lines per mm and 30 mm length. On the same substrate were fabricated two gratings with 50 nm and 150 nm depths (the schematic and the theoretical curve for ARMs are shown in the Fig. 4.2-1d and Fig. 4.2-3).

Off-resonance and resonance transmissions of the ARM

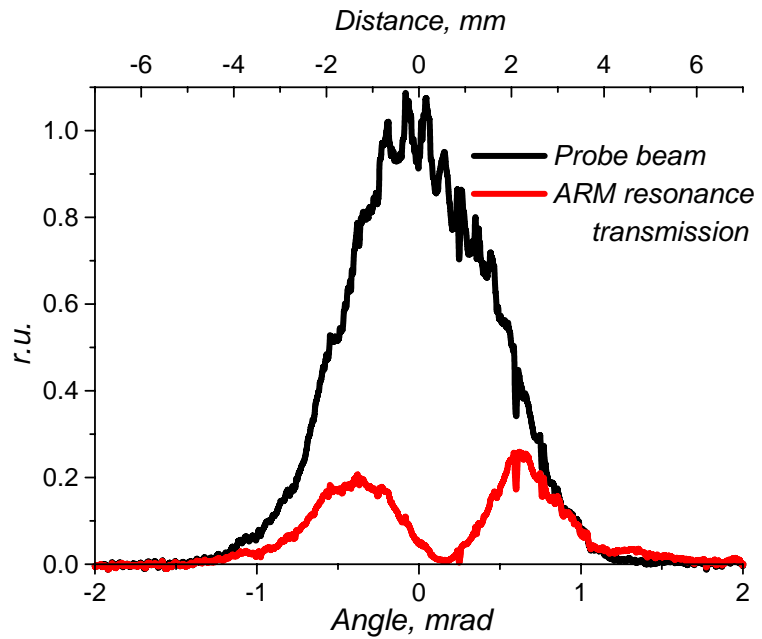


Fig. 4.2-5 Resonance and off-resonance transmissions of the ARM structure

structure with 150 nm grating depth are compared in the Fig. 4.2-5. The probe beam was a linear polarized output of LD pumped Nd:YVO₄ laser. The 1-inch CCD detector was placed at 300 cm distance from the laser output coupler and ARM was placed at 150 cm distance from the laser output coupler. The ARM resonance at 1064 nm wavelength and TE polarization (E vector is co directional to the grating grooves) has corresponded to the incidence angle of about 10°. As can be seen from the Fig. 4.2-5 (red curve), at resonance, the central part of the beam is almost totally reflected while the sidebands of the beam are partially passed through the structure since the angular divergence of the beam exceed the angular width of the ARM resonance. On the other hand, the slight tilt of the ARM has caused the total disappearance of resonance reflections (black curve on the Fig. 4.2-5). Thus, very strong angular (and hence spectral) selectivity of the fabricated ARM structure have been experimentally confirmed.

The laser experiments with ARM gratings have been carried out using LiF crystals with F₂⁻ color centers as a laser active medium. The optical pump source was passively Q-switched Nd:YLF laser at 1047 nm with 10 mJ pulse energy and 20 ns pulse duration. Schematic of the LiF:F₂⁻ laser with ARM cavity is shown in the Fig. 4.2-6. The LiF:F₂⁻ laser crystal was 60 mm long and plane-parallel cut. The laser was longitudinally pumped through the ARM. The cavity output coupler (OC) was the uncoated end of the laser crystal (3 % Fresnel reflection). The pump beam was focused in the crystal by the cylindrical lens. The laser active region has rectangular shape with dimensions variable by the diaphragm D from 10×0.5 mm to 0.5×0.5 mm.

The experimental measurements were carried out for the laser cavity equipped by ARM's with grating depth of 50 and 150 nm (ARM-50 and ARM-150 further in this section) and, for a comparison, by a standard dichroic mirror. The wavelengths of ARM laser operation were about 1170 nm for ARM-50 and 1120 nm for ARM-150. The shift of the resonance wavelengths from the expected positions (1167 nm and 1159 nm, see Fig. 4.2-3) is caused mostly by deviation of the actual grating grooves shape from perfect rectangular shape, which was con-

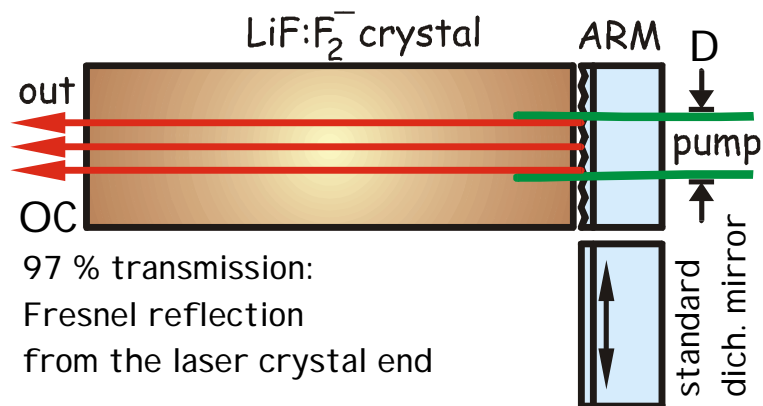


Fig. 4.2-6 Schematic of LiF:F₂⁻ laser with ARM cavity

sidered during the ARM modeling and optimisation.

The linewidth measurements were made using a set of Fizeau interferometers with different free spectral range (FSR). Dependencies of the laser linewidth $\Delta\nu$ as functions of the active region width D are shown in the Fig. 4.2-7. In accordance with the theoretical predictions, ARM-50 with weaker grating provides narrower laser output.

More interesting fact is that the linewidth depends on the active region width as well. The minimal linewidth of 0.35 cm^{-1} was measured for the ARM-50 and $1 \times 0.5 \text{ mm}$ laser active volume. For the full aperture of the pump beam ($10 \times 0.5 \text{ mm}$) the laser linewidth was measured about 3.5 cm^{-1} for ARM-50 and 10 cm^{-1} for ARM-150. When the cavity was equipped with standard mirror the laser linewidth as high as 450 cm^{-1} was measured. Thus, the use of ARM diffractive optics has provided 2 – 3 orders of magnitude improvement of the laser spectral characteristics.

The spatial divergence of the laser output of about 2 - 3 mrad was measured for both ARM's that was 5 - 7 times better than for the laser with standard mirror. It was found that the beam divergence of the ARM laser does not depends strongly on the active region width.

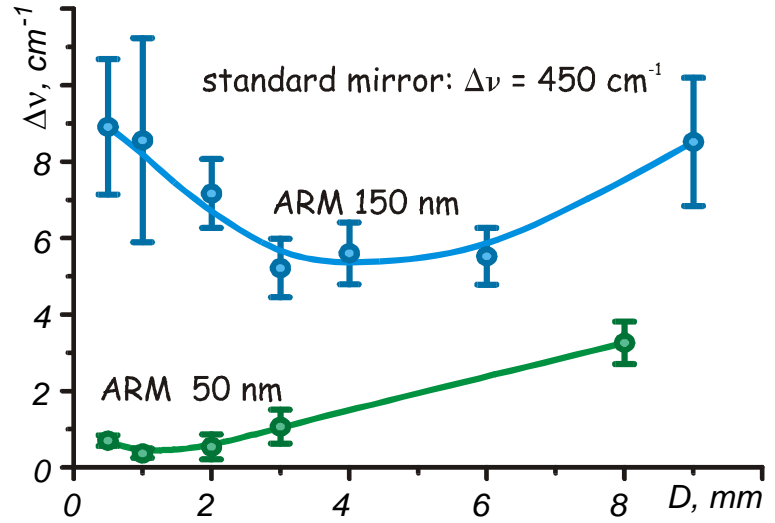


Fig. 4.2-7 ARM laser linewidth vs. active region width D

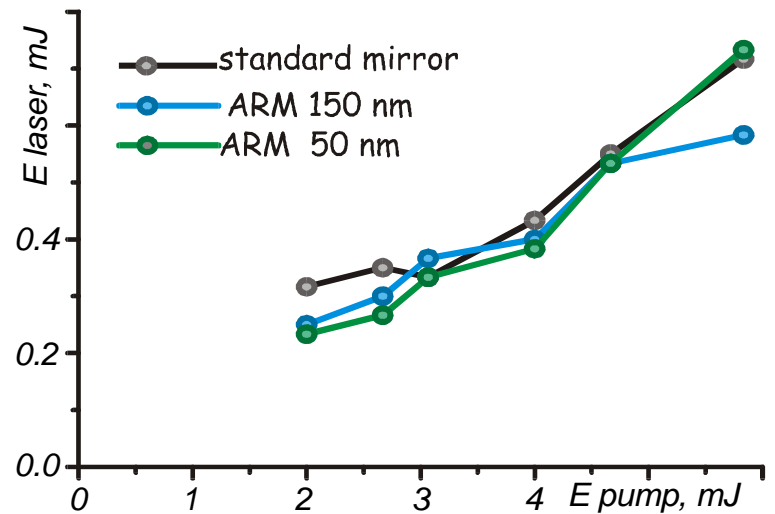


Fig. 4.2-8 ARM laser output vs. pump pulse energy

The ARM laser output energy was measured for the full aperture of the pump beam. Dependencies of the laser output energy as functions of the pump pulse energy are shown in the Fig. 4.2-8. One can see that the ARM laser output energy almost the same as for the laser with standard optics. Taking into account high transmission of the output coupler (97 %) one can estimate close to 100 % limit reflection from the ARM structure and abnormal reflection peak width of the same order as the laser emission linewidth. We expect that the laser efficiency (13 %) as well as its spectral and spatial characteristics could be improved by optimization of the output coupler transmission and laser crystal length.

4.2.4. Summary and conclusions

We have proposed and experimentally tested a novel cavity design for high power narrowband lasers. Our approach is based on the use of efficient dielectric grating diffractive optical elements in combination with slab geometry of the laser active element. Proposed cavity scheme allows increasing the volume of the laser active medium and scaling-up the laser power without deterioration of spectral and spatial quality of the laser output and reduction of the laser efficiency. Proposed cavity schemes are suitable for both the LD-pumped solid-state lasers and for new types of ultra low quantum defect lasers.

The dielectric diffraction grating fabrication technology has been developed. The technology is based on holographic process of the grating recording and use of inorganic chalcogenide glass photoresist. The vacuum photoresist deposition technique reduces to minimum the number of grating defects and variations of grating parameters. Thus, the technology allows manufacturing of large size high optical quality dielectric gratings.

The laser experiments with fabricated dielectric gratings have been carried out using LiF crystals with F_2^- color centers as a laser active medium. Efficient narrowband large active medium volume laser operation was achieved using very simple ARM cavity design. Compared with the same cavity configuration equipped by standard dielectric mirror, the use of ARM diffractive optics has improved thoroughly the spectral and spatial characteristics of the laser output: the ARM laser exhibited 2 - 3 orders of magnitude smaller linewidth (3.5 cm^{-1}) and 5 - 7 times better beam divergence (2 mrad) at the same conversion efficiency (13 %). That allows estimating close to 100 % narrowband reflection from ARM structure.

4.2.5. References

- 1 Botten, I.C., Craig, M.S., McPhedran, R.C., Adams, J.L. and Andrewartha, J.R. “*The dielectric lamellar diffraction grating*” *Optica Acta*, **v.28**, pp.413-428 (1981).
- 2 L. Li “*Multilayer modal method for diffraction gratings of arbitrary profile, depth, and permittivity*” *J. Opt. Soc. Am. A*, **v.10**, pp.2581-2591 (1993).
- 3 L. Li “*Bremmer series, R-matrix propagation algorithm, and numerical modeling of diffraction gratings*”, *J. Opt. Soc. Am. A*, **v.11**, pp.2829-2836 (1994).
- 4 S V Vasil'ev, V A Sychugov “*Simple method for optimisation of parameters of a combined diffraction grating at grazing incidence*” *Quantum Electronics*, **v.31** pp.72-78 (2001)
- 5 M.D. Perry, R.D. Boyd, J.A. Britten, D. Decker, B.W Shore, C. Shannon, E. Sults “*High-efficiency multilayer dielectric diffraction gratings*” *Optics Letters*, **v.20**, pp.940-942 (1995)
- 6 J.A. Britten, M.D. Perry, B.W. Shore, R.D. Boyd “*Universal grating design for pulse stretching and compression in the 800-1100-nm range*”, *Optics Letters*, **v.21**, pp.540-(1996)
- 7 B.W. Shore, M.D. Perry, J.A. Britten, R.D. Boyd, M.D. Feit, H.T. Nguyen, R. Chow, and G.E. Loomis, “*Design of high efficiency dielectric reflection gratings*” *J. Opt. Soc. Am. A* **v.14**, pp.1124–1136 (1997)
- 8 K. Hehl, J. Bischoff, U. Mohaupt, M. Palme, B. Schnabel, L. Wenke, R. Bödefeld, W. Theobald, E. Welsch, R. Sauerbrey, and H. Heyer, “*High-efficiency dielectric reflection gratings: design, fabrication, and analysis*” *Applied Optics* **v.38**, pp.6257-6271 (1999)
- 9 S.V. Vasil'ev “*Efficient diffraction grating for use in a grazing-incidence configuration*” *Quantum Electronics*, **v.28**, pp.416-419 (1998)
- 10 G.A. Golubenko, A.S. Svakhin, V.A. Sychugov, and A.V. Tischenko, “*Total reflection of light from a corrugated surface of a dielectric waveguide,*” *Sov. J. Quantum Electron.* **v.15**, pp.886–887 (1985).
- 11 I.D. Avrutskii, G.A. Golubenko, V.A. Sychugov, and A.V. Tischenko, “*Light reflection from the surface of a corrugated waveguide,*” *Sov. Tech. Phys. Lett.*, **v.11**, pp.401–402 (1985)
- 12 L. Mashev and E. Popov, “*Zero order anomaly of dielectric coated gratings*” *Opt. Commun.* **v.55**, pp.377–380 (1985).

- 13 D.K. Jacob, S.C. Dunn, M.G. Moharam, “*Design considerations for narrow-band dielectric resonant grating reflection filters of finite length*” J. Opt. Soc. Am. A **v.17**, pp.1241-1249 (2000)
- 14 Z.S. Liu, S. Tibuleac, D. Shin, P.P. Young, and R. Magnusson, “High-efficiency guided-mode resonance filter” Optics Letters, **v.23**, pp.1556-1558 (1998)
- 15 Z. Hegedus and R. Netterfield, “*Low sideband guided-mode resonant filter*” Applied Optics, **v.39**, pp.1469-1473 (2000)